Thèse en cotutelle avec
l'Université de Borås (Suède) et l'Université de Soochow (Chine)

3D Printing of polymers onto textiles :
an innovative approach to develop functional textiles
L'impression 3D de polymères sur textiles :
une approche innovante pour développer des textiles fonctionnels

Présentée par :

Prisca Aude EUTIONNAT-DIFFO

Pour obtenir le grade de Docteur de l'Université de Lille

Discipline : Mécanique des solides, des matériaux, des structures et des surfaces

Soutenue le 1er Décembre 2020 devant la commission d'examen

Prof: Abdelaziz LALLAM	Université de Haute-Alsace	Rapporteur
Prof: Barbara SIMONČIČ	University de Ljubljana	Rapporteur
Prof: Hui WANG	Université de Sochoow	Examinateur
Prof. Yan CHEN	Université de Sochoow	Examinateur
Prof. Jeremie SOULESTIN	IMT Lille Douai	Examinateur et Président du jury
Dr. Nils-Krister PERSSON	Université de Borås	Invité
Prof : Xianyi ZENG	Université de Lille/Génie des Matériaux Textiles	Invité
Prof. Christine CAMPAGNE	Université de Lille/Génie des Matériaux Textiles	Co-directeur
Prof. Vincent NIERSTRASZ	Université de Borås	Co-directeur
Prof. Jinping GUAN	Université de Sochoow	Co-directeur
Prof. Aurélie CAYLA	Université de Lille/Génie des Matériaux Textiles	Co-encadrant

Acknowledgments

I would like to express my sincere appreciation and gratitude to my dear co-supervisors Prof. Vincent Nierstrasz, Prof. Christine Campagne, Prof. Aurelie Cayla, Prof. Xianyi Zeng, Prof. Jinping Guan, and Prof. Yan Chen for giving me the opportunity to work on such an interesting research project. Their constructive criticisms, inputs, encouragement and supervision have guided me toward the production of this thesis.

I would like to thank my opponent Prof. Dr: Barbara Simoncic and my reviewer Prof. Dr: Abdelaziz Lallam , for offering valid and valuable comments and insights. Thank you to all the jury members of my defense for their time and their great comments and feedback.

I wish to thank Dr. Yuyang Zhou and Katarina Lindström Ramamoorthy for the Swedish and Chinese translations of the thesis abstract.

Thank you to all the people who supported me during my PhD journey at the University of Borås (HR, IT, etc.) and most specifically Magnus Bratt, Dr. Eva Gustafsson and Petri Granroth. Big thanks to the professors, lecturers, researchers and technicians who shared with me their advice and expertise particularly Dr. Andrers Persson, Dr. Junchun Yu, Stig Abrahamson, Hanna Lindholm and Haike Hike. Thank you to the employees of FOV limited principally Mr. Jesper Calsson for the opportunity of using their laboratory for testing and for their great support. To all the great researchers and friends, Nett, Sweta, Razieh, Molla, Tuser, Yuyang, Milad, Katarina, Sina, Tarun, Vijay, May, Felicia, Sheenam, Emanuel and Veronica, thank you for making these one year and half so interesting and full of memories. I wish to thank in particular my dear colleague and friend Sweta with who I have been working on innovative concepts that combine both our knowledge and thesis fields.

De plus, j'aimerai exprimer ma gratitude à l'ensemble du personnel de l'ENSAIT/GEMTEX et de l'Université de Lille pour leur soutien tout au long de ma mobilité en France. Je me souviendrai notamment de la patience et de l'efficacité de Marion Houyvet, Marie Hombert; Dorothée Mercier, Ludovic Macaire, Thi Nguyen et Malika Debuysschere. Un énorme remerciement à Guillaume Lemort, François Dassonville, Christian Catel, Louis Marischal, Vivien Barral, Ahmed Addad, Alexandre Fadel, pour leur aide très précieuse dans la réalisation des matières premières ainsi que l'exécution des essais et tests de caractérisation. Je souhaite vivement remercier Nicolas Martin et Lola Andrian d'Euromaterials pour l'opportunité d'utiliser leurs équipements dans le cadre de ma thèse ainsi que l'immense soutien apporté pendant cette période en France. Un énorme merci à mes deux stagiaires Jane Martin et Baptiste Marco pour leur soutien et leur bon travail. Merci à l'ensemble des doctorants et chercheurs du GEMTEX qui, pour certains sont devenus de vrais amis. Je vais notamment me souvenir de ma collègue de bureau et super amie Zineb, vraiment merci pour ton écoute et nos fous rires en toutes circonstances. Je n'oublie

évidemment pas Vivien, Louis, Charles, Maximilien, Shukla, Julie, Wenquian, Kehui, Balkiss, Henri, Anne-Clémence, Valentin, Nathalie, Nitin, Baptiste, Romain, Mulat et tous ces très bons moments passés ensemble.

To my former colleagues from Autoenum for their supportive words and messages. I was pleased to see some of you during my PhD journey.

To my current colleagues from Autins, thank you for welcoming me to the team and company, encouraging me and believing in me throughout the pre-defense and defense steps.

A mes meilleurs amis (to my best friends), mes amis de cœur et à ma famille qui ont su être là pour moi dans les bons comme les moments difficiles de ces trois années, plus particulièrement, Eppy, Clarisse et Ismaël, Madina et Louiny, Olivia, Lindsay, Michaël, Krystel, Lilia, Aurore, Marylin, Marius, Nicolas, Clarissa, Hubert, Lucas, Loic, Ludovic, Willem, Pascal, Jacky et Aga. A tous mes amis qui ne sont pas cités et qui ont été là pour moi je ne vous oublie pas et vous remercie du fond du cœur. A toi Lilia, merci d'avoir partagé avec moi cette opportunité de thèse trois jours avant la date limite de dépôt de dossier. Un immense merci d'avoir cru en moi dès le début.

A mes sœurs Sandy et Orianne Eutionnat, ma nièce Mayou, ma filleule Lilis et ma mère Manès Délivert, merci pour ces agréables moments ensemble.

Un immense merci à mon papa d'amour Dr. Luc Eutionnat pour ton soutien permanent, ta bienveillance, ton amour, ta joie et ta bonne humeur partagées au quotidien, tes encouragements et tes conseils. Tu as toujours su trouver les mots justes pour me booster dans mes études et ma vie personnelle.

A mon compagnon, mon meilleur ami, l'amour de ma vie, mon mari, mon tout, mon chaton d'amour, Dr. Denis Diffo un infini merci pour ton amour, ton soutien, ta positivité, d'être à mes cotés à chaque instant et surtout merci de me supporter au quotidien et me soutenir dans tous mes choix.

Thank you very much

Tack så mycket

Merci beaucoup

非常感謝你

Mèsi an pil

Dedication

To my lovely and precious husband Dr. DenisDiffo

To my super-daddy Dr. Luc Eutionnat

Abstract

This thesis aims at characterizing tridimensional (3D) printed polymers onto PET textile materials via fused deposition modeling (FDM) that uses both non-conductive and conductive polymers, optimizing their mechanical and electrical properties through statistical modeling and enhancing them with pre and post-treatments and the development of biphasic polymer blends. This research work supports the development of technical textiles through 3D printing that may have functionalities. The FDM process was considered in this thesis for its strong potential in terms of flexibility, resource-efficiency, cost-effectiveness tailored production and ecology compared to the existing conventional textile finishing processes, for instance, the digital and screen printings. The main challenge of this technology is to warranty optimized electrical and mechanical (bending, flexibility, tensile, abrasion, etc.) properties of the 3D printed polymer onto textiles for the materials to be used in textile industry. Therefore, the development of novel 3D printed polymers onto PET materials with improved properties is necessary.

First of all, 3D printed non-conductive Polylactic Acid (PLA) and PLA filled with 2.5wt% Carbon-Black filled onto PET fabrics were purchased and manufactured through melt extrusion process respectively, to characterize their mechanical properties including adhesion, tensile, deformation, washability and abrasion. Then, the relationship between the textile structural characteristics and thermal properties and build platform temperature and these properties through statistical modeling was determined. Subsequently, different textile pre-treatments that include atmospheric plasma, grafting of acrylic acid and application of adhesives were suggested to enhance the adhesion properties of the 3D printed PLA onto PET fabrics. Lastly, novel biophasic blends using Low-Density Polyethylene (LDPE) / Propylene- Based Elastomer (PBE) filled with multi-walled carbon nanotubes (CNT) and high-structured carbon black (KB) were developed and manufactured to improve the flexibility, the stress and strain at rupture and the electrical properties of the 3D printed PLA onto PET fabric. The morphology, thermal and rheological properties of each blends are also accessed in order to understand the material behavior and enhance the mechanical and electrical properties.

The findings demonstrated that the textile structure defined by its weft density and pattern and weft and warp yarn compositions has a significant impact on the adhesion, deformation, abrasion, tensile properties of 3D printed PLA onto PET fabrics. Compromises have to be found as porous and rough textiles with low thermal properties showed better wash-ability, adhesion and tensile properties and worse deformation and abrasion resistance. Statistical models between the textile properties, the platform temperature and the 3D printed PLA onto PET materials properties were successfully developed and used for optimization. The application of adhesives on treated PET with grafted acrylic acid did significantly improve the adhesion resistance and LDPE/PBE blends, filled with CNT and KB that have co-continuous LDPE and PBE phases as well as CNT and KB selectively located at the PBE/LDPE interface and in the LDPE phase, revealed enhanced deformation and tensile and electrical properties.

Keywords: 3D printing, Fused deposition modeling, Adhesion, Textile Functionalization, Statistical Modeling, Non conductive and conductive polymer, Multi-walled carbon nanotube, Carbon Black, Deformation, Tensile, Abrasion, Biphasic polymeric bends

Résumé

Cette thèse vise à caractériser des polymères imprimés tridimensionnellement (3D) sur des matériaux textiles PET via une méthode de dépôt de polymère fondu connu sur le nom de Fused Deposition Modeling (FDM) utilisant à la fois des polymères non conducteurs et conducteurs. Les propriétés mécaniques et électriques ont été optimisées par le biais de modèles statistiques et améliorées grâce à des pré et post-traitements ou le développement de mélanges de polymères. Ce travail de recherche apporte de nouveaux résultats sur le développement de textiles techniques par l'impression 3D de polymères fonctionnels. Le procédé FDM a été considéré dans cette thèse pour son fort potentiel en termes de flexibilité, d'efficacité des ressources, de production sur mesure et d'écologie par rapport aux procédés de finition textile conventionnels existants, par exemple, les impressions numériques et sérigraphiques. Le principal enjeu de cette technologie est de garantir des propriétés électriques et mécaniques optimisées (flexion, flexibilité, traction, abrasion, etc.) du polymère imprimé en 3D sur les textiles afin d'être utilisé dans l'industrie textile. Par conséquent, le développement de nouveaux polymères imprimés en 3D sur des matériaux PET avec des propriétés améliorées est nécessaire.

Dans un premier temps, de l''acide polylactique (PLA) non conducteur et du PLA contenant 2.5% de noir de carbone ont été imprimé en 3D sur des tissus en PET. Les polymères conducteurs ont été fabriqués par le procédé d'extrusion à voie fondu. Les propriétés mécaniques, notamment d'adhésion, de traction, de déformation, de résistance au lavage et d'abrasion ont été déterminées. Ensuite, la relation entre les caractéristiques structurelles et thermiques du textile et la température du plateau de l'imprimante 3D et ces propriétés par le biais de modèles statistiques a été déterminée. De plus, différents pré-traitements sur textiles incluant le plasma atmosphérique, le greffage d'acide acrylique et l'application d'adhésifs ont été suggérés pour améliorer les propriétés d'adhésion du PLA imprimé en 3D sur les tissus en PET. Enfin, de nouveaux mélanges biophasiques utilisant du polyéthylène basse densité (LDPE) et un élastomère à base de propylène (PBE) contenant de nanotubes de carbone à parois multiples (CNT) et de noir de carbone à haute structure (KB) ont été développés et fabriqués pour améliorer la flexibilité, le la contrainte et la déformation à la rupture et les propriétés électriques du PLA imprimé en 3D sur le tissu PET. La morphologie, les propriétés thermiques et rhéologiques de chaque mélange sont également determinées afin de comprendre le comportement du matériau et l'amélioration de ses propriétés mécaniques et électriques.

Les résultats ont démontré que la structure textile définie par sa densité en trame, son motif et la composition des fils de trame et de chaîne a un impact significatif sur l'adhésion, la déformation, l'abrasion et les propriétés de traction du PLA imprimé en 3D sur les tissus en PET. Des compromis doivent être trouvés car les textiles poreux, rugueux possédant de faible conductivité thermique ont montré de meilleures propriétés de lavage, d'adhésion et de traction et une moins bonne résistance à la déformation et à l'abrasion.

Des modèles statistiques entre les propriétés textiles et le PLA imprimé en 3D sur des matériaux PET et les propriétés ont été développés avec succès et utilisés pour les optimiser. L'application d'adhésifs sur des tissus en PET traité avec de l'acide acrylique greffé a considérablement amélioré la résistance d'adhésion.

Par ailleurs, les mélanges LDPE / PBE de phases co-continues et contenant du CNT et de KB localisés à l'interface ou dans la phase LDPE a révélé améliorer considérablement la déformation et les propriétés de traction et électriques des imprimés 3D sur textiles.

Mots clés: Impression 3D, Modélisation par dépôt de polymère fondu, Adhésion, Fonctionnalisation textile, Modélisation statistique, Polymère non conducteur et conducteur, Nanotube de carbone multi-parois, Noir de carbone, Déformation, Traction, Abrasion, Mélanges de polymères biphasiques

Abstrakt

Denna avhandling syftar till att karakterisera tredimensionella (3D) tryckta polymerer på textila material av polyester (PET) via *fused deposition modeling* (FDM) som använder både icke-ledande och ledande polymerer, optimerar deras mekaniska och elektriska egenskaper genom statistisk modellering samt förbättrar dem med för- och efterbehandlingar och utvecklingen av polymerblandningar. Detta forskningsarbete stöder utvecklingen av tekniska textilier genom 3D-utskrift som kan ha funktioner. FDM-processen valdes i denna avhandling för sin stora potential i flexibilitet avseende process, resurseffektivitet, kostnadseffektiv skräddarsydd produktion och ekologi jämfört med befintliga konventionella textilbearbetningsprocesser, till exempel digital- och skärmtryck. Den huvudsakliga utmaningen med denna teknik är att garantera optimerade elektriska och mekaniska egenskaper (böjning, flexibilitet, drag, nötning, etc.) för 3D-tryckta polymerer på textilier för material att användas i textilindustrin. Därför är utvecklingen av nya 3D-tryckta polymerer på PET-material med förbättrade egenskaper nödvändig.

Först och främst köptes icke-ledande polylaktid (PLA) och PLA fylld med 2,5 viktprocent kimrök tillverkades genom smältextrudering och 3D-trycktes på PET-tyger, för att karakterisera deras mekaniska egenskaper inklusive vidhäftning, draghållfasthet, deformation, tvättbarhet och nötningstålighet. Därefter bestämdes förhållandet mellan textilens strukturella och termiska egenskaper och plattformstemperatur och dessa egenskaper bestämdes genom statistisk modellering. Därefter testades olika textila förbehandlingar så som atmosfärisk plasma, ympning av akrylsyra och applicering av lim för att förbättra vidhäftningsegenskaperna hos 3D-tryckt PLA på PET-tyger. Slutligen utvecklades och tillverkades nya biofasiska blandningar med lågdensitetspolyeten (LDPE) / propylenbaserad elastomer (PBE) fyllda med flerväggade kolnanorör (CNT) och högstrukturerad kimrök (KB) för att förbättra flexibiliteten, spänning och belastning vid bristning och de elektriska egenskaperna hos 3D-tryckt PLA på PET-tyg. Morfologin, samt de termiska och reologiska egenskaperna hos varje blandning analyserades också för att förstå materialegenskaper och förbättrade mekaniska och elektriska egenskaper.

Resultaten visade att textilstrukturen så som den är definierad av dess väfttäthet och konstruktion och väft- och varpgarnskompositioner har en signifikant inverkan på vidhäftning, deformation, nötning och dragegenskaper hos 3D-tryckt PLA på PET-tyger. Kompromisser måste göras eftersom porösa och grova textilier med låga termiska egenskaper visade bättre tvättförmåga, vidhäftning och dragegenskaper och sämre deformation och nötningsbeständighet. Statistiska modeller mellan textilegenskaperna, 3D-tryckt PLA på PET-material och egenskaperna har framgångsrikt utvecklats och använts för optimering. Applicering av lim på behandlad PET med ympad akrylsyra förbättrade signifikant vidhäftningsresistensen och LDPE/PBE-blandningar fyllda med CNT och KB som har ko-kontinuerliga LDPE- och PBE-faser samt CNT och KB selektivt belägna vid gränssnittet och i LDPE-fasen gav förbättrad deformation, drag- och elektriska egenskaper.

Nyckelord: 3D-utskrift, smält deponeringsmodellering, vidhäftning, textilfunktionalisering, statistisk modellering, icke ledande och ledande polymer, flerväggigt kolnanorör, kolsvart, deformation, draghållfasthet, nötning, bifasisk polymerböjning

摘要

本论文旨在通过熔融沉积成型（FDM）将导电和非导电高分子材料通过3D打印到纺织品上。通过数据建模分析来优化纺织品的机械性能和导电性能，并通过纺织品的前处理和后处理来增强性能，以开发功能性高分子共聚物。本研究有助于3D打印功能性技术纺织品的研发。本研究采用的熔融沉积成型过程跟传统的纺织品整理过程如数码或筛网印花相比，具有较高的加工灵活性，原料使用的高效性以及成本低廉的优势。熔融沉积成型3D打印技术的关键在于确保加工后的纺织具有最优的电学和力学性能（弯曲、柔韧、拉伸、耐摩擦等）。因此，对熔融沉积成型3D打印技术应用于纺织品的研究具有十分重要的意义。

本课题首先通过熔融加工制备了含有2.5wt%炭黑的PLA复合材料并将其运用于PET织物上，并对该织物和3D打印非导电PLA材料进行机械性能包括粘附性、拉伸性、变形性、可洗性和摩擦性进行表征。运用数据建模分析了纺织品结构特征和热学性能以及加工平台温度的关系。然后通过不同的纺织品前处理过程如大气压等离子体、丙烯酸接枝和粘合剂应用以增强3D打印的PLA与PET织物的粘合性。最后，使用填充有多壁碳纳米管（CNT）和高结构炭黑（KB）的低密度聚乙烯（LDPE）/丙烯基弹性体（PBE）制备新型二相共混物，以提高PLA 3D打印PET织物的柔韧性、断裂应力应变以及电学性能。同时，对复合物的表面结构、热学性能和流变性能进行表征以了解材料机械和电学特性。

试验表明，织物的结构如纬密，样式以及经纬纱线的成分对3D打印PLA在PET织物上的粘附性、变形性、摩擦性和拉伸性能有明显影响。多孔和具有较低热学性能的粗糙的纺织品具有较好的可洗性、粘附性和拉伸性，变形性和耐磨性较差。通过数据建模分析对PLA 3D打印PET织物的性能进行分析和优化。将丙烯酸作为粘合剂运用于PET织物上时可以明显的提高粘合性。LDPE/PBE与CNT和KB的复合物具有共连续的LDPE和PBE相，且CNT和KB有选择性的分布于界面和LDPE相中的，从而提高了耐变形性和力学以及电学性能。

关键词：3D打印，熔融沉积成型，粘附性，纺织品功能性，数据建模，导电与非导电高聚物，多壁碳纳米管，炭黑，变形性能，拉伸性能，摩擦性能，二相高分子共混物。

Preface

The entire presented thesis work was conducted in these three research laboratories:

- Textile Materials Technology, Department of Textile Technology, Faculty of Textiles, Engineering and Business, University of Borås, SE-501 90, Borås, Sweden
- GEnie des Matériaux TEXtile (GEMTEX), École Nationale Supérieure des Arts et Industries Textiles (ENSAIT), F-59100, Roubaix, France
- College of Textile and Clothing Engineering, Soochow University, Suzhou, Jiangsu, 215006, China

A version of Chapter 3 was already published in Rapid prototypying journal [*P.A. Eutionnat-Diffo, Y. Chen, J. Guan, A. Cayla, C. Campagne, X. Zeng, V. Nierstrasz, Optimization of adhesion of poly lactic acid 3D printed onto polyethylene terephthalate woven fabrics through modeling using textile properties, Rapid Prototyp. J. (2020). https://doi.org/10.1108/RPJ-05-2019-0138*] and submitted in Rapid prototypying journal [*P.A. Eutionnat-Diffo, A. Cayla, C. Campagne, V. Nierstrasz, Enhancement of adhesion properties of polylactic acid monofilament 3D printed onto polyethylene terephthalate fabrics through surface functionalization and use of adhesives, Rapid Prototyp. J. (2020)*]. I was the main investigator, responsible for planning and conducting the experiments, data analysis and writing of the manuscript. The other authors were supervising the research work and giving advices throughout the project on findings interpretation and manuscript editing.

A version of Chapter 4 was published in Scientific reports and Materials journals [*P.A. Eutionnat-Diffo, Y. Chen, J. Guan, A. Cayla, C. Campagne, X. Zeng, V. Nierstrasz, Stress, strain and deformation of poly-lactic acid filament deposited onto polyethylene terephthalate woven fabric through 3D printing process, Sci. Rep. 9 (2019). https://doi.org/10.1038/s41598-019-50832-7*] and [*P.A. Eutionnat-Diffo, Y. Chen, J. Guan, A. Cayla, C. Campagne, V. Nierstrasz, Study of the Wear Resistance of Conductive Poly Lactic Acid Monofilament 3D Printed onto Polyethylene Terephthalate Woven Materials, Materials (Basel). 13 (2020) 2334. https://doi.org/10.3390/ma13102334*]. I was the main investigator, responsible for planning and conducting the experiments, data analysis and writing of the manuscript. The other authors were supervising the research work and giving advices throughout the project on findings interpretation and manuscript editing.

A version of Chapter 5 was submitted in the Smart textiles –special issue [*P.A. Eutionnat-Diffo, Y. Chen, J. Guan, A. Cayla, V. Nierstrasz, C. Campagne, Development of Flexible and Conductive Immiscible Thermoplastic/Elastomer Monofilament for Smart Textiles Applications using 3D Printing, 12(10), 23. doi: https://doi.org/10.3390/polym12102300 (2020)*]. I was the main investigator, responsible for planning and conducting the experiments, data analysis and writing of the manuscript. The other authors were supervising the research work and giving advices throughout the project on findings interpretation and manuscript editing.

The papers and proceedings, listed below, are not included in this version of the thesis but can be found on the particular publisher's print or electronic databases. Each research work was accepted for oral presentation or poster and the conferences were internationally recognized by the scientific community.

Eutionnat-Diffo, P. A. *et al.* (2018). Correlation between heat transfer of polyester textiles and its adhesion with 3D-printed extruded thermoplastic filaments. In 18th AUTEX World Textile Conference, June 20-22, 2018, Istanbul, Turkey.

Eutionnat-Diffo, P., *et al.* (2018). Investigation of tensile properties of direct 3D printed conductive and non-conductive poly lactic (PLA) filaments on polyester woven textiles In Aachen-Dresden-Denkendorf International Textile Conference, Stuttgart Germany, November 29-30, 2018
Best poster award at Aachen-Dresden-Denkendorf International Textile conference at Stuttgart in Germany (29-30 November 2018).

More information on : https://www.hb.se/en/About-UB/Current/News-archive/2019/January/Presentation-on-3D-printed-polymers-won-at-a-major-conference/
Eutionnat-Diffo, P. A. *et al.* (2019). Study of the electrical resistance of smart textiles made of three-dimensional printed conductive poly lactic acid on polyester fabrics. In 19th World Textile Conference on Textiles at the Crossroads, 11-15 June 2019, Ghent, Belgium.
Eutionnat-Diffo, P. A. *et al.* (2019). Adhesion improvement of conductive poly-lactic acid filament 3D printed onto polyethylene terephthalate fabric through chemical bonding. In 2nd International Conference on 3D Printing, 3D Bioprinting, Digital and Additive Manufacturing (I3D19) Thessaloniki, Greece, 1-5 July, 2019.

Eutionnat-Diffo, P. A. *et al.* (2019). Développement et caractérisation de mélange de polymères immiscibles chargés pour impression 3D sur textiles. In JEPO 2019; 29 Septembre-4 Octobre 2019, Aérocampus de Latresnes.

Iyer, S., Eutionnat-Diffo, P A., Nierstrasz, V., Campagne, C., *et al.* (2019). 3D printed conductive photoluminescent filament using flavinmononucleotide molecule for smart textile applications. In Aachen-Dresden-Denkendorf International Textile Conference, Stuttgart Germany, November 29-30, 2019. (Work not included in the thesis).

Eutionnat-Diffo, P. A. *et al.* (2020). A novel and sustainable technology for development of durable and flexible smart textiles: 3D printing onto textiles. IFATCC International Congress, 22-24 April 2020, Roubaix, France

Eutionnat-Diffo, P. A. *et al.* (2020). Effect of textiles' surface on the properties of conducting polymers composites deposited onto textile through 3D printing. Euromaterials 2020; 24-26 March 2020, Paris, France

Table of content

List of tables

List of figures

List of abbreviations

AA	Acrylic acid
ABS	Acrylonitrile butadiene styrene
ACHN	1,1′-Azobis(cyclohexanecarbonitrile)
AM	Additive manufacturing
BP	Benzophenone
CAD	Computer-aided design
CB	Carbon black
CCVD	Catalytic chemical vapor decomposition
CNT	Carbon nanotube
CPC	Conductive polymer nanocomposite
DBD	Dielectric barrier discharge’
DLD	Delay line detector
DSC	Differential scanning calorimetry
DWNT	Double-walled nanotubes
EAc	Ethyl acetate
EMI	Electromagnetic interference
Eq	Equation
FAT	Fixed analyzer transmission
FDM	Fused deposition modeling
FFF	Fused filament fabrication
GEMTEX	Genie des materiaux textiles
GMA	Glycidyl methacrylate
HDPE	High density polyethylene
ICI	Imperial chemical industry
KB	Ketjenblack
LED	Light-emitting diode
LDPE	Low-density polyethylene

LLDPE	Linear low density polyethylene
MDI	Metered-dose inhaler
MFI	Melt flow index
MMA	Methyl methacrylate
MWNT	Multi-walled carbon nanotubes
NW	Nonwoven
PAM	Pellet additive manufaturing
PA(6 or 6.6)	Polyamide (6 or 6.6)
PBE	Propylene based-elastomer
PBT	Polybutylene terephthalate
PDLA	Poly (d-lactic acid)
PE	Polyethylene
PEDOT	3,4-ethylenedioxythiophene
PEEK	Polyether ether ketone
PEI	Polyetherimide
PET	Polyethylene terephthalate
PLA	Polylactic acid
PLLA	Poly (l-lactic acid)
PP	Polypropylene
PPy	Polypyrrole
PSA	Pressure sensitive adhesive
PSS	Polystyrene sulfonate
PVC	Polyvinyl chloride
QSAR	Quantitative structure activity relationship
SAS	Statistical analysis system
SEM	Scanning electron microscopy
SMDTex	Sustainable management and design for textiles

SPSS	Statistical package for the social sciences
STL	Stereolithography
SWNT	Single-walled nanotubes
TEM	Transmission electron microscopy
TGA	Thermogravimetric analysis
Tg	Glass transition temperature
TPU	Thermoplastic polyurethane
UV	Ultraviolet
VAc	Vinyl acetate
W	Woven
XPS	X-ray photoelectron spectroscopy
2-EHA	2-Ethylhexyl acrylate
3D	Three dimensional
3D-PPOT	Three dimensional printing of polymer onto textiles
4 D	Four dimensional
4W	4-wire ohms measurement

Introduction

Over the past few years, the textile materials industry has offered to the market new innovations that create interesting and strong perspectives as a result of the emergence of new advanced finishing processes such as both Fused Deposition Modeling (FDM) and digital printing. FDM process has been widely used to freely design any object from simple to extremely complex shape through an easy-to-use software and using polymeric materials with acceptable mechanical and thermal properties.

However, depending on the targeted applications, the polymers utilized in the FDM process should respond to certain requirements. In case of Three Dimensional Printing of Polymers Onto Textiles (3D-PPOT), the polymers should be as flexible and mechanically strong as the fabrics and their adhesion has to be sufficient. Despite the research work done previously in order to apply FDM of non-conductive and conductive polymers on textiles' surface [1–6], many improvements are necessary for it to be widely utilized in many domains such as textile fashion design, medical accessories, reinforced protection equipments and functional textiles.

Functional textiles are created to enhance the life quality, the health and the way-of-living of people by using wearable technologies and integrating electronics in the textile materials. However, no solution was suggested combining comfort, mobility and easy-to-wear. "Intelligent" textiles are one of the potential applications of 3D printing using FDM process. It could allow the direct deposition of conducting polymers directly onto textiles.

Indeed, 3D printing present several advantages such as the several possibilities of customization, the reduced amount of waste after the process, the rapid prototyping and the possibility to print onto textiles complex shapes with variable thicknesses [7,8]. However, some challenges of this technology exist including its design not fully applicable for textile materials.

Therefore, since 2014, a group of three partners University of Borås (Sweden), GEnie des Materiaux TEXtiles (GEMTEX) / Ecole Nationale Superieure des Arts et Industries Textiles (France) and Soochow university (China) was created to deliver scientific knowledge of the 3D printing of polymers onto textiles technology. The research project, started in September 2017 and described in this thesis manuscript, is the continuation of the thesis work executed by Dr. Razieh Sanatgar and defended in September 2019. The entire work is part of an Erasmus Mundus joint Doctorate Program SMDTex - Sustainable Management and Design for Textiles financed by the European Union and Chinese government.

This thesis is divided into five chapters described as follows:

- Chapter I: **State-of-art**’

  In this chapter, a detailed literature review of the research topic is suggested. The review includes the 3D printing technology in general and the existing and recent work on the 3D printing onto textile materials. The main objectives and research approaches are also stated in this part.

- Chapter II: **Materials and Methods**

  This chapter presents the materials (textiles, polymers, etc.), the 3D printing process and other functionalization processes such as air- plasma treatment and the characterization methods which were used to determine the thermal and mechanical properties, the rheology and the surface morphology of the materials.

- Chapter III: **Characterisation and improvement of adhesion properties of 3D-PPOT using monophasic materials**

  This chapter describes the findings of the various methods used to enhance the adhesion strength of 3D-PPOT materials using monophasic materials. First, the optimization through statistical modeling, connecting the textile properties and process parameters to the adhesion force was investigated. Then , the functionalization through air-plasma treatment and grafting of acrylic acid followed by adhesive application were approached and their results presented and interpreted.

- Chapter IV: **Deformation, wear and tensile properties of 3D-PPOT using monophasic materials**

  In this chapter, the deformation, the abrasion resistance, the stress and the strain of 3D-PPOT using monophasic materials were enhanced through statistical models linking these properties to fabric properties and process parameters.

- Chapter V: **Enhancement of the deformation, tensile and electrical properties of 3D-PPOT by using biphasic materials**

  This chapter demonstrates the improvement of tensile, deformation and electrical properties of 3D-PPOT biphasic polymeric materials made of conducting polymer composites and elastomers.

Finally, a general conclusion of the overall thesis is suggested at the end of the thesis report.

Chapter I State of the art

This chapter describes the relevant literature regarding functional textiles field and their manufacturing process through deposition of conductive polymers onto the textiles field using 3D printing. *Section I.1* defines the FDM process onto textiles *Section I.2* relates the different properties of the 3D printed polymers onto textiles (adhesion between the 3D printed track and the textile material, abrasion resistance, wash ability, tensile properties and flexibility) and the manners of improving these properties. *Section I.3* presents the potential applications and *Section I.4* introduces the reader to the main scopes, objectives and approaches of the research project.

I.1 3D Printed Polymers Onto Textiles (3D-PPOT)

The integration of the functional elements into a textile has always been the main challenge in functional textiles area. The fulfillment of the requirements of a functional textile that include cost, fabric resistance, comfort, flexibility and reliability, an integration of technologies and functionalities, systems and applications is important to be considered through an interdisciplinary methodology. Thus, the use of 3D printing as a deposition technique of polymeric materials onto textiles reveals to be an interesting option to create added value functional textiles which possess the features that contribute to our economic and societal needs. Indeed, if a specific design or function needs to be added onto the surface of the textile, the 3D-PPOT technique is a more flexible, resource-efficient and cost-efficient functionalization method compared to the conventional screen method. This can be explained by the minimization of raw material waste combined with reduced consumption of energy, water, and chemicals creating a stronger ecological footprint. Besides, it allows thicker layers on textiles without a full penetration of the polymeric materials compared to the inkjet printing method. Additionally, a positive effect on the textile supply chain process, the free-customization of various designs with complex shapes can be highlighted with this technique Indeed, the energy consumption of the supply chain is reduced by designing and integrating the functional elements where it is needed on the textiles at the same step.

I.1.1 Presentation of FDM process

FDM process, also called Fused Filament Fabrication (FFF) is one of the Additive Manufacturing (AM) processes which was patented by Crump in 1988 and later trademarked by Stratasys. Indeed, by using polymeric materials (usually thermoplastic materials) in the form of a filament, granulates or paste (Figure I-1) the technique can manufacture complex geometries. In addition to the FDM process, other processes are included in the AM industry, for instance the material jetting, powder bed fusion, material extrusion, sheet lamination, directed energy deposition, photo polymerization, and binder jetting also presented in Figure I-1. Several 3D printers using this technique are commercially available for some applications, which are not connected to textile businesses yet. Among the various existing processes, the FDM one reveals to be the most suitable and practical for textile materials.

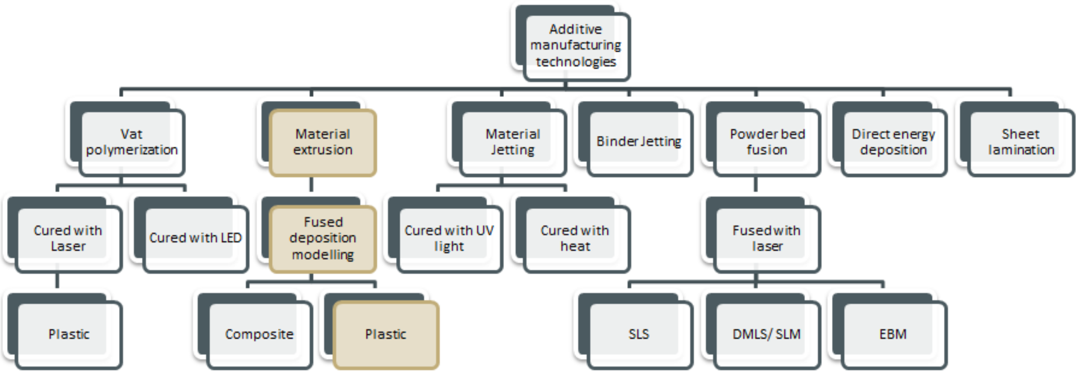

Figure I-1 Additive Manufacturing (AM) processes [9]

FDM process is a melt extrusion AM process where the heated extruder melts the filament as the extruder temperature is always set above the melting point of the polymer used depending on its viscosity. The 3D printing head assembly moves over a platform via stepper motors (Figure I-2). The melted polymer is pushed through the extruder towards the nozzle which deposits it along on the XY plane platform. Either the platform moves down or the 3D printing head moves up along the Z direction by exactly one layer thickness after the completion of the deposition at the successive cross-section. Thus, with this principle, the three-dimensional (3D) structure is created in a layer-by-layer technique. This process goes on until the part is built. The melting mechanism in the FDM process is governed by upon the time taken for solidification.

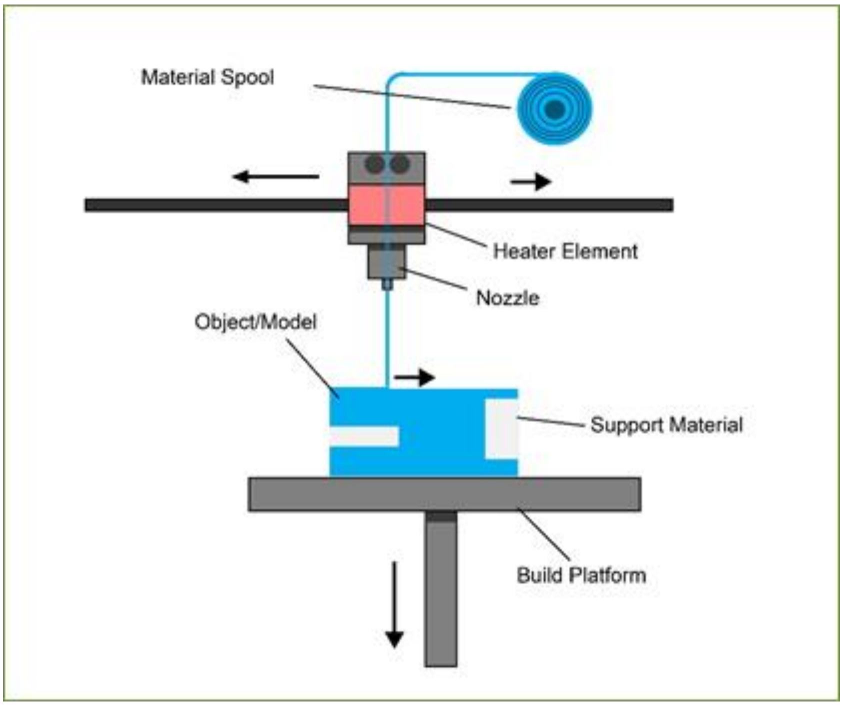

Figure I-2 FDM process [10]

The FDM process is executed following these steps:

1. The design/pattern of the desired object is created through a Computer-aided design (CAD) software
2. The CAD file is imported into the software of the 3D printer
3. All the parameters of the printer and the trial (including the design) are set and saved as an stereolithography (STL) file format
4. The SLT file is loaded in the 3D printer system to start the printing layer by layer. The printing is executed using the extrusion method of the polymeric material. Indeed, the thermoplastic polymer goes through the heated nozzle of the 3D printer before meeting the platform or bed (that can be heated)
5. Once the trial is finished, the object can be removed and its aesthetic improved through polishing for instance.

Numerous applications of FDM exist in many fields [11–15] and their percentage contribution in the literature is represented in Figure I-3. As an example, a mixture of starch-based polymer dust (corn starch, dextran and gelatine) was developed by Lam *et al.* to be used in FDM process. With this new mixture the mechanical and chemical properties were enhanced after 3D printing and post-treatment. Moreover, intake was manufactured using the FDM technique for automotive applications [16]. Electrically conductive polymers are created by FDM [17]. Espalin *et al.* explored the customization of orthopedic inserts and craniofacial reconstruction by using FDM of biocompatible poly-methylmethacrylate [18]. Diegel *et al.* produced electronic circuits created by curved layer made of conductive plastic through FDM [19]. Besides, the manufacturing of dental repairs is possible using the FDM technique [20]. Scaffold for organ printing and tissue engineering were printed FDM process. Korpela *et al.* have tried to use poly (e-caprolactone)/bioactive glass mixture to create decomposable porous scaffold structures [11]. Xu *et al.* manufacture polycaprolactone/hydroxyapatite artificial bones in order to imitate goat femur through computed tomography-guided FDM [21].

In addition, the FDM process is a more flexible, resource-efficient and cost-efficient technique which allows the printing of patterns by following a design without the need of any mold as it is the case with the injection molding process. Besides, through this technique, the anisotropy of the parts is better due to higher intra-layer bonding than interlayer one. As a result, sometimes, it is necessary to expose the parts to gamma radiation to create cross-link between and within the layers and thus, enhance the properties of the 3D printed part [22].

Hence, the development of functional textiles is based on the management of the 3D printing process presented above and the creation of novel polymer blends and Conduting Polymer Composites (**CPCs**) which present better properties and are easily used for the FDM process described in the next subsection.

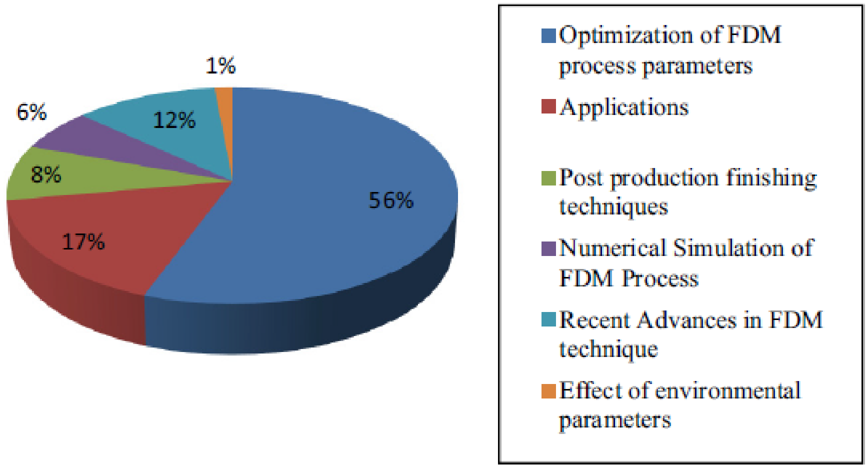

Figure I-3 FDM process: percentage contribution in the literature [15]

I.1.2 Introduction to Conductive Polymers Composites (CPCs)

The term “ composite “ in the polymer science field means at least two materials have joined or merged together in order to obtain a new material that presents different properties than those of each component. In the case of Conductive polymer composites (CPCs) materials (Figure I-4), the two components are an insulating matrix and electrically conductive charges. The matrix is often a polymeric material that possesses electrical insulating properties and the fillers are electrically conductive charges under various forms (microparticules, nanoparticles, fibers, rods, etc.). As stated by Jones *et al.*, “polymers are macromolecules that are composed of repeated subunits connected together” [23]. They are categorized into thermoplastics or thermosets shown in Figure I-5. The thermoplastics (e.g., polypropylene, polyethylene, polyvinyl chloride, etc.) are soft when heated and hard when cooled. These two states are totally reversible and repeatable. They are mainly linear polymers and branched structure polymers with flexible chains. In contrast to thermoplastic polymers, thermosets (e.g., polyester, epoxy, phenolic resins, etc.) do not soften when heated again due to strong covalent crosslinks. With better dimensional stability, thermoset polymers are commonly harder and stronger than thermoplastics. For 3D printing applications, the thermoplastics are the most used.

In general, the structural materials such as metals and their alloys exhibit elastic behavior, i.e. after a loading and unloading of the material within elastic limit, the instantaneous strain developed will disappear [24]. The stress induced in the material remains constant with time upon further constant deformation. In addition, the induced state of stress is dissipated in viscous materials. However, polymers possess a unique characteristic of viscoelasticity. In nature, a viscoelastic material exhibits both viscous and elastic behaviors which depend on the material’s microstructure and chemistry [24]. In the case of polymers, the stretching and binding of the atomic bonds create immediate strain and the chain uncoiling of the molecules provoke a delayed elastic response.

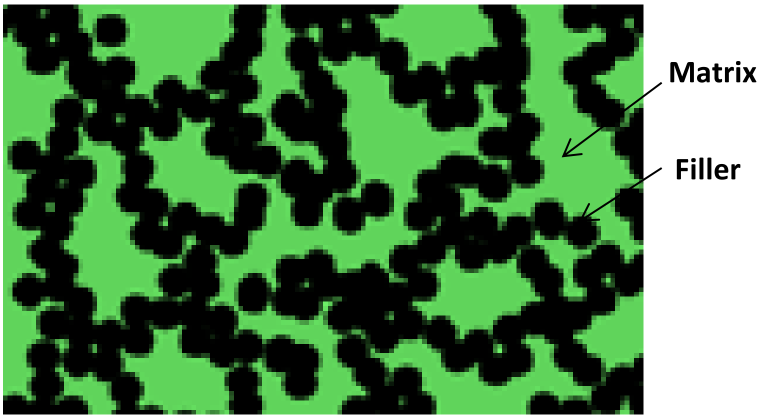

Figure I-4 Sketch of Conductive Polymer Composite materials

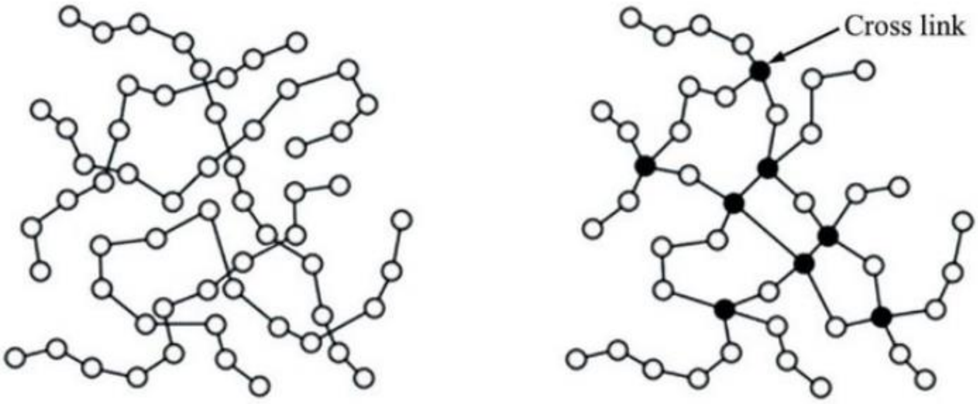

Figure I-5 Thermopastics (in left) and thermosets (in right) [25]

There are three distinct main classes of conductive charges used in CPCs described as follows:

1) Metallic (copper, silver, aluminum, nickel, etc.).
2) Carbon (graphite, carbon black (CB), carbon nanotubes (CNT), graphene, etc.).
3) Intrinsically Conductive polymers (polypyrrole (PPy), polyaniline, Poly (3,4-ethylenedioxythiophene) (Poly) (PEDOT), etc.).

Metallic materials are known for their excellent electrical and heat conductor as well as their high surface energy which leads to fast oxidation. Besides, carbon-based charges show excellent thermal stability and relatively low cost except for CNT and graphene materials. Intrinsically conductive polymers are defined as materials that alternatively present alternating single and double bonds between carbon atoms along the polymer main chains. Based on such bond conjugation and distribution, conduction bands and broad valence are generated. As a result, an interesting class of materials combining the mechanical features of the polymers (often thermoplastic) combined with the electrical properties of the conductive charges.

However, conductive polymers present several challenges such as their insolubility in commonly used organic solvents, their feeble mechanical properties and reduced processabiity. Although their high conductivity influenced by several factors (conjugation length, charge transfer to adjacent molecules), their good stability, their flexibility and their lightweight have attracted considerably researchers for more than 20 years, their use remains limited in the domain of functional textiles due to their high cost [26].

The extrusion process is the main process used to manufacture polymeric filaments with a specific diameter for 3D printing technology. The filament can be converted into granulates in a next step. Additionally, in the case of manufacturing of CPC materials using carbon-based fillers are firstly dispersed into the matrix. Different polymeric matrices such as Acrylonitrile butadiene styrene (ABS), Polylactic acid (PLA), Polyether ether ketone (PEEK) and PLA/ABS and ABS/Polyamide 6 (PA6 or Nilon) blends are mainly used for 3D printing applications. The influence of the 3D printing process parameters on the mechanical and chemical properties (tensile, surface roughness, porosity, print quality, elastic modulus,etc.) is investigated and summarized in the Table I-1 [8,15].

PLA is the most widely studied and exploited biodegradable and renewable aliphatic polyester. Also, defined as a bio absorbable polymer, PLA is one of the most encouraging biopolymers due to a non-toxic renewable production from feedstock of the monomers [27,28].

High density polyethylene (HDPE) which is defined as a polyolefin thermoplastic was already used in 3D printing by Schirmeister *et al.* [29]. Despite many existing challenges such as the shrinkage, the voiding and the warpage of the materials, HDPE-based 3D printed part with improved mechanical properties (tensile strength and Young's modulus) can obtain with appropriate 3D printing parameters such as nozzle temperature and extrusion rate [29]. In addition, softer thermoplastic polymers than the commonly used in 3D printing such as the ABS and PLA still need to be explored. Low-density Polyethylene (LDPE) is described as a polymer polymerized from ethylene and a highly branched structure composed of both long and short branches that interfere with crystallization. It possesses a very low glass transition and lower percent crystallinity that makes it softer and more flexible at ambient temperature compared to other thermoplastic polymers [30]. Furthermore, by adding fillers into polymer an increase of the viscosity and stiffness of the CPCs and decrease of its 3D printing process ability can be noticed [31–34].

As a notice, the CPCs are defined as electrically conducting nanoparticles- filled insulating polymeric matrix above the percolation threshold. The sensing mechanism of CPCs is based on the polymer's reaction to environmental changes which affect the electrically conductive CNT network. For instance, the change in temperature of the environment leads to modify the resistance of the CPCs [34–37]. Recently, some research has been conducted in order to combine both the FDM technology and CPCs materials to create 3D printed conductive composites with specific functions. As an example, the electrical, thermal and mechanical properties of 3D printed MWNT/ABS composites were investigated by Dorigato *et al.* [38].

Table I-1 Influence of the 3D Printing process on the properties of the 3D printed parts [15]

Material	Process parameter	Response	Significant factor

ABS	Raster orientation, air gap, model temperature and color, bead width	Tensile and compressive strength	Air gap and raster orientation
ABS	Air gap, raster width, build layer and build profile, build orientation	Compressive strength, compressive modulus and porosity	Air gap and raster width
ABS	Layer thickness, speed of deposition, road width and their interaction	Surface finish	All factors
PEEK	Raster angle and build orientation	Tensile strength, flexural strength and fracture toughness	All factors
PLA	Raster angle	Elastic constant	Raster angle
ABS	Contour width, contour depth, raster width, raster angle	Profile error and extruding temperature	All factors
ABS	Raster angle, air gap, orientation and raster width	Tensile strength and density	All factors
ABS	Chemical vapour	Surface roughness, hardness and thermal behaviour	All factors
ABS	Raster angle, slice height, raster width	Visco-elastic properties	Slice height and raster width
ABS	Print speed, nozzle temperature, layer temperature, fan speed	Print quality, elastic modulus and ultimate tensile strength	Fan speed, layer thickness
ABS P400	Orientation, raster angle, raster width, layer thickness, air gap	Tensile, flexural and impacts strength	All factors
ABS	Extrusion velocity, filling velocity, layer thickness, line width compensation	Dimensional error, warp deformation, and build time	All factors
ABS, ULTEM	Air gap	Thermal conductivity, and inter-layer thermal resistance	All factors
PLA	Raster angle, layer height and raster width	Flexural strength	Raster angle
ABS P400	Layer thickness, orientation, raster angle, air gap and raster width	Dimensional accuracy	Part orientation
CFRP	Infill speed, nozzle temperature and layer thickness	Tensile properties	All factors
PLA	Infill percentage or relative density, thickness, component orientation, extrusion temperature, orientation, infill direction, speed	Tensile and flexural properties	Layer thickness and speed
ABS **Nylon**	Shell thickness, model orientation, layer thickness	Ultimate tensile strength and dimensional accuracy	Orientation angle and shell thickness

They have noticed that the 3D printing direction might influence the mechanical and electrical properties of 3D printed objects. Lebedev *et al.* have developed 3D biodegradable scaffolds and heat sinks using PLA conductive composites containing single-walled carbon nanotubes and powder of natural graphite through 3D printing or injection molding [39]. Gnanasekaran *et al.* created 3D printed CNT-based or graphene-based Polybutylene terephthalate (PBT) parts [40]. The findings demonstrated that 3D printed PBT/CNT objects have better conductive and mechanical properties as well as performance compared to the 3D printed PBT/graphene structures. Besides, the electrodes and lightweight electromagnetic interference (EMI) shielding materials can be potentially created through 3D printing of these CPCs structures.

With the purpose of better understanding the properties of the 3D printed polymers onto textiles, there is an important need to highlight the mechanical and electrical properties of the conductive polymer composites in the next *section 1.1.3.*

I.1.3 Properties of Conductive Polymers Composites (CPCs) after 3D printing

I.1.3.1 Electrical properties and percolation phenomenon

An increase of the concentration of the conductive charges in the CPCs leads to relatively increase the polymer matrix content, and therefore the electrical conductivity rises up to a certain value. However, this former sentence is true only if the conductive fillers or charges are completely well-dispersed in the polymer matrix. In reality, the increase of the electrical conductivity is not linear and three zones of the conductivity characteristic can be identified depending on the concentration of conductive fillers and their arrangements that create conductive paths in the polymer matrix as shown in Figure I-6. First, the resistivity is slowly decreased forming a superior asymptote. Zone I represents the state in which the conductive particles are very few in the polymer and cannot form conductive paths. In that case, the CPC is either insulator or has its electrical resistivity is close to the one of the virgin polymer (ρm). Zone II is characterized by a rapid decrease of electrical resistivity corresponding to the comparatively small difference in the concentration of the conductive particles. The amount of fillers is high enough to be connected to each other and form conductive network. The state of the zone II is called the percolation threshold (φ_c) and can be reached as a result of direct contact between the fillers or tunneling effect. The percolation theory is given by the **Eq. I.2**. The last zone (III) is a curve which is horizontally asymptotic which means that the concentration of conductive particles does not influence the resistivity. The electrical conductivity (or resistivity) highly depends on the nature and the shape of the particles [31,41].

$$\sigma_c = \sigma_0(\varphi_f - \varphi_c)t \qquad \textbf{(Eq. I.2)}$$

where σ_c is the electrical conductivity of the CPC (S/cm); σ_0 , the filler electrical conductivity (S/cm); φ_f, the fraction of conductive filler (v/v or wt. %); φ_c, the percolation threshold (v/v or wt. %) and t, the critical exponent as a fitting parameter.

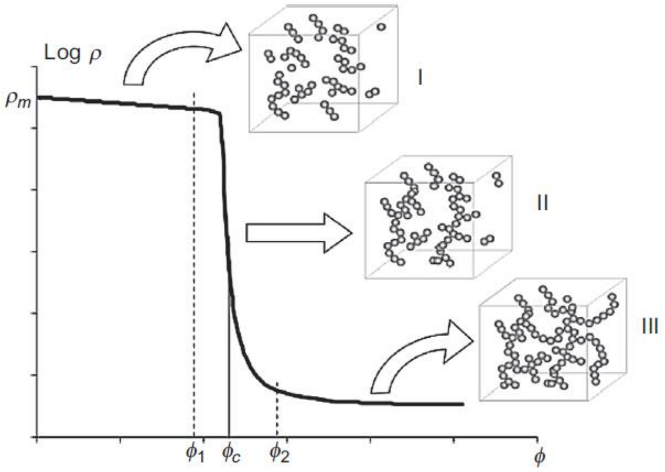

Figure I-6 Evolution of the Log of the resistivity of a conductive polymer composite according to the concentration of the conductive fillers and their arrangements (I, II and III) [41]

Furthermore, Sanatgar *et al.* investigated the influence of the cross-sectional area of the 3D printed tracks composed of 5% highly structured carbon-black (KB)–filled PLA and 2.5% multi-walled carbon nanotubes (MWNT) on their electrical properties [31]. They found that the resistance exponentially decreases with an increase of the cross-sectional area (Figure I-7). In another study, they could prove that the electrical conductivity and percolation threshold of PLA based- CPCs depend on the type of fillers used (KB or MWNT) as shown in Figure I-8. Indeed, the percolation threshold happens happened when wt.% KB and 1 wt.% MWNT are added into PLA [31].

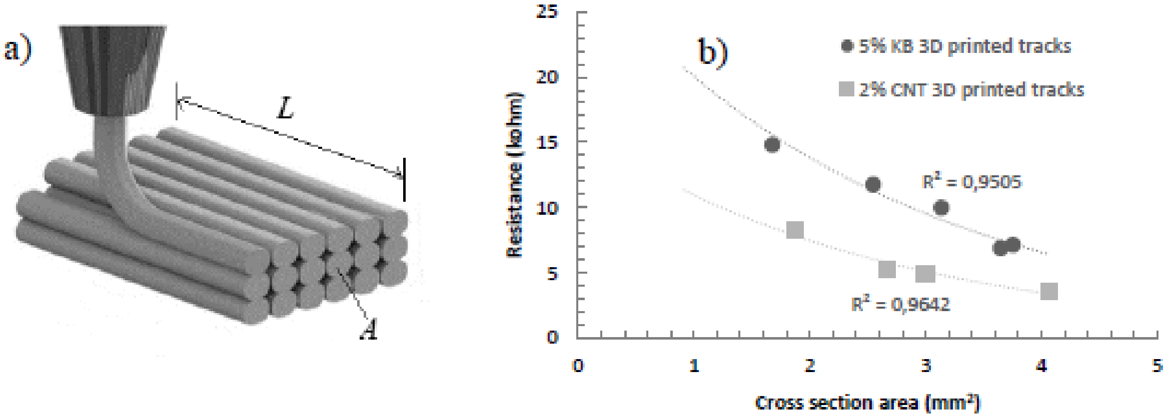

Figure I-7 (a) Schematic of 3D printing of the conductive tracks (b) Resistance (kΩ) as a function of the cross-section area (mm2) of 3D printed tracks made of 2% MWNT -filled PLA and 5% KB- filled PLA [31]

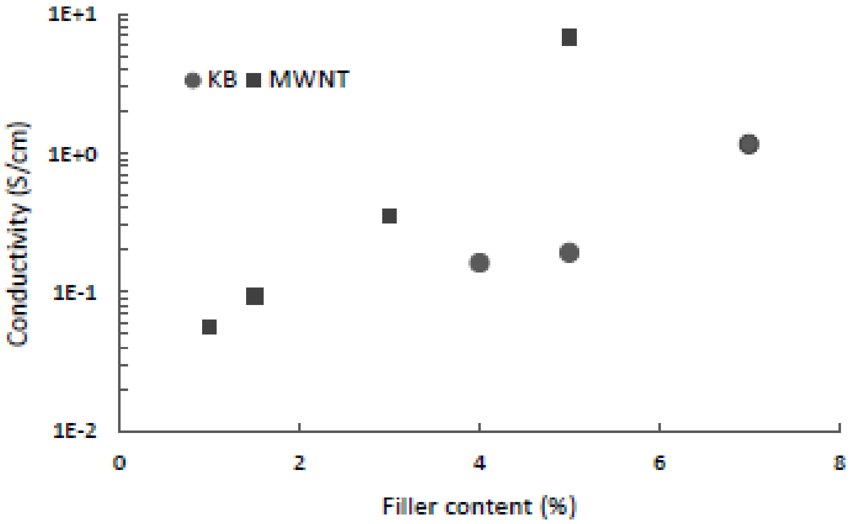

Figure I-8 Electrical conductivity as a function of the filler content in the case of 3D printed layers of PLA [31]

I.1.3.2 Mechanical properties

Formerly, researchers demonstrated that the mechanical properties of parts produced through AM technique were mostly influenced by both the manufacturing process parameters and the physico-chemical properties prior to printing [42]. Mechanical anisotropy is the main issue of elements created through FDM process which was largely due to the shrinkage of the extruded thermoplastic deposited by the 3D printer on the 3D printer platform, the layer-to-layer adhesion and the changeable porosity of the printed track under tension and pressure [43–48]. The majority of the studies put their attention on tensile and yield strengths and elongation at break of the 3D printed elements made of the most commercial filaments (ABS, PLA,..etc.) [49]. The layer thickness [50], the orientation of the filament and the build platform [45,49,51], the gap between the roads [45], the printing trajectory [52], the raster angle [45,49–51] and other printing parameters [49,53–56] have been defined as parameters which could influence the mechanical performance of the 3D-printed elements. Somireddy *et al.* also investigated the impact of the layer thickness, road shape and air gap on the elastic moduli of a 3D printed layer through FDM process [47]. Moreover, the highest tensile strength of printed PLA sample was found in the case of a printing using a 45^{o} raster angle [49]. Tensile yield strength and tensile modulus of virgin PLA were 40.3 MPa and 4258 MPa respectively [43]. Besides, it was shown that the denser and thinner the layer of the 3D printed specimens, the greater the tensile strength [45,50].

In addition, it is well-known that polymeric blends or blended materials have the tendency to diminish the anisotropy of the tracks [1,22,46,57]. Therefore, fillers or reinforcements are incorporated in polymers to improve their mechanical properties [58]. Several studies have reported the mechanical properties of 3D printed using CPC materials [59–62]. The effect of the process parameters and textile characteristics on mechanical properties of printed textiles through other printing techniques such as digital printing was already explored and publicized to be significant for fabric density and printing speed [63].

I.1.3.3 Thermal properties

The thermal properties of FDM parts were also approached by many researchers. For example, Masood and Song assessed the thermal properties of a new CPC material made of iron- filled nylon and found them to be acceptable for fast tooling for injection molding process [64]. Sun *et al.* (2008) investigated the effect of thermal factors on the cooling and overall qualities of the parts, their esostructure and flexural strength and the bonding strength between the printed layers. Finally, the envelope temperature and differences in the convection coefficient were found to be the most impacting process parameters [65]. Gurrala and Regalla explored the influence of solidification process of the parts on the adhesion between the filaments to the strength of the components through experimental approaches and mathematical modeling. They found that the bonding strength was highly dependent on the intra-layer and inter-layer bonds [66].Singh Boparai *et al.* studied the mass and phase change of a Nylon 6-based nano-composite material through differential scanning calorimetry (DSC) and thermogravimetric analysis (TGA) [67]. Prajapati *et al.*described the experimental measurement technique of the interlayer thermal contact resistance and anisotropic thermal conductivity by changing the air-gap between the FDM parts made of ABS and Polyetherimide (PEI). Also, an analytical model was utilized to predict the thermal conductivity of the corresponding air-gaps. Besides, there is a strong thermal contact resistance in building direction due to the anisotropy in the parts produced [68].

I.1.3.4 Quality and performance improvements of the FDM parts

Most of the investigations concerning the quality and performance enhancements of the FDM parts presented in Figure I-9 were focused on improving the surface finish, the build time, dimensional exactness and static mechanical properties, such as compressive, tensile, impact and flexural strengths [15,45,69,70]. Additionally, research studies on dynamic mechanical properties for instance viscoelastic and morphological properties and process reliability are increasing nowadays [71–74]. However, limited literature is available on process parameter optimization related to thermal, chemical and magnetic properties enhancement for various filament materials [65–67,75]. Agarwala *et al.* categorized the process parameters such as the material temperature, the layer height, the extrusion speed and temperature, the bead width, and the raster fill pattern and cited them as potential solutions for parts quality improvements. In addition, the filament and nozzle diameters, the material flow and feed rates, and thermal conductivity, viscosity, flexibility and stiffness of the material are also properties to consider for a better part quality [71].

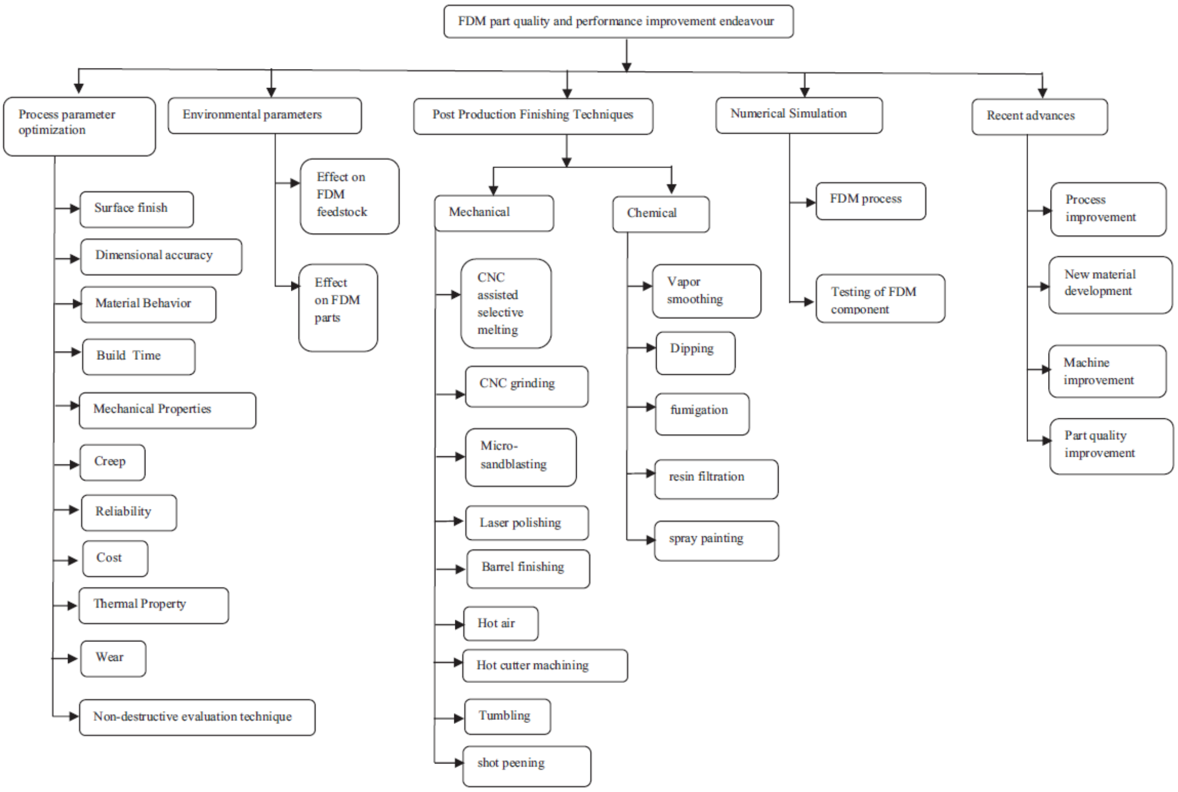

Figure I-9 Categorization of the FDM part quality and performance improvement techniques based on literature [69]

It has been already published that 3D printing technologies via FDM attracted widespread interest because of its very low waste of raw materials, flexibility, low-cost and easily handled apparatus and raw materials. As a result, this technology is utilized more and more at laboratory level, to incorporate functional elements into textile materials through deposition of thin layers of conductive thermoplastic filaments. Some researchers have already started to contribute into the development of functional textiles by using 3D printing technologies [2,4,5,76–80]**.** The adhesion properties and the wash ability of the 3D-PPOT materials were the two main properties investigated by the scientific community up to now.

I.2 Properties of 3D-PPOT materials

I.2.1 Adhesion between the textile and the deposited layer and its enhancement

The adhesion resistance between the fabric and the printed layer was the main focus of research work as it is one of the fundamental properties of 3D-PPOT materials for functional textiles.

I.2.1.1 Mechanisms and theories of adhesion

Adhesion refers to the ability of two materials to remain bonded to each other. In general, the two materials are called the adhesive and the substrate (i.e. adherent). This adhesion can be mainly explained by different types of interactions between the surfaces and their surface area [81].

The adhesion mechanisms of materials are mainly explained by mechanical interlocking, physical absorption, chemical bonding, diffusion and dispersive theories. The diffusion theory explains that the adhesion between polymers is caused by their compatibility and the movements of their chains under certain conditions. An high compatibility between the polymers their chains are observed if they are able to be merged which results in a mutual diffusion of polymer molecules across the interface and therefore, a better adhesion occurs [82]**.** This theory has been used to understand various findings on adhesion between CPCs deposited onto textiles through FDM process. Indeed, the adhesion strength was found to be higher in the case of PLA-based CPCs printed onto PLA fabrics compared to Polyamide 6.6 (PA 6.6) or Polyethylene terephthalate (PET) fabric. Another outcome, that found its explanation in the diffusion theory, is the better diffusion of the molecules, leading to the formation of stronger bonds between the polymeric material and the textile substrate chains, is obtained by higher extruder temperature [2]. Nonetheless, the diffusion theory possesses limited applications where the polymer and the substrate may perhaps not adhere due to highly cross-linked or crystalline polymers applied at a temperature below their glass transition temperature [82]. In addition, the diffusion theory can hardly explicate the change in the adhesion strengths between 3D printed CPCs and surfaces made of the same polymer that could be smooth and rough such as textile fabrics. For this reason, researchers mostly utilized the mechanical adhesion theory in order to explain bonding of any materials to textiles [82–99]. This theory explains the enhancement of the adhesion strength based on the mechanical interlocking principle. Mechanical interlocking mechanism refers to a adhesion strength between an adhesive and rough and porous substrate stronger than to a smooth and closed surface. Indeed, in that case, the adhesive can penetrate through the pores of the rough surface and be entangled mechanically to the substrate. However, some findings demonstrated using rough surfaces could lead to a decrease of the adhesion force [100]. Additionally, dispersive adhesion is due to rather weak intermolecular forces called Van der Waals Forces, which are in all materials. The Van der Waals forces have longer bond lengths than those of the intra-molecular forces (London forces) but they are still short, thus, they act over very small distances [81]. In chemical adhesion, the atoms/molecules of the two adhering materials create chemical bonds that could be of covalent or ionic character. This is commonly the strongest form of adhesion because the polymers adhere to a substrate at multiple sites along the chain [81].

Some of these mechanisms and theories of adhesion were used by researchers in order to explain the adhesion findings of 3D-PPOT materials using CPCs. The recent results are presented in the next sub-section.

I.2.1.2 Factors influencing the adhesion strength of 3D-PPOT

Several researchers proved that textile characteristics such as the fabric density, pattern and yarn type, the affinity between the printed polymer and the textile materials [101], the selected polymer of the textile structure[2] and the 3D printing process parameters as the extruder temperature, the speed, the infill angle and the platform temperature [2–6,101], had an important impact on the adhesion properties of 3D-PPOT materials.

First, the possible applications of 3D printing technology on textile base materials was explored Korger *et al.* Based on visual assessments, they found that rough and thick textiles presented better adhesion and an increase of the wettability of the textile surface could enhance its adhesion performance [76]. In addition, Sanatgar *et al.* tried to understand the adhesion behavior between PLA, carbon black (CB) and multi-wall carbon nanotube (MWCNT) – filled PLA monofilaments 3D printed onto PLA, PA6, PA66 textile base materials and the influence of the 3D printing parameters [2].They found that the printing speed and the extruder temperature were the most impacting parameters of the adhesion resistance compared to the platform temperature. The platform temperature did not have influence because its range was lower than the glass temperature (Tg) of the PLA (Tg_{PLA} = 60°C). Also, they have introduced statistical models that showed a significant linear effect of extruder temperature and significant quadratic effect of printing speed on the adhesion strength of PA6.6 and PA6 printed onto PA6.6 fabric. There is no significant effect of the platform temperature on adhesion force for a temperature lower than the glass transition temperature of the fabric [2]. An increase of the printing platform temperature up to 100˚C (above the glass temperature) for PLA printed onto PET fabric led to enhance the adhesion force while affecting the print quality [4]. Besides, an extrusion wide identical to nozzle diameter shows the uppermost adhesion and a thicker first 3D-printed layer declined the adhesion [4]. Moreover, Tadesse *et al.* studied the adhesion of thermoplastic polyurethane (TPU) monofilament 3D printed onto PEDOT:PSS-Coated polyester and cotton plain weave fabrics for electroluminescence applications [80]. The adhesion strength of acrylonitrile butadiene styrene (ABS), poly-lactic acid (PLA) and PA6 (nylon) 3D printed directly onto fabrics using FDM was investigated by Pei *et al.* (2015) [102].

Deposited PLA could not adhere to woven cotton, viscose, wool fabrics and showed a better adhesion on net polyester with fixed pattern on fabric [103]. The adhesion of 3D printed polymers on knitted fabrics as textile materials was explored [5,78]. The distance between the printing nozzle and printing bed is another significant factor which impact the adhesion force. The results exposed that the smaller z distance result in higher adhesion forces due to a higher pressure applied on the fabric during the 3D printing process [104]. Eutionnat-Diffo *et al.* point out that higher mean pore size and roughness coefficient and lower thermal conductivity of polyester woven textile materials enhance the adhesion properties and the build platform quadratically affects this property. The pores of the PET fabrics that were mainly located at their surface. Additionally, the washing process affects significantly the adhesion strength decreases by half by rougher and more porous textile structures are more durable. The findings are mainly explained by the surface topography of the textile materials which allow more anchorage areas between the two materials. Reliable statistical models were also developed in order to predict the adhesion properties with the textile characteristics [101]. The influence of the unevenness of the textile surface and the fiber–fiber friction inside the fabric on the adhesion to the polymer has also to be considered during the development of 3D-PPOT materials [105]. Finally, the impact of fabrics made of cotton, polyester and acrylic fibers on the adhesion to PLA –based 3D printed layer were approached. Based on regression models, the findings indicated that fabric areal density, warp count (Tex), weft count (Tex), fabric thickness and fabric handle positively influence the adhesion of PLA onto woven fabrics while warp ends/inch and weft picks/inch are negatively correlated with the adhesion strength [106].

I.2.1.3 Improvement of adhesion of 3D-PPOT materials

The adhesion properties of the 3D-PPOT materials reveal to be too low until now especially in the case of soft fabrics. Thus, some studies were conducted in order to enhance the bonding strength between the 3D printed layers and the textile.

A higher adhesion was obtained by pre-treating a cotton fabric substrate through coating of glue stick, washing , and ironing processes [107]. Indeed, the enhancement of adhesion strength between the layers was due to the creation of covalent bonds or/and increase of intermolecular and interfacial forces (Van Der Waals forces) and dipole-dipole interactions. Coupling agents are usually utilized to chemically enhance the adhesion strength. The use of the same polymer for both printed track and fabric [2] and an increase of the extruder temperature and platform temperature without damaging the polymer [2,5,6,101] could also allow a better inter diffusion of the macromolecules between the two materials [108]. Besides, if the textile material used as a support is porous and rough , the 3D printed layer can easily be fused in it [101] because the polymer penetrates the pores and thus is going to be mechanically bonded [82,83,85,86,101,108,109]. Finally, an insertion of an additional layer at the printed polymer/fabric interface was executed to chemically bond them [78].

I.2.1.4 Limitations of the studies

Despite the intensive research work on the improvement of the adhesion properties of 3D-PPOT materials, the bonding strength is not enough to guarantee their use in functional textiles field. If the materials are weakly bonded they cannot remain attached after washing or mechanical solicitations. The wash ability, rubbing, deformation and tensile properties of the 3D-PPOT materials are described in the section 1.2.2-1.2.4. .Except the adhesion properties of the 3D-PPOT materials, other mechanical properties such as the wash ability, rubbing, deformation and tensile were also investigated by a few researchers.

I.2.2 Wash-ability of 3D-PPOT materials

Wash-ability defines the ability of the material to be washed without any damages of either its surface or its structure. More generally, the resistances to the humidity and water issues have always been a challenge in terms of a reliable application in functional textile materials and making them not robust enough to be suggested in the market. Indeed, several experimental wearable textile devices cannot be used in the actual life due to the wash ability issue. Even if the textiles utilized are “hydrophobic”, i.e. they are able to repel water, the textile substrate might still absorb the water due to capillary effect and that can damage the electronic components. Moreover, the mechanical stresses and solicitations induced during the washing process could destroy the electrical contacts between the 3D-printed conductive tracks and connectors.. Consequently, the electric impedance starts being uncontrollable after several washing cycles and the wearable device can stop functioning [41]. Tadesse *et al.* investigated washing resistance of TPU monofilament deposited onto PEDOT:PSS-Coated polyester cotton and plain weave fabrics through 3D printing for electroluminescence applications [80]. Eutionnat-Diffo *et al.* studied the wash ability of carbon-black (CB) –filled PLA 3D printed onto woven materials made of Polyethylene Terephthalate (PET). They found that the textile properties (mean pore size and roughness) of the substrate of the 3D printed materials have an impact on the wash ability [101].

I.2.3 Abrasion resistance of 3D-PPOT materials

Abrasion (or rubbing or wear) resistance of PLA 3D-printed onto fabrics was also approached by Sabantina L. *et al.* [103]. They revealed that after rubbing the polyester net fabric was damaged, however, the PLA printed pattern, however, was not influenced by the test – neither the surface was changed, nor the strips were pulled off from the fabric. In that case, they found that the connection between the textile and the PLA printed is stronger than the textile itself.

In addition, various scientists have considered the wear resistance of thermoplastic-based nanocomposites materials [110–112] and textiles [113–117]. Bhimaraj *et al.* studied the wear resistance and friction of poly(ethylene) terephthalate filled with up to 10 wt.% alimuna nanoparticles were increased by two times and decreased compared to the unfilled polymer respectively [111].

In polymer science, two mechanisms of wear can occur : the cohesive and interfacial wear processes. Cohesive wear process refers to the fretting, fatigue and abrasion wears. Abrasion is the main common kind of wear and depends on several parameters such as the softness of the materials, the load applied during the test and the features of the abrasive particles. Besides, in textile field, different test procedures are used and the most common ones are the martindale and taber equipment (usually utilized in carpets industry) [118,119]. Abrasion of textiles reveals the mechanical deterioration of textile surfaces after rubbing them again a rougher surface. During the rubbing process the surface of the textile is firsly damaged and then, its internal structure [120]. Abrasion properties of fabrics are mainly affected by the yarn and fiber properties as well as the textile ones [120].

I.2.4 Tensile properties and deformation of 3D-PPOT materials

Tensile properties describe the behaviors shown by textile materials (fiber, yarn, fabric etc.) when it is exposed to load or tension. The tensile strength is a very important parameter of textile materials which signifies the proportion between the force required to break a specimen and the cross-sectional area of the sample. Eutionnat-Diffo *et al.* focused on investigating the effect of the fabric properties and printing platform temperature on the tensile properties and deformations of both non-conductive and conductive PLA filaments deposited onto PET textiles through 3D printing process and enhancing them by means of theoretical and statistical models [121]. The findings showed that the FDM process affected the stress and strain at rupture properties of the 3D-PPOT materials in comparison with the ones of the textiles. The stress and strain at rupture of the 3D printed PLA on PET textile material is a combination of those of the3D printed track and the PET cloth. This is due to a lower flexibility and diffusion of the fused polymer through the textile fabric leading to a fragile adhesion strength between the two materials. Besides, Ehrmann *et al.* supported the combination of 3D printed structures and textiles to enhance the originally low tensile strength of 3D printed products [103].

I.2.5 Optimization of material properties through statistical modeling

I.2.5.1 Basic Statistical Analysis Methods for Analyzing Data

Statistics is a domain of science that manages the collection, organization, analysis of data and sketch of extrapolations from the samples to the whole population [122]. This process has need of a proper design of the trials, an appropriate selection of the samples and the choice of a suitable statistical method. An adequate knowledge of statistics is essential for appropriate designing of the selected experiments. Incorrect statistical methods might cause inaccurate conclusions which can lead to unethical practice [123]. The term variable defines a characteristic that differs from one individual of population to another individual [124]. Two types of variables exist: the quantitative (for instance the pressure or the temperature) and the qualitative ones (the color or the design of the fabric). The quantitative variables can be subdivided into discrete and continuous measurements while the qualitative one cannot.

The descriptive statistics describe the correlation between variables in a sample or population, such as a mean, median and mode.

However, in inferential statistics, the main purpose is to test the hypotheses which are defined as a proposed explanation for a phenomenon. In that case, two hypotheses are necessary: a ‘null hypothesis’ (named H_0 ‘H-naught,’ ‘H-null’) and an alternative hypothesis (H_1 and H_a). H_0 and H_1 mean that there is no and there is a difference between the population variables or factors respectively [122].

A P- value is a calculated probability of the event happening accidentally if the null hypothesis is true. It is a numerical between 0 and 1 that is utilized by various researchers in order to evaluate if some defined factors or variables (for instance a process parameter or a material characteristics) have significant impact or not on the responses (the targets). The interpretation of the P-value is mentioned in the Figure I- 10.

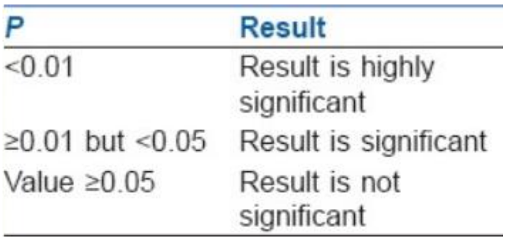

P	Result
<0.01	Result is highly significant
≥0.01 but <0.05	Result is significant
Value ≥0.05	Result is not significant

Figure I- 10 P-value interpretation

Several statistical software systems are available currently and commonly used such as the Statistical Package for the Social Sciences (SPSS – manufactured by IBM corporation), Minitab (developed by Minitab Inc), Stata (developed by StataCorp), Statistical Analysis System ((SAS – developed by SAS Institute, North Carolina, United States of America), R (designed by Ross Ihaka and Robert Gentleman from R core team) and the MS Excel (developed by Microsoft) [125].

In general, the statistical modeling is used by researchers to help them to conduct their research studies through well-designed experiments leading to valid and reliable findings. Inappropriate use of statistical procedures can lead to defective conclusions, inducing inaccuracies and undermining the significance of the research article [125].

I.2.5.2 Statistical modeling and machine learning algorithms in Science

Recently, scientific fields created unique information science connected to disciplines through statistical modeling approaches and machine learning algorithms. For instance, the material informatics (material science), chemoinformatics (chemistry), bioinformatics (biology), health informatics (health sciences) can be cited. These algorithms endeavor to discover correlations between specific activities for a set of objects (e.g., compounds, materials) and their properties and characteristics typically expressed with, either linear or non-linear mathematical models.

In material science, chemistry, biology and environmental sciences, statistical modeling is frequently denoted as Quantitative Structure Activity Relationship (QSAR) or Quantitative Structure Property Relationship (QSPR) [126]. The main roles of QSAR models are to deliver insight into factors affecting properties, recognizing new compounds and optimizing processes. The majority of QSAR models were created for drug design and medicinal chemistry applications. However, in recent times, multiple QSAR models have been developed in numerous other fields, for instance the nano-materials, cosmetics, solar cells, catalysts, anticorrosive, optical devices and explosives [127]. In the material science field, several reviews were reported in the literature over the last few years [126–129]. Generally, the four stages are necessary to establish QSAR models: (1) Data collection; (2) Data processing; (3) Model generation; (4) Model validation.

As an example Xue *et al.*[130] have used an adaptive design approach, tightly coupling computations and experiments. The main objective was to discover of new low thermal hysteresis (DT) NiTi-based shape memory alloys from within a chemical space consisting of ~800,000 alloys. The use of QSAR models allowed the authors to reduce the design and utilize 36 compositions out of which 14 demonstrated improved DT values. Besides, Sanatgar *et al* [2] developed linear and non-linear models connecting the adhesion force of 3D printed PA6.6 onto PA6.6 to the temperature of the 3D printer extruder and the printing speed as shown on Figure I-11. The statistical modeling was done using Minitab software in order to evaluate the influence of extruder temperature, platform temperature and printing speed on the adhesion strength between the 3D printed track and the textile; and then create the statistical relationship. It was found that the platform has no significant impact on adhesion (Figure I-11).

After approaching the different properties of 3D-PPOT and their optimization in the sub-sections *1.2.4.* and *1.2.5* respectively, the next section *1.3* is going to present the applications that are or can be targeted with 3D-PPOT materials.

I.3 General applications of 3D-PPOT materials

The 3D printing process of polymers onto textiles found their applications in various domains such as in wearables with sensor and heat properties, safety equipment for the defense industry, smart bandages, virtual reality gloves, unique sportswear that manages body temperature, aviation and aerospace accessories, medical equipment (for instance template for cells), automotive, …etc. [2]. Another application is the development of auxetics textiles used in filtration and robust shock absorbing materials, like body armor and knee and elbow pads. Auxetics materials are textiles that have a negative Poisson’s ratio which expend laterally while stretched longitudinally [131]. Auxetics materials are made of different designs printed onto knitted materials through FDM process. This kind of fabric can be transformed from an air and water permeable state to lamellae state in order to protect the people from rain and wind and vice versa [132]. Also, the 3D printing of the label “Braille” onto the textiles were executed to support blind people [133]. A continuous 3D printing onto textile process has been partially patented by Eurecat. This process can customize any type of fabric, in any colour, texture or length.

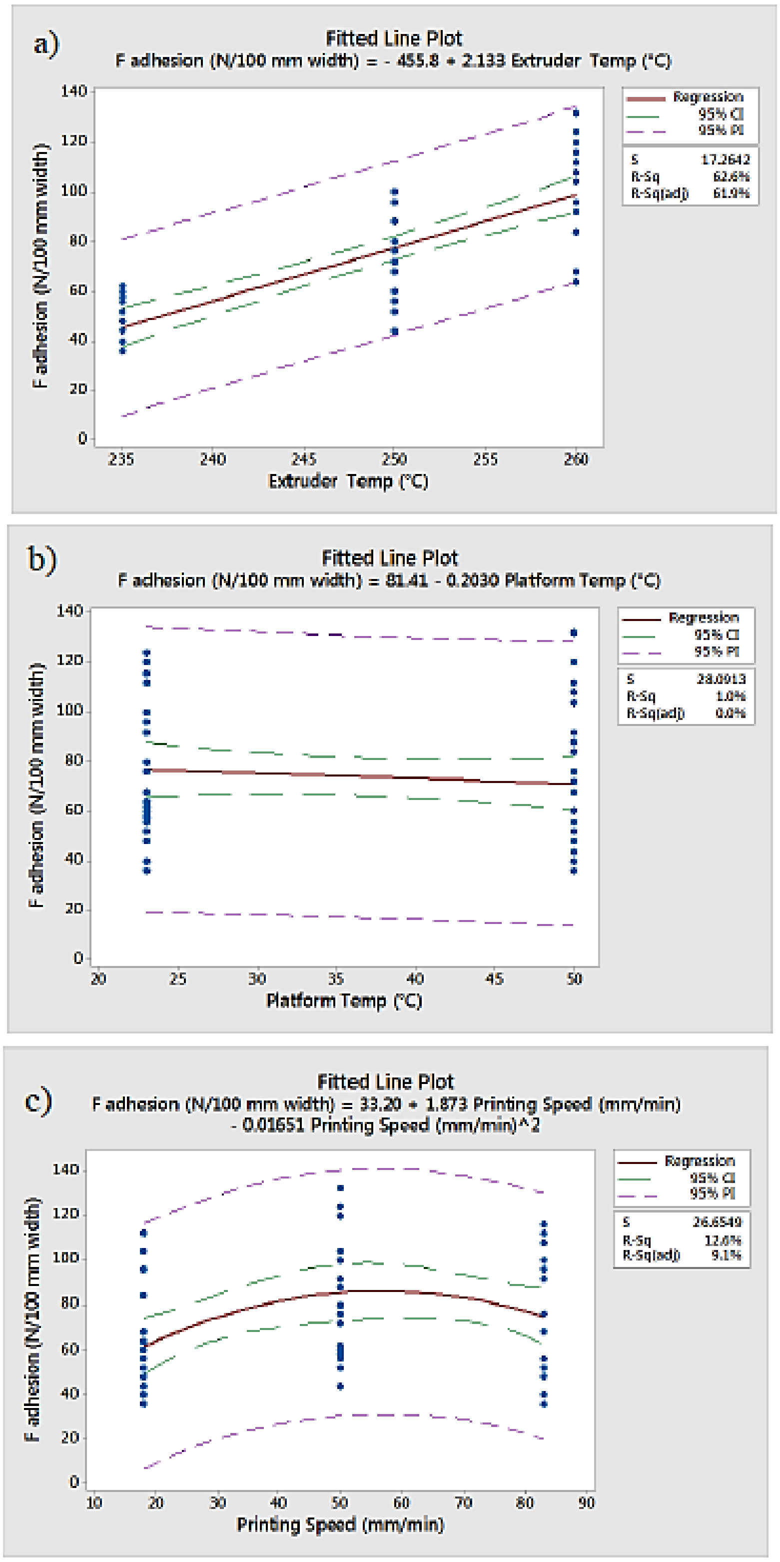

Figure I-11 Statistical models between the adhesion force and the extruder temperature (a), the platform temperature (b) and the printing temperature (c) [2]

3D printing process of polymeric materials onto textiles is definitely opening doors in many areas especially in the design domain. 3D printing is also a novel technique which could demonstrate interesting advantages in the domain of smart and functional textiles development through the deposition of conductive polymers onto textile materials. The functional and smart textiles and systems are commonly defined by European Committee for Standardization as “Textile material to which a specific function is added by means of material, composition, construction and finishing”. In smart textile field; sensors, actuators, data processors, communication units, and energy supply are fundamental components that can be integrated onto textiles by using the FDM process. Despite all the existing possible and interesting applications of 3D-PPOT materials, the one considered in this thesis for final prototyping is the smart (or functional or intelligent textiles) field. However, all the findings described in this thesis can be applied in any other domains. The section *1.4* presents the scope and research guidelines of the thesis to better understand the existing gap in the literature and also the innovate ideas and approaches.

I.4 Scope and research approaches of the thesis

As part of the European program named Sustainable Management and Design for Textiles (SMDTex) – the originality of the current research project is to suggest a novel and reliable process for the creation of functional and intelligent textile materials by using the existing 3D printing process. The main idea is to utilize the FDM process (3D printing) of conducting polymers onto textile materials or the development of functional textiles. This process addresses solutions for existing global issues of shortage of energy and non-renewable raw materials by suggesting processes and materials with added values and functionalities which respect the environment diminish the waste of raw materials and reduce the textile supply chain. As demonstrated in the literature review, the use of 3D printing as a deposition technique of CPCs onto textiles were already approached in about a dozen of articles, however, several challenges remain present to guarantee its application in functional textiles field. Therefore, this project, which is the continuation work of the thesis of Dr Sanatgar defended in 2019 (SMDTex project), focuses on optimizing the key properties using specific impacting factors and enhancing these performances through material and process developments. The polymeric materials have to be 3D printable, electrically-conductive and flexible enough to be used in the manufacturing of electrodes and sensors through FDM technology.

The research questions set from the beginning of the project were the following:

1) What are the most impacting textiles’ properties on the mechanical properties (adhesion, tensile, abrasion, wash ability, deformation)?
2) How can we enhance the adhesion and the flexibility of the 3D-PPOT materials while maintaining or increasing its electrical conductivity?

Indeed, as the effect of the 3D printing parameters on the adhesion of the 3D-PPOT and the electrical and thermal properties of CPCs materials were massively studied by other researchers, the main focus was to investigate the influence of the textile material properties and temperature of the build platform of the 3D printer, directly in contact with the textiles, on the adhesion, stress and strain, deformation and abrasion properties and wash ability of the 3D-PPOT materials made of virgin PLA and PLA/2.5% CB blends. The impact of abrasion on the electrical conductivity of the material was also examined. Reliable and statistical models were developed in order to be able to predict the performance of 3D-PPOT based on the properties of the selected textile. The main limitation is the use of the findings only when using polyethylene terephthalate (PET) woven fabrics as a substrate and virgin PLA and PLA/2.5% CB blends as polymeric materials.

In addition, an alternative solution to improve the adhesion properties of the 3D-PPOT was to combine the grafting process of acrylic acid onto the textile substrate and the application of a solution based-adhesive or a Polyurethane (PU) adhesive film onto it by spraying or thermocompression respectively, prior to 3D printing of CPCs. These methods demonstrated to be very efficient, however, the adhesion strength still need to be higher for textile applications.

Finally, the majority of the studies have approached the development of 3D-PPOT by using only monophasic conducting polymer nanocomposites, which considerably reduce the elastic and permanent deformations in comparison with the ones of the textiles. In order to enhance their deformations, the manufacturing of highly conductive CPCs /elastomer biphasic blends using Low Density Polyethylene (LDPE), highly structured carbon black (KB) and Carbon Nanotubes (CNT) with co-continuous structures was preferred.

Chapter II Materials and methods

This chapter focuses on the materials and processes utilized in the thesis. *Section 2.1* introduces the materials that include both the textiles and polymeric materials of the study. *Section 2.2* defines the manufacturing processes. *Section 2.3* presents the functionalization processes of textiles considered in this thesis. Finally, the s*ection 2.4* relates the methods and standards used to characterize the polymers and textile materials.

II.1 Materials

II.1.1 Non-flexible virgin and conductive monofilaments for 3D printing process

At first, non-flexible virgin and conductive monofilaments were used to optimize the adhesion, tensile and abrasion properties of the 3D printed layers onto textiles through textile properties only. Therefore, the electrical conductivity is enhanced in Chapter V and not in Chapters III and IV. The virgin PLA monofilament utilized in the 3D printing process was purchased from Creative tools AB (reference: ECO-PLA orange) . The composition of the polylactic acid – based conductive polymer composites was defined based on former research [31]. In chapter III and IV, the conductive polymer composite was made of PLA and 2.5 percent of carbon black as electrically conductive filler.

II.1.1.1 Polylactic acid (PLA)

First discovered in 1932 by Wallace Carothers, polylactic acid is a bioactive and biodegradable polyester made up of lactic acid building blocks. Low and high-density PLA can be produced by processing lactide through ring-opening polymerization or direct poly-condensation reaction. The lactide usually comes from the fermentation of corn, sugar beet, sugarcane or other biomass, but corn is the most common source The molecular structure of PLA is presented in Figure II-. Polylactic acid exists under two distinct forms: the poly (L-lactic acid) and poly (D-lactic acid). Pure poly (L-lactic acid) (PLLA) and poly (D-lactic acid) (PDLA) are semi crystalline polymers with spherulites that are composed of crystalline lamellae and amorphous areas positioned between lamellae and between spherulites [134]. In general, the polymer adopts a 103 helical structure within the lamellae. The melting point and the degree of crystallinity and of PLLA are influenced by the stereo-irregularity in the polymer [135]. The degree of crystallinity and the spherulite size can be reduced by incorporating other isomer in a primarily stereo pure PLA. The mechanical and thermal properties of PLA are described in Table II -.

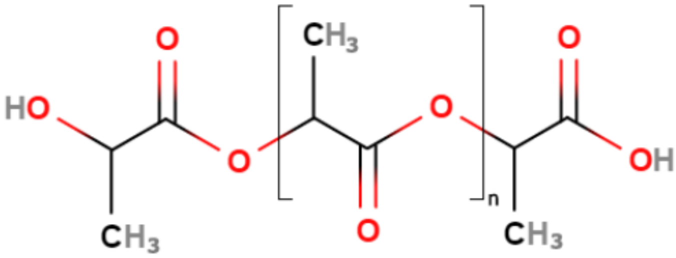

Figure II-1 Molecular structure of PLA[136]

Table II -1 Properties of PLA

	Properties	**Values (units)**
Mechanical properties	Density	1.21–1.43 g/cm^3 (20 °C)
	Young's modulus (E)	0.3-3.5 GPa
	Tensile strength (σ_t)	21-60 MPa
	Elastic at break	6-11 %
Thermal properties	Glass transition temperature (T_g)	45-60 °C
	Melting point (T_m)	150-162 °C

II.1.1.2 Carbon black (CB) nanoparticles

Carbon black (CB) is a term that refers to a group of industrial materials comprising furnace, thermal and acetylene blacks. The form of CB particles is spherical. Furnace blacks are manufactured by combustion of oil or natural gas with deficient oxygen. Thermal blacks are produced by using natural gas in heated chambers without air. The morphological structure of one carbon black is shown in Figure II- 2. Particle sizes of carbon black range from 20 to 300 nm [137]. The carbon black (CB) fillers used in the thesis were from Evonik Degussa Co., Ltd., Germany. Their Brunauer–Emmett–Teller (BET) surface area was 83 m^2/g.

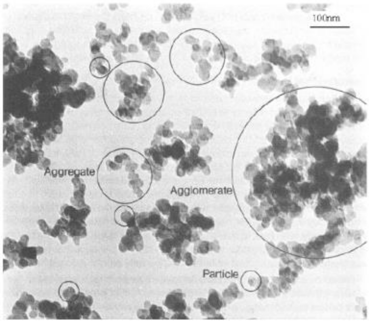

Figure II- 2 Morphology of carbon black [138]

II.1.1.3 Manufacturing of conducting polymer composites

The extrusion defined as a continuous process is used to manufacture conducting polymer composites and polymer blends. It is the primary shaping process where the pellets of thermoplastic polymer are pumped in the die and are orientated and shaped, in general, as a monofilament with ideally constant cross-sections. Couples of requirements exist to execute properly the extrusion process:

- Consistent transport of the polymer
- Homogeneous thermal and mechanical properties of the polymer
- No thermal, chemical or mechanical degradation
- Appropriate and cost-effective operation.

Two types of extruder exist: the single screw and twin screw ones (Figure II- 3). A single screw extruder is generally utilized to pump the very important mass outputs at a very high pressure required for very dense materials and big profiles. The twin screw extruder is mainly used for and compounding [139]. The extruder is composed of various parts, presented in Figure II- 4: the hopper, the barrel, the screw, the heating-cooling, and the drive gear.

The screw reveals to be the main part of extruder because it provides the feedstock and transport, the compression, the melting and the homogenizing of the polymers to give the exact amount of pressure for the melt to go through the die. The polymeric material going out of the die is cooled by blowing air or in water bath [140]. The conducting polymer composites are manufactured by first incorporating the conductive fillers into the polymer granulates and mechanically mix them prior to the extrusion process.

In this thesis, the extrusion process of the non-conductive or conductive thermoplastic polymers was executed in a room, with a controlled temperature of 20 °C ± 0.2 and humidity of 65 % ± 5. In the case of CPCs, 2.5 wt. per cent of CB fillers were mechanically incorporated into virgin PLA granulates and then dry in an oven set at 60°C for 12 hours. The dispersion of the blend was executed using a Thermo Haake rotating (ref: PTW 16/25p with Length/Diameter = 25) and intermeshing twin-screw extruder at the process parameters presenting in Table II- 2.

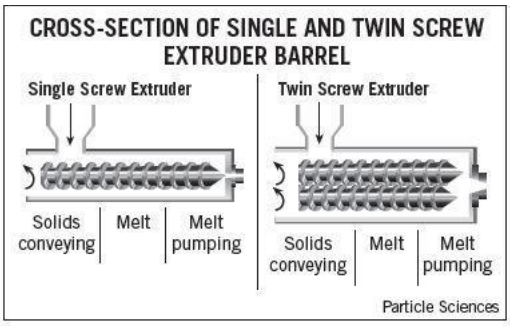

Figure II- 3 Single and twin screw extruders [141]

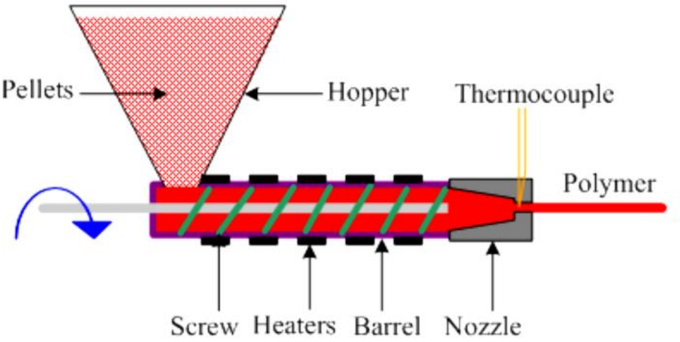

Figure II- 4 Extrusion of polymers [139]

Table II- 2 Extrusion parameters [101]

Screw speed (rpm)	**Temperature (°)**				
N	$T_{zone\ 1}$	$T_{zone\ 2}$	$T_{zone\ 3}$	$T_{zone\ 4}$	$T_{zone\ 5}$
100	170	175	180	185	190

II.1.2 Flexible conductive monofilaments for 3D printing process

As already discussed in chapter I, in order to increase the flexibility, stress, strain and electrical conductivity of functional textiles through 3D printing of polymer onto fabrics, the development of flexible and conductive filament was required. The enhancement of the properties, mentioned above, was achieved by creating biphasic blends using low-density polyethylene and propylene-based elastomer as polymeric materials and highly structured carbon-black (Ketjenblack) and carbon nanotubes as fillers. The main idea is to utilize biphasic blends with selective location of fillers in the low-density polyethylene phase or at the interface between the two phases. This part will be developed in chapter V.

II.1.2.1 Polymers utilized

Low-density polyethylene (LDPE)

In the 1950s, polyethylene became the first commodity thermoplastic polymer used on packaging, came into general. Polyethylene (PE) is a family of polymers which includes the low-density polyethylene (LDPE), the linear low-density polyethylene (LLDPE) and the high-density polyethylene (HDPE). These PE are different principally in their density, which is related to their degree of crystallinity. Indeed, defined as the first grade of polyethylene produced in 1933 by Imperial Chemical Industries (ICI), LDPE is a thermoplastic made from the monomer ethylene manufactured through a high pressure process using a free radical polymerization.[142]. The molecular structure of PE is presented in Figure II- 5. Some classical properties values ranges for PEs are illustrated in Table II- 3. LDPE presents several advantages and challenges described in Table II - 4.

LDPE possesses about 2% more branching of the carbon atoms than HDPE (Figure II- 5), thus its intermolecular forces (for instance instantaneous-dipole induced-dipole attraction) are weaker. Consequently, its tensile strength is lower and its flexibility is higher. Also, its low density is explained by its less tightly packed and less crystalline structure.

Table II- 3 Properties of LDPE [136,143]

	Properties	**Values (units)**
Mechanical properties	Density	0.910-0.940 g/cm^3 (20 °C)
	Young's modulus (E)	0.13 - 0.3 GPa
	Tensile strength (σ_t)	25 – 45 MPa
	Elastic limit	200 – 600 %
Thermal properties	Glass transition temperature (T_g)	-25 °C
	Melting point (T_m)	98-115 °C

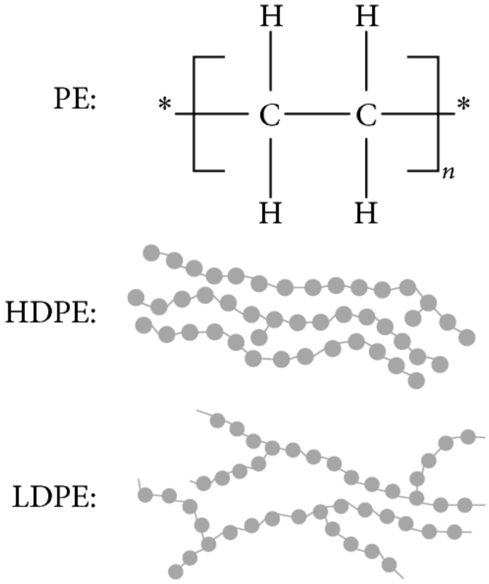

Figure II- 5 Molecular structure of PE and chains distributions of HDPE and LDPE [144]

Table II - 4 Advantages and challenges of LDPE [136]

Advantages	Challenges
Very low cost	Susceptible to environmental stress cracking
Excellent electrical insulating properties	Poor UV resistance
Excellent chemical resistance	Low strength, stiffness and maximum service temperature
Very good process ability	High gas permeability, particularly carbon dioxide
High impact strength at low temperature	Highly flammable
Very low water absorption	High-frequency welding and joining impossible

Polyolefin-based elastomers

Polyolefin thermoplastic elastomers (PBE) are materials which combine polyolefin semi-crystalline thermoplastic and amorphous elastomeric polymers. They have rubber-like characteristics and can be processed through common melt thermoplastic processing equipment. Several types of polyolefin-based thermoplastic elastomers (TPEs) exist, which comprise [145]:

- Blends obtained through mechanical mixing and extrusion denoted as TPOs
- Block copolymers, for example, olybutadiene-isoprene-butadiene block copolymer
- Random block copolymers, for instance, ethylene a-olefin copolymers
- Graft copolymers, e.g. polyisobutylene-g-polystyrene.
- Stereoblock polymers, such as stereoblock polypropylene
- Dynamically vulcanized blends of an olefin (TPVs) with ethylene-propylene random copolymer (EPM) or ethylene propylene diene monomer (EPDM).

Polyolefin blends TPEs (named as TPOs) are the PBE used the most and represent an important family of engineering materials. They are based primarily on isotactic polypropylene (iPP) and ethylene-propylene random copolymer (EPM). The blends are usually manufactured by mixing the thermoplastic polymer and the elastomer together on a high shear compounding device, such as a continuous mixer (e.g., single- or twin-screw extruders). In an elastomeric material, the three-dimensional structure is co-continuous. The hard phase provides the strength and the continuous soft phase confers the flexibility. Both phases can flow as they never cross-link (Figure II- 6) [145].

Thermoplastic elastomer blends based on polypropylene are widely commercialized because polypropylene is a low cost polymer with low density. Its high melting point (T_m=145–165°C, depending on grade) and crystalline structure make it resistant to oil, elevated temperatures and solvents. Besides, the elastomeric phase possesses a good thermal stability, low cost and flexibility at low temperatures and a good compatibility with polypropylene.

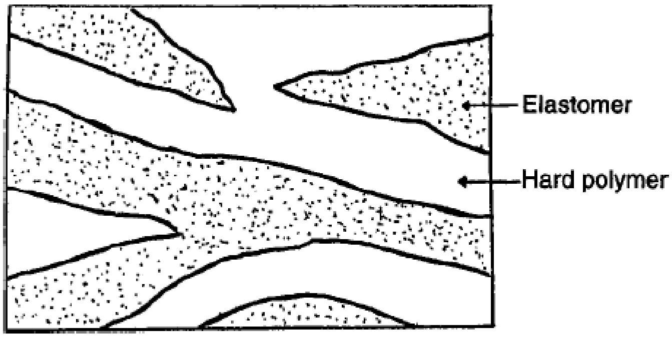

Figure II- 6 Morphology of Hard (or thermoplastic) Polymer/Elastomer blends [145]

In this thesis, the elastomer considered was the Propylene Based-Elastomer (PBE) granulates –(ref: Vistamaxx 6202) purchased at ExxonMobil Chemical (Texas, United States of America). Vistamaxx 6202 is defined as an ethylene/propylene random copolymer manufactured using the metallocene catalyst technique from ExxonMobil. It was already demonstrated by some researchers that the whole molecular chain of propylene-based elastomer consisted of soft segments in room temperature [146].

II.1.2.2 Fillers

Carbon nanotube (CNT)

Since their discovery by Iijima in 1991, carbon nanotubes (CNTs) have been used in various research studies of different fields [147]. With their unique seamless cylindrical structure with nano-scale diameters, CNTs possess are produced by rolling up a sheet of graphene into a cylinder [148]. Depending on the amount of concentrically rolled-up graphene sheets, CNTs are also categorized as single-walled nanotubes (SWNT), double-walled nanotubes (DWNT), and multiwalled nanotubes (MWNT) (Figure II- 7)

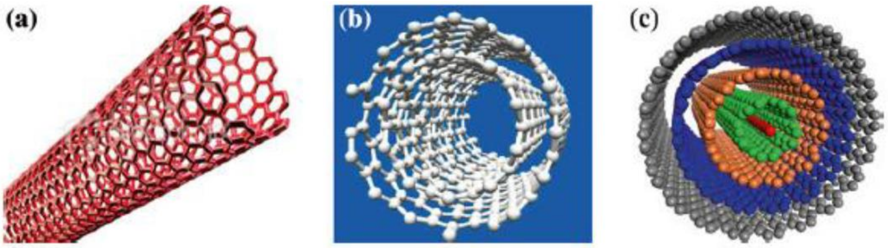

Figure II- 7 Structure of a single-walled (a), double-walled (b), and multi-walled CNTs (c)[148]

Its distinctive structure leads to notable properties such as low densities, high electric and thermal conductivity, large surface area to volume ratios, high aspect ratios, high mechanical and tensile strengths. In this thesis, multi-wall carbon nanotubes (MWNTs) (reference: Nanocyl®-7000) with a purity of 90% were supplied by Nanocyl (Belgium). Synthesized via catalytic chemical vapor decomposition (CCVD), they have a diameter of about 10 nm, lengths of 0.1-10 µm and a surface area of 250 m^2/g.

Ketjenblack (KB)

The highly structured carbon black- ketjenblack (KB) was provided by AKZO NOBEL (Amersfoort, the Netherlands) under the reference Ketjenblack® EC-600JD. The aggregate size of the nanoparticles was between 10 and 50 nm, the BET surface area of 1400 m2/g and the apparent bulk density of 1-1.2 g/cm^3. Indeed, KB nanoparticles have much larger surface area than CB ones. Their morphology is presented in Figure II- 8. Its morphology and large surface area allow the creation of bigger conducting networks, which enhance the electrical conductivity of the conductive polymer composites.

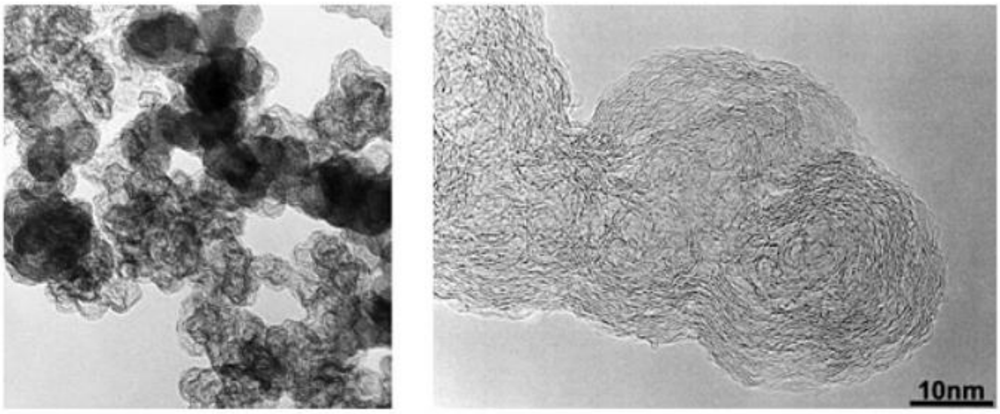

Figure II- 8 Morphology of Ketjenblack [149]

II.1.2.3 CPCs/elastomer blends manufacturing process

Before the melt extrusion process, the two polymers used were the LDPE and the PBE granulates were dried at 70°C and 40°C for 12h respectively. A co-rotating intermeshing twin-screw extruder (ref: PTW 16/25p with Length/Diameter = 25) from Thermo-Haake was utilized for the extrusion process. Each extrusion process was executed at a rotating speed of 100 RPM and a shear stress close to 20 s^{-1}. The CPCs/elastomer blends were manufactured following two distinct extrusion scenarios named as the 1-step extrusion and the 2-step extrusion processes. The 1-step extrusion consists in blending of the LDPE, PBE and fillers (MWCNT and/or KB) in one step through a homogeneous dispersion of the fillers in the granulates of the polymers. Two different stages are necessary for the 2-step extrusion: a first dispersion and extrusion process of KB and CNT with the LDPE followed by a second extrusion of LDPE- based CPC with PBE at different percentages according to a specific design of experiments detailed in the Chapter V of this thesis. Different temperature profiles were used for the five zones of the extruder for each experiment depending on the amount of fillers and PBE in the blend. The extrusion parameters of each blends are presented in Chaptr V.

II.1.3 Textile materials

Woven textile materials composed of PET monofilament of 0.2mm in diameter as weft yarn and PET twisted multi-filaments of Nm 40 as warp yarn were manufactured. In textile field, Nm is the "normal metric" –defined as 1,000 m of yarn per kg. These woven fabrics were manufactured in the weaving laboratory of the Swedish school of textiles (or University of Borås) in Sweden. Two weave patterns were selected and used in the research studies: the plain and twill 2/2 structures presented in Figure II- 9. In this figure, it is possible to see that the structure of the twill 2/2 is more open due to the presence of several floats compared to the plain one. Depending on the design of experiment defined for each study, different weft densities from 14 picks/inch to 22 picks/inch could be chosen. These fabrics are used in Chapters III and IV while only the 14picks/inch twill fabric was used in Chapter V.

For the study about the enhancement of adhesion properties through textile's surface functionalization presente in Chapter III, two materials were used:

- A washed, unsized and heat set (i.e. thermally processed in a steam atmosphere to enhance its dimensional stability) plain-woven fabric of 80 ± 0.8 g/m^2 made of PET 56 dtex yarn and 110 dtex (1Tex equals 1 gram per 1000 meters) as weft yarn supplied by FOV Fabrics (Sweden) shown in Figure II- 10.
- A washed, unsized and spunlaced non-woven (Figure II- 11) made of PET 4 dtex fibers from IMS Non-woven (Sweden). A spunlaced non-woven is described as a textile material mechanically bonded to a dry-laid staple fabric through water jet. This process trends to entangle the individual fibers of both fabrics. The mass per unit area of the material was 80 ± 0.8 g/m^2.

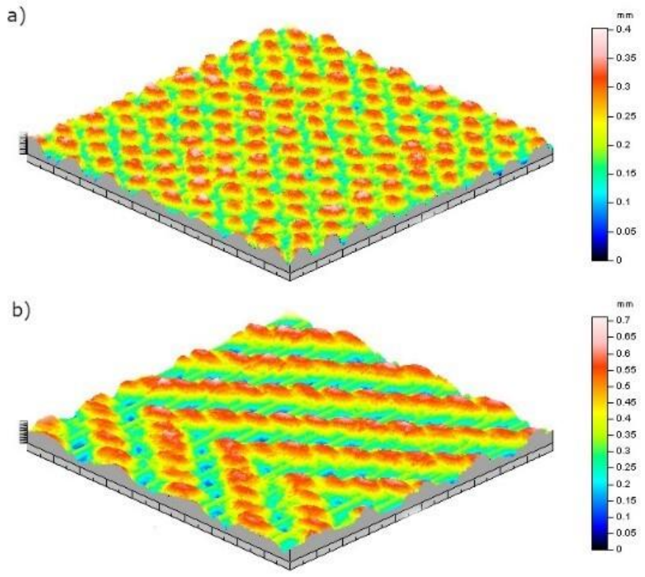

Figure II- 9 Weave structures: plain (a) and twill 2/2 woven materials

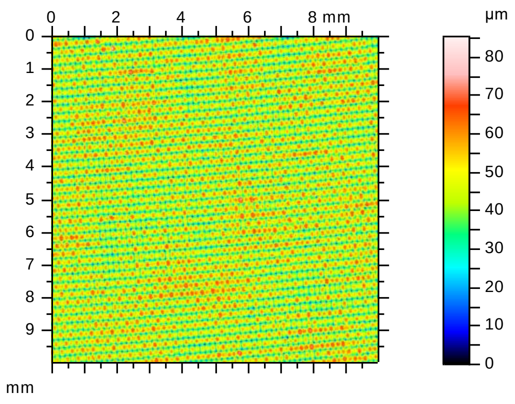

Figure II- 10 Structure of the PET plain weave fabric from FOV

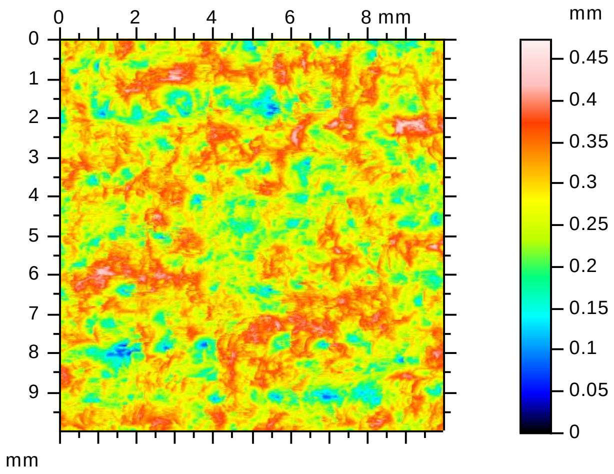

Figure II- 11 Structure of the PET non-woven fabric from IMS

Polyethylene terephthalate (PET), which is sometimes written poly(ethylene terephthalate), is commonly abbreviated PET. It is the thermoplastic polymer of the polyester family the most common used in the development of fibers for clothing, creation of containers for liquids and foods, thermoforming for manufacturing, and in mixture with glass fiber for engineering resins. The semi-developed formula of PET is presented in Figure II-12.

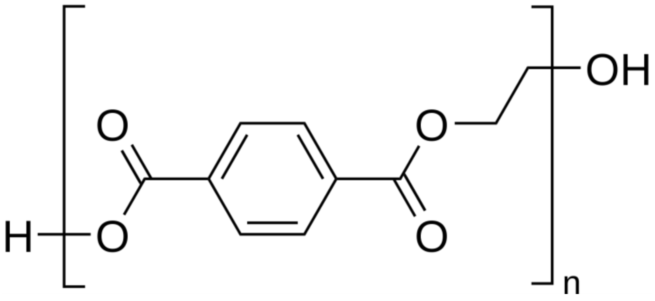

Figure II-12 Semi-developed chemical formula of PET

The main stream of the world's PET production is for synthetic fibers, which represents almost 60% and then the one for the bottle production accounting for about 30% of global demand. In addition, polyester makes up approximately 18% of global polymer production. After polyethylene (PE), polypropylene (PP) and polyvinyl chloride (PVC), it is the fourth-most-produced polymer. Commonly recycled, PET is composed of polymerized units of the monomer ethylene terephthalate, with repeating ($C_{10}H_8O_4$) units. PET may exist in both states: amorphous and semi-crystalline. With a particle size less than 500 nanometers, the semicrystalline PET material might appear transparent while it becomes opaque and white when the particle size reaches a few micrometers. This observation depends also on the crystal structure of the PET. The monomer bis(2-hydroxyethyl) terephthalate is synthesized through various methods: the esterification reaction between ethylene glycol and terephthalic acid with water as a byproduct, or by transesterification reaction between dimethyl terephthalate (DMT) and ethylene glycol with methanol used as a byproduct. The polymerization is obtained by a polycondensation reaction of the monomers with water as the byproduct, executed immediately after esterification/transesterification. The properties of PET are described in Table II- 5.

Table II- 5 Properties of PET

	Properties	**Values (units)**
Mechanical properties	Density	1.38 g/cm^3 (20 °C)
	Amorphous	1.37 g/cm^3
	Single crystal	1.455 g/cm^3
	Young's modulus (E)	2800–3100 MPa
	Tensile strength (σt)	55–75 MPa
	Elastic limit	50–150%
Thermal properties	Glass transition temperature (T_g)	67–81 °C
	Melting point (T_m)	260 °C
	Thermal conductivity	0.15 – 0.24 W m^{-1} K^{-1}

II.1.4 Adhesives used to functionalized textile materials

Pressure sensitive adhesives (PSA) in the form of solution and film were used in the study of the enhancement of adhesion properties of 3D-PPOT materials. The main goal of using these adhesives was to create more anchorage points between the printed layer and the textile materials after functionalizing the fabrics.

II.1.4.1 Solution based- PSA

A pressure-sensitive adhesive (PSA) was made through solution polymerization with 40 wt% solids based on the synthesis method defined by Song et. al (2006) [150]. As an initial step, 126 g of 2-Ethylhexyl acrylate (2-EHA), 10.5 g of methyl methacrylate (MMA), 1–3 g of glycidyl methacrylate (GMA), 10.5 g of vinyl acetate (VAc),0.3 g of 1,1′-Azobis(cyclohexanecarbonitrile) - 98% (ACHN), and 75 g of ethyl acetate (EAc) were mixed in a 1000 ml flask equipped with a stirrer, an addition funnel, and a thermometer. The polymerization reaction was taking place at 70◦C with a stabilization of the same temperature for 30 mins. At that point, a blend of 150 g EAc and 0.6 g of ACHN was gradually introduced into the flask over two hours. Finally, the polymerization was proceeding at 65 ± 5◦C for 4 additional hours. All the chemicals cited above were received from Sigma-Aldrich.

II.1.4.2 PSA film

A polyurethane structural bonding film of 40±1.6 µm thickness was bought from Lohmann GmbH & Co. The recommendations were given by the supplier: the curing temperature and pressure ranges of 90-120°C and 22-109 Pounds per Square Inch (psi) respectively.

II.2 Manufacturing processes

II.2.1 3D Printing process onto textile materials

The 3D printing, manufacturing process utilized in the thesis is the FDM process defined in Chapter I. Three different 3D printers were used three distinct studies of the thesis. Indeed, a dual-head WANHAO Duplicator 4/4x 3D printer purchased from Creative Tools AB (Halmstad, Sweden), a flying head Delta WASP 2040 3D printer supplied by 4D Nordic (Sweden) and WASP (Italy) and located in the University of Borås, and the Pellet Additive Manufaturing (PAM) 3D printer from Pollen (France) based at Euromaterials (France) shown in Figure II- 13. The two first 3D printers (WANHAO and WASP) are fed by monofilament while granulates are introduced into the third one (PAM) as it can be seen in Figure II- 14. Each 3D printer is located in a room with controlled temperature of 20°C (±2) and humidity of 65 per cent (±5). Before each experiment, woven or non-woven samples were fixed directly onto the metallic platform of the 3D printer without plastic film between the platform and the textile (Figure II- 15). Then, a rectangular track, formerly designed using a Rhinoceros CAD software and then imported into Simplify3D software, was printed on each set of samples. The 3D printing parameters (Table II- 6) are optimized depending on the polymeric material used and kept the same for all the samples of a study. The Z offset refers to the distance between the head of the extruder and the surface of the textile. This parameter is set according to the thickness of the fabric and remained constant for all the samples.

Table II- 6 **3D Printing parameters**

Parameters	Values (unit)
Infill percentage	20 – 100 (%)
Z offset (distance between the head)	0 (mm)
Extruder diameter	0.4 (mm)
Extruder temperature	200 – 250 (ºC)
Platform temperature	25 – 100 (ºC)
Number of layers	1

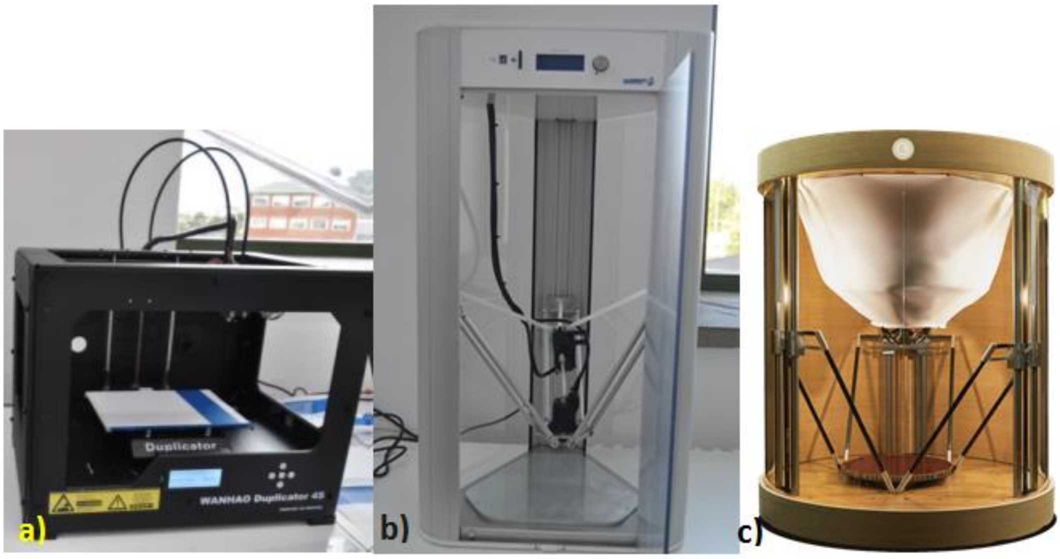

Figure II- 13 Wanhao Duplicator 4/4x (a), Delta Wasp 2040 (b) and PAM Pollen (c) [151] 3D printers

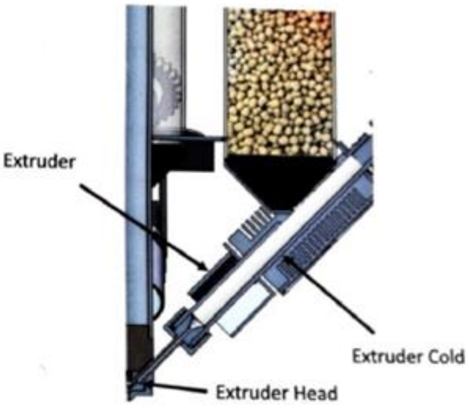

Figure II- 14 Extruder of PAM Pollen 3D printer

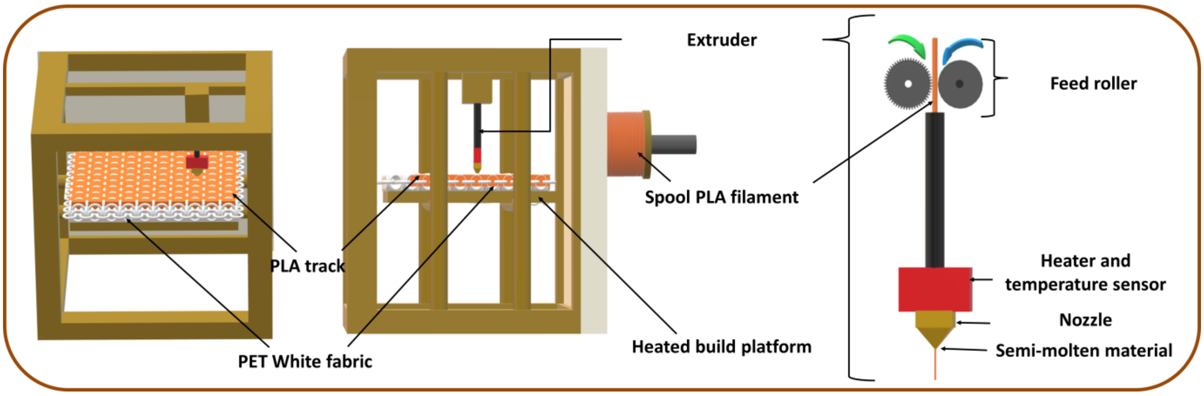

Figure II- 15 3D-Printing (FDM) process onto fabrics

II.2.2 Washing processes

The washing test was executed in a domestic washing machine following the standard SS-EN ISO 6330:2012. The process parameters of this washing method are presented in Table II- 7. One washing cycle was performed on the plain and twill woven fabric samples of Chapters III and IV. After the washing process, a visual assessment was done on each 3D-PPOT sample to evaluate the washability of the samples by considering the percentage of printed track still bonded to the fabric between 10% and 100% (Figure II-16). This test was mainly utilized to evaluate the impact of the washing on the adhesion properties of 3D-PPOT materials. Only the samples with 100 percent of PLA track bonded to the textile materials after the washing test were compared.

Table II- 7 Washing process of the standard SS-EN ISO 6330:2012 [101]

Process parameters	Value (unit)
Detergent reference	European colourfastness establishment formulation non-phosphate reference detergent (A) without optical brightening agent – from James Heal
Detergent quantity	20 g (±0.5 g)
Complementary load fabric types	White cotton fabric – 950 g
Washing procedure	40° C (±3° C) – 15 min including rinse and spin times (one cycle)
Drying procedure	Open-air dry

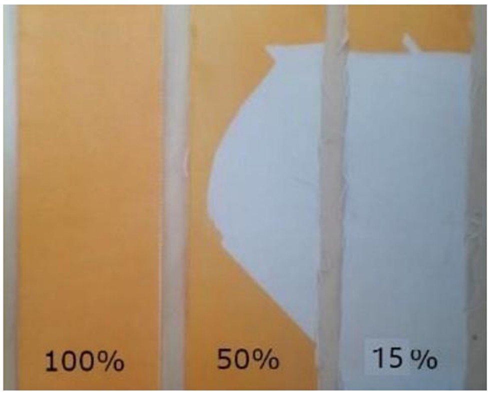

Figure II- 16 Visual assessment of 3D printed samples after the washing process [101]

II.2.3 Textile surface treatment procedures

II.2.3.1 Atmospheric plasma treatment

The atmospheric plasma treatment process refers to the activation of polymeric materials' surfaces by attaching to them various active species. Sotton and Nemoz have already explained the chemistry of functional groups attachment through electron beam plasma on textiles [152]. They described the phenomenon as first, initiation of radicals on the surface and then attachment of ionized groups to the initiated radicals (Figure II- 17). Thus, high hydrophilicity and polar characteristics are obtained by grafting functional groups such as carbonyl, hydroxyl or carboxyl onto the surface [153]. Several researches have already used this technique to functionalize the textile materials for different applications [154–157].

The atmospheric plasma treatment was realized through a "Coating Star" machine (Ahlbrandt System, Germany). The functionalization of textiles through plasma technique consist in one electrode and one counter-electrode, produced with dielectric ceramic, that were exposed to a potential difference resulting in a glow discharge named 'Dielectric Barrier Discharge' (DBD) applied onto the fabric. The machine parameters which were kept constant during the entire study are presented in Table II- 8. The treatment was accomplished on both sides of the fabrics. The most important parameter is the processing power defined in **Eq. II - 1** [156,158] . The plasma treatment was applied on a 80 ± 0.8 g/m^2 washed, unsized and spunlaced non-woven from IMS Non-woven (Sweden) and a 80 ± 0.8 g/m^2 washed, unsized and heat set plain-woven fabric from FOV (Sweden).

Table II- 8 Air plasma treatment process parameters

Process parameters	Value (unit)
Frequency (kHz)	26
Electrode length (m)	0.5
Distance between electrodes (mm)	1.5

$$\text{Processing power (kJ}/m^2) = \frac{\text{P}}{\text{V}\times\text{L}} \times 0.06 \qquad \textbf{(Eq. II - 1)}$$

Where P is the electrical power (W), V the speed and L the electrode length.

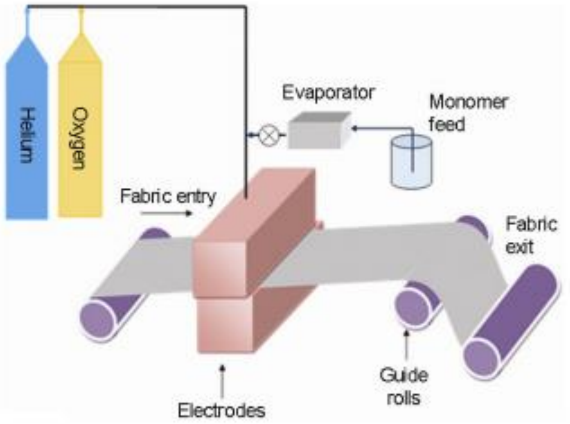

Figure II- 17 Schematic view of atmospheric pressure plasma equipment [159]

II.2.3.2 *Digital printing: ChromoJET technology*

The ChromoJET is a digital printing process (Figure II- 18) that uses the valve-jet technology principle. The principle of this process consists in the activation a plunger by an electromagnet in order to open and close the outlet of a nozzle. This technology has been developed by Zimmer in Austria and is mainly used in carpet industry applications. These jets are also applicable for coating technique of solution onto materials. The volume of the jets can be controlled by changing the coverage, the viscosity, the pressure, the nozzle diameter and the speed of the head [160,161]. As described below, this technique was used to realise the grafting of acrylic acid onto textiles and apply adhesive on the fabrics.

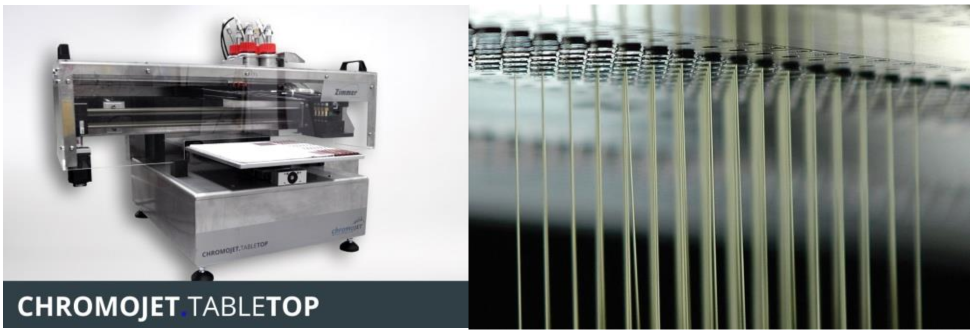

Figure II- 18 Digital printing: ChromoJET [160,161]

II.2.3.2.1 Grafting process

The grafting process was executed into different steps. First, a solution containing 90 wt% of Acrylic Acid (AA) and 10 wt% Benzophenone (BP) was coated with a pick-up of 50% onto PET woven fabrics and PLA monofilament through a Chromojet device (ref: Chromojet.Tabletop, Zimmer, Austria). The PET fabric used is a 80 ± 0.8 g/m^2 washed, unsized and heat set plain-woven fabric from FOV (Sweden). At that moment, the textile was dried at 60 ºC in an oven during ten minutes, followed by the curing and grafting processes of AA onto the PET woven fabrics and PLA monofilaments under a UV-LED lamp FireJet (Phoseon Technology, USA) with emission wavelengths of 380 to 420 nm and a maximum emission power density of 6 W cm^2 including. Each sample was cured three times at 15 mm/sec. Finally, the samples were washed successively with toluene, methanol, and water, and then dried at 60 ºC in an oven for 20 minutes to remove the ungrafted homopolymer and the ungrafted AA. The surface modification processes of the PET with grafted AA (Figure II - 19. (a)) and PLA with grafted AA (Figure II - 19. (b)) were given by Y. W. Song *et al.* (2006) [150] and Y. Xiao *et al.* (2010) [162].

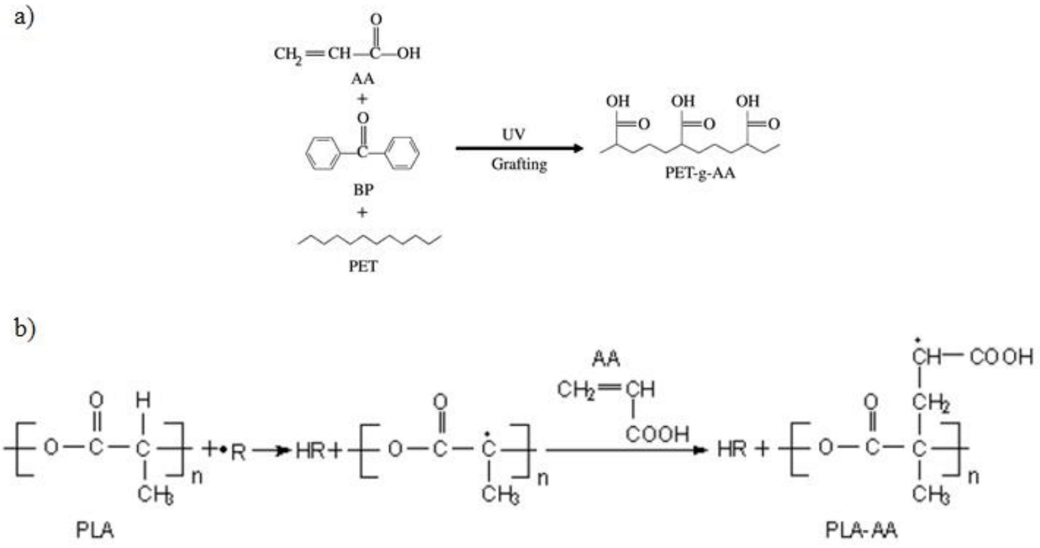

Figure II - 19 Grafting process of Acrylic Acid (AA) onto PET (a) [150] and PLA (b) [162] materials through UV radiation

II.2.3.2.2 Application of adhesive onto textile surfaces

The solution based- PSA was applied onto the surface of PET fabrics using the Chromojet (ref: Chromojet.Tabletop, Zimmer, Austria). The pick-up of the coating was 50%. The PET fabric used is the same as the one utilized in the grafting process. Afterwards, the treated fabric was dried at 60 ºC in an oven for 10 minutes. Finally, the samples were washed with water to remove the unbound adhesive and dried a drying rack at room temperature during three hours. Besides, the application of polyurethane film on the surface of PET fabrics was achieved using a heat press at 10 bars and 180 ºC during 15 seconds.

II.3 Characterization methods

II.3.1 Thermal properties

II.3.1.1 Transient Plane Source (Hot Disk)

The hot disk test method is the modified version of the standard TDA-501 to evaluate the thermal properties of textile materials. The test consists in a thin disk shaped sensor (hot-disk sensor) which measures the thermal conductivity and resistivity and the specific heat of the material (Figure II - 20). Indeed, three layers of the textile fabric, necessary to attain the required thickness, were compressed on a surface of 90 mm^2 and a pressure of 2 kPa with the hot disk positioned according to ISO 22007-2. The measurements were realized at 22°C for a duration of 320 seconds using a Kapton disk type having an output power of 0.12 Watts. For each material, three measurements were performed to certify the repeatability of the measurement results.

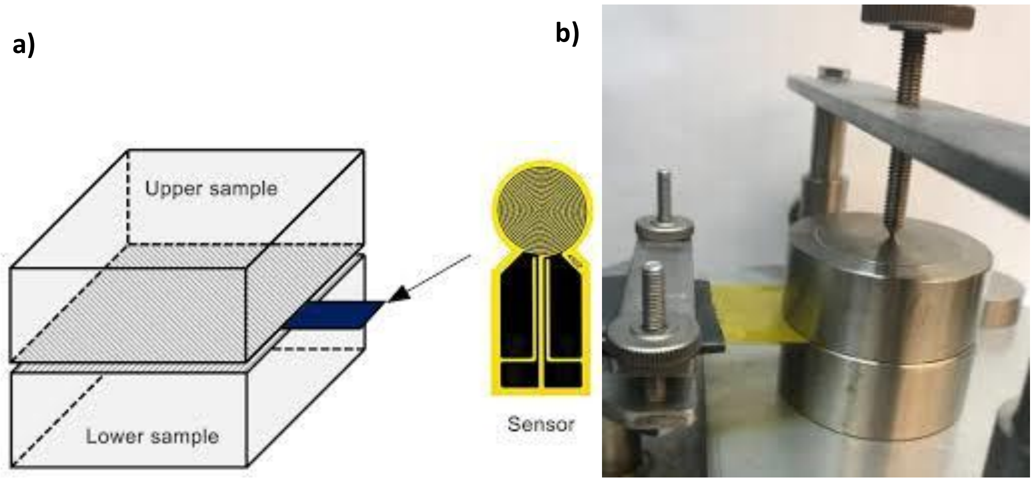

Figure II - 20 Sketch (a) and picture of the equipment (b) used in the Transient Plane Source (Hot Disk) test [163]

II.3.1.2 Thermogravimetric Analysis (TGA)

TGA is an analytical technique utilized to define the thermal stability of a material and its fraction of volatile constituents by recording the weight change that occurs while the sample is heated at a constant rate. The thermogravimetric analyzer of this experiment was the TGA Q500 (TA Instruments, DE). Each sample of about 30 mg, was heated in an atmosphere of nitrogen at a heating rate of 5 °C/min. The temperature range depends on the polymer or polymer blends used in the study.

II.3.1.3 Differential Scanning Calorimetry (DSC)

DSC measurements of the different studies were executed on DSC3 StarTM (Mettler Toledo, Columbus, Ohio, USA). Both of them were conducted under nitrogen atmosphere, at a purge rate of 50 ml/min, in a temperature range from 25 °C to 260 °C and at a heating rate of 10-15 °C.min^{-1}. Six milligrams of each sample were necessary for DSC measurements. Heating and cooling cycles between the range were carried out twice. However, only the decrease of the first cycle and the increase of the second cycle were considered in order to remove the thermal history of the involved polymers. In the case of PLA- based CPCs, **Eq. II - 2** is utilized to calculate the degree of crystallization. The melting enthalpy of 100% crystalline PLA is is 93 J/g [164].

$$degree\ of\ crystallization\ (\%) = \frac{Melting\ enthalpy\ (in\ J/g)}{Melting\ enthalpy\ (100\%\ crystalline)(in\ J/g)} \times 100 \qquad \textbf{(Eq. II - 2)}$$

For the studies using CPCs/PBE blends, the melting enthalpy and the crystallinity ratio of each constituent of the blends could not be separately determined through software such as Origin as it was challenging to execute the deconvolution of the merged melting peaks and the melting enthalpy of the 100% crystalline PBE is not in the literature.

II.3.2 Adhesion properties: T-Peel test

The adhesion experiments were carried out according to the standard test methods SS-EN ISO 11339:2010, DIN EN ISO 13937-2 and ISO 11339 named T-peel test, by using a Zwick/Z010 tensile tester at FOV Fabrics Limited (Sweden). Prior to the adhesion testing, rectangular shape layers (200 mm × 50 mm × 0.1 mm) were deposited onto the fabric through FDM process following the sample preparation steps (Figure II - 21) already pre-defined and commonly used by researchers for this application [2]. Both sides (3D printed layers and fabric) are separately clamped as shown on Figure II - 22 only the printed layer is pulled out at a separation rate of 100 mm/min. For each sample, three replicate values were necessary to obtain an accepted standard deviation of 10 per cent.

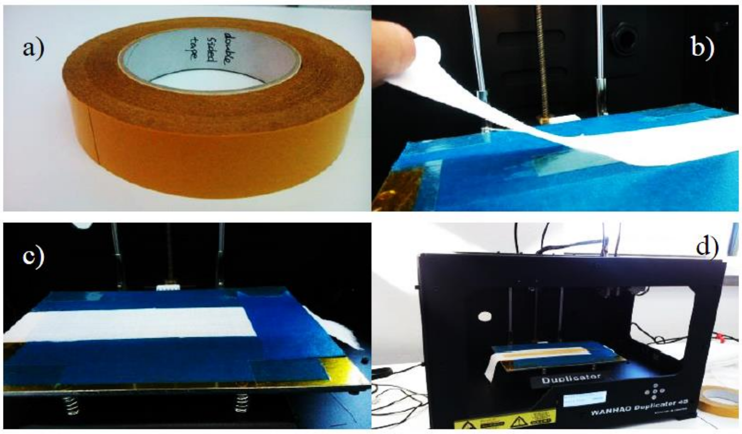

Figure II - 21 Preparation of samples prior to 3D printing process [2]

Figure II - 22 Adhesion testing of 3D-PPOT materials

II.3.3 Textile surface, structure and morphology

II.3.3.1 Capillary flow porometry

The capillary flow porometry method is defined by the principle of a gas pressure, which forces a wetting liquid out of through-pores in a sample. Before each measurement, the sample is immerged into a fluorocarbon solution with a surface tension of 15.77 dynes/cm. Through this method, the largest, mean, median and smallest pore sizes and pore distribution are measured. However, for the adhesion strength modeling study, only the mean pore size is considered as similar trends of results are observed using the other parameters [101]. It is well-known that the higher the pore size, the lower the pressure at which the pores empty and reversely (Dittler and Kasper, 2018) [165].

II.3.3.2 Profilometry

The profilometry is described as a 3D technique which determines the roughness coefficients through surface variation measurements as a function of position, by using a diamond stylus (Figure II - 23). The coefficient R_a is commonly utilized as the arithmetic mean height of the surface to characterize the surface roughness of the material. However, in this thesis, the coefficient S_a defined as the extension of the roughness coefficient R_a to a surface is used. Indeed, it is an absolute value of the difference in height of each point. Rougher textile materials possess higher "S_a" roughness coefficients. This technique allows visualizing 3D images of the surface's profile as shown in Figure II - 24. The profilometer utilized in the thesis is an Altisurf 500 (Cotec, France).

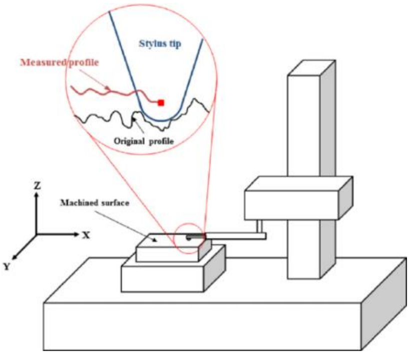

Figure II - 23 Profilometry technique [166]

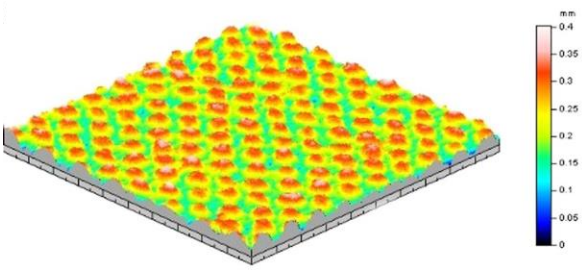

Figure II - 24 Example of image obtained using profilometer technique [121]

II.3.3.3 Scanning electron microscopy (SEM)

Textile materials observation

The surface morphology of the surface of the fabrics was observed by scanning electron microscope of reference JEOL JSM-6301F. For this experiment, the size of the sample was 10 mm × 10 mm, the voltage and resolution and the magnification at 1 kV were 6 kV and 0.5 nm and 50x respectively. A FEG JEOL JSM7800F Scanning electron microscope with a voltage of 5kV and magnification of 2000x was used to observe the effect of grafting on PLA monofilament.

CPCs and CPCs/PBE blends observation

Prior to the observation, the monofilament samples were prepared through immersion in a nitrogen liquid for a duration of 3 minutes, followed by a cut in longitudinal and transverse directions using the cryogenic fracture method (Figure II - 25). At that point, a 300 Å thickness layer of metalized chrome or carbon was applied on the surface of the monofilament. The SEM images were acquired by using an SEM Hitachi S4700 equipment located at University of Lille (France) and operating at different voltages (2-10kV) and magnifications depending on the targets of the observations.

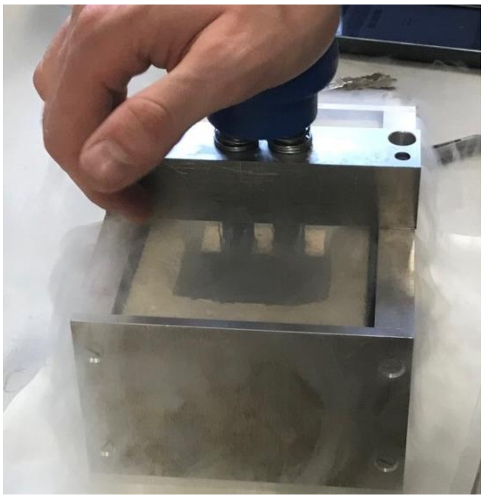

Figure II - 25 Cryogenic fracture procedure

II.3.3.4 X-ray photoelectron spectroscopy (XPS)

Spectra were recorded on a Kratos Axis Supra X-ray Photoelectron Spectrometer employing a monochromated Al Kα (hν = 1486.7 eV) X-ray source, hybrid (magnetic/electrostatic) optics with a slot aperture, hemispherical analyzer, multichannel plate and delay line detector (DLD) with a take-off angle of 90°. The analyzer was operated in fixed analyzer transmission (FAT) mode with survey scans taken with a pass energy of 160 eV and high resolution scans with a pass energy of 20 eV. The resulting spectra were processed using CasaXPS software. Empirical relative sensitivity factors supplied by Kratos Analytical (Manchester, UK) were used for quantification. The XPS characterization was executed to identify the composition of the polyurethane film and detect the presence of functional groups which could access the effectiveness of the grafting process on the different materials presented in Chapter III.

II.3.3.5 Thickness of textile and 3D-PPOT materials

In this thesis, the thickness of the fabrics and 3D-PPOT materials was determined by using the thickness – micrometer KES-FB3 according to the ISO 5084 standard. Three replicates of this measurement were necessary to acquire a standard deviation below 10 per cent.

II.3.3.6 Mass per unit area of textile and 3D-PPOT materials

The mass per unit area (or weight) of each textile and 3D-PPOT material is measured by using a standardized weighting scale following the ISO 3801:1977 standard. Three replicates of the measurements were done to guarantee a standard deviation below 10 per cent.

II.3.3.7 Transmission electron microscopy (TEM)

Transmission electron microscopy (TEM) is a technique used to detect the features of very small samples. The principle of this technology is based on an accelerated beam of electrons, which passes through a very thin specimen to allow, for instance, the observation of the structure and morphology.

II.3.4 Mechanical properties

II.3.4.1 Dynamic surface deformations

A Universal Surface Tester (UST) is a device which determines the dynamic surface deformations of a material which include its permanent and total deformations, its elasticity, its plasticity and visco-elastic properties. The principle of the UST measurement consists in several moves of a stylus on the surface of the sample with or without a load. As a first step, with a minimum load of 1 mN, the stylus scans continuously the surface of the material along a definite path. Afterwards, the same stylus scans the same path with a constant load of 60 mN. At that point, a deformation of the material's surface happens and is so-called total deformation. Then, the scanning of same path was executed again with a minimum load of 1 mN. During that stage, the elastic part of the total deformation is recovered while the permanent deformation does not recuperate. Finally, the total, permanent and elastic deformations were calculated based on the differences between surface profiles of the different steps. Five replicates were necessary to guarantee a standard deviation below 10 per cent. In this thesis, a 1.8 mm diameter stylus was selected to be close to the diameter the extruder head of the 3D printer. The applied load tries to simulate the applied pressure of the extruder head on a textile substrate during the 3D printing process [121].

II.3.4.2 Tensile resistance

Tensile and elongation at break of textile materials and 3D-PPOT materials were determined according to ISO 13934-1 standard. The sample dimensions, the distance between the clamps and the speed are 230 mm × 25 mm, 100 mm and 100 mm/min respectively. The tensile and elongation at break values were an average of the three measurements and the maximum accepted standard deviation was 10 percent.

II.3.4.3 Wear resistance

The abrasion resistance of the 3D-PPOT materials is measured as stated by ASTM D4966-12 (2016) method. The materials used in this test are a polyurethane foam backing with a thickness of 3 ± 0.01 mm, a felt of 750 ± 50 g/m^2 mass and 3 ± 0.3 mm thick with a density of 29 to 31 kg/m^3 (as abrasive fabrics) and a standard wool abrasion fabric of 215 ± 10 g/m^2. After 1000, 2000, 5000, 10000, 20000 and 30000 cycles for the 3D-PPOT material samples and 200, 500, 1000 and 2000 cycles for the textiles prior to 3D printing process, the weight loss percentage is determined through the equation (**Eq. II – 3**). The weight loss describes the difference (in percentage) between the original weight and the eight after abrasion. The maximum number of cycles, i.e. the endpoint is also determined. The three duplicates for each sample are necessary in order to warranty a standard deviation below 10 per cent.

$$Weight\ loss\ (\%) = \frac{W_0 - W_X}{W_0} \times 100 \qquad \textbf{(Eq. II - 3)}$$

Where W_0 is the initial weight of the 3D-PPOT materials or fabric, W_X the weight of the 3D-PPOT materials or neat fabric after X number of cycles.

II.3.4.4 Rheological properties: Melt Flow Index (MFI)

The Melt Flow Index (MFI) defines the flow-ability of the polymer at a certain temperature during a limited time of ten minutes. A Melt Flow Tester - ThermoHaake (Figure II - 26) was utilized according to the standard ISO-11333. Prior to the MFI test, the material is dried at 40°C for twelve hours. The test can be decomposed into various steps. In the first step, the piston goes inside the chamber of the machine and stayed for four minutes at a set temperature. At that moment, the loading and pre-heating of the polymer is executed at the same temperature during four minutes and then, it is guided through the die. Every 15 seconds, a knife automatically cuts the extruded polymer which is then collected and weighted to obtain the MFI value. The unit of the MFI value is given in g/10min. Five replicates are performed to guarantee a standard deviation below 10 percent. In this thesis, the ranges of temperature and weight used to applied the pressure were 200 - 245 °C and 2.16 - 10 Kg.

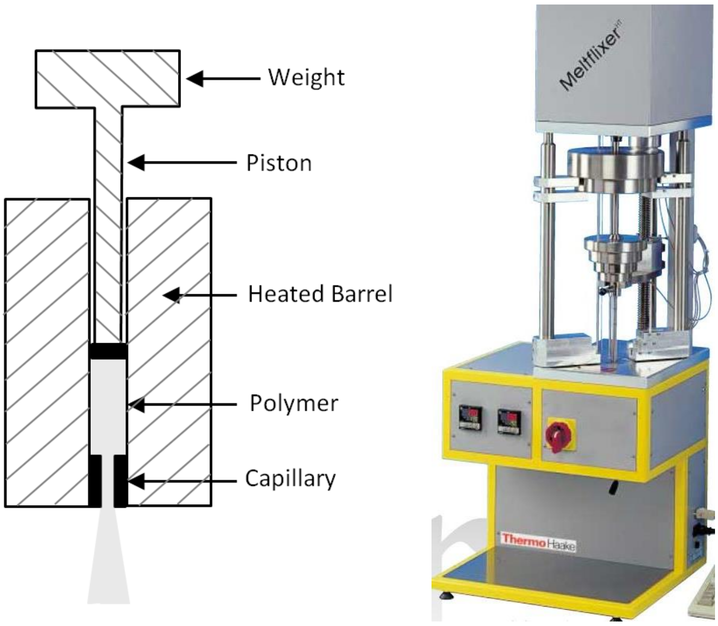

Figure II - 26 Stetch (a) and picture (b) of the Melt Flow Tester

II.3.5 Electrical properties

II.3.5.1 General principle for monofilament and 3D-PPOT materials

The electrical resistance of CPC monofilaments was measured through a hand-made four-wire system connected to Keithley 2461 SourceMeter (Beaverton, OR, USA). The set-up is presented in Figure II - 27 (a). The home-made four-point also comprises eight identical tubes that support the conductive material which need to be tested such as a monofilament, single thread, rod or track made of conductive materials. The dimensions of each tube are: a diameter of 30 mm and a length of 80 mm. For resistance measurement setup, four tubes were placed in the plexiglass holder and sample was positioned on the tubes and then, four tubes were put on the top surface of the samples. The two pairs of outer tubes and inner tubes were connected into the input terminals and the sense terminals respectively as it is shown in Figure II - 27 (b) [31]. The distance between two pairs of inner tubes is 6 centimeters. Through this configuration with the multimeter set on four-wire option, the current (I) is pushed through the resistance (R) via the first set of leads, while the voltage (VM) is determined through the second set of leads named sense leads.

The electrical resistance of conductive 3D-PPOT materials was determined through a standardized Keithley box connected to a Keithley 2461 SourceMeter (Beaverton, OR, USA). The set-up of the experiment using the Keithley box can be visualized in Figure II - 28 (a).

In this thesis, five measurements per CPCs monofilaments and 3D-PPOT materials were carried out to get a standard deviation below 10 percent [167]. The voltage applied was between −0.5 Volts and 3 Volts with an increment of 0.5 Volts. Although applying the voltage to the material, the current intensity was measured. The resistance was determined from the slope of the characteristic-curve (

Figure II - 29). Finally, the electrical conductivities for the monofilaments and the 3D-PPOT materials were calculated through **Eq. II - 4** and **Eq. II – 5** respectively.

$$\sigma = L/(R \times S) \qquad \textbf{(Eq. II - 4)}$$

Where σ is the electrical conductivity (S/m), R is the resistance of the sample (Ω) R=1/slope, L is the distance between the electrodes (m), and S is the cross-sectional area of the sample (m^2).

$$\sigma_s = 1/(R/S) \qquad \textbf{(Eq. II – 5)}$$

Where σ_s is the surface conductivity (S), R is the resistance of the sample (Ω) R=53.4/slope and S is the cross-sectional area of the sample (m^2).

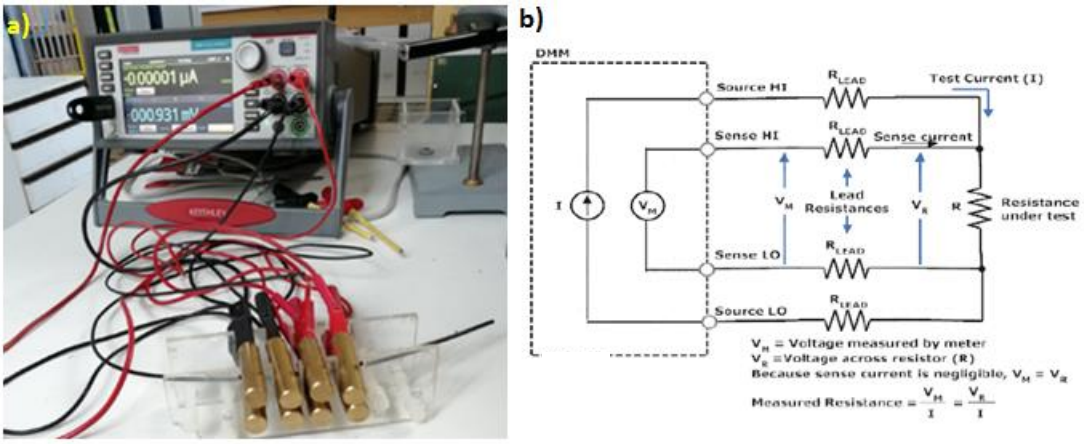

Figure II - 27 Four-wire system for electrical resistance measurements. (a) Measurement setup and (b) Schematic of connections and the circuit [31]

Figure II - 28 Standardized Keithley box (a) and measurement set up (b) [167]

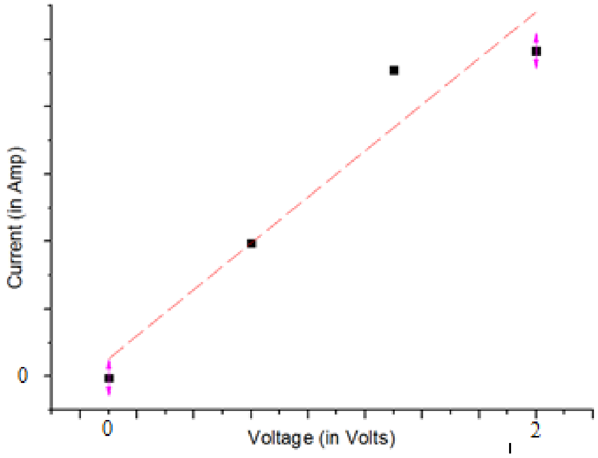

Figure II - 29 Current-voltage characteristic with the linear fitting between 0 V and 2 V [167]

II.3.5.2 Before and after abrasion test

The existing procedures [168,169] for in-plane measurements of the electrical resistance of materials could not be applicable for 30 mm diameter samples made of 3D printed conducting polymer 3D printed only onto one side of the textile material used in abrasion test. Therefore, a new and in-house customized system, with an acceptable reliability, presented in Figure II - 30, was developed for the purpose.

The principle is the following: a three centimeters diameter electrode applied to non-abraded and abraded 3D-PPOT materials under a weight of 300 grams was connected to a Keithley 3706A digital multimeter. As for the general method of electrical conductivity measurement of 3D-PPOT materials, a visualization of the current-voltage characteristic for a voltage value from -0.5 Volts (V) to 3 V and a step of 0.5 V, was necessary to determine the surface electrical resistance (Figure II - 29). The surface electrical conductivity is obtained by using the equations **Eq. II - 6** and **Eq. II - 7**. Five replicates for each sample of the three samples were required to ensure a standard deviation below 10 percent.

$$\sigma_S = \frac{e}{L \times R} \qquad \textbf{(Eq. II - 6)}$$

$$R = \frac{1}{f} \qquad \textbf{(Eq. II - 7)}$$

Where R the electrical resistance (Ohm), e is the distance between the electrode (e = 5 mm), L is the apparent length (L = 39 mm) and f is the slope of the current/voltage linear fitting curve between 0 V and 2 V and σ_S in Siemens (S) is the surface electrical conductivity.

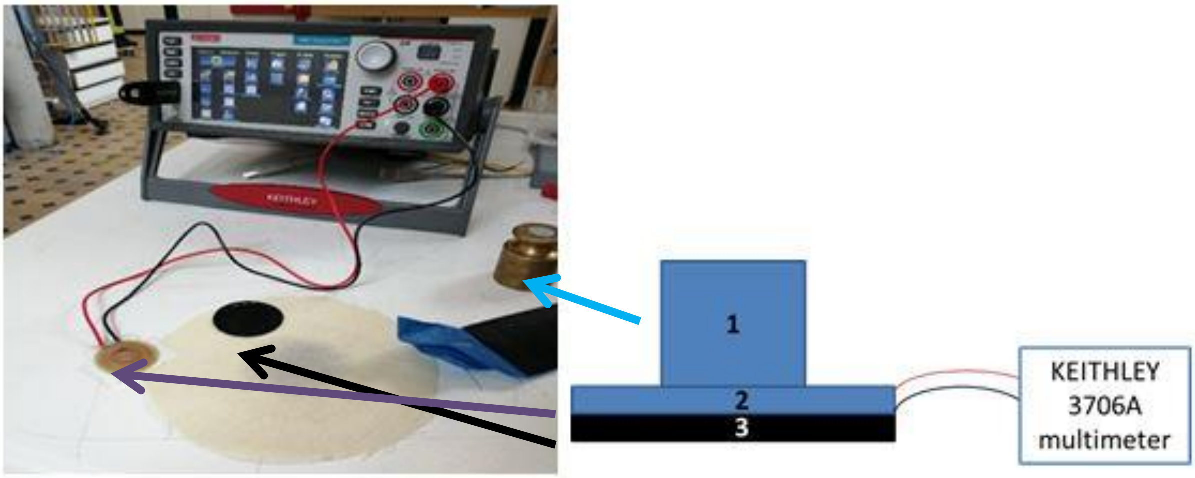

Figure II - 30 Electrical conductivity measurement system used for 3D-PPOT materials before and after abrasion ("Martindale"). (1), (2) and (3) represent the weight of 300 grams, the electrodes and the textile material respectively.

II.3.6 Wettability-Capillary

The wettability and capillary measurements are carried out using a weighting scale called "3S balance" from GBX Instrument (France). It allows to demonstrate the tendency of one fluid (mainly water) to spread on or adhere to a solid surface [170]. The method utilized is based on vertical wicking test method, which was formerly defined in the literature.[153] The capillary rise is defined as the ratio between the weight of liquid absorbed by the textile material in two minutes (M_c) and the initial weight of the sample (W_i). The value of this parameter is obtained through Eq**. II – 8** :

$$C_r(\%) = \frac{M_C}{10^{-3} W_i} \times 100 \qquad \textbf{(Eq. II – 8)}$$

II.3.7 Contact angle measurement of textile materials

A Theta Optical Tensiometer instrument (ref: Attension Theta) was used to measure water contact angle θ between the water and the samples after 5 seconds. The method consists in a 7 mL water droplet deposited onto the textile samples of 2 cm^2 cut and positioned on a glass slide prior to test. Each sample was tested three times at three different locations and the average of the three values was analyzed. The contact angle value was obtained directly using the Attention Theta software.

II.3.8 Location of fillers in biphasic blends

The contact angle between polymeric materials or nanoparticles and two different liquids (water and α-bromonaphthalene) with specific and different surface tensions were determined using a GBX MCAT V6 Digidrop (Dublin, Ireland). Prior to measurement, the pellets of polymeric films were prepared through thermocompression and the pellets of compressed KB particles powder were prepared using paraffin. The theoretical values of the surface tensions for the water and α-bromonaphthalene are defined in Table II- 9 [33]. The contact angles of each sample were assessed after the 30 µL –drop of wetting liquids was standing for 30 seconds on the surface at room temperature. The average value of the contact angle was obtained by using five drops of each liquid, one polar and the other one apolar.

Table II- 9 Surface tensions of water and α-bromonaphthalene

Liquid	γ_L **(mN/m)**	$\gamma_L{}^D$ **[1](mN/m)**	$\gamma_L{}^P$ **[2](mN/m)**
Water	72.6	21.6	51
α-bromonaphthalene	44.6	44.6	0

[1] Dispersive component of surface tension of the liquid $\gamma_L{}^D$

[2] Polar component of surface tension of the liquid $\gamma_L{}^D$

Besides, based on different equations already demonstrated by Fowkes [171] and Cardinaud *et al.*[172] the interfacial energies between the polymer and the particles can be calculated with the contact angle values. The surface tension of the CNT nanoparticles, its dispersive and polar components utilized in the calculation were 27.8, 17.6, and 10.2 mN/m [32]. As a last step, the location of the fillers in each biphasic blend was calculated with the equation **Eq. II – 9**.

$$\omega_{A-B} = \frac{\gamma_{filler\,1-B} - \gamma_{filler\,1-A}}{\gamma_{A-B}} \qquad \textbf{(Eq. II – 9)}$$

Where ω_{A-B} is the wettability coefficient between the polymers A and B, $\gamma_{\text{filler 1-B}}$ is the interfacial energy between the filler 1 and polymer B (Nm/m), , $\gamma_{\text{filler 1-A}}$ is the interfacial energy between the filler 1 and polymer A (Nm/m) and $\gamma_{A\text{-}B}$ is the interfacial energy between the polymer A and the polymer B.

The interfacial energies are calculated as below .

$$\gamma_{1-2} = \gamma_1 + \gamma_2 - \frac{4\gamma_1{}^{\mathbf{D}}\gamma_2{}^{\mathbf{D}}}{\gamma_1{}^{\mathbf{D}} + \gamma_2{}^{\mathbf{D}}} - \frac{4\gamma_1{}^{\mathbf{P}}\gamma_2{}^{\mathbf{P}}}{\gamma_1{}^{\mathbf{P}} + \gamma_2{}^{\mathbf{P}}} \qquad \textbf{(Eq. II – 10)}$$

$$\gamma_{1-2} = \gamma_1 + \gamma_2 - 2\sqrt{\gamma_1{}^{\mathbf{D}}\gamma_2{}^{\mathbf{D}}} - 2\sqrt{\gamma_1{}^{\mathbf{P}}\gamma_2{}^{\mathbf{P}}} \qquad \textbf{(Eq. II – 11)}$$

where γ_{1-2} is the interfacial energy between the components 1 and 2 (mN/m), γ_1 is the surface tension of the component 1 (mN/m), γ_2 is the surface tension of the component 2 mN/m), $\gamma_1{}^{\mathbf{P}}$ and $\gamma_2{}^{\mathbf{P}}$ are the polar part of the component 1 and 2 (mN/m), $\gamma_1{}^{\mathbf{D}}$ and $\gamma_2{}^{\mathbf{D}}$ is the dispersive part of the component 1 and 2 (mN/m).

The following scenarios may occur:

- The wettability coefficient is inferior to −1, which means that the filler 1 is located in the polymer B;
- The wettability coefficient is between −1 and 1, which means that the filler 1 is found at the interface of the two polymers;
- The wettability coefficient is superior to 1, which means that the filler 1 is in the polymer A.

Chapter III Improvement of adhesion properties of 3D-PPOT using monophasic materials

As described in Chapter I, one of the fundamental properties of 3D-PPOT materials is the adhesion strength between the deposited layer and the textile materials. Despite the several suggested solutions to enhance this property, the adhesion resistance remains very low in some cases, which makes the use of 3D-PPOT materials in textile industry difficult. However, an important fact to point out is the change in adhesion strength depends on the properties of the polymeric printed track and the textile fabrics as well as their interface. Many different types of textiles are produced every day in the world for various applications. In order to understand and predict the influence of the properties of the textiles the use of the statistical modeling is needed. At that point, the properties of 3D-PPOT materials can be optimized and improved through selective choice of fabrics, pre or post treatments.

Thus, this chapter focuses on describing two methods utilized in this thesis to optimize and enhance the adhesion of 3D-PPOT using monophasic materials: statistical modeling using the textile properties' values and functionalization of the textiles' surface followed by the application of adhesive. *Section III.1* introduces the materials, the manufacturing processes and the methods utilized to characterize both the textiles and polymeric materials of the study. *Section III.2* defines in details the statistical design of each experiment of the study, including the selected factors, targeted responses and the analysis method of the findings. *Section III.3* presents the results of the first experiment about the optimization of the adhesion properties of the 3D-PPOT materials through models using the properties of the textiles. *Section III.4* relates the wash-ability of the 3D-PPOT materials by explaining what are its impacting factors and how does it influence the adhesion. *Section III.5* demonstrates the effectiveness of the functionalization processes (plasma and grafting) and application of film and solution- based adhesives, and their influence on the adhesion. Finally, *Section III.6* gives an overview and summary of the current study on the enhancement of adhesion properties of 3D-PPOT.

For each material, process, characterization method and previous work already presented in Chapters I and II, the referred section will be written in brackets.

III.1 Materials, processes and characterization

In the study of the optimization of the adhesion through statistical modeling using the properties of textiles, virgin ECO-PLA and conductive PLA (PLA/2.5%CB) monofilaments obtained through extrusion process are used as raw materials for 3D printer and PET woven textile as support materials. The monofilaments are already described in the section *II.1.1.* Six PET fabrics with two different patterns (plain and twill 2/2) and three different weft densities (14, 18 and 22 picks/inch) were manufactured in house and their mass per area and thickness (*II.4.3)* are presented in Table III- . The composition and structure of the fabrics were already defined in the section *II.1.3.* These fabrics were selected due to their significant difference in term of structure, mass per area and thickness leading to different porosity, thermal conductivity and roughness. Therefore, the relationship between these properties and the adhesion could be confirmed. The 3D printing (FDM) manufacturing process was executed using a printer WANHAO Duplicator 4/4x (*II.2.3*). The dimensions of the woven samples were 80 mm × 225 mm × thickness, according to Table III- was directly placed onto the 3D printing platform prior to printing. Then, a rectangular track made of non-conductive and conductive PLA (50 mm × 200 mm × 0.1 mm) was deposited on each different set of woven materials. The constant value of the infill percentage, the Z offset (i.e. the gap between the head of the extruder and the surface of the fabric), the printing speed, the diameter of the selected extruder (the right one) and the extruder temperature were 20%, 0 mm, 3600 mm/min, 0.4 mm and 250 ℃ respectively. The different characterization methods of the PET fabrics before 3D printing were the capillary flow porometry to determine the pore size, the profilometry to measure the roughness and the hot-disk method to obtain the thermal conductivity value. All the characterization methods mentioned above are already described in the section *II.4.* After 3D printing process, the adhesion between the printed track and the fabric (*II.4.2*) and the durability of 3D-PPOT materials after washing (*II.2.4*) were approached.

Table III- 1 Mass per area and thickness of PET fabrics

Pattern	Weft density (picks/inch)	Mass per area (g/m^2)	Thickness (mm)
Plain	14	157.9 ± 1.6	0.59 ± 0.01
Twill 2/2	14	159.0 ± 1.6	0.79 ± 0.02
Plain	18	173.9 ± 1.7	0.50 ± 0.01
Twill 2/2	18	176.8 ± 1.8	0.75 ± 0.02
Plain	22	194.1 ± 1.9	0.58 ± 0.01
Twill 2/2	22	202.3 ± 2.0	0.76 ± 0.02

Besides, in the study concerning the enhancement of adhesion via the functionalization of the textile's surface, a washed, heatset and unsized PET spunlaced plain-woven fabric from FOV (Sweden), a washed and unsized PET non-woven from IMS non-woven (Sweden) (*II.1.1),* the virgin ECO-PLA and conductive PLA monofilaments were utilized. Throughout this chapter, the designations "NW" and "W" were used for non-woven and woven materials. The grafting of Acrylic Acid (AA) (*II.3.3*) and atmospheric plasma (*II.3.1*) processes onto PET fabrics were used to functionalize the surface of the PET textiles. Two different types of adhesives were employed: a solution based pressure-sensitive adhesive and a PU film adhesive (*II.1.1.4*) from Lohmann GmbH & Co. Their application processes are described in the section *II.3.4*. The 3D printing onto textile process (*II.2.3*) was realized by using a 3D printer (DELTA model 20/40), where PLA layers (50 mm × 200 mm × 0.1 mm) were printed onto PET fabric samples (80 mm × 250 mm) directly fixed onto the platform of the 3D printer. The 3D printing parameters are presented in

Table III- 2. The characterization methods (*II.4)* used in these experiments are the following: the wettability-capillarity, the contact angle, the Scanning Electron Microscope (SEM) , the profilometry , capillary flow porometry method and the adhesion strength measurements of 3D-PPOT.

Table III- 2 Printing process parameters

Parameters	**Values (units)**
Infill percentage	20 (%)
Z offset	0 (mm)
Printing speed	15000 (mm.min-1)
Extruder diameter	0.4 (mm)
Extruder temperature	250 (°C)

III.2 Statistical design of experiments

In the study of the optimization of the adhesion through statistical modeling using the properties of textiles, four distinct factors (platform temperature and weft density as continuous factors and fabric orientation and pattern as discontinuous factors) were utilized to randomly create a design of experiment in Minitab 17 software (*I.2.5*). The design of experiments that uses non-conductive PLA includes 60 runs and the one of conductive PLA, 36 runs in total. The different factors with their values and codes are described in Table III- 3 and Table III- 4.

Table III- 3 **Factors of statistical design of experiments conducted with non-conductive PLA monofilaments [101]**

Factors	**Values (unit or code)**
Platform temperature	25, 40, 60, 80 and 100 (°C)
Weft density of the fabric	14, 18 and 22 (picks/inch)
Fabric direction	Machine (M)^{1}and Cross (C)^2
Fabric pattern	Plain (P) and Twill 2/2 (T)

The study about the improvement of adhesion through the functionalization of the textile's surface, the two sets of experiments with their various factors described in Table III- 5 and Table III- 6, were also randomly created (*I.2.5*).

Table III- 4 Factors of statistical design of experiments conducted with conductive (PLA/2.5% CB) monofilaments. [1]Conductive and non-conductive PLA layer printed along the warp threads. [2]Conductive and non-conductive PLA layer printed along the weft threads [101]

Factors	Values (unit or code)
Platform temperature	25, 60 and 100 (°C)
Weft density of the fabric	14, 18 and 22 (picks/inch)
Fabric direction	Machine (M) and Cross (C)
Fabric pattern	Plain (P) and Twill 2/2 (T)

The first one (Table III- 5) was developed to evaluate the effect of grafting of acrylic acid onto both PET woven fabrics and PLA monofilaments by UV radiation and application of adhesives on the adhesion resistance of 3D-PPOT materials. The second one (Table III- 6) was exploited to investigate the influence of the air-plasma treatment onto the PET woven and non-woven fabrics on the adhesion strength between the 3D printed layer and the fabric. Three replicates of each experiment were completed for each run.

Table III- 5 Grafting experiment: factors in the statistical design of experiments and their levels

Factors	Name	Level			
		-1	0	1	2
A	Adhesive type	Pressure-sensitive adhesive (PSA)	Polyurethane film		
B	Pre-treatment	No pre-treatment	Grafting of acrylic acid	Grafting of acrylic acid and pressure-sensitive adhesive	Grafting of acrylic acid and polyurethane film
C	Platform temperature (°C)	40	60	80	100
D	Post-treatment	No post-treatment	Thermo-compression using a heat press machine		

Table III- 6 Air-plasma treatment experiment: factors in the statistical design of experiments and their levels

Factors	Name	Level	
		0	1
A	Fabric type	Woven	Nonwoven
B	Plasma treatment	Treated	Untreated
C	Electrical Power (W)	750	1000
D	Speed of the sample relative to plasma (m/min)	2	10

III.3 Adhesion optimization through textile properties

III.3.1 Impacting textiles' properties on the adhesion resistance

In general, based on the design of experiments described in Table III- 3 and The study about the improvement of adhesion through the functionalization of the textile's surface, the two sets of experiments with their various factors described in Table III- 5 and Table III- 6, were also randomly created (*I.2.5*).

Table III- 4, the difference in adhesion between non-conductive and conductive PLA to textile structures highly depends on their surface and their structure (Figure III-). Indeed, it was seen that the conductive PLA (PLA/2.5%CB i.e. Carbon Black –filled PLA) adhered better to plain structure than non-conductive and reversely when printing them on twill 2/2 fabric. The lower adhesion of conductive PLA to twill 2/2 might be explained by its lower viscosity which did allow it to penetrate strongly and deeply through the structure. In other words, despite the presence of pores in the structure, the polymer cannot penetrate due to its important viscosity.

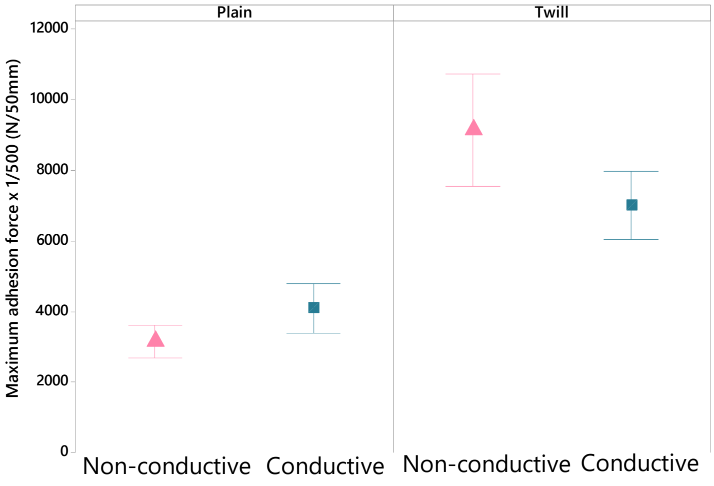

Figure III- 1 Comparison of maximum adhesion forces of 3D printed materials using non-conductive and conductive PLA monofilaments [101]

Additionally, one of the benefices of using statistical modeling is the possibility to detect which factors among the four cited in the section *III.2* impact significantly the adhesion strength. As a reminder, depending on the value of the p-value the factors have (p-value <0.05) or not (p-value >0.05) an impact on the response which is, in that case, the adhesion force. The study revealed that the pattern, the weft density and the direction had a significant influence (p<0.05) on the adhesion force of 3D-PPOT materials using both conductive and non-conductive PLA filaments (Figure III- 2) and the pattern of the fabric had the greatest contribution compared to the other factors (Table III- 7-Table III- 8) i.e. there is an important difference in adhesion when using different patterns. In statistics, the contribution percentage of the variables (or factors) defines if the factors have to be included in the regression models linking the adhesion properties and the variables. Only factors high percentages of contribution will be considered. 3D printing of both non-conductive and conductive PLA in the cross direction of PET twill fabrics with lower weft densities demonstrates a better adhesion property of the 3D-PPOT materials. In addition, a significant quadratic effect (p=0) of the platform temperature on the maximum adhesion strength was observed when using non-conductive PLA filament while no significant impact in the case of conductive PLA filament (p-value=0.006) was detected, which might be due to the range of platform temperature not sufficient enough to observe a difference[101].

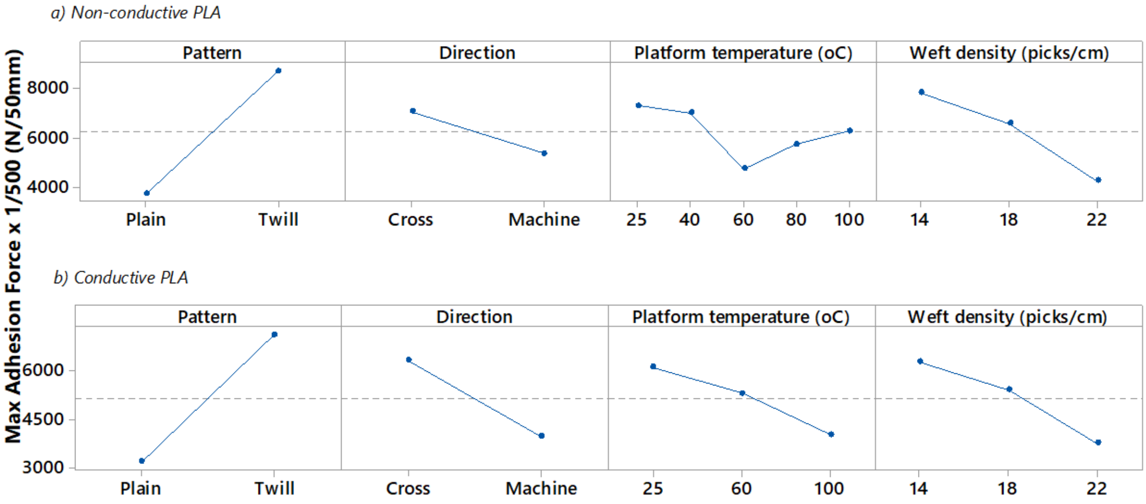

Figure III- 2 Main effects plots (with trend lines) of maximum adhesion force of 3D printed using non-conductive (a) and conductive (b) PLA filaments [101]**.**

Table III- 7 Maximum adhesion forces of 3D printed PET fabric with non-conductive PLA monofilament: main contributions and p-values [101]

Source	Contribution	P-value
Full Model	86.94%	
Pattern	25.78%	0.000
Direction	2.91%	0.000
Platform temperature (°C)	3.50%	0.000
Weft density (in picks/inch)	8.93%	0.000
Pattern*Platform temperature	4.21%	0.000
Platform temperature*Weft density	4.77%	0.000
Direction*Platform temperature	3.53%	0.000
Pattern*Weft density	2.77%	0.000

Table III- 8 Maximum adhesion force of 3D printed PET fabric with conductive PLA monofilament: main contributions, p-values [101]

Source	**Contribution**	**P-value**
Full Model	87,54 %	0,000
Pattern	25,09 %	0,000
Direction	10,45 %	0,001
Platform temperature (°C)	10,54 %	0,006
Weft density (picks/cm)	5,50 %	0,000
Platform temperature*Weft density	13,3 %	0,000
Pattern*Weft density	8,22 %	0,008

In order to understand why the textile properties, especially thoses linked to the structure and the surface, and the build platform temperature impact significantly the adhesion, it was necessarily to characterize the textile materials by measuring their average pore sizes (i.e. the opening of the fabric structure), the roughness of their surface and their thermal conductivity. As formerly mentioned, in the case of 3D-PPOT materials made of conductive PLA printed onto PET fabric it was seen that the maximum adhesion strength was stronger if the textile pattern was Twill 2/2 woven fabric compared to plain weave. This can be explained by the higher porosity (Figure III- 3) and roughness (Figure III- 4), and lower thermal conductivity of the twill 2/2 than the plain one (Figure III- 5). Similar trends of thermal conductivity values were found by Karaca *et al.* (2012) [173].

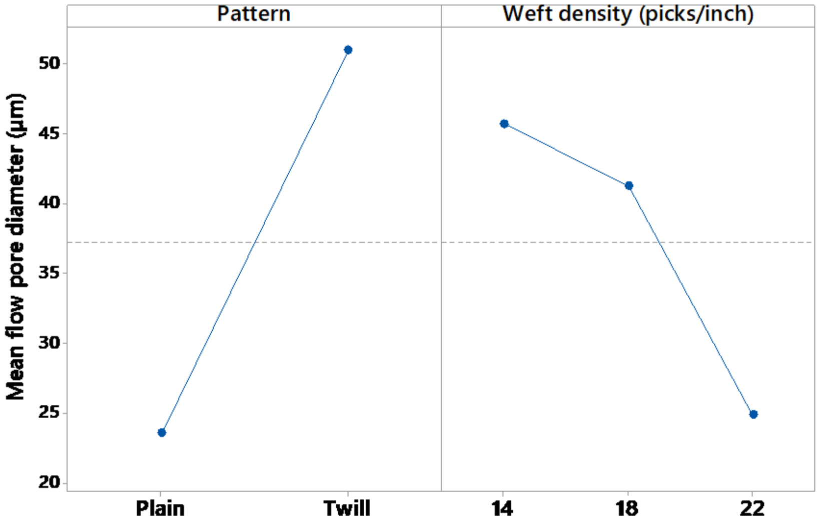

Figure III- 3 Mean pore diameter (µm): main effects (with trend lines) [101]

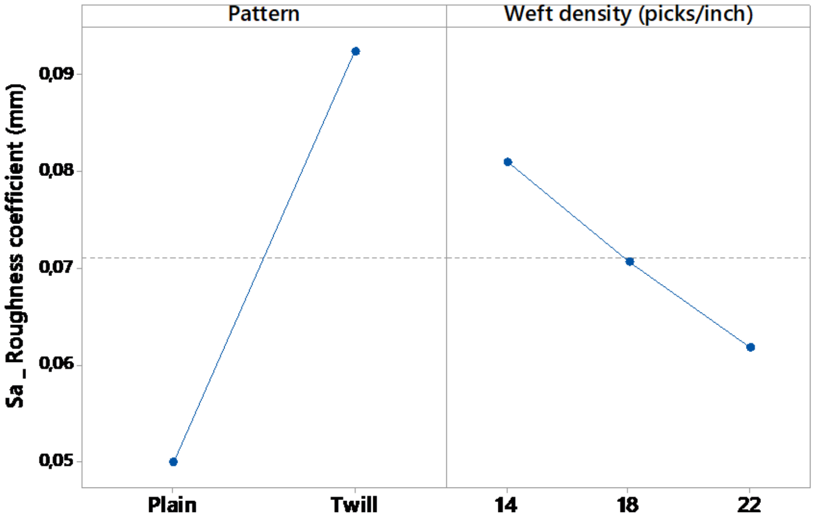

Figure III- 4 Sa roughness coefficient (mm): main effects (with trend lines) [101]

Furthermore, Mooneghi *et al.* (2014) and Ezazshahabi *et al.* (2017) discovered that, with a confidence range of 95%, there is a significant correlation between weft density and surface roughness as well as and weave structure and surface roughness coefficient [174,175]. Indeed, an increase of the weft density leads to reduce the gaps between yarns in the fabric structure and increase the constancy of the fabric to finally create a smoother surface [175]. Formerly, based on the the mechanical theory of adhesion, some researchers have already demonstrated the improvement of the adhesion strength by increasing the roughness and porosity of the textile materials [82,83,92–99,84–91]. An increase in the adhesion strength through the use of rougher surface was explained by an rise of the Van der Waals forces and the interactions between both surfaces resulting in higher mechanical interlocking [109]. As stated in the mechanical theory of adhesion, rougher and more porous textile surfaces allow the molten thermoplastic monofilament to penetrate and fill the valleys, resulting in anchorage areas between them [108].

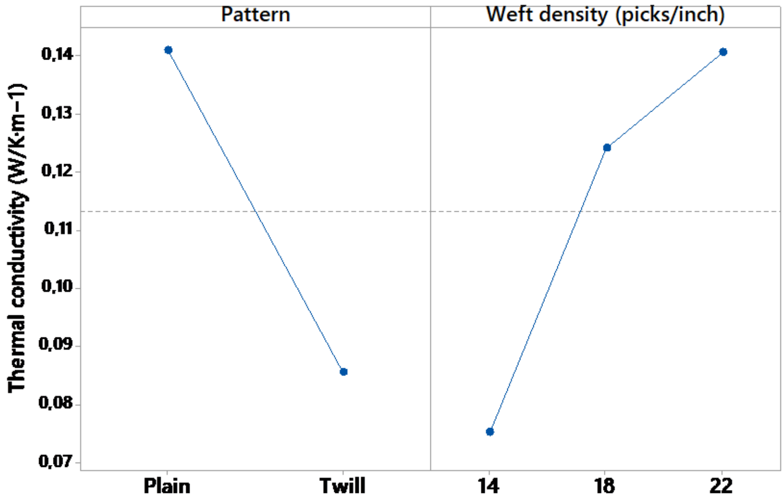

Figure III- 5 Thermal conductivity (W/K·m−1): main effects [101]

Apart from the roughness and porosity of the substrate surface, a low viscosity of the thermoplastic monofilament will be preferred. Furthermore, a low thermal conductivity of the textile materials might lead to a better absorption of the heat coming from both the extruder and the build platform, and maintain it within the structure during the 3D printing process. Therefore, the crystallization kinetics of non-conductive and conductive PLA changes while going through the textile structure.

III.3.2 Theoretical statistical models between textiles' properties and adhesion

As it was previously mentioned, statistical modeling (*I.2.5*) allows the detection of impacting factors on responses (in our case, the adhesion force of 3D-PPOT). However, the use of statistical modeling is also appreciated in the development of mathematical models correlating the most impacting factors to the responses but also some defined variables to the responses. Thus, statistical models were developed for both non-conductive and conductive materials to optimize their adhesion properties.

III.3.2.1 For non-conductive 3D-PPOT materials

Based on the findings described in the section (*III.3.1*), a linear relationship between the textile properties that are the variables and the maximum adhesion force using non-conductive filament defined as responses were observed at different platform temperatures and in both directions (Figure III- 6). This observation confirmed, once more, that a decrease of the thermal conductivity and increase both roughness coefficient and mean pore size led to an increase of the adhesion force. Therefore, a variable named f_{tex} which connects the three textile properties was created using Minitab 17 software and its mathematical equation **Eq. III- 1** is mentioned below.

$$\boldsymbol{f_{tex} = -0,5410 \times T_c + 0,6039 \times MP_o + 0,5854 \times S_a} \qquad \textbf{(Eq. III- 1)}$$

where T_c: Thermal conductivity (W/K.m^{-1}), MP_o: Mean flow pore diameter (µm) and S_a (mm): Roughness coefficient.

a) Cross direction

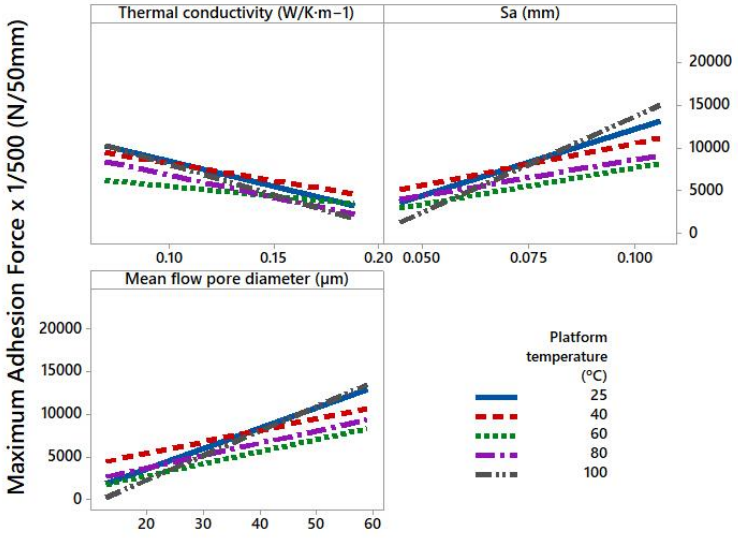

b) Machine direction

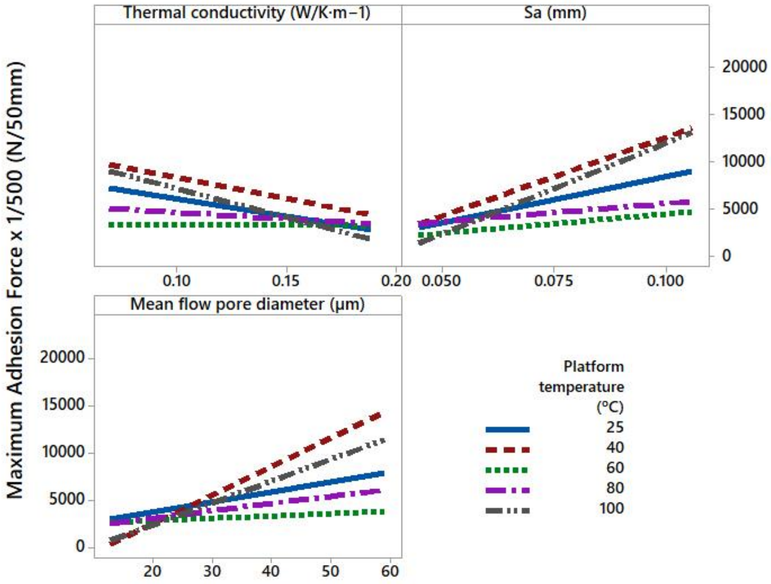

Figure III- 6 Regression curves: Maximum adhesion values in cross (a) and machine direction (b) versus thermal conductivity, roughness coefficient Sa and mean pore size [101] for each platform temperature (25°C in blue, 40°C in red, 60°C in green, 80°C in purple and 100°C in grey)

Thus, two theoretical models between f_{tex} and the maximum adhesion strength in cross (**Eq. III- 2**) and machine (**Eq. III- 3**) directions were successfully developed and simulated through Origin software and with an R-square range of 86- 90% as shown in Figure III- 7. It can be noticed that the suggested models are close to the experimental values and are also in accordance with the trends of adhesion results formerly stated (Figure III- 6).

$$\text{Maximum Adhesion force (N/50mm)} = \frac{1}{500}(257.2 \times f_{tex} + 3.16 \times {f_{tex}}^{2}) \qquad \textbf{(Eq. III- 2)}$$

$$\text{Maximum Adhesion force (N/50mm)} = \frac{1}{500}(203.4 \times f_{tex} + 0.96 \times {f_{tex}}^{2}) \qquad \textbf{(Eq. III- 3)}$$

$$\text{Where } f_{tex} = -0{,}541 \times \mathrm{T_C} + 0{,}6039 \times \mathrm{MP_O} + 0{,}5854 \times \mathrm{S_a} \qquad \textbf{(Eq. III- 1)}$$

f_{tex}: textile parameters constant, T_c: Thermal conductivity (W/K.m^{-1}), MP_o: Mean Pore size (µm) and S_a: Roughness coefficient (mm).

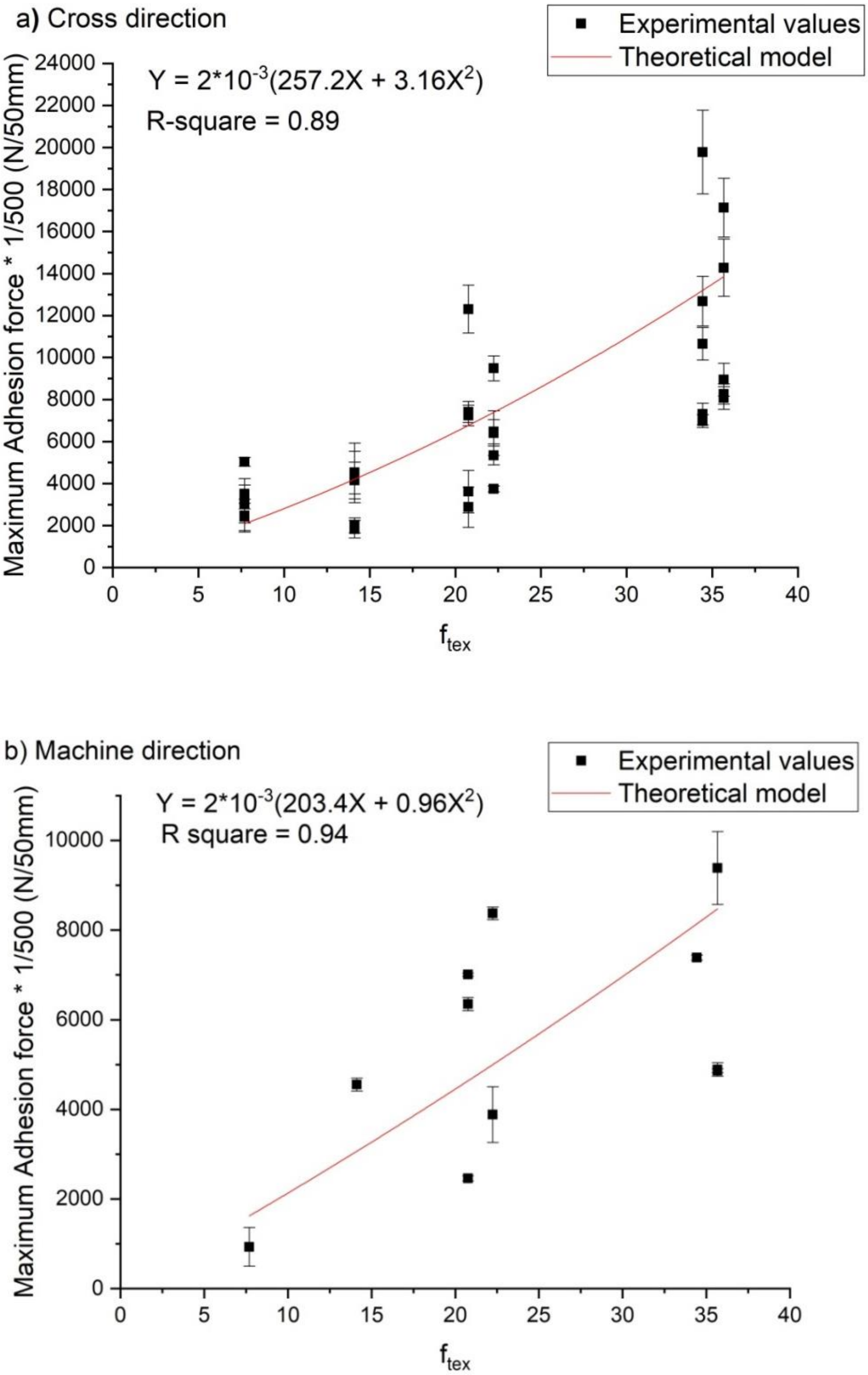

Figure III- 7 Maximum adhesion forces: experimental values versus theoretical model [101]

Finally, theoretical models between the maximum adhesion force, platform temperature and f_{tex} in both directions, i.e. cross (Eq. III- 4) and machine (Eq. III- 5) were generated based on the experimental values (Figure III- 8).

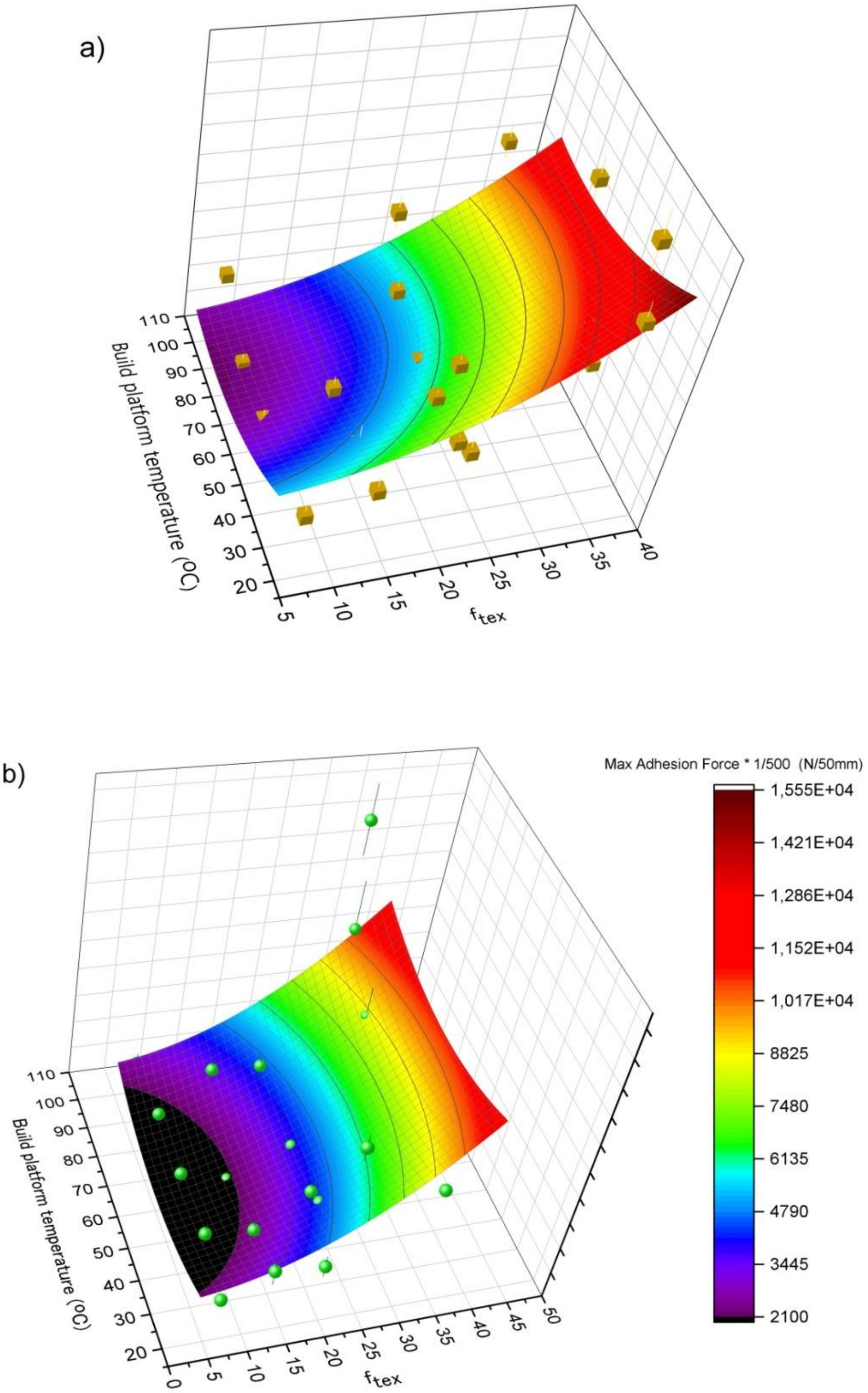

Figure III- 8 3D surface plots of max adhesion force models in the cross (a) and machine (b) directions versus the experimental data (scatterplots in gold (cross) and green (machine)) [101]

The R-square range of values of these suggested models were 70- 80%. The findings revealed that f_{tex} variable has the greatest influence on the maximum adhesion force compared to the platform temperature (Figure III- 8).

$$\text{Maximum Adhesion force (N/50mm)} = \frac{1}{500}(8983 - 177{,}5 \times T_p + 9 \times f_{tex} + 1{,}115 \times T_p{}^2 + 6{,}19 \times f_{tex}{}^2) \quad \textbf{(Eq. III- 4)}$$

$$\text{Maximum Adhesion force (N/50mm)} = \frac{1}{500}(4678 - 134{,}2 \times T_p + 9 \times f_{tex} + 1{,}115 \times T_p{}^2 + 6{,}19 \times f_{tex}{}^2) \quad \textbf{(Eq. III- 5)}$$

Where $f_{tex} = -0{,}541 \times T_C + 0{,}6039 \times MP_0 + 0{,}5854 \times S_a$ **(Eq. III- 1)**

f_{tex}: textile parameters constant, T_p: Build platform temperature (°C), T_c: Thermal conductivity ($W/K.m^{-1}$), MP_o: Mean Pore size (µm) and S_a: Roughness coefficient (mm)

III.3.2.2 Conductive 3D-PPOT materials

A linear relationship between the textile properties and the maximum of adhesion force were similarly developed for 3D-PPOT materials using the conductive PLA. All the experiments printed in the cross direction demonstrated an increase of the maximum adhesion force for textiles with lower the thermal conductivity and higher roughness coefficient and mean pore size (Figure III- 9). These outcomes are in accordance with those obtained with non-conductive PLA monofilaments. Moreover, based on the findings presented in Figure III- 9, theoretical model between f_{tex} and the maximum adhesion strength was effectively developed and simulated using Origin software (R-square = 88%) as shown in Figure III- 10.

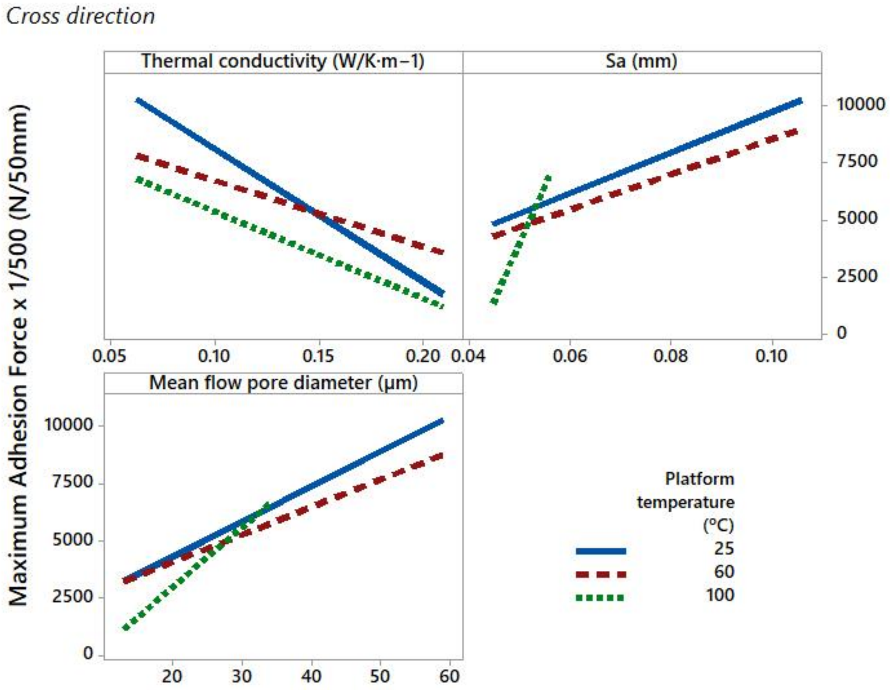

Figure III- 9 Regression plots of maximum adhesion of 3D printed material using conductive monofilaments [101] for each platform temperature (25°C in blue, 60°C in red and 100°C in green)

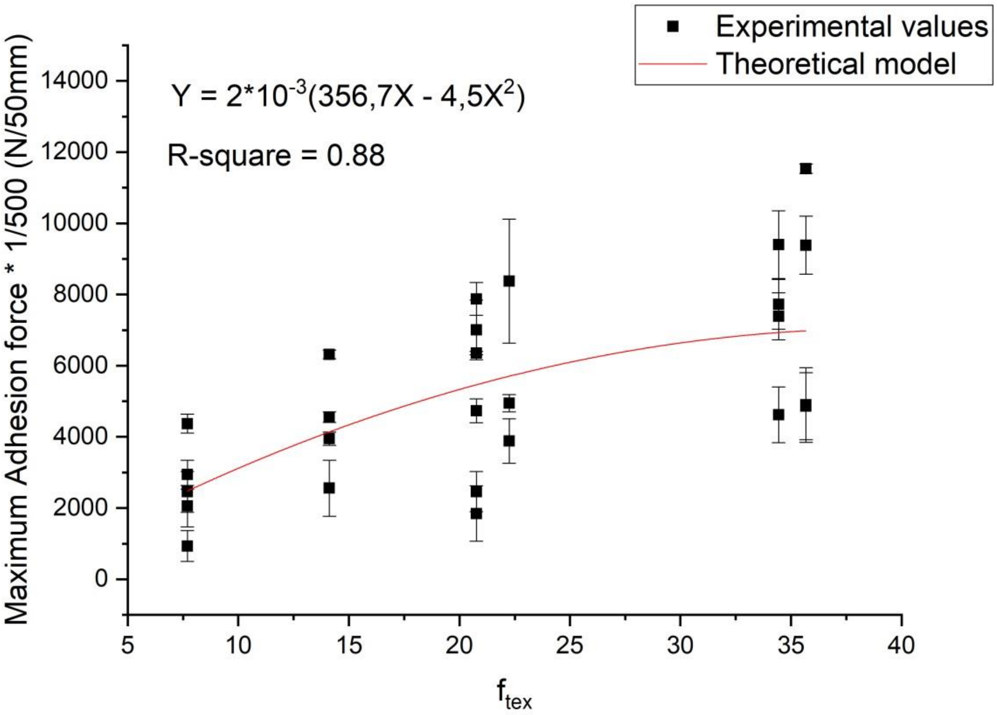

Figure III- 10 Maximum adhesion force of conductive 3D-PPOT: experimental values (black dots) versus 2D theoretical model (red straight line) in the cross direction versus thermal conductivity, roughness coefficient and mean pore size [101]**.**

This theoretical model is defined in the cross direction by using the equation **(Eq. III- 6)**. A rise of f_{tex} coefficient improved the values of the maximum adhesion force.

$$\text{Maximum Adhesion force (N/50mm)} = \frac{1}{500}(\,356.7 \times f_{tex}\; - \;4.51\; \times \;{f_{tex}}^{2}) \qquad \textbf{(Eq. III- 6)}$$

Where $f_{tex} = \; -0{,}541 \times \mathrm{T_C} + 0{,}6039 \times \mathrm{MP_O} + 0{,}5854 \times \mathrm{S_a}$

f_{tex}: textile parameters constant, T_c: Thermal conductivity (W/(m*K)), MP_o: Mean Pore size (µm) and S_a: Roughness coefficient (mm)

III.4 Wash-ability of 3D-PPOT materials

The adhesion strength of 3D-PPOT materials is an important property approached in the previous section III.3. However, the wash-ability of 3D-PPOT is essential to assess in order to use such materials in the textile industry.

III.4.1 Durability of 3D-PPOT after washing process

First of all, the durability of 3D-PPOT materials after washing process was qualitatively assessed. It was shown that washing resistance highly depends on the selected pattern of the textile materials. Indeed, the virgin PLA monofilament printed on twill 2/2 fabrics better resisted to the washing process than plain fabric because 100% of the PLA printed track was still bonded onto the majority of the twill 2/2 samples (Figure III- 11). This greater durability of 3D-PPOT materials might be explained by the strong mechanical interlocking noticed prior to the washing process. It could be observed that the pattern, the printing direction and the temperature of the platform also impacted the washing resistance (Figure III- 12) [101]. The weft density does not have a significant influence on the washing resistance (Figure III- 12).

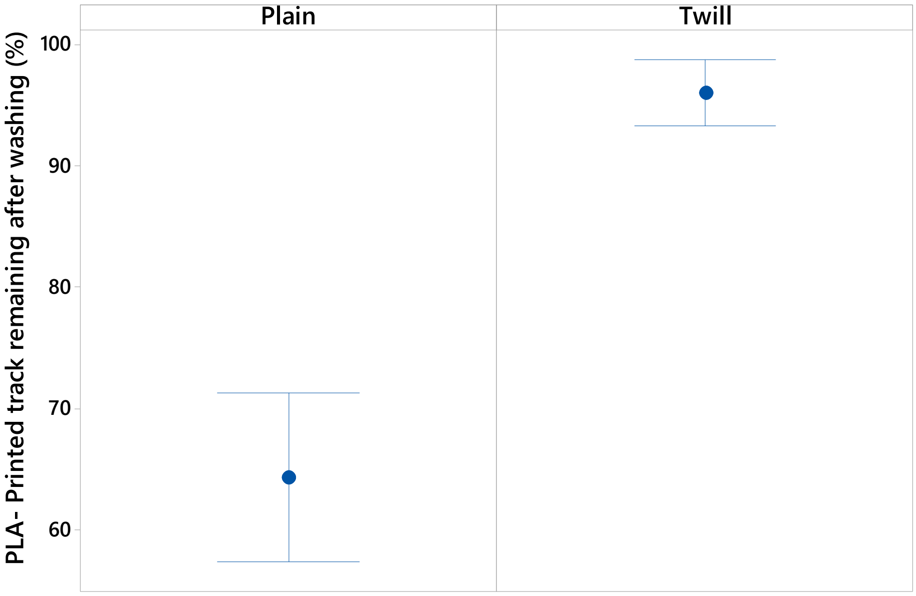

Figure III- 11 Durability after washing process of 3D-PPOT materials using twill 2/2 and plain structures [101]

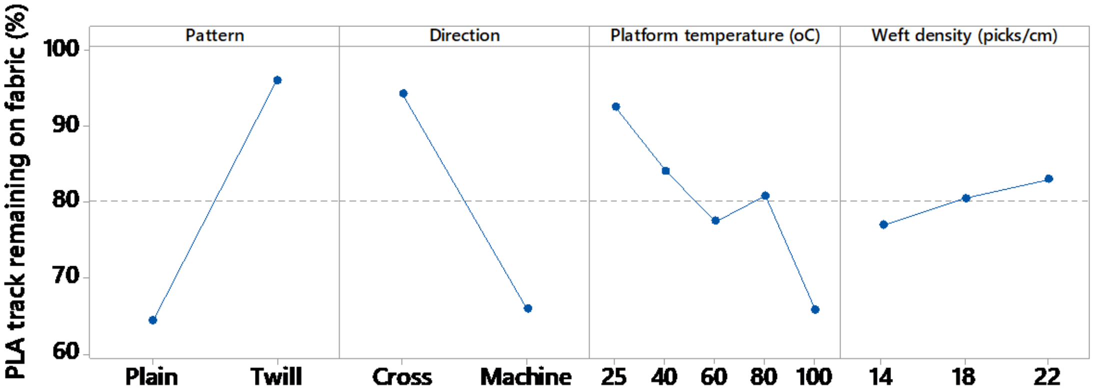

Figure III- 12 Durability after washing process: main effects with trend lines [101]

III.4.2 Impacting textiles' properties on the adhesion after washing

In addition to the washing resistance of 3D-PPOT materials, the adhesion strength after washing was evaluated. In general, it was demonstrated that the washing process impacted the adhesion properties of the 3D-PPOT samples (Figure III- 13). Indeed, the adhesion force values after washing is decreased by 50-80%, depending on the textile substrate utilized. Besides, the main contributions, the p-values and the main and interaction effects of the maximum adhesion force after washing are shown in Table III- 9 and Figure III- 14 [101]. The pattern, the direction and the platform temperature were the factors which impacted the maximum adhesion force after washing the most (p-value =0). By observing the findings, the factor with the highest contribution (i.e. the highest impact) in the adhesion after washing was the pattern. Besides, the use of twill 2/2 textile structure confirmed better adhesion than plain.

This result can be explained by the existing mechanical movements during the washing process destroying the weakest Van der Waals bonds. Finally, the 3D printing of PLA monofilament onto PET fabric in the cross direction guaranteed better adhesion due to stronger bonds at the interface and an affinity with the PET monofilament of the textiles prior to the washing process[101].

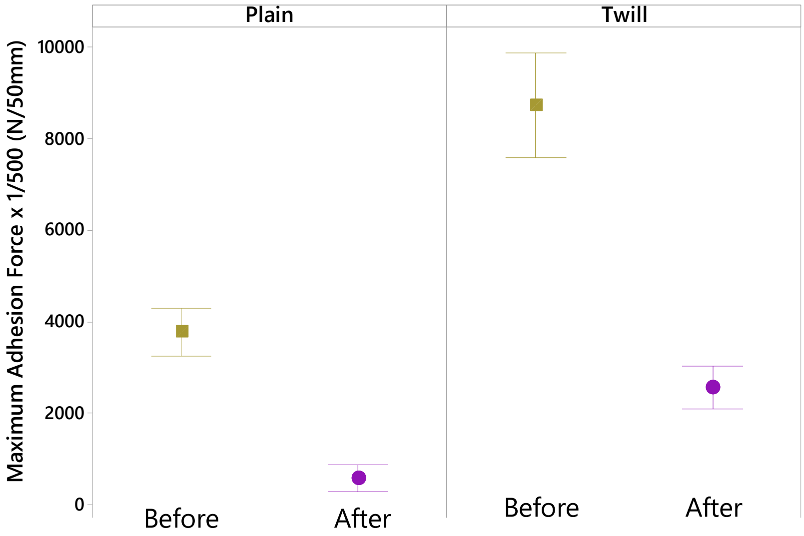

Figure III- 13 Comparison of the maximum adhesion forces before and after washing [101]

Table III- 9 Maximum adhesion force after washing: main contributions and p-values of the model [101]

Source	Contribution	P-value
Full Model	84,7	0,000
Pattern	28,79 %	0,00
Direction	4,11 %	0,00
Platform temperature (°C)	11,71 %	0,00
Pattern*Platform temperature	8,06 %	0,00

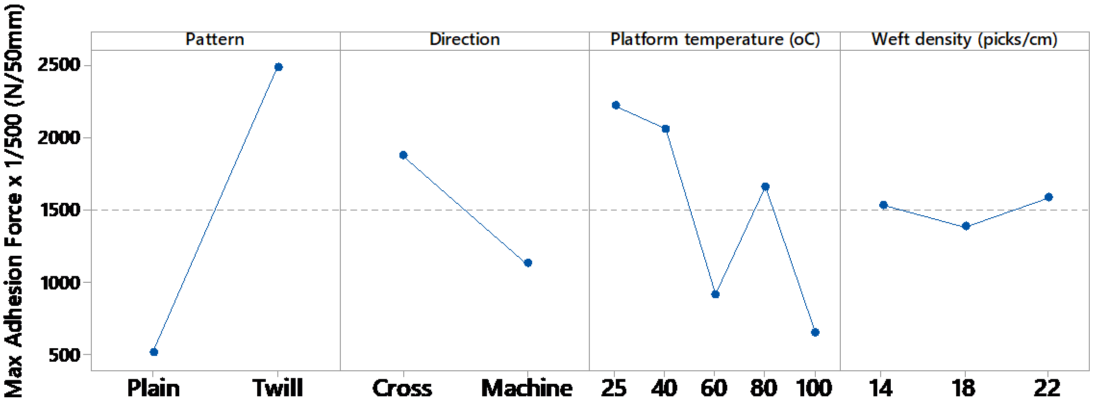

Figure III- 14 Main effects of maximum adhesion force after washing (with trend lines) [101]

III.5 Improvement of adhesion through functionalization processes

In the former section, it was presented the possibility of improving the adhesion properties of the 3D-PPOT materials through statistical modeling. Based on the findings, fused PLA layers can hardly adhere to soft PET woven fabrics. Thus, it is necessary to modify the surface of the textile and/or the polymer in order to allow the diffusion of the deposited polymeric materials.

In the next section, two functionalization techniques were used to change the surface of the polymeric materials: the grafting of Acrylic Acid (**AA**) followed by the application of adhesives and the atmospheric plasma methods. In the atmospheric plasma process study, the improvement of adhesion of 3D-PPOT materials using the soft PET woven materials was demonstrated and compared with the one of the PET non-woven at equivalent weight. The enhancement of adhesion was proven by using different scenarios of combined processes.

III.5.1 Effect of grafting on textile's surface properties

III.5.1.1 Effect of grafting process and application of adhesive on the surface of PET fabric

On one hand, in order to justify the effectiveness of the grafting process of acrylic acid onto PET fabrics, the topography of the surface of the PET woven fabrics was examined through profilometry method (*II.4.3.2)* before and after grafting process and their roughness, their weight and their mean pore sizes were compared (Table III- 11). After grafting process (*II.3.3*), an increase of the surface roughness, the weight and the pore size distribution (mean pore size and bubble point i.e. the largest pore size of the structure) of the treated polyester fabric were detected. Thus, during the grafting process (including washing at the end) AA might be grafted onto the surface of the PET fabric leading to a functionalisation of the surface of the textiles [101]. Due to the low amount of chemicals used for the grafting process and the instability of the generated free radicals, the difference between the treated and untreated samples was hardly detectable.

The XPS findings are presented in the Appendix A of the thesis. Previous researchers have analyzed the surface topography of PET films before and after grafting and they concluded that the surface roughness was increased with an increasing of the UV grafting time by dint of the grafting process [150].

Furthermore, the application of the PU film (*II.3.4)* on the surface of the textile decreased the pore size size and the roughness of the materials. Indeed, the thermocompression of the adhesion onto the treated PET fabric allowed the polymer to fill the gap of the textile material, and thus led to decrease the porosity and the roughness of the fabrics. Besides, the XPS results of the polyurethane (PU) film are presented in Figure III- 15 and Table III- 10. The elemental composition of the PU sample, as determined from survey scan data, showed a sample primarily consisting of carbon and oxygen, with low concentrations of nitrogen, sodium and silicon. By comparison of the carbon (78.6 at.%), oxygen (20.2 at.%) and nitrogen (0.3 at.%) concentrations with the concentrations in MDI (71.4 at.% C, 19.1 at.% O, 9.5 at.% N) it can be seen that there is either a very large soft segment in the PU, or surface segregation of the soft and hard segments has occurred, with the soft segments predominantly at the surface (Figure III- 15 and Table III- 10). The presence of the polyether soft segments of the polyurethane might explain the higher adhesion when using the polyurethane adhesive film [176]. The presence of the polyether soft segments of the polyurethane might help in enhancing the adhesion force between the printed track and the fabric [176].

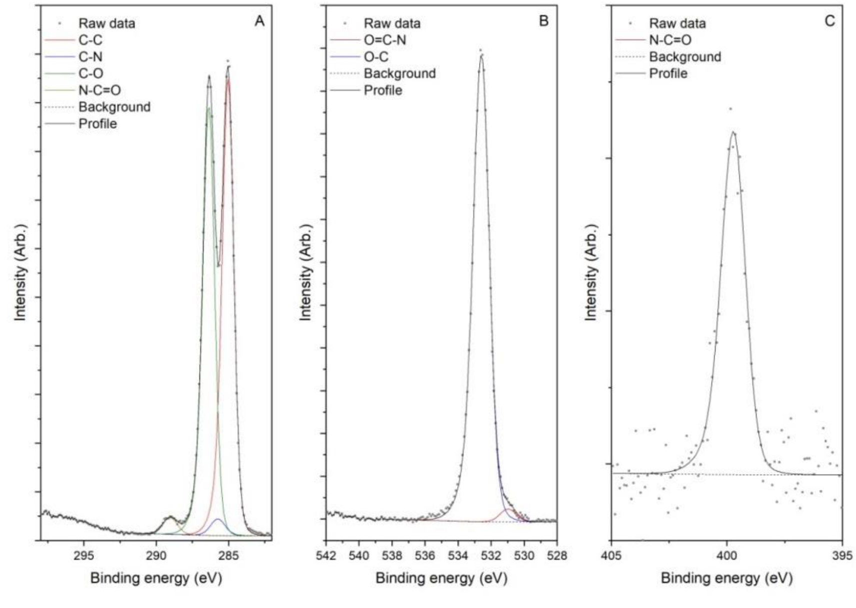

Figure III- 15 C1s(A), O1s (B) and N1s (C) XPS spectra of the PU adhesive

Table III- 10 Atomic concentration (%) determined by XPS for Polyurethane (PU) film

Concentration /Atomic percentat.%

Sample	**Na_{1s}**	**O_{1s}**	**N_{1s}**	**C_{1s}**
PU	0.23 ± 0.12	20.18 ± 0.79	0.32 ± 0.1	78.55 ± 1.16

Table III- 11 Roughness coefficient(µm), weight(g/m2), mean pore size (µm)and bubble point (µm)of the untreated PET fabric, treated PET fabric and treated PET fabric with adhesive film [177]

	Roughness coefficient Sa (µm)	**Weight (g/m^2)**	**Mean Pore size (µm)**	**Bubble point (µm)**
Untreated PET fabric	9.38	80 ±0.8	2.5	34.8
Treated PET fabric	14.7	89± 1	5.0	36.0
Treated PET fabric with adhesive film	13.7	130.2 ± 2	1.3	16.9

III.5.1.2 Effect of grafting process on surface structure of PLA monofilament

In order to analyze the grafting effect of the PLA monofilament on its surface, SEM images of the polymer were captured before and after AA grafting (Figure III- 16 (a) and (b)). It can be perceived that the surface of the untreated samples was smoother than the ones for AA grafted samples. Thus, a modification of the surface morphology of the monofilament occurred during the grafting process. It might be caused by the presence of grafted acrylic acid onto the surface of the PET fabric. A possible degradation of the surface of the PLA monofilament should not be excluded in the interpretation of the results.

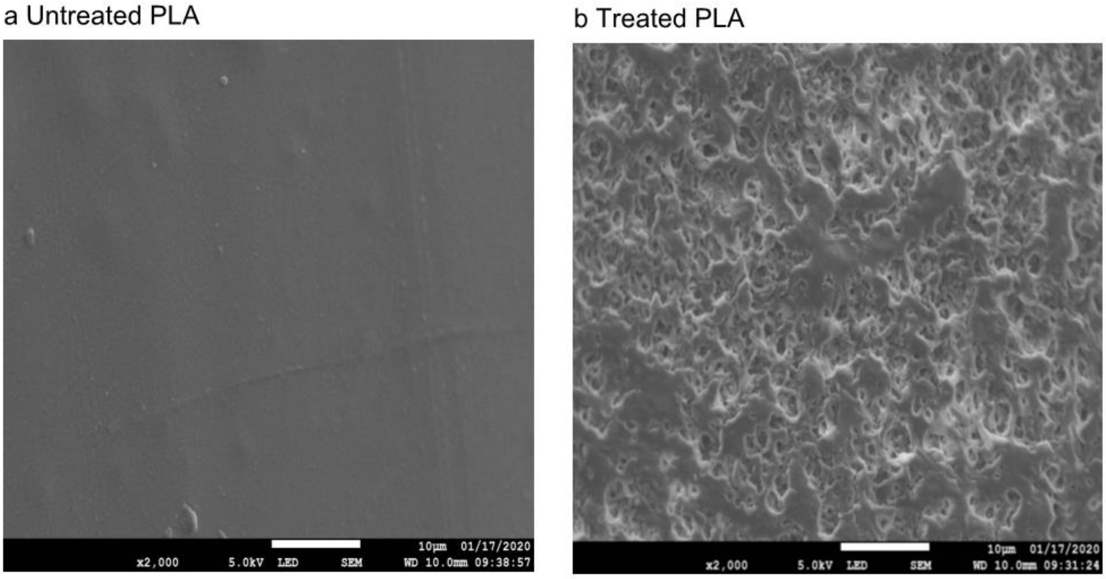

Figure III- 16 SEM images of PLA monofilament surface before (a) and after (b) grafting treatment [177]

III.5.2 Effectiveness of the atmospheric plasma treatment

The effectiveness of the functionalization of the PET fabric through atmospheric plasma treatment was evaluated by using different characterization techniques. For instance, the roughness, the pore size, the contact angle and the wettability of the untreated and treated samples were realized to be compared.

III.5.2.1 Capillarity and wettability analysis

The contact angle and capillary rise between the water and the untreated and atmospheric plasma treated samples were measured and presented in Figure III- 17, Figure III- 18 and Figure III- 19. Both methods (*II.4.6-II.4.7*) could allow the determination of the contact angles named θ_1 and θ_2. Similar trends of results are observed using both methods as shown in Figure III- 19 and Figure III- 20. Based on the main effect plots that considered the overall set of data factor by factor i.e. the trend of result for each factor, it could be seen that the atmospheric plasma treatment significantly increased the capillary rise while decreased considerably the contact angle value with water (Figure III- 17 - Figure III- 18). As a result, after air plasma treatment, the surface of the textile becomes much more hydrophilic with high wettability. These findings are comparable with the ones obtained previously by researchers [154,178–185].

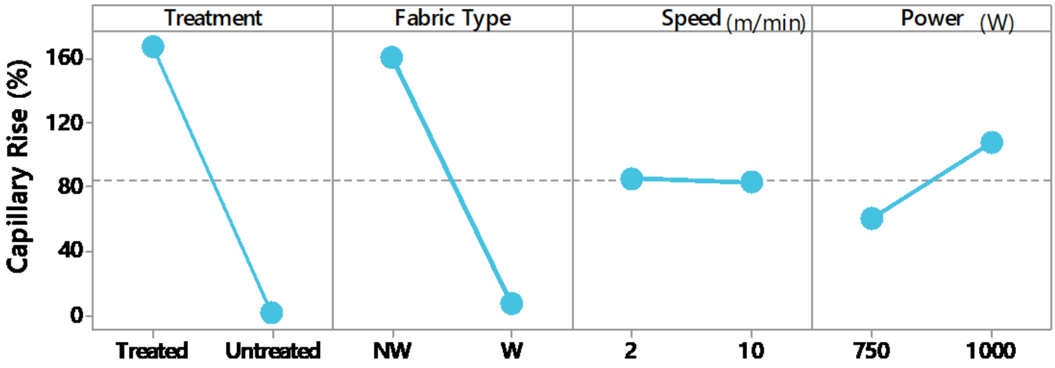

Figure III- 17 Main effect plots of capillary rise (%). NW means nonwoven and W means woven materials. The lines between the values are considered as trend lines and not connecting lines between mean values considering the entire design of experiments

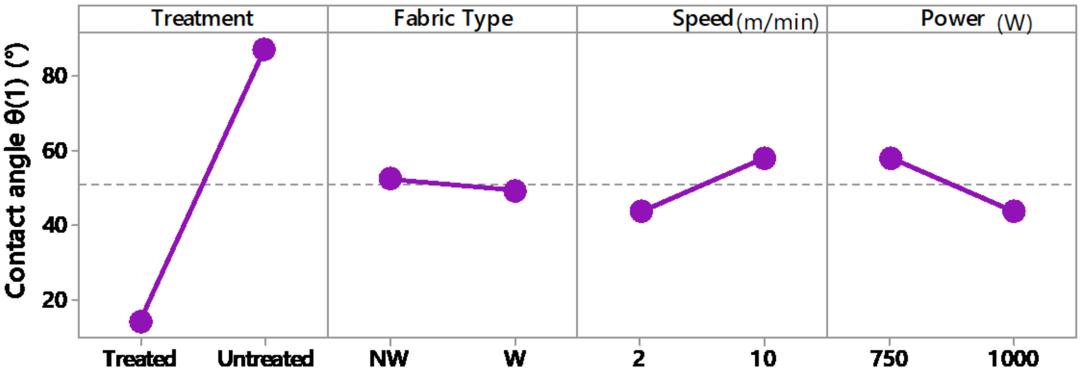

Figure III- 18 Main effect plots of contact angle (°) using the wettability test called θ_1. NW means nonwoven and W means woven materials. The lines between the values are considered as trend lines and not connecting lines

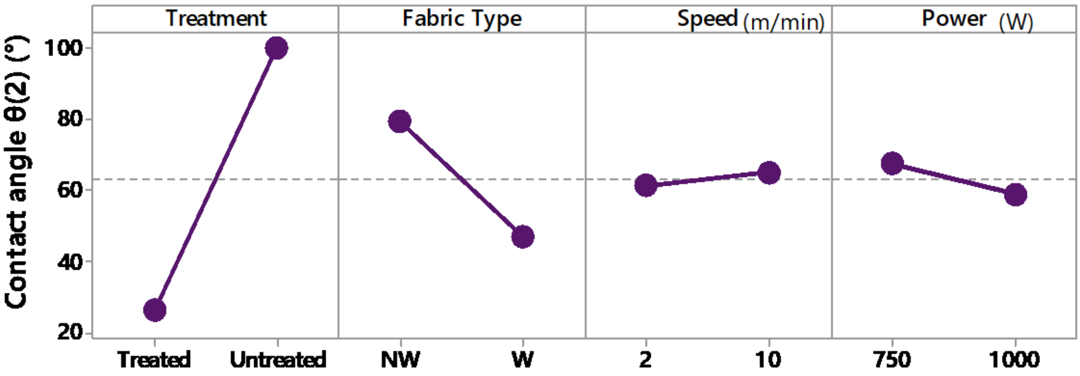

Figure III- 19 Main effect plots of contact angle (°) using a Theta Optical Tensiometer called θ_2. NW means nonwoven and W means woven materials. The lines between the values are considered as trend lines and not connecting lines

Formerly, various researchers reported the improvement in wettability of plasma -treated polyester fibers and textiles and fibers.[153,157,186–189] Indeed, it was established that air-oxygen plasma treatment introduces polar functional groups which are, for instance, carbonyl and alcohol groups. The presence of these groups on the surface reduces the contact angles with water and rise the wettability (Figure III- 17 - Figure III- 19). The better wettability is due to the etching of the surface and the change in chemical composition of the surface. Also, as already found by researchers, the speed of the fabric's movement during the plasma treatment did not demonstrate any significant impact on the wettability (Figure III- 17 - Figure III- 19) [153]. Indeed, the difference in capillary rise was not observed because of, for this trial the selected power range above 400 Watts [153]. The fabric type also influenced the capillary rise ratio of the textile materials. Indeed, a nonwoven fabric possesses a high capillary rise value. due to its important porosity and roughness (Figure III- 20).

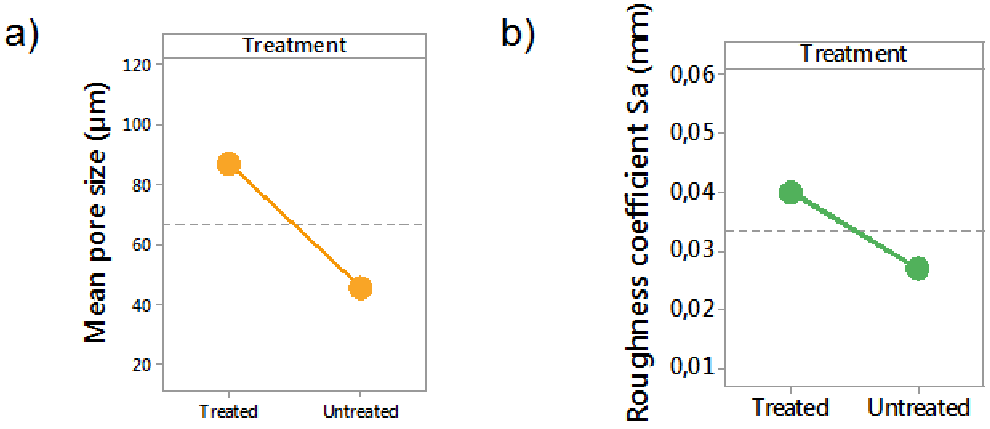

Figure III- 20 Main effect plots of the mean pore size (µm) (a) and roughness coefficient Sa (mm) (b) : effect of treatment. The lines between the values are considered as trend lines and not connecting lines.

Furthermore, a more detailed view on the effect of the plasma treatment on the capillary rise and contact angles θ_1 and θ_2 was given in Figure III- 21. It can be noticed that the change in capillarity of the nonwoven surface was more influenced by the atmospheric plasma treatment. Previous work evidenced that the pore size greatly impacted the degree of penetration of the plasma treatment [190,191]. In fact, bigger pore sizes of the fabrics lead to a deeper penetration of the plasma treatment as the field has a larger surface area with the textile. A complete penetration of the treatment was noticed for textile materials with pore sizes larger than 200 µm, whereas no penetration was seen for those with a pore size smaller than 10 µm [191]. In our case, the mean pore size ranges of the non-woven and the woven fabrics prior to the plasma treatment were 90-100 µm and 20-30 µm respectively (Figure III- 22). Therefore, the plasma treatment was more successfully applied on the PET non-woven materials and provoked an improved in the wettability and contact angle. Besides, the standard deviation of the capillary rise of the treated non-woven fabric was superior to 10% because of the random arrangement of the fibers of textile. The contact angles θ_1 and θ_2 of both woven and non-woven materials were impacted by the plasma treatment (Figure III- 21). Besides, the power of the treatment revealed to have an important influence on the capillary rise and the contact angle and by using PET non-woven as substrate showed much impact than PE woven fabric (Figure III- 23).

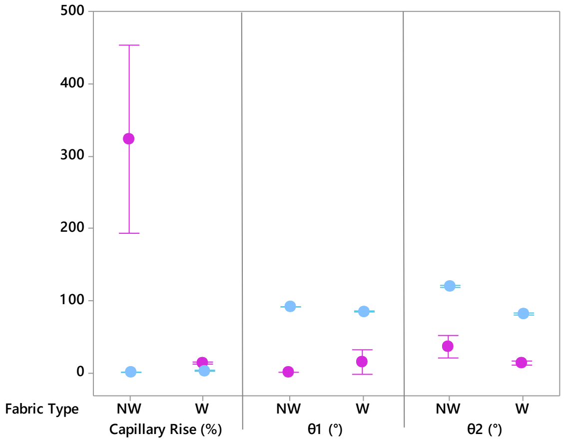

Figure III- 21 Capillary rise (%) and contact angles θ_1 (°) and θ_2 (°) of treated (pink dots) and untreated (blue dots) samples. NW means non-woven and W means woven materials.

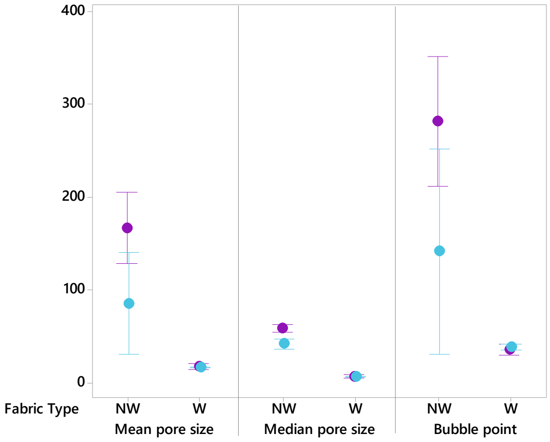

Figure III- 22 Mean, median and maximum (bubble point) pore sizes) of treated (purple dots) and untreated (blue dots). NW means non-woven and W means woven materials.

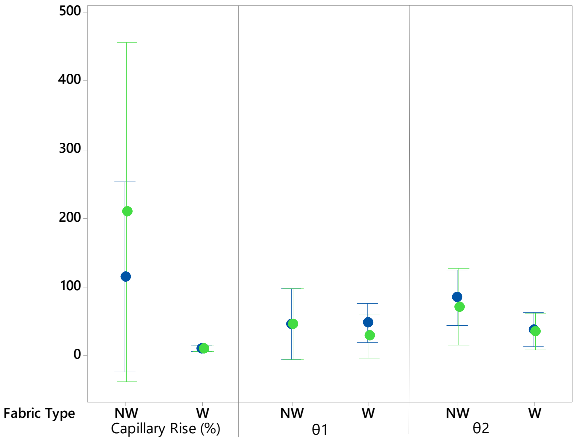

Figure III- 23 Capillary rise (%) and contact angles θ_1 (°) and θ_2 (°) of samples treated by plasma method using powers of 750Watts (in blue) and 1000Watts (in green). NW means non-woven and W means woven materials.

III.5.2.2 Effect of plasma on textile's surface properties

The surface roughness and the pore size of the textile materials before and after plasma treatment were investigated and their main effect plots were displayed in Figure III- 20. It was demonstrated that the mean and median pore sizes were identical before and after applying the atmospheric plasma treatment on woven materials. In the case of PET non-woven materials, the pore sizes were higher after treatment (Figure III- 20, Figure III- 22 and Figure III- 24). In addition, the mean pore size of the non-woven fabric was approximately six times higher than woven fabric. This is due to its more open surface and cross structures (Figure III- 20). Furthermore, the mean pore size of the woven fabric slightly increased by a diminution of the speed of the textile movement during the treatment (Figure III- 20). The mean and the median pore sizes of the fabric were not impacted by the power used for the treatment. Only the largest pores were changed after treatment. After plasma treatment at too high electrical power (1000W) might lead to the presence of a small number of spots on the non-woven fabrics and probably leading to the degradation of the textile. Thus, it is important to find a compromise between functionalization of the surface and degradation of the fabric. Additionally, the effect of the atmospheric plasma treatment on the roughness of the non-woven and woven materials was also assessed (Figure III- 25). In was found that after plasma treatment, the roughness coefficient S_a slightly improved for woven materials, whereas for non-woven textiles the effect is more significant.

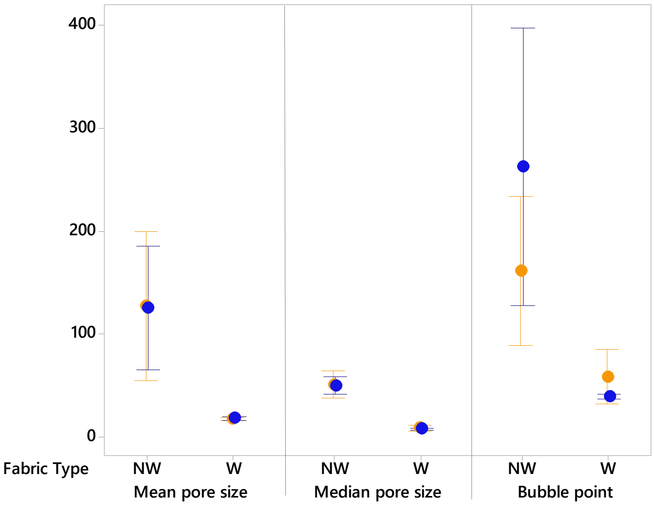

Figure III- 24 Mean, median and maximum (bubble point) pore sizes of samples treated by plasma method using powers of 750Watts (in orange) and 1000Watts (in blue). NW means nonwoven and W means woven materials.

The speed presented no impact on the surface roughness of the non-woven material while the power led to obtain a rougher non-woven fabric. In the case of woven materials, either the speed and the power did not change its surface roughness(Figure III- 25). SEM visualizations of the woven and non-woven textile structures prior to and after plasma treatment confirmed that nonwoven materials contain higher pores than woven ones (Figure III- 26).

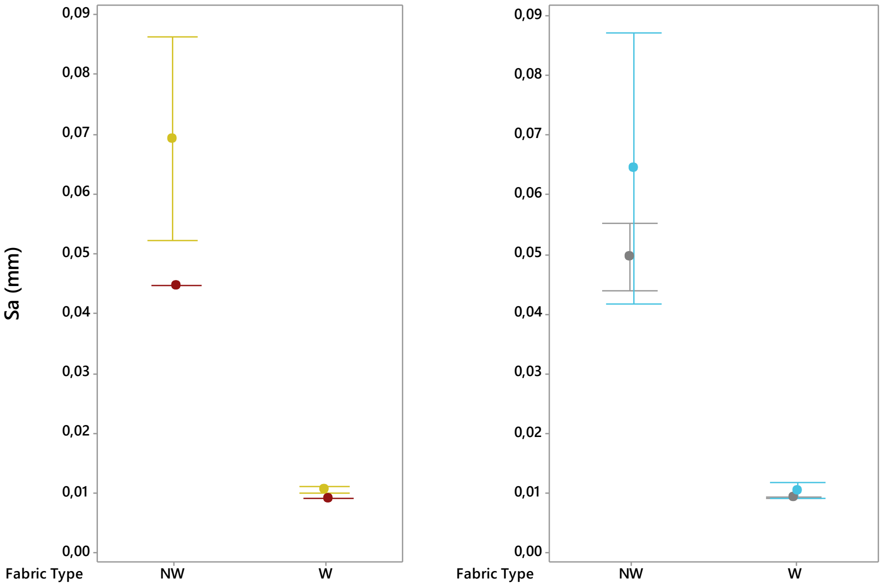

Figure III- 25 Roughness coefficient of treated (yellow dots) and untreated (red dots) samples and of samples treated by plasma method using powers of 750Watts (in grey) and 1000Watts (in blue) samples. NW means non-woven and W means woven materials.

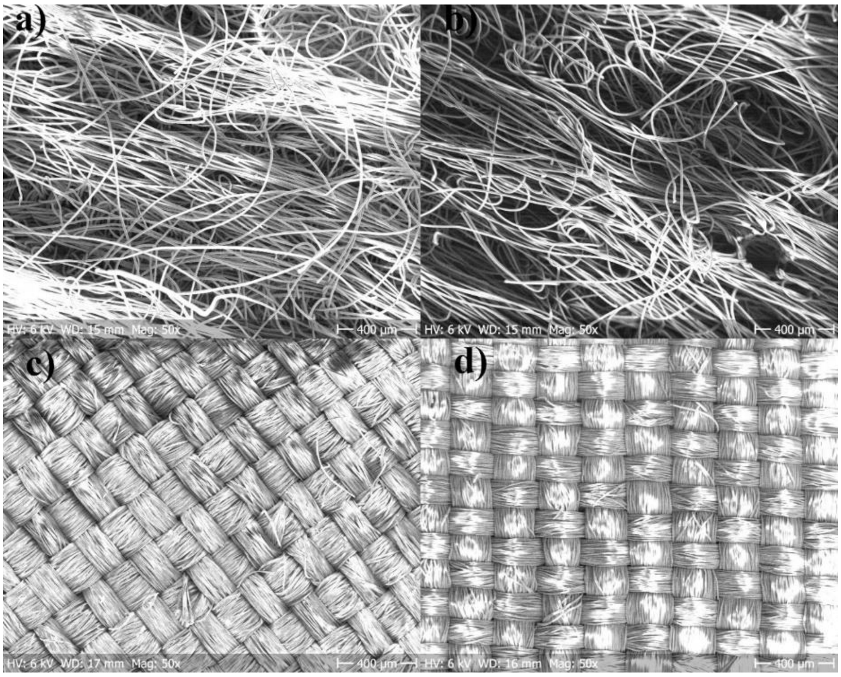

Figure III- 26 SEM images of untreated PET non-woven (a), air plasma-treated PET non-woven (b), untreated PET woven (c) and air plasma-treated PET woven fabric (d). Magnification =50x and applied voltage =6V

III.5.3 Findings on adhesion resistance of 3D-PPOT materials

After the grafting of acrylic acid process, the findings of the adhesion force of 3D-PPOT materials using untreated and treated PET fabrics are presented in Figure III- 27. It was demonstrated that the grafting process onto the surface of both the PET fabric and the PLA monofilament enhanced about ten times the adhesion strength of 3D-PPOT. Indeed, it could be seen that the untreated PLA printed onto untreated PET fabric has a very adhesion strength, however, once it is treated through grafted acrylic acid an important enhancement can be highlighted.

Besides, the application the pressure sensitive adhesive solution on the PET fabric after grafting process of acrylic acid, the adhesion force was slightly further increased due to the small quantity of solution adhesive applied during the entire coating process. However, by applying the polyurethane (PU) - based adhesive on treated PET fabrics the adhesion strength of the 3D-PPOT was twenty times higher than the one of the untreated PET fabric. After the different pre-treatments, the use of 3D-PPOT materials using conductive PLA showed better adhesion resistance than the one of the non-conductive PLA, as already proven in former studies [2,101].

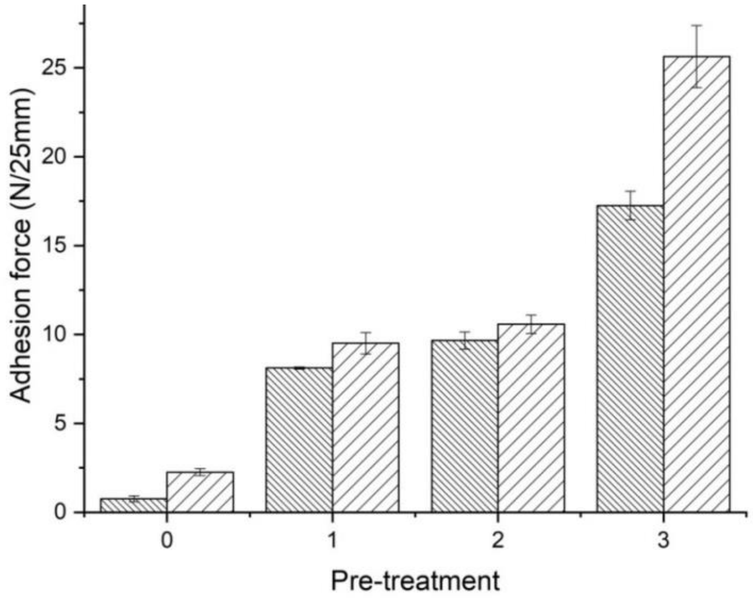

Figure III- 27 Adhesion strength (N/50mm) of non-conductive (▧ =tight stripes) and conductive (▨ =large stripes) 3D-PPOT materials using treated virgin PLA or PLA/2.5CB% printed on untreated (pre-treatment 0) or pre-treated (pre-treatments 1, 2 and 3) of the PET woven fabrics. *Pre-treatment 1 refers to the grafting of AA+BP on the PET woven fabrics and the monofilament, pre-treatment 2 to the grafting of AA+BP followed by the pressure sensitive adhesive solution coating on the PET woven fabrics and the grafting process on PLA monofilament and pre-treatment 3 refers to the grafting of AA+BP on PET fabric and PLA monofilament, followed by the application of polyurethane adhesive on the PET woven fabrics. The platform temperature was 40°C.*

The impact of the build platform temperature of the 3D printer on the adhesion strength of the 3D-PPOT using conductive and non-conductive PLA printed on PET fabric after grafting of AA pre-treatment followed by the coating of the pressure-sensitive adhesive solution is presented in Figure III- 28.

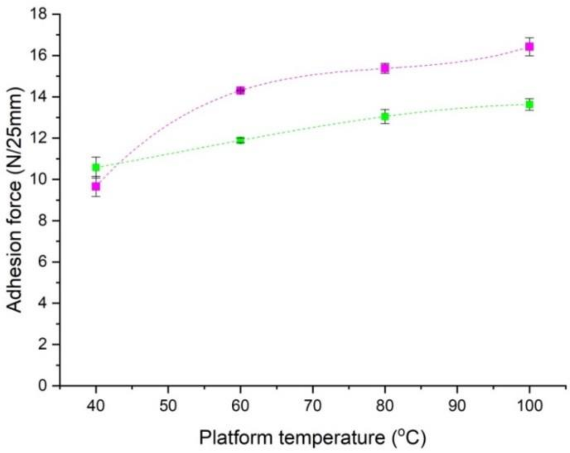

Figure III- 28 Adhesion strength (N/50mm) of non-conductive (in green) and conductive (in pink) 3D-PPOT materials using virgin PLA or PLA/2.5CB% printed at different platform temperatures (40, 60, 80 and 100 ºC) on pre-treated PET woven fabrics with grafting of AA+BP followed by a coating of the pressure sensitive adhesive solution. The trend lines are presented in this graph.

An increase of the build platform temperature from 40 ºC to 100 ºC led to enhance the adhesion force. In former work, it was already proven that the platform influenced the adhesion resistance, however, in this study, the adhesion enhancement is also explained by the reaction of the adhesive solution upon heating [3,101].

The structure of the textile material, i.e. the use of non-woven compared to woven fabric revealed to significantly impact the adhesion properties compared to the other plasma process parameters (Figure III-29). Indeed, at an equivalent weight of 80 ± 0.8 g/m2, the adhesion resistance of 3D-PPOT materials using PET non-woven fabric was hundred times higher than one utilizing woven structure (Figure III- 29). This finding might be explained by the surface and structural morphology of the woven and non-woven materials described in the section *III.5.2.2*.

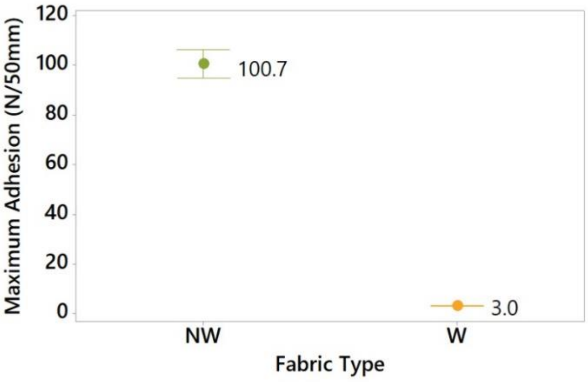

Figure III- 29 Maximum adhesion forces (N/50mm): comparison between non-woven (NW) and woven (W) materials

In addition, no significant improvement in adhesion was observed on 3D-PPOT using conductive materials printed after applying on an atmospheric -plasma pre-treatment on PET woven textiles (Figure III- 30).

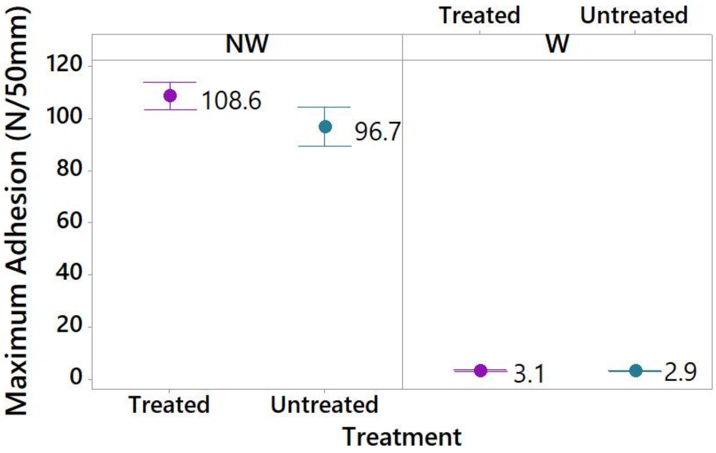

Figure III- 30 Maximum adhesion forces (N/50mm): effect of air-plasma treatment for nonwoven (NW) and woven (W)

A stronger effect was noticed after plasma treatment if the substrate is a PET non-woven material (Figure III- 30). The speed and power of the atmospheric plasma process did not impact the adhesion strength (Figure III- 31 -Figure III- 32).

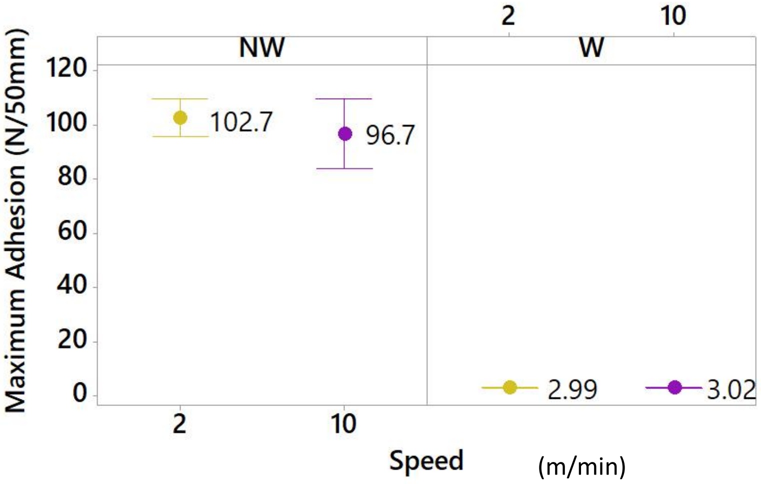

Figure III- 31 Maximum adhesion forces (N/50mm): effect of speed (m/min) for nonwoven (NW) and woven (W)

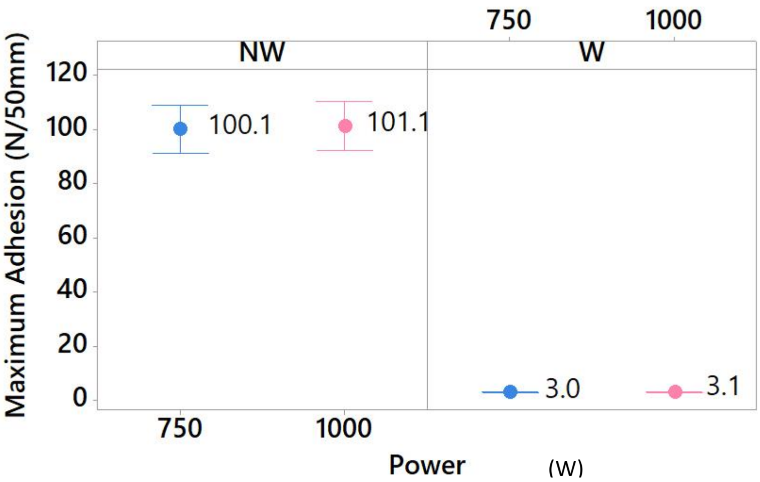

Figure III- 32 Maximum adhesion forces (N/50mm): effect of power (W) for nonwoven (NW) and woven (W)

SEM images of the 3D printed conductive PLA deposited onto PET non-woven and woven fabrics are displayed in Figure III- 33. A deeper penetration and diffusion of the conductive PLA were observed in the case of PET non-woven materials.

Thus, there was a strong interlocking between the fused polymer and the PET fibers of the non-woven fabric as it could be seen on the backside of the peeled conductive PLA track. For PET woven fabric, no fiber was observed on the backside the track after the t-peel test method. Similar observations were found for air plasma treated non-woven and woven samples.

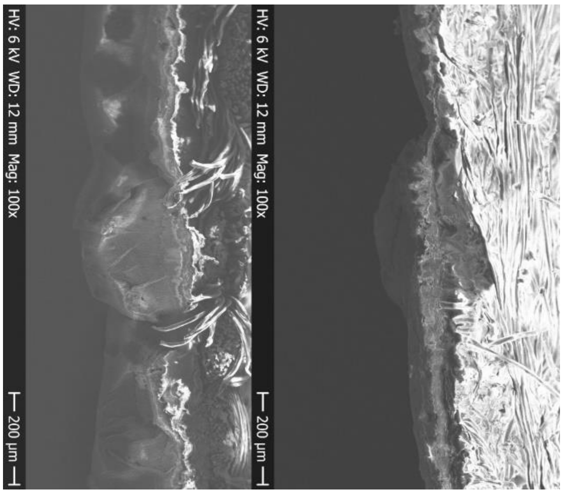

Figure III- 33 SEM images of the cross-section of 3D-PPOT conductive materials using woven (on the right) and non-woven (on the left). Magnification =100x and applied voltage =6V

III.6 Conclusion

In this chapter, the adhesion properties of 3D-PPOT materials using PLA-based monophasic materials were enhanced through different methods: the use of statistical modeling utilizing the material properties and the functionalization of the surface of the PET fabric and PLA monofilament by grafting of acrylic acid and application of adhesive. The atmospheric plasma treatment was also used to attempt to enhance the adhesion of 3D-PPOT materials by functionalizing the PET fabrics.

On one hand, the influence of the structure and the thermal conductivity of PET textiles and the build platform temperature of the 3D printer on the adhesion properties and wash-ability of 3D printed polymer onto textile materials using thin layers of non-conductive and conductive PLA monofilaments deposited onto (PET) woven fabrics through FDM process was investigated. Before the FDM process, the thermal conductivity, the surface roughness and the mean pore size of PET woven fabrics were measured through the “hot disk”, the profilometry and the capillary flow porometry test methods respectively. After the FDM process, the adhesion resistance (via T-peel test) and durability after the washing process of the materials were examined and optimized with developed reliable statistical models connecting the properties of the textile substrate (surface roughness, mean pore size and thermal conductivity) to the adhesion strength. The main results showed that higher roughness coefficient and mean pore size and lower thermal conductivity of the PET fabrics enhanced the adhesion force. Besides, the build platform quadratically influenced the adhesion force. Furthermore, the washing process decreased by half the adhesion strength. The rough and porous textile structures demonstrated better durability after washing. These outcomes could be explained by the surface topography of PET fabrics that defined the anchorage areas between the fused polymeric layer and the textiles.

On the other hand, the atmospheric plasma treatment with different settings, was applied on PET fabrics to improve the adhesion force between conductive 3D printed track and PET textile substrates. The application of a pressure-sensitive adhesive (PSA) or a polyurethane (PU) film adhesive onto acrylic acid grafted- PET fabric and PLA monofilament was executed to enhance the adhesion resistance. Both methods demonstrated an improvement of the adhesion resistance. The applied polyurethane (PU) film onto treated PET fabrics showed a better adhesion performance as a result of the existence of soft segments onto the PU film.

Additionally, there was no significant improvement in adhesion between the PET woven and non-woven textiles and the deposited polymeric layer through the FDM process (p-value >0.5) after pre-treated the fabrics with the atmospheric plasma process. This might be due to weak bonds created between the two polymeric materials. Finally, the use of non-woven fabric showed upper adhesion performance of the 3D-PPOT materials compared to the woven fabric, i.e. the textile type and the structure have more impact on the adhesion resistance.

Chapter IV Deformation, wear and tensile properties of 3D-PPOT using monophasic materials

One of the main challenges in the development of monophasic 3D-PPOT is to deliver materials with equal or better mechanical properties, durability and comfort than the one of the textile substrates themselves prior to FDM process. In Chapter III, the adhesion resistance, which is one of the main mechanical properties and the influence of the washing process were investigated.

This chapter focuses on studying the impact of the textile properties and printing platform temperature on the deformations, the tensile properties, the wear resistance and its impact on the electrical conductivity of PLA filaments 3D printed onto PET textiles through FDM process. Besides, theoretical and statistical models are developed to predict and optimize the 3D-PPOT properties. The influence of the FDM process parameters on the thickness and the pore size of the 3D-PPOT materials is also approached. *Section IV.1* introduces the materials, the manufacturing processes and the characterization methods utilized in the study. *Section IV.2* describes the statistical design of each experiment of the study, that includes the selected factors and targeted responses. *Section IV.3* presents the findings about the deformation properties of the 3D-PPOT materials. *Section IV.4* relates the stress and strain at rupture and the wash-ability of the 3D-PPOT materials and the optimization of these properties through statistical modeling. *Section IV.5* defines the wear resistance and its impact on the electrical conductivity of the 3D-PPOT materials. The influence of the FDM process on the pore sizes and the thickness of 3D-PPOT are also investigated. Finally, *Section IV.6* gives an overview and summary of the current study on the overall findings about the deformation, wear and tensile properties of 3D-PPOT.

For each material, process, characterization method and previous work already presented in Chapters I, II and III, the referred section will be written in brackets.

IV.1 Materials, processes and characterization

In the studies of this chapter, virgin ECO-PLA and conductive PLA monofilaments are utilized as raw materials for the FDM process and the textile materials used were PET woven textile. Six different PET fabrics using two different patterns (plain and twill 2/2) and three different weft densities (14, 18 and 22 picks/inch) were produced in house as already described in Chapter III. The mass per area and thickness of each textile were already presented in Table III- . A printer WANHAO Duplicator 4/4x was used to execute the FDM process. The 80 mm × 225 mm textile samples were positioned on the 3D printing platform prior to printing. After that, non-conductive and conductive PLA monofilaments are fused and applied on each different set of woven materials by creating a 50 mm × 200 mm × 0.1 mm rectangular track. The infill percentage, the Z offset (i.e. the gap between the head of the extruder and the surface of the fabric), the printing speed, the diameter of the selected extruder (the right one) and the extruder temperature presented in Table IV- are constant during the experiments. The dynamic surface deformations (*II.4.1.1*), the tensile and elongation at break properties (*II.4.1.2*), the durability after washing process (*II.2.4*), the thickness and pore size measurements of fabrics and 3D-PPOT materials, the thermal properties (crystallization and melting temperatures) through Differential Scanning Calorimetry (DSC) analysis (*II.4.1.3)*, the abrasion resistance (*II.4.1.3*) and the electrical conductivity of 3D-PPOT material before and after abrasion (*II.4.5.2*) were determined.

Table IV- 1 Printing process parameters [167]

Parameters	Values (unit)
Infill percentage	20 (%)
Z offset (distance between the head)	0 (mm)
Printing speed	3600 (mm.min^{-1})
Extruder (or printing) diameter	0.4 (mm)
Extruder temperature	250 (ºC)

IV.2 Statistical design of experiments

In the current study, the platform temperature and weft density were used as continuous factors and the fabric orientation and the pattern as discontinuous ones and a random design of experiment was created in Minitab 17 software (*I.2.5*). The values and codes of different factors of the different experiments are designated in Table IV- 2 -Table IV- 7.

Table IV- 2 Factors of statistical design of experiments for tensile measurements of the non- conductive and conductive 3D-PPOT materials and deformation of the textiles prior to printing process [121]

Factors	Values (units)
Platform temperature	25, 60 and 100 °C
Weft density of the fabric	14, 18 and 22 picks/inch
Warp density of the fabric	20 picks/inch
Fabric direction	Machine (in warp yarn direction) and Cross (in weft yarn direction)
Fabric pattern	Plain or Twill 2/2 shown in Fig.. 1 (a) and (b) respectively

Table IV- 3 Factors of statistical design of experiments for deformation of the 3D-PPOT materials [121]

Factors	Values (units)
Platform temperature	40 and 60 °C
Weft density of the fabric	14, 18 and 22 picks/inch
Warp density of the fabric	20 picks/inch
Fabric pattern	Plain or Twill 2/2

Table IV- 4 Factors of the statistical design of experiments for abrasion of the 3D-PPOT materials [167]

Factors	Values (units)
Platform temperature	25 and 60 °C
Weft density of the fabric	14, 18 and 22 picks/inch
Warp density of the fabric	20 picks/inch
Fabric direction	Cross or machine
Fabric pattern	Plain or Twill 2/2

Table IV- 5 Factors of the statistical design of experiments for mean pore size of the 3D-PPOT materials [167]

Factors	**Values (units)**
Weft density of the fabric	14 and 18 picks/inch
Warp density of the fabric	20 picks/inch
Fabric pattern	Plain or Twill 2/2

Table IV- 6 Factors of the statistical design of experiments for thickness of 3D-PPOT materials [167]

Factors	**Values (units)**
Weft density of the fabric	14 and 22 picks/inch
Warp density of the fabric	20 picks/inch
Fabric pattern	Plain or Twill 2/2
Platform temperature	25,60 and 100°C

Table IV- 7 Factors of the statistical design of experiments for electrical conductivity of 3D-PPOT materials [167]

Factors	**Values (units)**
Weft density of the fabric	14,18 and 22 picks/inch
Warp density of the fabric	20 picks/inch
Fabric pattern	Plain or Twill 2/2
Platform temperature	25,60 and 100°C
Fabric direction	Cross or machine

IV.3 Deformation of 3D-PPOT materials

IV.3.1 Effect of 3D printing on the deformation of 3D-PPOT materials

The impact of the FDM process (3D printing) onto textiles on the flexibility was evaluated by measuring the permanent, elastic and total deformations of the 3D-PPOT materials. These deformations were compared to the ones of the original PET woven fabrics prior to 3D printing.. As already described in Chapter II, during the deformation test, a stylus is applied onto the material without, with and without a force respectively. The total deformation of the material refers to the one when the force is applied by the stylus. After releasing the force, the material recover and the remaining deformation named permanent deformation is then determined. The elastic is the difference between the total deformation and the permanent one.

As it was demonstrated that by depositing fused PLA onto textiles, the textile materials become stiffer and more stable and the permanent, elastic and total deformations of the 3D-PPOT materials decreased by 88 %, 85% and 87 % respectively (Figure IV-).

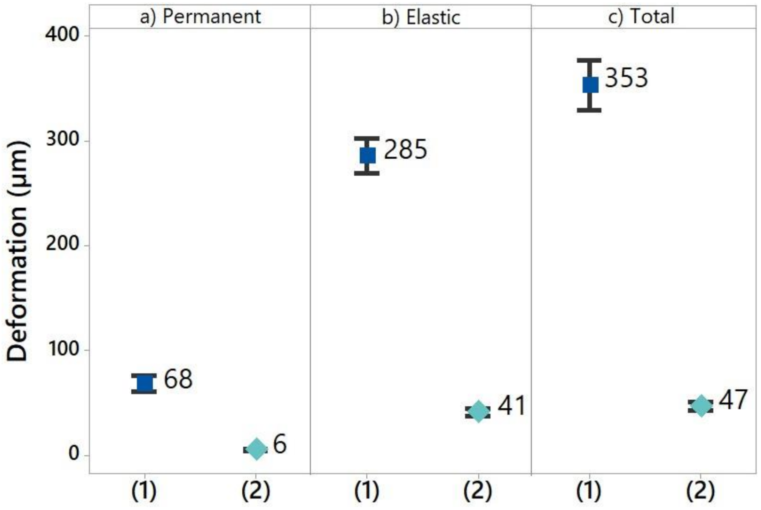

Figure IV- 1 Permanent (a), elastic (b) and total (c) deformations before (1) and after (2) deposition process through 3D printing [121]

Indeed, the high young’s modulus (~3.5GPa) and crystallization of the processed PLA monofilament caused stiffer materials and thus, very low deformations of the 3D-PPOT materials. The flexibility and drapability of the 3D-PPOT materials are reduced due to a lower porosity of the materials compared to the original PET fabrics.

IV.3.2 Effect of textiles’ properties on the deformation of 3D-PPOT materials

Prior to the 3D printing process, the weft density and the pattern of the fabrics revealed to have significant impact on its deformation (or flexibility). Indeed, twill pattern revealed to be more flexible than plain one with greater permanent, elastic and total deformations (Figure IV- 2); and an increase of the weft density of the fabric diminished its flexibility (Figure IV- 2). These observations might be interpreted by the arrangement of the yarns within the two different structures. Indeed, in the twill 2/2 the weft thread passes simultaneously over and under two warp threads whereas in a plain fabric each weft thread crosses the warp one by going simultaneously over and under. Consequently, twill 2/2 weave fabrics possess floats that deliver more stretch ability to the fabrics and thus, upper elastic, permanent and total deformations. Based on the p-values (p-value = 0) mentioned in the Table IV-8, it was confirmed that, the pattern, weft density and platform temperature influenced considerably the permanent deformation (Figure IV- 3). Nevertheless, the elastic and total deformations were only impacted by the weft density (p-value = 0 in Table IV- 9 and

Table IV- 10). the permanent (Figure IV- 2) and total deformations declined with a rise increase of the weft density which means that the dimensional stability and the comfort of the fabrics were enhanced [192]. Finally, the permanent deformation value of the 3D-PPOT materials was diminished with an increase of the platform temperature (Figure IV- 3).

Table IV-8 Permanent deformation of the 3D-PPOT materials (in µm): p-values and contributions of the main factors [121]

Factors	P-values	Contribution (%)
Platform temperature (◦C)	0.00	6.97
Weft density (picks/cm)	0.00	50.7
Pattern	0.00	9.38

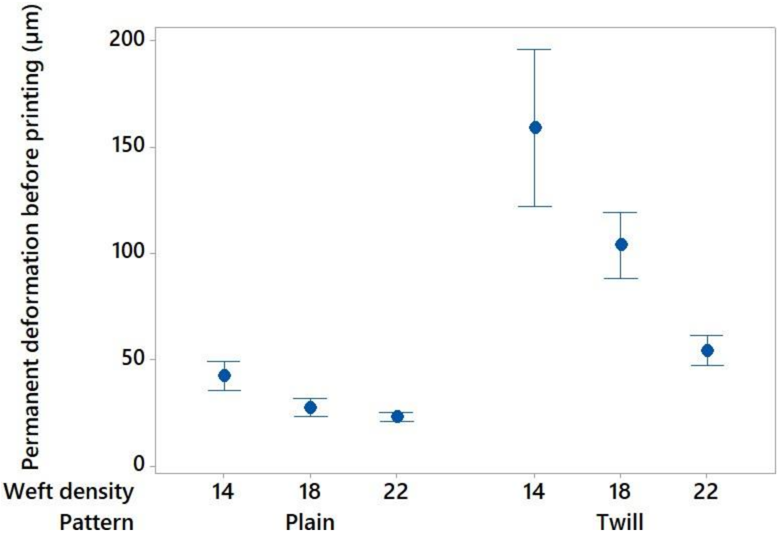

Figure IV- 2 Main effects plot: permanent deformation (in µm) of fabrics before printing versus weft density (picks/inch) and pattern [121]

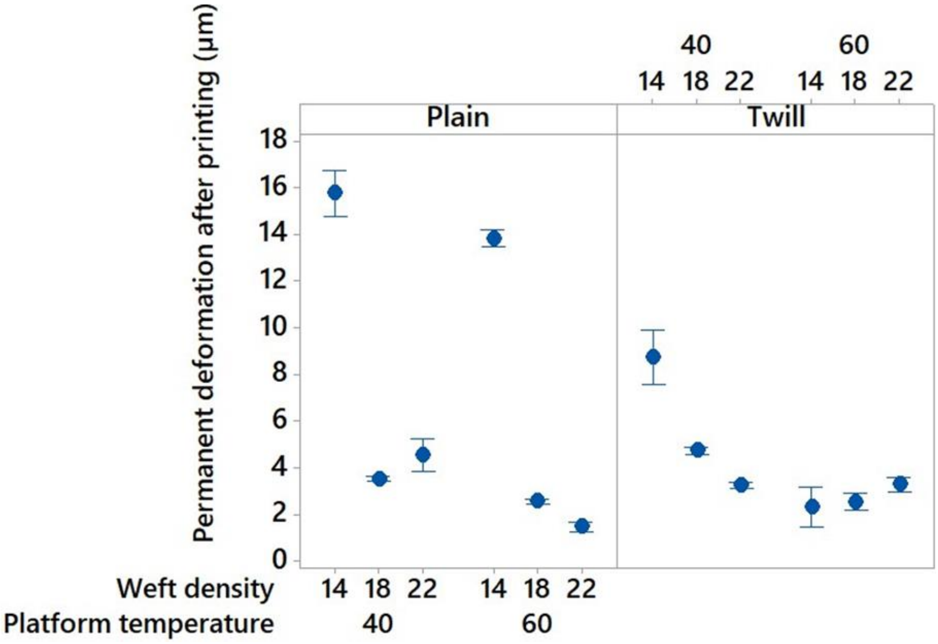

Figure IV- 3 Main effects plot: permanent deformation (in µm) of the 3D-PPOT materials versus weft density (picks/inch), pattern and platform temperature (°C) [121]

Table IV- 9 Elastic deformation of the 3D-PPOT materials (in µm): p-values and contributions of the main factors [121]

Factors	P-values	Contribution (%)
Platform temperature (◦C)	0.15	0.20
Weft density (pick/cm)	0.00	46.99
Pattern	0.59	0.03

Table IV- 10 Total deformation of the 3D-PPOT materials (in µm): p-values and contributions of the main factors [121]

Factors	P-values	Contribution (%)
Platform temperature (◦C)	0.005	0.92
Weft density (pick/cm)	0.00	44.07
Pattern	0.146	0.21

IV.4 Tensile properties of 3D-PPOT materials

Previously, it was proven that the deformations of 3D-PPOT were hardly reduced and need to be enhanced by materials and 3D printing process changes. However, the deformations of the materials are not the only important mechanical properties to be studied. The tensile properties which include the stress and the strain of the 3D-PPOT materials have to be considered. Thus, in the next sub-section the influence of the 3D printing on the tensile properties of the 3D-PPOT and the impact of the washing on the properties is approached.

IV.4.1 General findings

The findings of stress and strain of the 3D-PPOT materials through FDM process are presented in Figure IV- 4 to Figure IV- 9. The strain and stress at rupture were measured by using a constant loading rate (Figure IV- 4) and the tensile force–elongation curves were reported for each sample made of non-conductive and conductive PLA 3D printed onto PET plain woven fabric as shown in Figure IV- 5 , Figure IV- 6 ,Figure IV- 8 and Figure IV- 9. During the tensile test and for both non-conductive and conductive 3D-PPOT materials, the PLA track broke always first at low elongation range of [0.5%-3.5%] and low tensile force range of [50N-250N] (Figure IV- 5 and Figure IV- 6 (2)) followed by the PET woven fabric at an elongation range of [20%-35%] and tensile strength range of [300N-500N] (Figure IV- 5 and Figure IV- 6 (3)). Additionally, it could be noticed that the tensile strength of the PET fabric was reduced after 3D printing compared to the one before the printing process as shown on the stress-strain curves (Figure IV- 5 and Figure IV- 6 (1) and (3)). The stress and strain at rupture depend on the ones of the track and the textile independently, and also, the adhesion properties of their interface of the both layers [2,4,78,79,101]. During the test, the PLA printed layer was not fragmented in the same way in the case of a polymer deposition in machine or cross direction of the polyester textile material (Figure IV- 4). In the cross direction of the fabric, it was observed that the adhesion at the interface was greater than in the machine direction (Figure IV- 4). The PLA track was broken at only one position without delamination in the cross direction while in the machine direction, the PLA track was broken at several points across the width to finally delaminate completely due to a poor adhesion at the interface [101].

Prior to the analysis of the overall stress and strain data through Minitab 17 (DOE analysis tool), they were converted in mega pascal according to the equation **Eq. IV- 1**.

$$Stress\ (MPa) = \frac{tensile\ force\ (N)}{25 \times t} \qquad \textbf{(Eq. IV- 1)}$$

where t is the thickness of the material (in mm).

After an in-depth analysis of all data of the DoE, the stress and strain 3D-PPOT materials' observation formerly stated were confirmed as to be a combination of the ones of the PET fabrics and the PLA printed track. With stress and strain mean values of 34.5 MPa and 34.3% for the textile substrate and 8.7 MPa and 2.2 % for non-conductive PLA layers, the fabric remained the strongest (Figure IV- 7). Similar findings are obtained when printing conductive PLA onto PET fabric.

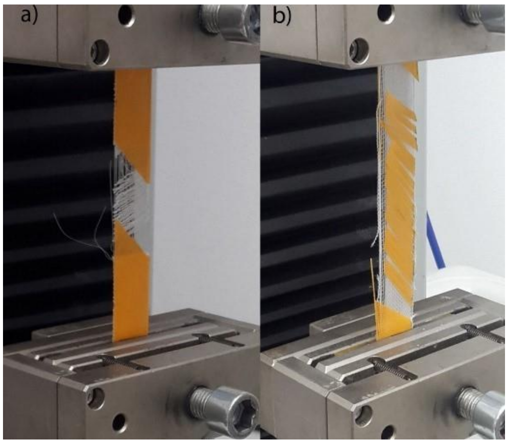

Figure IV- 4 Strain and stress measurements of 3D-PPOT materials in cross direction (a) and machine direction(b) [121]

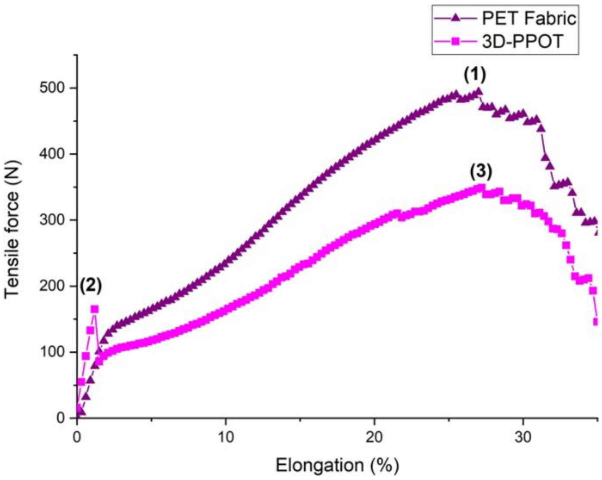

Figure IV- 5 Tensile force–Elongation curves[1] of 14 picks/inch PET plain woven fabric in cross direction and 3D-PPOT using PLA filament printed on 14picks/inch PET woven fabric at 25◦C in cross direction [121]

[1] *(1), (2) and (3) represent the maximum strength of the 14 picks/inch PET plain woven fabric before printing, the maximum strength of the PLA/2.5%CB track of the 3D-PPOT and the maximum strength of the 14 picks/inch PET woven fabric of 3D-PPOT respectively*

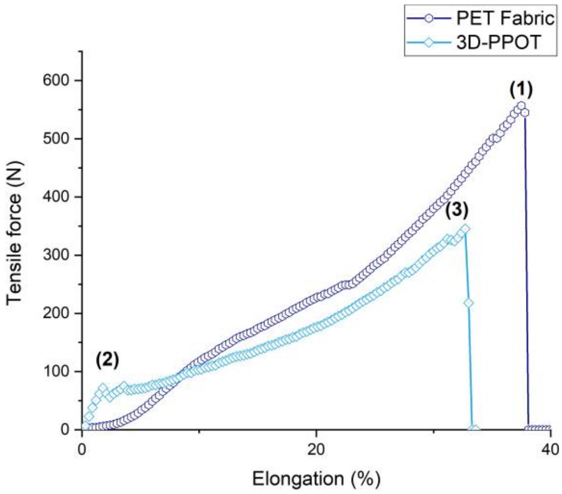

Figure IV- 6 Tensile force–Elongation curves[1] of 14 picks/inch PET plain woven fabric in machine direction and 3D-PPOT using PLA filament printed on 14picks/inch PET woven fabric at 25°C in machine direction**.** [121]

[1] *(1), (2) and (3) represent the maximum strength of the 14 picks/inch PET plain woven fabric before printing, the maximum strength of the PLA/2.5%CB track of the 3D-PPOT and the maximum strength of the 14 picks/inch PET woven fabric of 3D-PPOT respectively.*

Thus, as it was proven that the 3D printed layer has a tensile strength and elongation at rupture much lower than the one of the fabric, an improvement of these properties is essential. In Chapter V, some potential solutions based on polymer nanocomposite blends development are presented in order to enhance these properties.

IV.4.2 Influence of fillers on the stress and strain of 3D-PPOT materials

Prior to the FDM process, the maximum tensile strength of the pure PLA monofilament and 2.5% CB-filled PLA were 11659 cN/tex and 11890 cN/Tex respectively (1Tex represents 1 gram per 1000 meters). This observation showed that there is a slight enhancement of the tensile strength with the addition of conductive fillers. Besides, by considering the entire DoE findings, the stress and strain of the 3D-PPOT materials made of 2.5% of Carbon Black (CB) deposited onto PET fabric (9.1 MPa and 2.1%) are compared with the one of the virgin printed onto PET fabric (8.7 MPa and 2.2%) and presented in Figure IV- 7. It was noticed that the percentage of CB incorporated into the PLA matrix did not meaningfully influence the tensile properties of 3D-PPOT through FDM process.

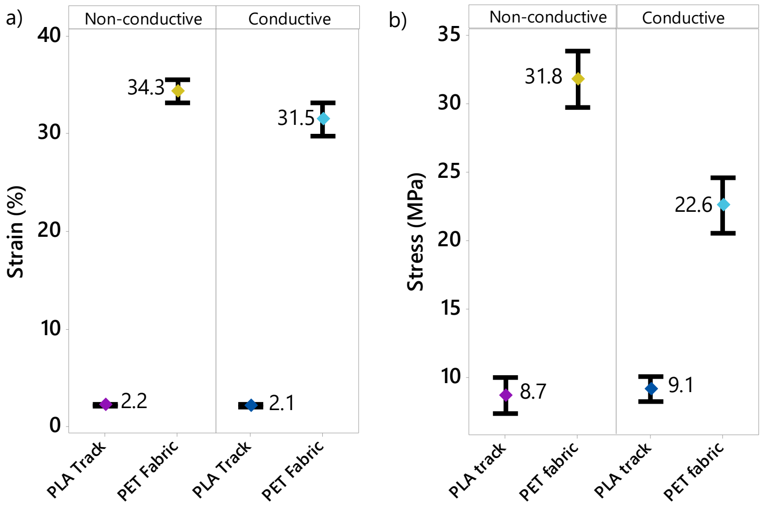

Figure IV- 7 Strain in % (a) and stress in MPa (b) and at rupture of the non-conductive and conductive PLA track printed deposited onto PET fabric (3D-PPOT) composed of both stress and strain at rupture of PLA track and PET Fabric.[121]

The stress-strain curves of 3D-PPOT materials using 14 picks/inch plain woven fabric, displayed in Figure IV- 8 and Figure IV- 9, confirmed that the adding CB fillers into the matrix enhanced noticeably the stress of the PLA track. Kausar *et al.* have previously proven that addition of nanomaterials into polymers in 3D printing applications frequently reinforce the CPCs and enhance the mechanical properties of the printed composite parts [193]. However, the percentage of fillers should be low, i.e. depending on the polymers there is a maximum amount of fillers. The tensile strength of the printed parts made of 10 wt. % carbon nanofiber- filled CPCs [194] or 10 wt. % multi-walled carbon nanotubes (MWCNT)-filled CPCs [195] was raised by 39 wt. % and 7.5 wt. % respectively while their elongation was reduced. Therefore, in the case of our study, it might be to incorporate a weight percentage of carbon black higher than 2.5 wt. % without impacting its strain. Additionally, it was remarked that the stress of the PET woven fabric of the 3D-PPOT is declined by about 3% compared to the original PET fabric and, however, the strain is not impacted (Figure IV- 7).

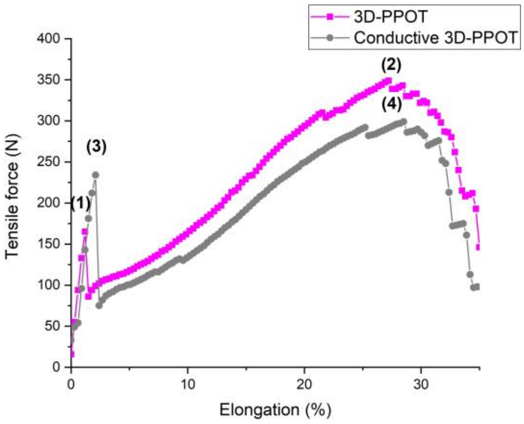

Figure IV- 8 Tensile force–Elongation curves[1] of 3D-PPOT materials using virgin PLA filament and PLA/2.5%CB (conductive) filament printed on 14 picks/inch PET woven fabrics in cross direction [121]

[1] (*1) and (2) represent the maximum strength of the PLA layer and the PET fabric of the 3D-PPOT using virgin PLA filament printed in cross direction respectively. (3) and (4) represent the maximum strength of the conductive PLA layer and the PET fabric of the 3D-PPOT using PLA/2.5wt.% CB filament printed in cross direction respectively*.

IV.4.3 Effect of textiles' properties and platform temperature on the stress and strain

The printing platform temperature and the properties of the textile such as the weft density, the pattern and the direction (cross or machine) of the fabric significantly influence the stress of the 3D-PPOT materials (Table IV- 11, Table IV- 12, Table IV- 13, Figure IV- 8, Figure IV- 10 and Figure IV- 9) but no impact was noticed on their strain. The direction of the fabric showed to have the highest contribution in the non-conductive and conductive PLA stresses while the platform temperature revealed to be the factor with the lowest one. Also, the pattern of the fabrics had a greater impact on the stress of the conductive PLA of 3D-PPOT materials in comparison with the stress of the one using non-conductive PLA (Table IV- 11 and Table IV- 13). The direction and the weft density were highly contributed factors of the stress of the PET woven fabric, i.e. in proportion they had important effect on the response.

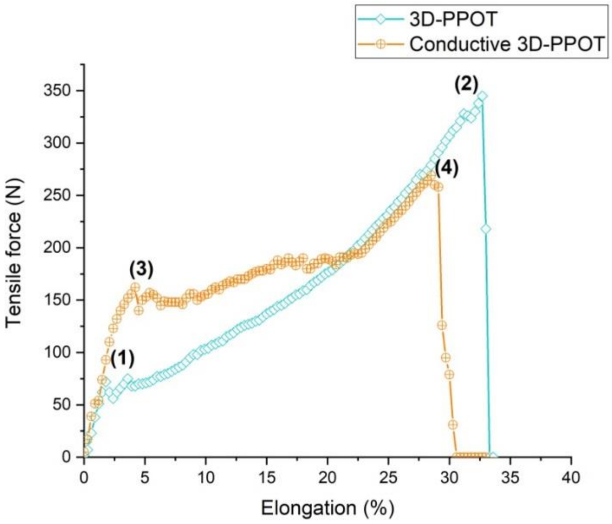

Figure IV- 9 Tensile force–Elongation curves[1] of 3D-PPOT materials using virgin PLA filament and PLA/2.5%CB (conductive) filament printed on 14 picks/inch PET woven fabrics in machine direction. [121] [1] *(1) and (2) represent the maximum strength of the PLA layer and the PET fabric of the 3D-PPOT using virgin PLA filament printed in machine direction respectively. (3) and (4) represent the maximum strength of the conductive PLA layer and the PET fabric of the 3D-PPOT using PLA/2.5wt.% CB filament printed in machine direction respectively*.

Table IV- 11 Stress at rupture of non-conductive of PLA track of 3D-PPOT material (MPa): p-values and contributions of the main factors. [121]

Factors	**P-values**[5]	**Contribution** [6]**(%)**
Platform temperature (◦C)	0.00	11.42
Weft density (pick/cm)	0.00	3.87
Pattern	0.00	0.66
Direction	0.00	65.66

[5] *determine statistical significance of factors' effect on non-conductive PLA stress*

[6] *describes the weight of each main factor in the statistical model*

Table IV- 12 Stress at rupture of PET woven fabric of 3D-PPOT material (MPa): p-values and contributions of the main factors [121]

Factors	P-values	Contribution (%)
Platform temperature (◦C)	0.00	1.29
Weft density (pick/cm)	0.00	19.57
Pattern	0.00	0.02
Direction	0.00	53.50

Table IV- 13 Stress at rupture of conductive PLA track of 3D-PPOT conductive material (MPa): p-values and contributions of the main factors [121]

Factors	P-values	Contribution (%)
Platform temperature (◦C)	0.00	11.15
Weft density (pick/cm)	0.00	0.51
Pattern	0.00	12.93
Direction	0.00	53.40

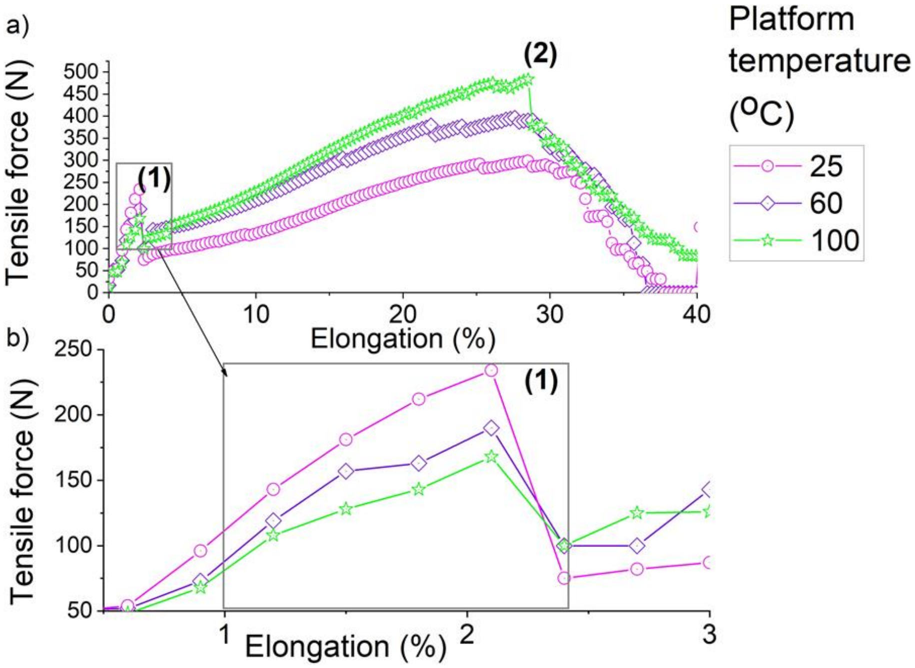

Figure IV- 10 Tensile force–Elongation curves[7] of 3D-PPOT using PLA filament printed on 14 picks/inch PET woven fabrics at three different temperatures 25, 60 and 100°C in machine direction (a). (b) is a focus image of (a). [121] [7] (1) and (2) represent the maximum strength of the PLA layer and the PET fabric of the 3D-PPOT using virgin PLA filament respectively.

The influence of the platform temperature, the fabric orientation (cross or machine), the pattern and the weft density of the woven material on the stress of 3D-PPOT (the textile and the printed track) using non-conductive and conductive PLA was described in Figure IV- 10, Figure IV- 11 and Figure IV- 12 [121]. First, it was proven that the stress of the non-conductive and conductive PLA track is lower in the machine direction than in the cross direction (Figure IV- 11 and Figure IV- 12). The stress of the non-conductive PLA track of the 3D-PPOT materials was higher with low platform temperature and high weft density as presented in Figure IV- 10 and Figure IV- 11 [121]. Similar findings could be obtained by using conductive PLA filaments (Figure IV- 12). As shown in Figure IV- 13 and Table IV- 15, a rise of the build platform temperature within a temperature range of [25-100 °C] might have led to increase the degree of crystallinity of PLA polymer caused by a decrease of its crystallization kinetics, for instance the speed [121]. The melting enthalpy of 100% crystalline considered in the calculation of the crystallinity degree of PLA was calculated was 93 J/g [164]. Formerly, the most critical parameter which affected the crystallization behavior of polymers was found to be the temperature [196,197]. Indeed, by increasing the temperature the mobility of the molecular chain that controls the crystallization capacity of polymer is enhanced. Additionally, the re-arrangement of the molecular chains of the polymer may have been impacted because of a very fast cooling process of the polymer creating a less ordered structure (e.g., degree of crystallization and modification of the crystal size) [198]. As the glass transition temperature range of PLA is 50-60 °C, the polymer is more rigid and brittle (at glassy state) below this range of temperature and thus, the stress at high platform temperature is lower. Previously, it was already proven that the adhesion strength of the conductive and non-conductive 3D-PPOT materials is enhanced with the increase of the printing platform temperature above the glass transition temperature of the polymer [77,78,101]. At 100 °C, the polymer, which comes from the extruder set at 250°C, can stay longer at rubbery or molten stage leading to a stronger penetration of the polymer through the structure of the textile and thus, a better anchor. Therefore, at higher temperature, the low stress of the PLA track might be due the great adhesion to the textile that leads to a lower thickness and much higher affinity with the PET fabric. Additionally, it was shown that the higher the platform temperature, the lower the crystallization kinetics of PLA and the higher its crystallinity degree as shown in Table IV- 14. Indeed, the DSC results and analysis of the conductive PLA was determined from the DSC test executed on the 3D-PPOT materials. Only the PLA peaks were considered.

Moreover, Taubner and Shishoo investigated the influence of the extrusion process temperature PLA on its average number molecular weight and found that an important increase of the temperature led to the degradation of the polymer especially for L-lactide (PLLA) which presented ester linkages that degraded under high temperature conditions [199].

Table IV- 15 DSC characterization of conductive PLA of 3D-PPOT materials when using 25, 60 and 100 °C as platform temperature during 3D printing process. [121]

Platform temperature (°C)	**PLA Melting temperature (◦C)**	**PLA Melting enthalpy (J/g)**	**Crystallinity Degree of PLA (%)**
25	160	4.6	5.0
60	161	6.5	7.0
100	162	13.5	14.5

Ma *et al.* proved that ultimate tensile of twisted sisal yarns reinforced composites principally failed because of the interfacial deboning whereas the yarn breakage was the main failure mode for non-twisted sisal yarns reinforced composites [200]. As already mentioned, in the current study, the yarns used in the warp direction of the woven fabrics were PET twisted multi-filaments of Nm 40 and in the weft one were 0.2 mm diameter polyester monofilaments.

Therefore, during tensile test, the different fissures and the debonding of the PLA layer in the machine direction might be explained by the affinity between the PLA monofilament and the PET monofilament probably higher than the one with the twisted PET multi-filaments. Indeed, after 3D printing process, the Van-der-Waals strengths could be more important between the layers in the cross direction than those in the machine direction. In general, greater adhesion led to a better stress and strain at rupture [101].

Prior to the FDM process, the four factors significantly impacted the stress of the fabric of the 3D-PPOT materials (p-value <0.05). It was revealed that the tensile strength of the fabric was better if using a plain structure compared to a twill 2/2 one. In general, high crimp of plain could lead to lower mechanical properties than twill structure [201], however, the findings were fully supported by researchers who described how the properties of the textile had an effect on its tensile strength [200,202,203]. After the FDM process, the stress of 3D-PPOT materials made of non-conductive and conductive monofilaments printed in the cross direction of PET fabrics is significantly high. The finding could be explained by the use of a more resistant monofilament as weft yarn and an increase of the weft density that created a closer packing structure.

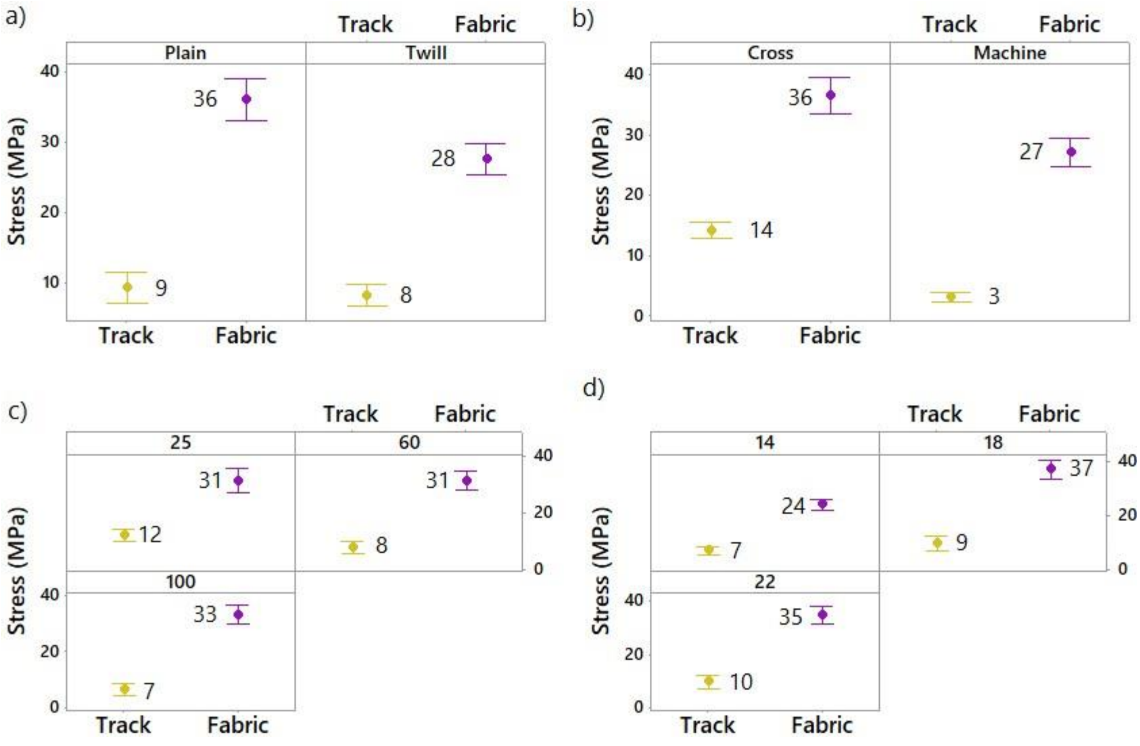

Figure IV- 11 Effect of textile pattern (a), fabric direction (b), platform temperature (c) and textile weft density (d) on stress (MPa) of 3D-PPOT materials made of non-conductive PLA track and PET fabric. Both the stress of the PLA track and PET fabric have to be considered. [121]

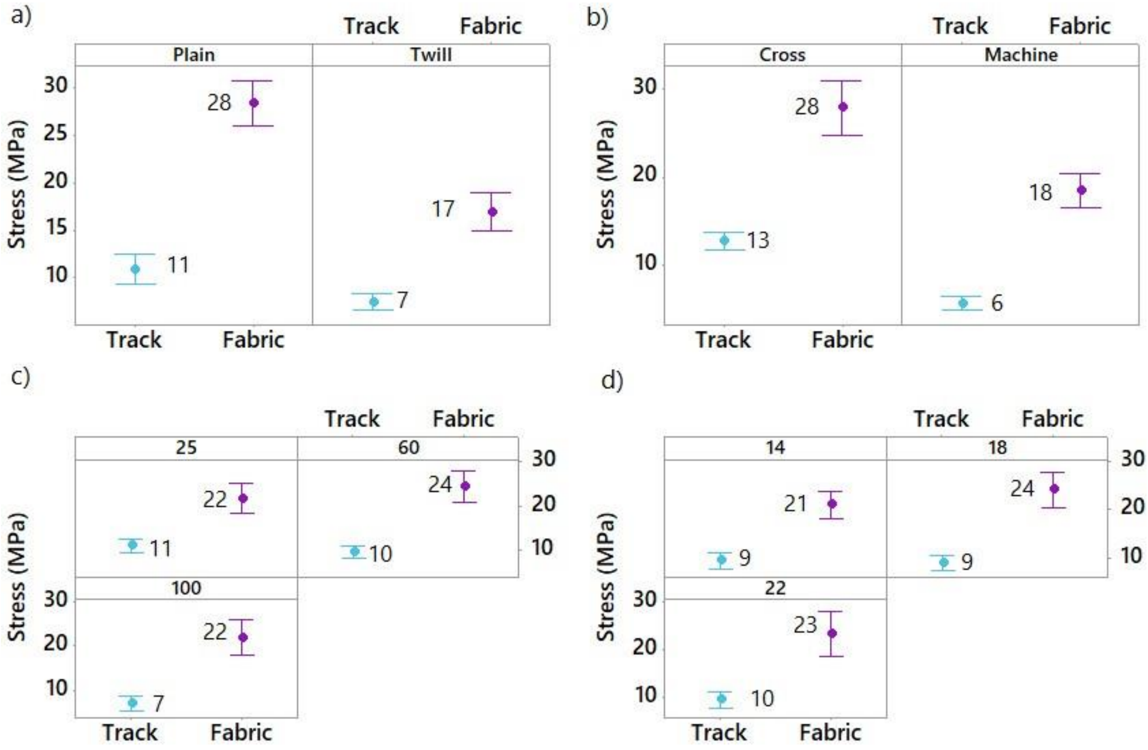

Figure IV- 12 Effect of textile pattern (a), fabric direction (b), platform temperature (c) and textile weft density (d) on stress (MPa) of conductive 3D-PPOT materials made of conductive PLA track and PET fabric. Both the stress of the PLA track and PET fabric have to be considered. [121]

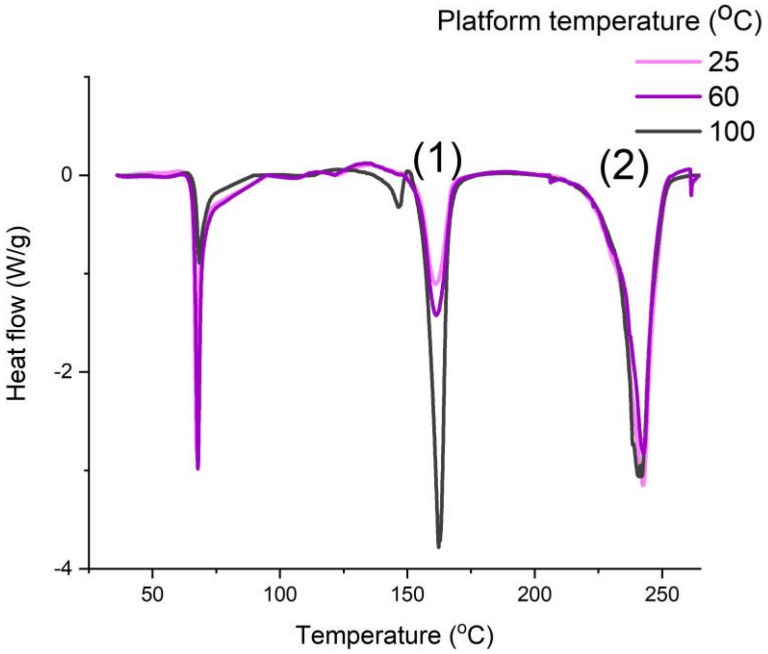

Figure IV- 13 DSC curves of conductive 3D-PPOT materials when using 25, 60 and 100 ◦C as platform temperature. (1) is the melting peak of PLA and (2) is the melting peak of PET. [121]

IV.4.4 Optimization of the tensile properties through modeling using textiles' deformations

IV.4.4.1 Theoretical models of the stress of the PLA printed layer

The experimental findings described in the section (*IV.4.4*) were used to successfully develop theoretical models of the stress of both non-conductive (**Eq. IV- 2** for the cross direction and **Eq. IV- 3** for the machine direction) and conductive (**Eq. IV- 4** for the cross direction and **Eq. IV- 5** for the machine direction) PLA printed layers of the 3D-PPOT materials. The R-Square range of their simulations, presented in Figure IV- 14 and Figure IV- 15, was [80% - 90] [121].

Statistical models of stress of non-conductive PLA track :

- in cross direction

$$Z = -9.1 + 2.97Y - 0.32X - 0.07Y^2 + 0.0014X^2 + 0.0042XY \qquad \textbf{(Eq. IV- 2)}$$

- in machine direction

$$Z = -1.8 + 1.95Y - 0.32X - 0.07Y^2 + 0.0014X^2 + 0.0042XY \qquad \textbf{(Eq. IV- 3)}$$

Where Z is the stress of non-conductive PLA track, Y the weft density and X the platform temperature. The boundary conditions of X and Y are 14-22 pick/inch and 25-100 °C respectively [121].

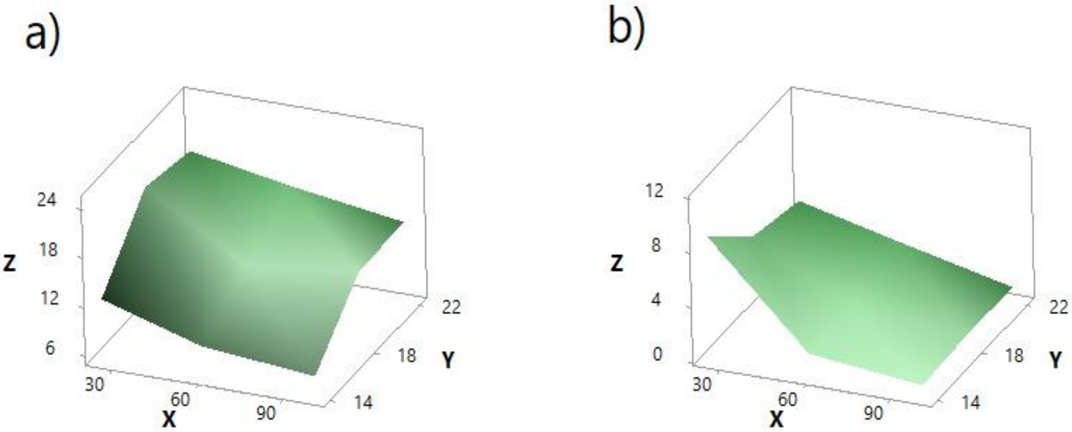

Figure IV- 14 Theoretical models of stress of non-conductive PLA track (MPa) of 3D-PPOT materials in Z axis, in function of weft density (picks/inch) in Y axis and platform temper- ature (°C) in X axis in cross direction (a) using the statistical model of Eq. IV- 2 and machine direction (b) using the statistical model of Eq. IV- 3. [121]

Statistical models of stress of conductive PLA track:

- in cross direction

$$Z = 8.18 + 0.356Y + 0.0646X - 0.00531XY \qquad \textbf{(Eq. IV- 4)}$$

- in machine direction

$$Z = 3.75 + 0.356Y + 0.0213X - 0.00531XY \qquad \textbf{(Eq. IV- 5)}$$

Where Z is the stress of non-conductive PLA track, Y the weft density and X the platform temperature. The boundary conditions of X and Y are 14-22 pick/inch and 25-100 °C respectively [121].

The theoretical models were created to predict the stress at rupture of the 3D-PPOT materials and support their enhancement and most precisely the one of the PLA track by modifying two parameters: the platform temperature and the weft density of the fabric. The interaction between the factors weft density and platform temperature were also considered as a coefficient of the equations [121].

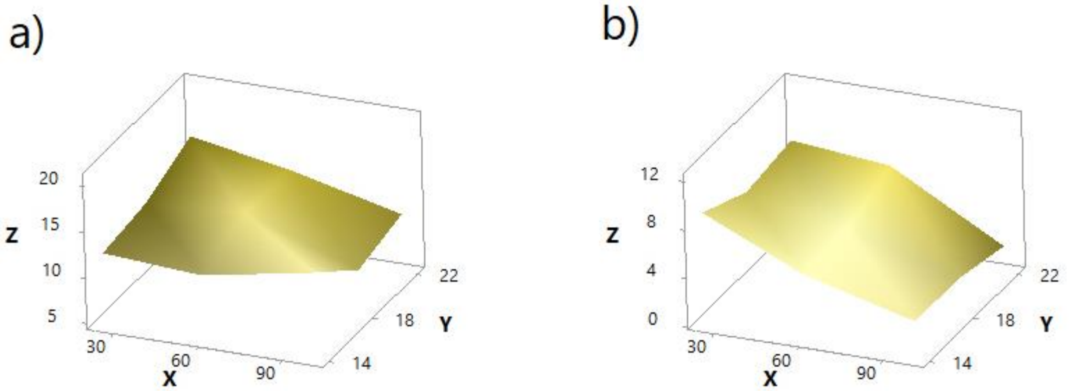

Figure IV- 15 Theoretical models of stress of conductive PLA track (MPa) of 3D-PPOT conductive materials in Z axis, in function of weft density (picks/inch) in Y axis and platform temperature (◦C) in X axis in cross direction (a) using the statistical model of Eq. IV- 4 and machine direction (b) using the statistical model of Eq. IV- 5. [121]

IV.4.4.2 Correlation between stress and textile deformation prior to printing

The existence of a correlation between the stress of the PLA printed layer of the 3D-PPOT materials and the deformations of PET fabrics was observed through simulated models presented in Eq. IV- 6 to Eq. IV- 7 based on the findings obtained in the cross direction (Figure IV- 16). Quadratic regressions of between the stress of the PLA printed are displayed for each platform temperature and the permanent, elastic and total deformations. Therefore, the deformation properties of the textile substrates directly impact the 3D-PPOT materials' properties. A rise of the permanent, elastic or total deformation of the textile led to diminish the stress of the non-conductive layers to a minimum value and then remain stable. Higher permanent, elastic and total deformations could be explicated by deeper penetration of the fused polymer through the structure as the structure can be easily compressed under the 3D printing head and thus, an increase in adhesion. A lower platform temperature resulted in reducing the stress at rupture of the non-conductive PLA track. The optimization of the tensile force of the 3D-PPOT materials might be completed by setting the deformations of the PET textiles and adjusting the platform temperature.

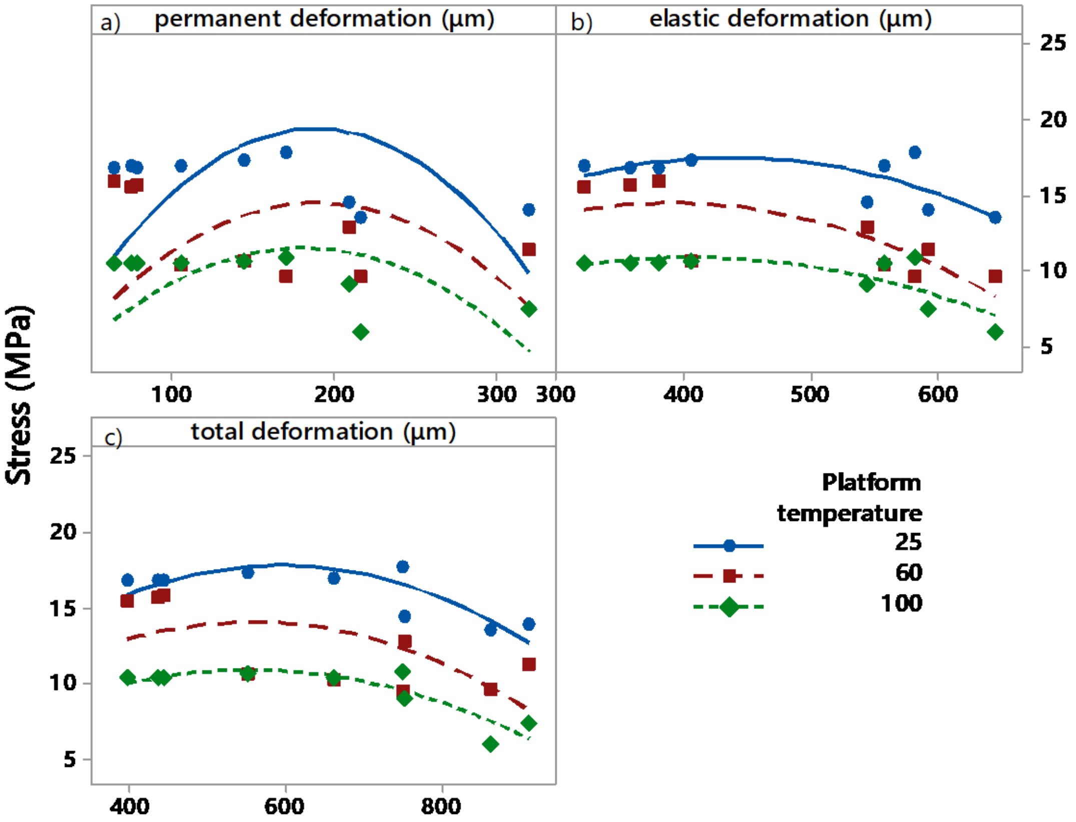

Figure IV- 16 Experimental values and curve fits of the stress (MPa) of non-conductive PLA track of 3D-PPOT material printed at three platform temperatures 25, 60 and 100 °C in the cross direction on twill fabrics versus permanent (a), elastic (b) and total (c) deformations (in µm) of the fabrics before printing. [121]

Statistical models of stress of non-conductive PLA track:

– in cross direction

$$Z = 28.2 - 9.0 \times 10^{-2}X_1 - 0.25Y - 2.1 \times 10^{-4}{X_1}^2 + 1.4 \times 10^{-3}Y^2$$ **(Eq. IV- 6)**

$$Z = 27.41 - 1.3 \times 10^{-2}X_2 - 0.25Y - 2.2 \times 10^{-5}{X_2}^2 + 1.4 \times 10^{-3}Y^2$$ **(Eq. IV- 7)**

$$Z = 31.98 - 3.2 \times 10^{-2}X_3 - 0.25Y - 2.2 \times 10^{-5}{X_3}^2 + 1.4 \times 10^{-3}Y^2$$ **(Eq. IV- 8)**

– in machine direction

$$Z = 11.13 - 2.0 \times 10^{-3}X_1 - 0.25Y - 2.1 \times 10^{-4}{X_1}^2 + 1.4 \times 10^{-3}Y^2$$ **(Eq. IV- 9)**

$$Z = 10.85 + 3.6 \times 10^{-3}X_2 - 0.25Y - 2.2 \times 10^{-5}{X_2}^2 + 1.4 \times 10^{-3}Y^2$$ **(Eq. IV- 10)**

$$Z = 12.39 - 9.3 \times 10^{-3}X_3 - 0.25Y - 2.2 \times 10^{-5}{X_3}^2 + 1.4 \times 10^{-3}Y^2$$ **(Eq. IV- 11)**

Where Z is the stress of non-conductive PLA track, X_1, X_2 and X_3 are the permanent, elastic and total deformations of the textile before printing and Y the platform temperature. The boundary conditions X_1, X_2 and X_3 are 50-350 mm, 200-700 mm and 350-950 mm respectively [121].

The R-squares of the different models are 84.2%, 82.7% and 81.6% for the combination [**Eq. IV- 6**; **Eq. IV- 9**], [**Eq. IV- 7**; **Eq. IV- 10**] and [**Eq. IV- 8**; **Eq. IV- 11**] respectively [121]. Similar models were created for the stress of the track of 3D-PPOT materials using conductive monofilaments.

IV.4.5 Effect of washing on the stress and strain of 3D-PPOT materials

The durability of the 3D-PPOT materials made of non-conductive PLA filament deposited on PET woven fabrics was assessed by testing their stress and strain after one cycle of washing process previously described. Their mean values and interval are reported in Figure IV- 17 (a) and (b). Moreover, it was shown that the washing process did not influence the tensile properties of the PLA track while the stress and the strain of the PET fabric of the 3D-PPOT material decreased drastically because of damaged fibers of the structure caused by the mechanical frictions of the washing process (Figure IV- 18 and Figure IV- 19). Similar to the findings obtained prior to the washing process, the weft density and the direction of the textile substrates as well as the platform temperature impacted the stress of the PLA track stress the most (Figure IV- 20) and no factors influence its strain.

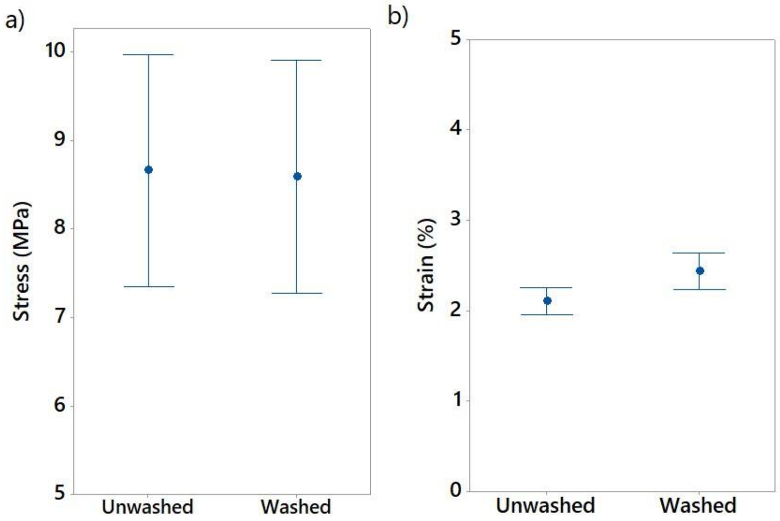

Figure IV- 17 Stress in MPa (a) and Strain in % (b) at break of non-conductive PLA track of 3D-PPOT materials before and after washing process [121]

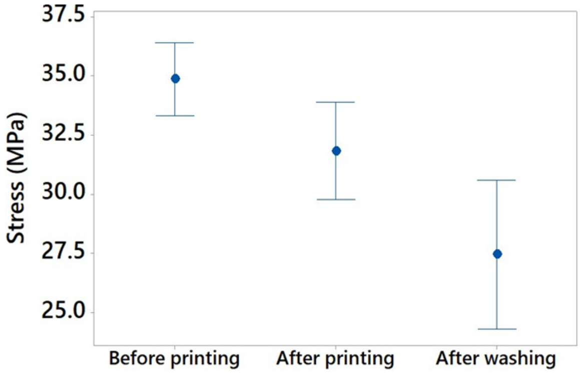

Figure IV- 18 Stress (in MPa) of PET woven fabric before and after printing using non-conductive PLA filament (3D-PPOT materials) and after washing of 3D-PPOT materials. [121]

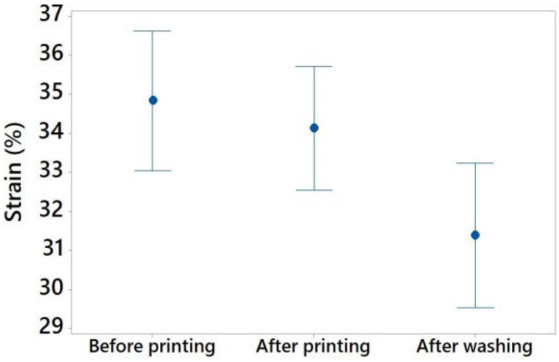

Figure IV- 19 Strain (in %) of PET woven fabric before and after printing using non-conductive PLA filament (3D-PPOT materials) and after washing of 3D-PPOT materials. [121]

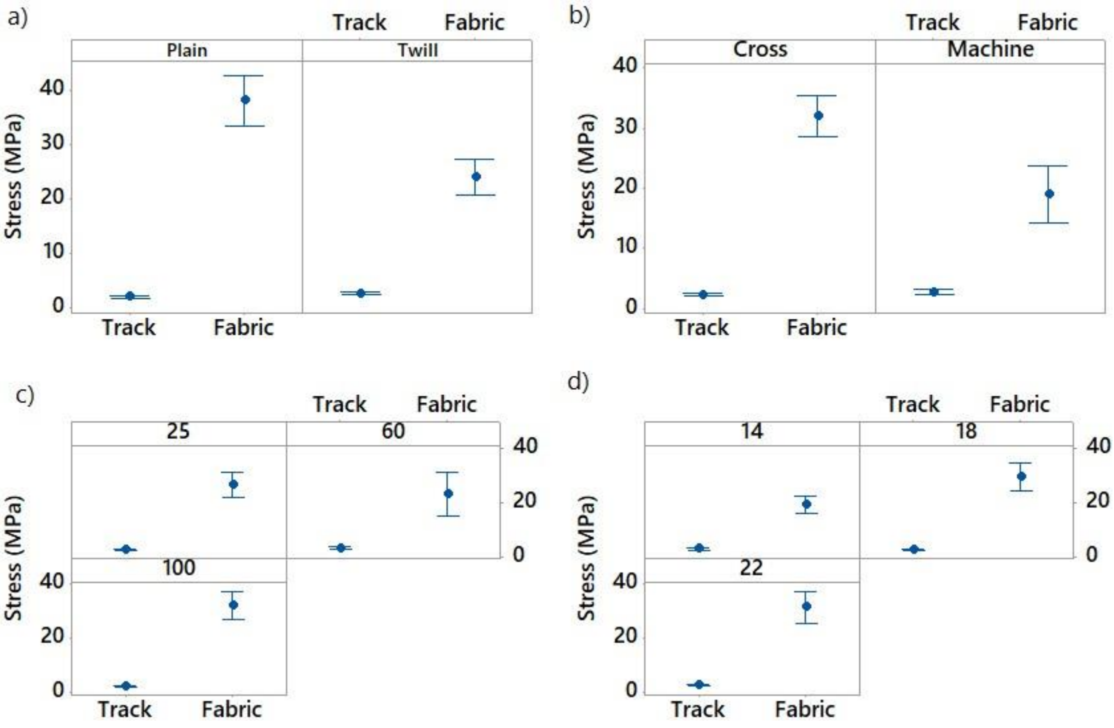

Figure IV- 20 Effect of textile pattern (a), fabric direction (b), platform temperature (c) and textile weft density (d) on stress (MPa) after washing test (wash durability) of conductive 3D-PPOT materials made of conductive PLA track and PET fabric. Both the stress of the PLA track and PET fabrics have to be considered [121]

IV.5 Wear resistance of 3D-PPOT materials

The abrasion resistance is one of the wear properties of 3D-PPOT materials considered in this thesis and the findings are described in this sub-section. The assessment of the abrasion resistance of the 3D-PPOT materials was performed through the weight loss of the material after set rubbing revolutions and the maximum number of revolutions before degradation of the samples designed as “end point” [167].

IV.5.1 Effect of textiles’ properties on the abrasion resistance of 3D-PPOT materials

First of all, the mean values of the weight loss of the PET fabrics and the 3D-PPOT materials after 1000, 2000, 5000, 10,000, 15,000 and 20,000 are measured and reported in Figure IV- 21 and Table B-1 and Table B-2 of Appendix B. Based on the findings, it was proven that the pattern and the weft density of the weave textiles had a significant impact on the weight loss of the PET woven materials after 2000, 5000, 10,000, 15,000 and 20,000 rubbing revolutions [167]. This observation was confirmed with the p-values of the measurement after each set number of cycles were below 0.05. Indeed, the weft density described how open is the textile structures, i.e. the higher the weft density, the more compact the structure. It was found that 3D-PPOT materials using tight PET fabric structure had a low amount of weight loss (Figure IV- 21). More precisely, twill materials demonstrated more important weight loss than plain one and the weft density quadratic ally influence this property. These findings are explained by the presence of few interlocking (or crossing) points and larger floats in twill 2/2 structure (*II.1.1.3*). Therefore, as described in the abrasion test findings, such structures presented low abrasion resistance with high weight loss [167]. Kaynak *et al.* obtained similar trend of results in their study concerning the impact of fabric pattern on the wear properties of woven fabrics [114].

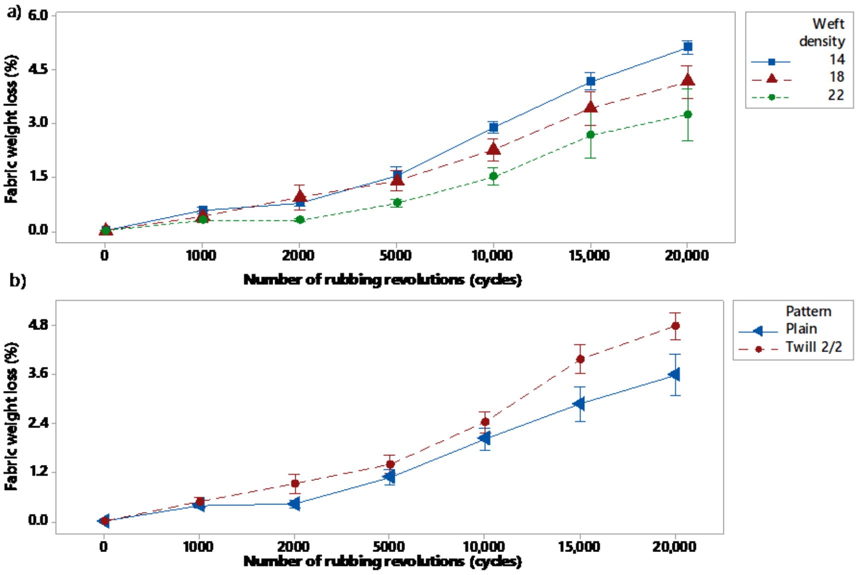

Figure IV- 21 Relationship between fabric weight loss (%) prior to FDM process and number of rubbing cycles when varying (a) the weft density and (b) the pattern. The 14, 18, 22 picks/inch are in blue, red and green, respectively) and the plain and twill patterns are in blue and red, respectively. [167]

IV.5.1.1 Impacting Factors on the Abrasion Resistance of the conductive 3D-PPOT Materials

The potential factors that could significantly impact the abrasion strength of the 3D-PPOT materials were investigated and the findings of this study are presented below. Due to no clear differences qualitatively observed between the samples after abrasion (Figure 1-B and Figure 2-B of Appendix B), a quantitative evaluation based on the determination the weight loss (in percentage) and end point after set numbers of cycles was preferred to analyze the influence of the FDM process.

In general, the findings presented in Figure IV- 22 revealed that the weight loss of 3D-PPOT materials was significantly changed by the weave type or pattern (p-value < 0.01 above 20,000 cycles), the platform temperature (p-value = 0.000 above 20,000 cycles) and the weft density (p-value < 0.05 above 30,000 cycles)[167]. However, the printing direction had no influence on the 3D-PPOT materials.

The lower the weight loss and the higher the end point, the greater the abrasion resistance. By using a plain fabric as textile substrate, a low platform temperature and high weft density, the abrasion strength of the 3D-PPOT materials was better. Indeed, the plain fabric has a more compact structure than a twill 2/2 one which confers a better cohesion between the yarns and the fibers after the deposition process of the fused polymer and therefore, this structure is more difficult to abrade and damage than the one utilizing twill 2/2 fabrics[167]. The higher abrasion resistance of the plain fabrics compared to the twill 2/2 was also noticed prior to FDM process (Figure IV- 21). Moreover, in a former study presented in Chapter III, it was demonstrated that due to stronger mechanical interlocking and deeper penetration of the polymer through the structure, their adhesion force between the conductive PLA printed track and the textile material was much higher with twill 2/2 fabric compared to plain one[101]. However, based on the current study, it seemed that a positive influence on the adhesion it led a negative effect on its abrasion resistance[167].

Similar explanations could support our understanding on the abrasion resistance of the 3D-PPOT materials depending on the density of the fabric. Indeed, it was demonstrated that weak adhesion property and stronger abrasion resistance were obtained by using a high weft density fabric as substrate for 3D-PPOT materials[167]. This is because of the limited accessibility of the entire textiles' structure through the thickness.

Additionally, it was found that the end point of the 3D-PPOT materials was mainly affected by the weave type or pattern (p-value = 0.001), the weft density (p-value = 0.000) and the platform temperature (p-value = 0.002) (Figure IV- 23) and the printing direction did not impact the end point. As for the weight loss analysis, higher end point values were acquired when using the densest plain PET fabric as a substrate and the lowest platform temperature.

IV.5.1.2 Abrasion Resistance of the 3D-PPOT Materials and the PET Woven Fabrics

The weight loss and the maximum number of rubbing revolutions were measured for the PET fabrics and the 3D-PPOT materials. The findings showed that the application of fused polymer onto textiles delivered much higher the abrasion resistance to the 3D-PPOT materials than the one of the original PET woven fabrics [167]**.** Indeed, the weight loss was twice lower at 5000 rubbing cycles and about four times lower at 20,000 rubbing cycles (Figure IV- 24) and an improvement of the end point of the 3D-PPOT material was noticed in comparison with the one of the PET woven fabric [167]. In other words, the deposition of polymeric materials onto PET textiles did improve the abrasion properties of the fabrics. The visualization of the 3D-PPOT samples and the PET fabrics in Figure 1-B and Figure 2-B of Appendix B confirmed the results as no significant changes could be observed between the two samples. In fact, the deposition of a thin layer of conductive PLA on the textile surface enhanced the cohesion between the fibers of the woven fabric which give a thicker, stiffer and more stable material with greater resistance to abrasion[121].

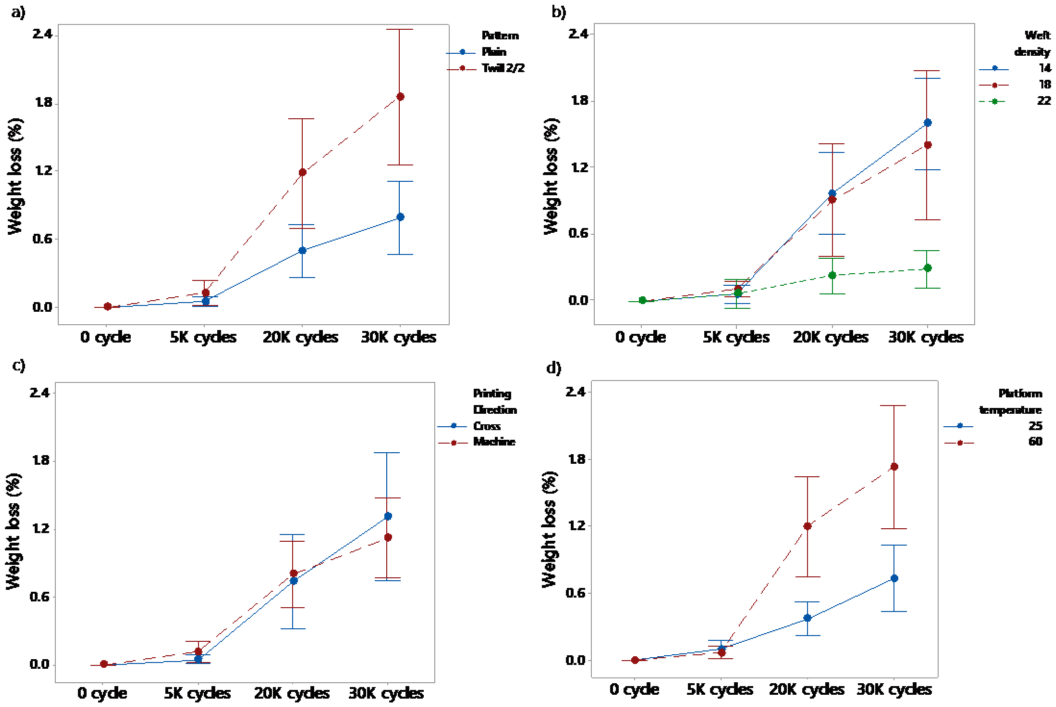

Figure IV- 22 Weight loss (%) of the 3D-PPOT conductive materials after 0 cycles, 5000 (5 K), 20,000 (20 K) and 30,000 (30 K) rubbing cycles using two different patterns (a) plain in blue and twill 2/2 in red, three different weft densities (b) 14, 18 and 22 in blue, red and green, respectively, two different printing directions (c) cross in blue and machine in red and two different platform temperatures (d) 25, 60 °C in blue and red, respectively. [167]

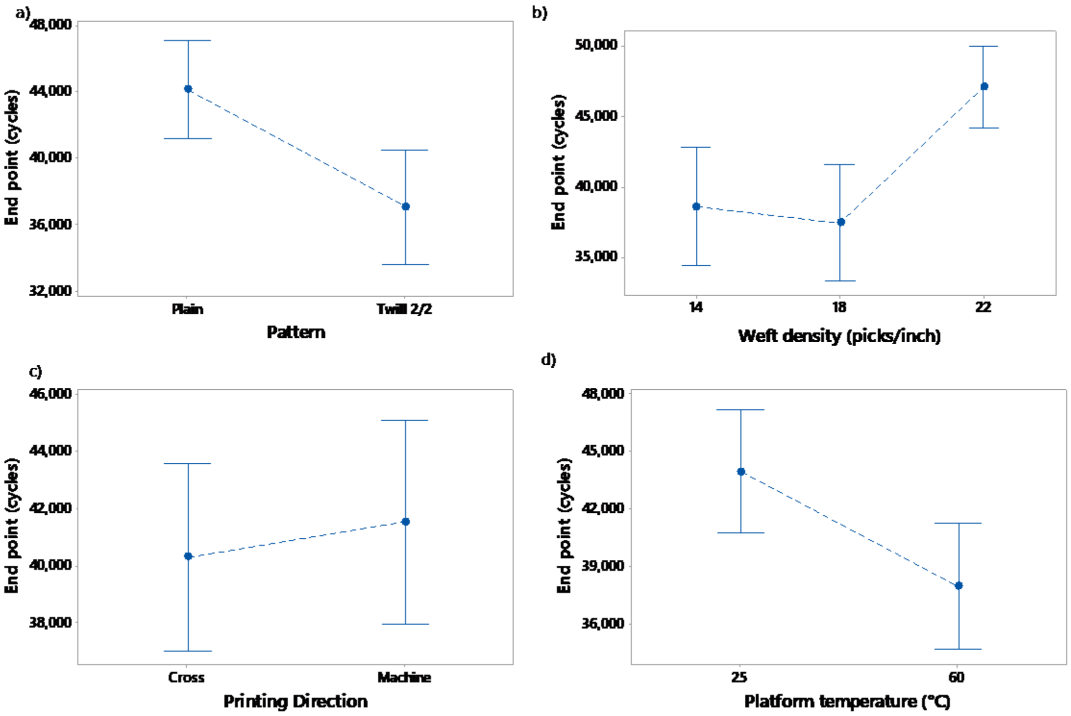

Figure IV- 23 Influence of (a) fabric pattern, (b) weft density, (c) printing direction and (d) platform temperature on the end point which is the maximum number of cycles (cycles) of 3D-PPOT conductive materials. [167]

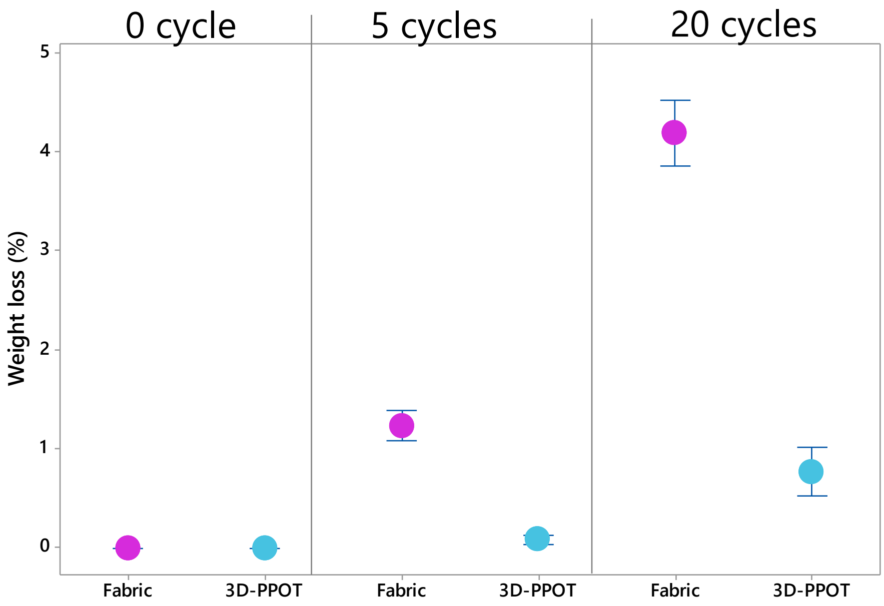

Figure IV- 24 Weight loss (%) of woven fabric and 3D-PPOT material after 0, 5 and 20 cycles. [167]

IV.5.2 Effect of abrasion on the electrical conductivity of the 3D-PPOT materials

On one hand, it was shown that the abrasion process did influence the electrical conductivity of the 3D-PPOT materials particularly when using a twill structure as substrate (Figure IV- 25). Indeed, there was an important gap between the electrical conductivity prior to and after abrasion test. The highest electrical conductivity values could be obtained with the fabrics that possess the highest weft densities [167]. An increase of the platform temperature up to the glass transition of the polymer led to diminish the electrical conductivity of the 3D-PPOT materials.

On the other hand, the impact of the weft density, platform temperature and the pattern (or fabric design) on the electrical conductivity after 20,000 revolutions was described in Figure IV- 26. After abrasion test, 3D-PPOT materials using plain fabrics demonstrated superior electrical conductivities to the ones utilizing twill structure. Besides, the weft density of the PET fabric and platform temperature significantly impacted the electrical properties of 3D-PPOT materials after wear (or abrasion) test. Indeed, high electrical conductivity was obtained with denser PET fabrics (i.e. with high weft density). Finally, the platform temperature had a quadratic effect on the electrical conductivity after abrasion.

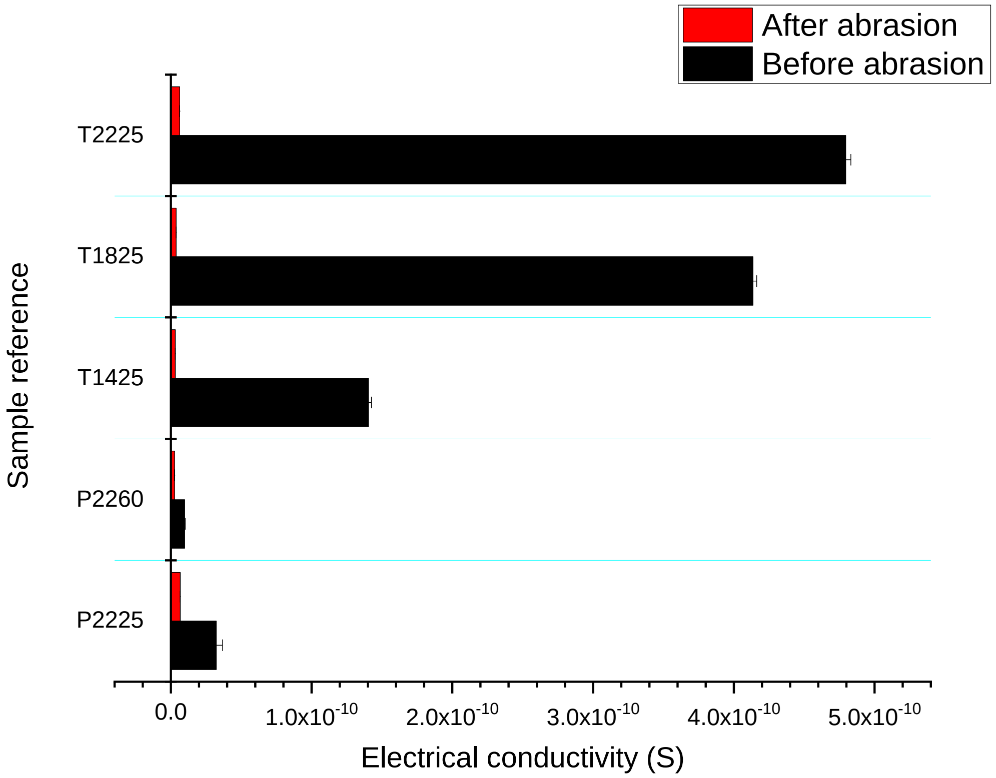

Figure IV- 25 Electrical conductivity (S) before (in black) and after (in red) abrasion (20 K cycles) for the 3D-PPOT materials samples P2260, P2225, T1425, T1825 and T2225. P2260, P2225, T1425, T1825 and T2225. The letter P and T means Plain and Twill fabrics respectively. The two next digits mention the weft density and the last two digits the platform temperature. For example, P2260 is designed as the following: plain of 22 picks/inch weft density and printed at a platform temperature of 60 °C [167]

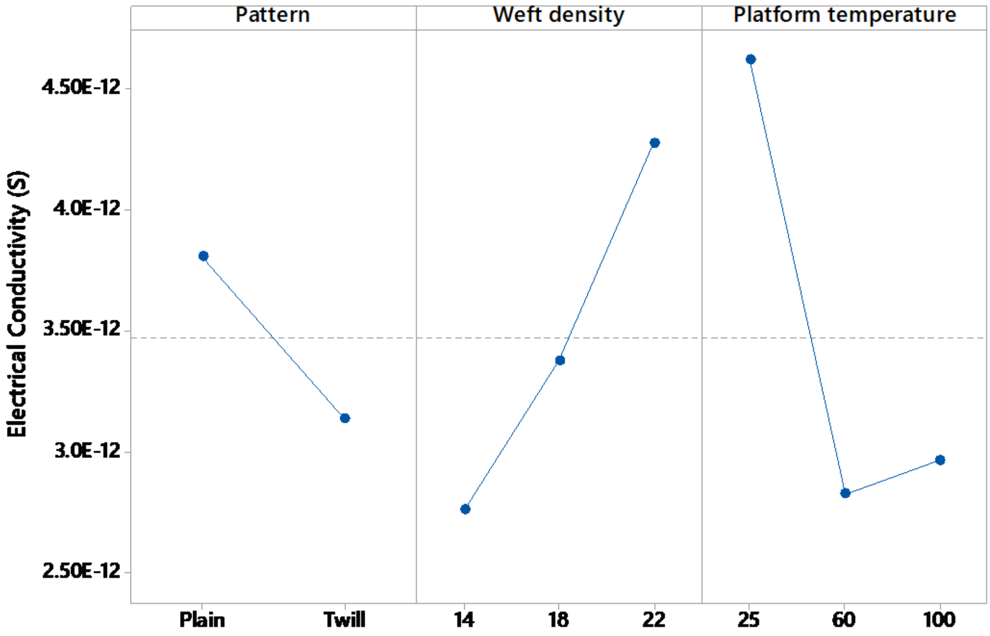

Figure IV- 26 Influence of pattern (plain and twill), weft density (14,18 and 22 picks/inch) and platform temperature (25, 60 and 100 °C) on the electrical conductivity (S) of the samples after abrasion (20 K cycles). In y-axis the following scientific notation 2.50E-12 means 2.50 × 10^{-12} [167]

IV.5.3 Effect of 3D printing and textiles' properties on pore size and thickness of textile fabrics and 3D-PPOT materials

The pore size and the thickness of the 3D-PPOT materials were determined and compared to the ones of the PET textiles. First, the factors that significantly impacted the average pore size before FDM process the most were : the weft density and the pattern of the PET fabrics (Figure IV- 27(a)). Previously, it was already proven that the arrangement of the fibers and compacity of the textile structure was defined by its weft density and pattern [101]. The lower the weft density, the more open the structure. Twill fabrics are also more porous than plain ones [101].

However, after 3D printing process (Figure IV- 27(b)), the pattern, the weft density and the platform temperature impacted importantly the pore size of the 3D-PPOT materials. Formerly, studies showed that high platform temperatures led to stronger adhesion explained by strong mechanical interlocking [101]. Therefore, this phenomenon could explain the reduction of the sizes of the pores in the textile structures as they are completely filled with polymeric materials.

Besides, the influence of the 3D printing on the mean pore size of the materials after FDM process was examined (Figure IV- 28). The 3D PPOT materials are porous with very small pores compared to the PET woven fabrics. Indeed, after FDM process, the mean pore size of the textiles was diminished by about 77% (from 24.47 µm to 5.62 µm) and 82% (from 16.05 µm to 2.88 µm) and for twill and plain fabrics respectively[167]. It can be understood that the FDM process on textiles closed its pores mainly located at its surface, and thus, the mean pores size (average size of pores) declined. Same trends can be obtained for 3D-PPOT samples with different weft densities (Figure IV- 29) showing that the mean pore size was reduced from 21.48 µm to 2.7 µm for 14 picks/inch and from 19.03 µm to 5.8 µm for 18 picks/inch [167].

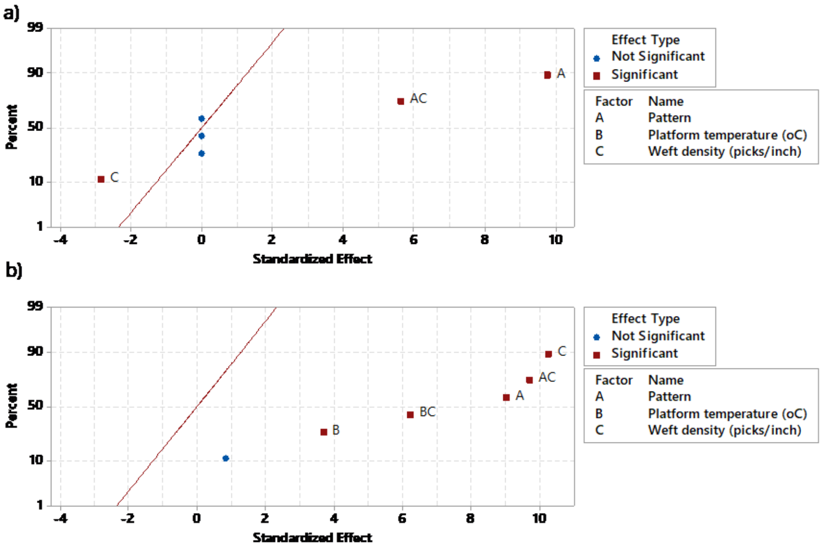

Figure IV- 27 Effect of (A) pattern, (B) platform temperature in °C, and (C) weft density in picks/inch on (a) pore size of the fabric prior to 3D printing process and (b) 3D-PPOT materials after 3D printing process, obtained through pareto analysis of Minitab 17. AC and BC represent the interaction between the factors A and C and, B and C, respectively [167].

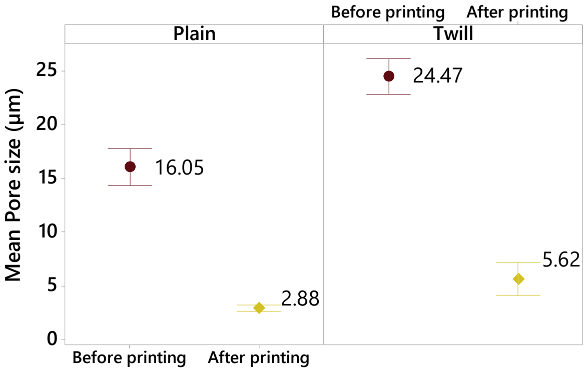

Figure IV- 28 Mean pore size (µm) of the pores located at the surface of the textile fabrics before 3D printing (in purple) and the 3D-PPOT materials after 3D printing (in yellow) depending on the fabric pattern (plain and twill) [167]**.**

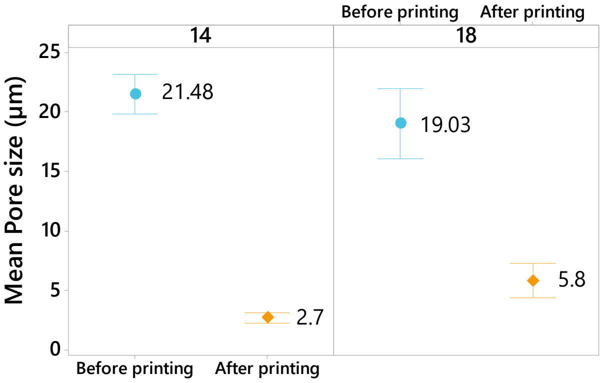

Figure IV- 29 Mean pore size (µm) of the pores located at the surface of the textile fabrics before 3D printing (in blue) and the 3D-PPOT materials after 3D printing (in orange) depending on the weft density of the fabric (14 and 18 pick/inch) [167]**.**

The mean thickness of the woven textiles and the 3D-PPOT was determined and their values are presented in Figure IV- 30. On one hand, it was demonstrated that the thickness of the 3D-PPOT materials was reduced from 301.5 µm to 275.7 µm by printing with the same conditions onto plain and twill fabrics respectively; and printing onto PET fabrics that have high weft densities increased the thickness. These findings can be explained by the higher penetration of the polymer through the structure [101] and the combination between the high temperature and the compression strength that the extruder of the 3D printer applied on the textiles [167].

On the other hand, the influence of the platform temperature on the thickness of 3D printed layer of the 3D-PPOT materials was assessed. This thickness was determined by deducting the thickness of the original fabrics to the thickness of the 3D-PPOT materials (Figure IV- 31). The findings showed that a rise of the platform temperature beyond the glass temperature of the polymer reduced the thickness of the PLA layer. Formerly, it was already proven that an increase of the platform temperature above the glass transition led to an enhancement of the adhesion between the textile and the printed layer [101] resulting in a decline of the thickness of the 3D printed PLA layer of the 3D-PPOT materials.

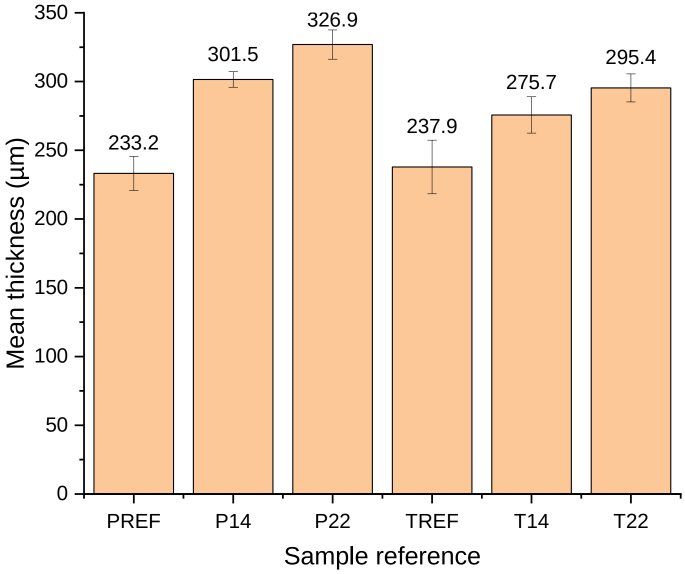

Figure IV- 30 Mean thickness (µm) of the textile fabrics before 3D printing (PREF and TREF) and the 3D-PPOT materials after 3D printing (P14, P22, T14 and T22). PREF and TREF stands for plain fabric reference and twill fabric reference, respectively. P14, P22, T14 and T22 are designed as the following 3D-PPOT materials: plain—14 picks/inch, plain—22 picks/inch, twill—14 picks/inch, twill—22 picks/inch [167]**.**

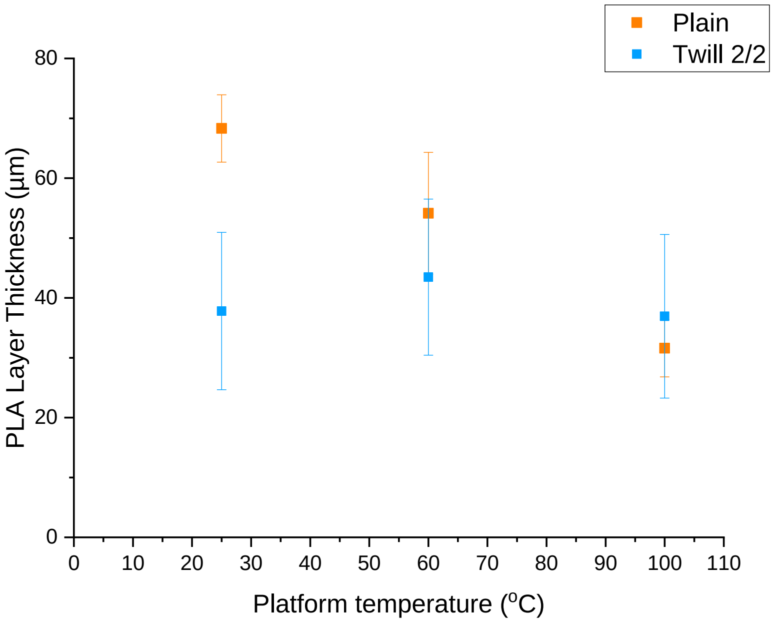

Figure IV- 31 Poly lactic acid (PLA) track thickness (µm) depending on the platform temperature of the 3D printer (25, 60 and 100 °C) for plain fabrics (in orange) and twill fabric (in blue) [167]**.**

IV.6 Conclusion

In this chapter, the influence of the properties of the textiles and the build platform temperature on the tensile, the deformation, the abrasion resistance, the thickness and the porosity of the deposited virgin or conductive PLA printed onto polyethylene terephthalate (PET) woven fabrics (i.e. 3D-PPOT materials) was studied. The impact of the conductive fillers and the washing process on the tensile properties of the 3D-PPOT materials PLA were also investigated in this study.

Based on the overall data of the findings, it was demonstrated that the tensile properties (including stress and strain) of the PLA printed track were three times lower than the one of the PET textile fabric because of its very low flexibility and weak adhesion to the PET fabric. Therefore, an improvement of the adhesion properties might lead to enhance the tensile properties. In addition, using a platform temperature higher than the crystallization temperature led to decrease the tensile strength of the PLA track of the 3D-PPOT materials and printing in the cross direction showed better tensile performance explained by the higher affinity of the PLA monofilament with the PET monofilament of the fabrics. The wash-ability and tensile resistance of the 3D-PPOT after washing were acceptable, however, the stress at rupture of the woven fabric (after FDM process) was affected by the washing process. In addition, the three factors that are the build platform temperature, the weft density and orientation of the fabric had a significant impact on the both the tensile and deformation of 3D-PPOT materials. It was also found that the elastic, permanent and total deformations of the 3D-PPOT materials were inferior than the one of the fabric prior to FDM process. Thus, these materials presented better dimensional stability and higher stiffness than the fabrics themselves but the 3D-printed track are less flexible than the textile materials.. The three deformations of the PET textile substrate quadratic ally influenced the tensile of the PLA printed track of the 3D-PPOT materials.

Furthermore, the weight loss and end point (i.e. the maximum number of cycles) of the 3D-PPOT were impacted by the weave type, the weft density and the platform temperature and the printing direction did not influence the abrasion resistance at all. 3D-PPOT materials using denser PET plain fabrics and manufactured at low platform temperature presented the best abrasion properties. However, the abrasion resistance is weak for 3D-PPOT materials strongly bonded together as it is the case for 3D-PPOT using rough and porous PET fabric. Compared to the abrasion resistance of PET fabric the one of 3D-PPOT is significantly enhanced due to a stronger fiber-to-fiber cohesion. The abrasion process did considerably impact the electrical conductivity of 3D-PPOT materials.

Finally, the thickness and the mean pore size of the 3D-PPOT materials were mainly influenced by weave type of the fabric and the platform temperature. The findings found had a direct relationship with the structure of the 3D-PPOT and the penetration depth of the polymer through the thickness.

Chapter V Enhancement of the deformation, tensile and electrical properties of 3D-PPOT by using biphasic materials

In the Chapter IV, the need of improving the deformation (i.e. flexibility) and tensile properties of 3D-PPOT using rigid thermoplastic-based monophasic materials was highlighted for better comfort and durability of functional textiles made through this technology. Indeed, Eutionnat-Diffo *et al.* Demonstrated that the stress and strain at rupture of the 3D Printed PLA and CB-filled PLA layers of 3D-PPOT materials were very low compared to the one of the PET fabric. In addition, the 3D-PPOT materials were stiffer, less flexible and more fragile while being bent than the ones of the fabric. In Chapter V, several Low Density PolyEthylene (LDPE) and Polypropylene - Based Elastomer (PBE) blends are suggested to obtain better flexibility, lower viscosity, improved strain and stress at rupture and greater electrical conductivity and process ability through 3D printing process. *Section V.1* introduces the materials, the manufacturing processes and the characterization methods used in this chapter. *Section V.2* describes the statistical design of each experiment, including the selected factors and targeted responses. *Section V.3* presents the location of fillers in CPCs/PBE blends based on two methods: prediction utilizing mathematical models and microscopy visualizations. *Section V.4* summarizes the various morphologies of CPCs/PBE blends found in the different experiments. *Section V.5 and Section V.6 report* the thermal, rheological and electrical properties of the CPCs/PBE blends. *Section V.7* presents the findings about the improvement of the 3D-PPOT material deformation and tensile properties through the use of biphasic blends. *Section V.8* relates the enhancement of the electrical properties of 3D-PPOT materials. *Section V.9* gives an overview and summary of the current study on the overall results.

For each material, process, characterization method and previous work already presented in Chapters I-IV, the referred section will be written in brackets.

V.1 Materials, processes and characterization

V.1.1 Materials

A PET 14 picks/inch twill 2/2 woven fabric was manufactured in house and also used in the former studies presented in the Chapter III and IV (*II.1.1* and *II.1.1.3)* and its mass per area (*II.4.3.6)* and thickness (*II.4.3.5)* are mentioned in Table III- 1. Several blends of LDPE- based CPCs/PBE blends presented in the next sub-section were developed.

V.1.1.1 LDPE- based CPCs/PBE blends development

LDPE (*II.1.1.1*) was found to be an alternative polymer that could be used in FDM process onto textiles, as it is a softer thermoplastic than the polymers commonly used in the 3D printing process such as ABS or PLA. However, conductive fillers that are usually incorporated into polymers increase their rigidity and fragility. These CPCs are easily breakable even if the virgin polymer is soft. Therefore, their viscosity, stiffness and process ability can be improved by blending the CPCs with an immiscible elastomeric polymer such as polyolefin-based elastomers, and most specifically the Propylene-Based Ethylene elastomers (PBE) (*II.1.1.1*) [204]. PBE was selected because of its low density and cost, great chemical resistance and good resilience without permanent deformation. The development of highly conductive and flexible LDPE/PBE monofilaments for 3D printing applications is based on the existence of two co-continuous phases of each immiscible polymer. In the various experiments of this chapter, the two immiscible polymers used were the LDPE and the PBE defined in the section *II.1.1.1*. The conductive fillers were Carbon Nanotubes (CNT) and KetjenBlack (KB) (*II.1.1.2*) preferably located in the LDPE or at the interface in order to preserve the flexibility given by the elastomeric phase while providing high electrical conductivity with continuous filler networks. In general, the mechanical, rheological, thermal and electrical properties of immiscible polymer blends highly depend on the morphology of the two phases [205].

V.1.1.2 Manufacturing of LDPE-based CPCs/PBE blends

Two extrusion scenarios (*II.2.1*) were suggested in the experiments which use LDPE and PBE formerly heated at 70°C and 40°C for twelve hours respectively [206]. The two scenarios termed 1-step and 2-step extrusions are already described in section *II.2.2* of the Chapter II. In the various blends, different proportions of LDPE, PBE, CNT and KB were explored. The main objectives were to evaluate their influence on the selective location of the electrically conductive fillers and the morphology of the polymer phases. A designation was followed in this chapter to exhaustively define each polymer blend, for instance, $40LDPE_{KB\ 5\ CNT\ 2.5}/60PBE$ described 40wt% of 5wt%KB and 2.5wt%CNT – filled LDPE mixed with 60wt% of PBE. The constant parameters of the extrusion process are described in the section *II.2.1* and the different temperature profiles of the five zones of the extruder are summarized in Table V- 1.

In the first experiment, four CPCs/PBE samples were developed with different ratios of KB (5 and 10 wt%) and CNT (2.5 and 5 wt%) (Table V- 2) to create immiscible conductive LDPE/PBE blends with various percentages (0, 40, 60 and 100 wt %) of both polymers shown in Table V- 3. The main objective of this experiment was to independently investigate the impact of fillers and PBE contents on the properties of CPCs and CPC/PBE blends [206].

Table V- 1 Temperature profiles (°C) of the extrusion of the CPCs and polymer blends [206]

Polymer blends	T_1 (˚C)	T_2 (˚C)	T_3 (˚C)	T_4 (˚C)	T_5 (˚C)
$LDPE_{KB\ 10\ CNT\ 5}$	125	175	215	225	240
$40LDPE_{KB\ 10\ CNT\ 5}/60PBE$					
$60LDPE_{KB\ 10\ CNT\ 5}/40PBE$					
$LDPE_{KB\ 10\ CNT\ 2,5}$	125	175	210	220	240
$40LDPE_{KB\ 10\ CNT\ 2,5}/60PBE$					
$60LDPE_{KB\ 10\ CNT\ 2,5}/40PBE$					
$LDPE_{KB\ 10}$	125	175	205	215	240
$40LDPE_{KB\ 10}\ /60PBE$					
$60LDPE_{KB\ 10}\ /40PBE$					
$LDPE_{KB\ 5}$	125	175	195	210	230
$40LDPE_{KB\ 5}\ /60PBE$					
$60LDPE_{KB\ 5}\ /40PBE$					
$40LDPE/60PBE$	125	170	175	180	200
$60LDPE/40PBE$	125	170	175	180	200
$60LDPE_{KB\ 6,7\ CNT\ 4,2}\ /40PBE$	120	220	250	260	270
$80LDPE_{KB\ 12,5\ CNT\ 3,1}\ /20PBE$	120	220	250	260	270

Table V- 2 Percentages of KB and CNT in LDPE-based CPC samples of experiment 1 [206]

Sample Reference	Percentage of KB in LDPE	Percentage of CNT in LDPE
A	5	0
B	10	0
C	10	2.5
D	10	5

Table V- 3 Percentages of LDPE-based CPC and PBE in immiscible conductive polymeric blends of experiment 1 [206]

Sample Reference	Percentage of LDPE - based CPC in immiscible biphasic blend	Percentage of PBE in immiscible biphasic blend
1	100	0
2	60	40
3	40	60
4	0	100

In the second experiment, different ratios of KB and CNT defined in Table V- 4 were mechanically incorporating into the LDPE or LDPE and PBE granulates. The percentages of LDPE and PBE are presented in Table V- 5. The difference between the first and the second experiments is the global content of each filler in the CPC/PBE blends. Indeed, in the first experiment the fillers were diluted while the content of PBE in the blend increases. The main goals of the experiment were to compare LDPE-based CPCs/PBE blends with the same filler contents and the influence of the 1-step and 2-step extrusions on the properties of the biphasic blends. Full descriptions of the samples used in the experiments 1 and 2 are presented in table C-1 and table C-2 of the appendix C. Moreover, the 1-step and 2-step extrusions are described in figure C-1 of appendix C.

Table V- 4 Percentages of KB and CNT in LDPE-based CPC samples of experiment 2 [206]

Sample Reference	Percentage of KB in LDPE	Percentage of CNT in LDPE
A	10	2.5
B	12.5	3.1
C	16.7	4.2

Table V- 5 Percentages of LDPE-based CPC and PBE in immiscible conductive polymeric blends of experiment 2 [206]

Sample Reference	Percentage of LDPE - based CPC in immiscible biphasic blend (wt%)			Percentage of PBE in immiscible biphasic blend (wt%)
	A	B	C	
1	100	-	-	0
2	-	80	-	20
3	-	-	60	40

V.1.2 FDM (3D printing) process

The 3D printing process (*II.2.3*) was executed with a Pellet Additive Manufacturing (PAM) printer from Pollen (France) based at Euromaterials (France). Thin layers (50 mm × 200 mm × 0.1 mm) made of the CPCs/PBE blends were deposited onto the PET woven textiles. The constant parameters of the FDM process are reported in **Table V- 6**.

Table V- 6 Printing process parameters [206]

Parameters	Values (unit)
Infill percentage	100 (%)
Z offset (distance between the head)	0 (mm)
Printing speed	3600 (mm.min^{-1})
Extruder diameter	0.4 (mm)
Extruder temperature	245 (°C)

V.1.3 Characterization methods

The characterization methods were already described in Chapter II. In this chapter, the dynamic surface deformations (*II.4.4.1*), the tensile and elongation at break properties (*II.4.4.2*), the contact angle with water and α-bromonaphthalene (*II.4.7*), the wettability coefficient (*II.4.6*), the predicted location of fillers (*II.4.8*), the Melt Flow Index (MFI) (*II.4.4.4*), the thickness (*II.4.3.5*) and pore size (*II.4.3.1)* measurements of fabrics and 3D-PPOT materials and the electrical conductivity of conductive monofilament and of 3D-PPOT (*II.4.5.1*) were determined. Moreover, the Differential Scanning Calorimetry (DSC) (*II.4.1.3)*, the Scanning Electron Microscopy (SEM) (*II.4.3.3*), the Transmission Electron Microscopy (TEM) (*II.4.3.7*) were methods also utilized in the different studies of this chapter.

V.2 Statistical design of experiments

The detailed of the two sets of experiments presented in Table V- 7 and

Table V- 8 respectively. For both experiments, the number of replicates depends on the characterization methods of the studied properties.

Table V- 7 Factors of statistical design of experiments for the morphological, rheological and electrical characterization of Conducting Polymers Composites (CPCs) [206]

Factors	Name	Level			
		-2	-1	0	1
A	Ketjenblack (KB) wt%	-	5	10	-
B	MultiWalled Carbone Nanotube (CNT) wt%	-	2.5	5	-
C	Low density Polyethylene (LDPE) wt%	0	40	60	100

D	Propylene Based Elastomer (PBE) wt%	0	40	60	100

Table V- 8 Factors of statistical design of experiments for the morphological, rheological and electrical characterization of Conducting Polymers Composites (CPCs) and properties of 3D-PPOT materials [206]

Factors	**Name**	**Level**		
		-1	0	1
A	Ketjenblack (KB) wt%	10	12.5	16.7
B	MultiWalled Carbone Nanotube (CNT) wt%	2.5	3.1	4.2
C	Low density Polyethylene (LDPE) wt%	60	80	100
D	Propylene Based Elastomer (PBE) wt%	40	20	0
E	Extrusion scenario	1-step*	2-step**	

***dispersion of the KB and CNT in LDPE and PBE in one step.**
****dispersion of the KB and CNT in LDPE and then blend with PBE**

V.3 Location of fillers in CPCs/PBE blends

V.3.1 Prediction of fillers' location through theoretical models

The selective location of the fillers in the biphasic blends is fundamental in the development of flexible and highly conductive biphasic blends with minimum amount of fillers. Indeed, an optimization of the electrical conductivity of these materials is possible by selecting the location of the fillers in one of the phases or at their interface. The location of KB and CNT nanoparticles was predicted through mathematical models using the wettability coefficient based on the contact angles of PBE with water and α-bromonaphtalen and the dispersive and polar components of the surface and interfacial energies of each nanoparticle and polymer mentioned in Table V- *9* and

Table V- 10 respectively. The interfacial energies ($Y_{CNT-PBE}$, $Y_{CNT-LDPE}$, $Y_{KB-LDPE}$, Y_{KB-PBE} and $Y_{LDPE-PBE}$) between the nanoparticles and the polymers, the wettability coefficient and the location of the fillers are stated in Table V- 11 and Table V- 12.

Table V- 9 Contact angle (°) of PBE with water and α-Bromonaphtalen [206]

Material	**Contact angle (°)**	
	Water	α-Bromonaphtalen
PBE	102.1 ± 1	45.6 ± 2

Table V- 10 Surface energies (mN/m) of LDPE, PBE, CNT and KB at room temperature [206]

Material	Υ_s (mN/m)	Υ_s^d (mN/m)	Υ_s^p (mN/m)
LDPE	33.2[207]	33.2[207]	0[207]
PBE	11.7	5.5	6.3
CNT	27.8[32]	17.6[32]	10.2[32]
KB (carbon black)	71.2[208]	36.8 [208]	34.4 [208]

Table V- 11 Interfacial energies (mN/m) between components A and B (CNT, KB, PBE and LDPE) [206]

$\Upsilon_{\text{component A/component B}}$	Values
$\Upsilon_{\text{CNT-PBE}}$	7.32
$\Upsilon_{\text{CNT-LDPE}}$	4.71
$\Upsilon_{\text{KB-LDPE}}$	12.52
$\Upsilon_{\text{KB-PBE}}$	33.75
$\Upsilon_{\text{LDPE-PBE}}$	8.37

Table V- 12 Wettability coefficient and predicted location of fillers in conducting LDPE/PBE blends [206]

Parameters	KB	CNT
$\omega_{\text{PBE / LDPE}}$	0.31 ± 0.02	-0.29± 0.01
Location of fillers	Interface	Interface

Due to a wettability coefficient between -1 and 1 for both fillers KB and CNT, it could be theoretically proven that the nanoparticles are located at the interface. The findings are relevant because the location of the fillers at the interface allows obtaining continuous and lengthy electrical networks. Additionally, the elastomeric phase of the blends does not contain fillers which means that the elasticity of this phase can be maintained. Thus, the flexibility of the 3D-PPOT should be enhanced. Further analysis, such as TEM and SEM are important to confirm the prediction as the extrusion process parameters are not considered in the model and might have an impact in the location of the conductive fillers.

V.3.2 Validation of the fillers' location models through SEM and TEM analysis

For the first and second experiments, SEM analysis was used to confirm the location of KB and CNT nanoparticles in the different blends (**Figure V- 1** and Figure V- 2). The location of fillers in each phase of the biphasic polymers could be observed as the density of the two polymers are different and therefore, the changes in brightness and color contrast of the LDPE and the PBE are significant. As the LDPE is denser than PBE, through SEM and in backscattered mode, LDPE is whiter compared to PBE observed in a dark grey color. In the $40(\text{LDPE}_{\text{KB 10 CNT 5}})/60\ \text{PBE}$ and $60(\text{LDPE}_{\text{KB 10 CNT 5}})/40\ \text{PBE}$ blends, the CNT nanoparticles were visualized only at the interface and the KBs in both the LDPE and at the interface [206]. The PBE, composed of soft segments, has a specific morphology through SEM that is completely different than the one of the LDPE. All the blends of the first experiment, no KB nanoparticles were seen in PBE, and therefore the mechanical properties (strain, deformation, etc.) of the 3D-PPOT should be enhanced as the nanoparticles were found to be only in one phase (LDPE) or at the interface (**Figure V- 1** and Figure V-2). However, based on the theoretical models, the KBs should only be observed at the interface and not in the LDPE [206]. This finding might be explained by the use of CB instead of KB interfacial energy value in the calculation as the one of KB could hardly be found and be measured.

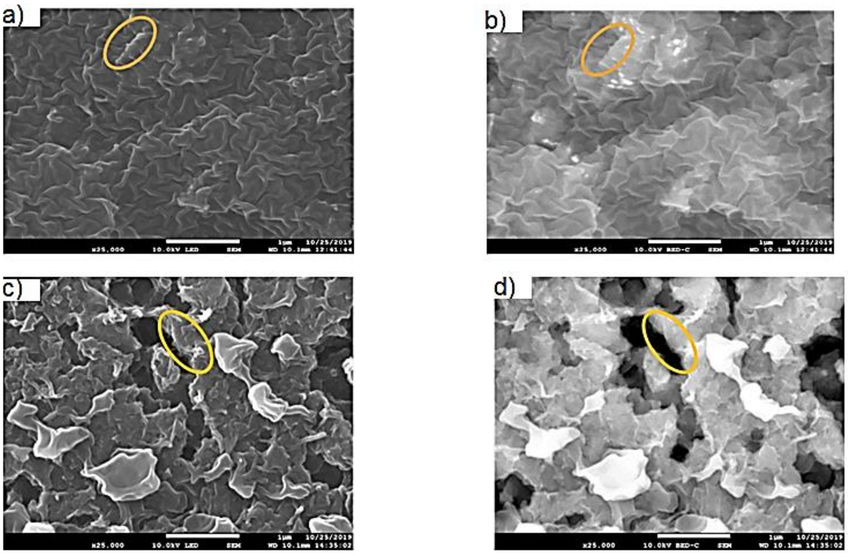

Figure V- 1 SEM images in cross section of the $\mathbf{40(\mathit{LDPE}_{\mathit{KB}\,10\,\mathit{CNT}\,5})/60\ \mathit{PBE}}$ and $\mathbf{60(\mathit{LDPE}_{\mathit{KB}\,10\,\mathit{CNT}\,5})\ /\ 40\ \mathit{PBE}}$ blends: location of CNT nanoparticles. (a) and (c) are in normal LED mode and (b) and (d) in backscattered mode. LDPE is whiter and in the PBE is darker [206]

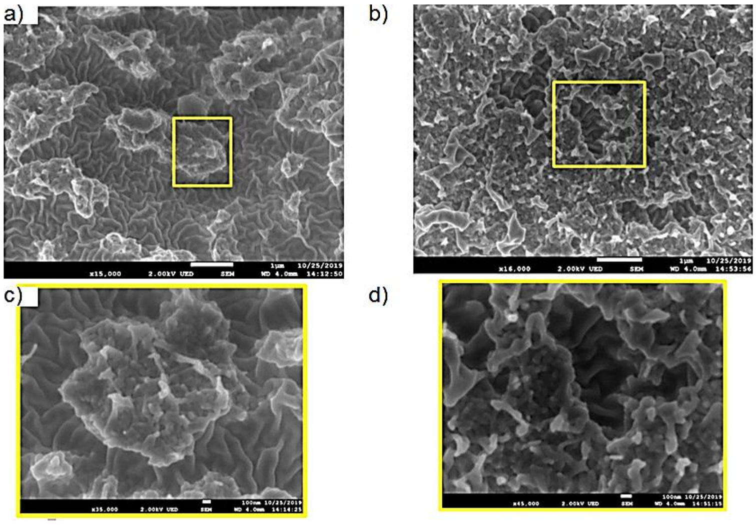

Figure V- 2 SEM images in cross section of the $\mathbf{40(\mathit{LDPE}_{\mathit{KB}\,10\,\mathit{CNT}\,5})/60\ \mathit{PBE}}$ (a and c) and $\mathbf{60(\mathit{LDPE}_{\mathit{KB}\,10\,\mathit{CNT}\,5})/40\ \mathit{PBE}}$ (b and d) blends: location of KB nanoparticles. LDPE is whiter and in the PBE is darker [206]

Additionally, as shown in Figure V- *3* and Figure V- *4*, the 1-step or 2-step extrusion scenarios did not influence the selective location of fillers, i.e. no migration of electrically conductive charges was observed. Both nanoparticles are located at the interface and the KBs also remain in the LDPE (Figure V- *3*). No charges were noticed in the PBE (Figure V- *4*) [206].

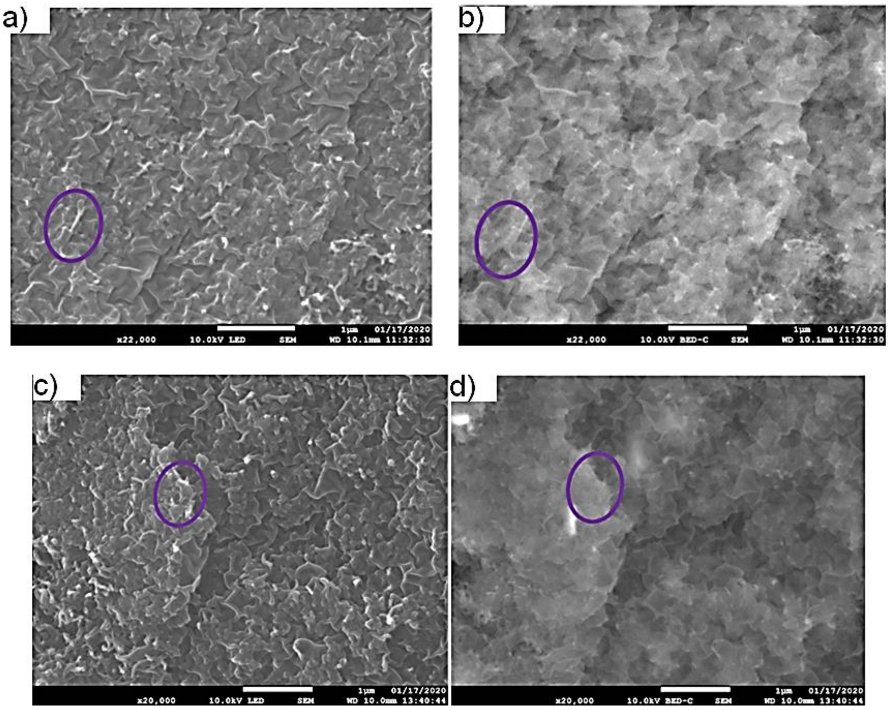

Figure V- 3 SEM images in the transverse direction of the 1-step ((a) and (b)) and two-steps ((c) and (d)) $\boldsymbol{60(LDPE_{KB\ 16.7\ CNT\ 4.2})/40PBE}$ blend : location of the CNT nanoparticles. (a) and (c) are in the normal LED mode and (b) and (d) in backscattered mode. LDPE is whiter and the PBE is darker. [206]

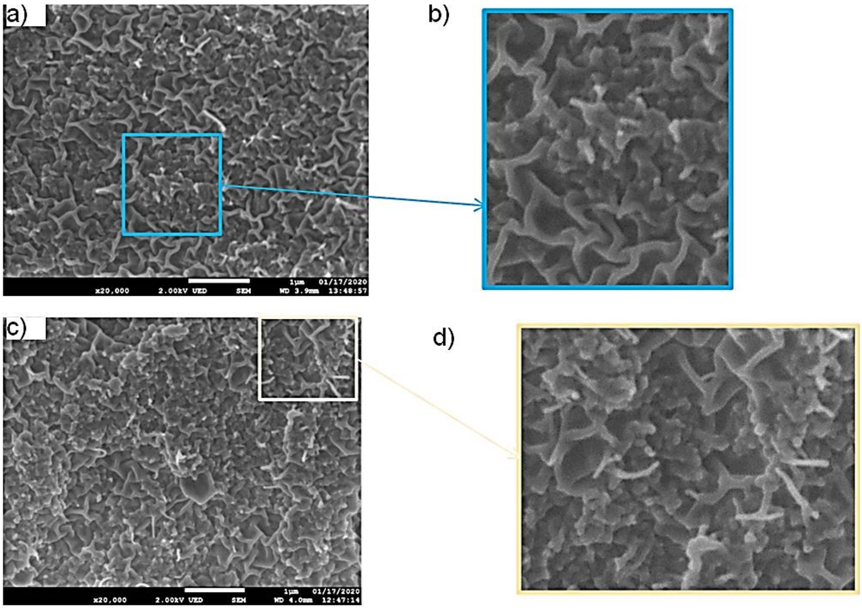

Figure V- 4 SEM images in the transverse direction of the 1-step ((a) and (b)) and two-steps ((c) and (d)) $\boldsymbol{60(LDPE_{KB\ 16.7\ CNT\ 4.2})/40PBE}$ blend : location of the KB nanoparticles. LDPE is whiter and the PBE is darker. [206]

In addition, some of the mentioned observations were confirmed through TEM visualizations in the longitudinal direction of the 1-step and 2-step extruded- $60(LDPE_{KB\ 16.7\ CNT\ 4.2})/40PBE$ blends and as shown in Figure V- 5. Indeed, the KBs and CNTs were preferably located in both the LDPE and at the interface between the PBE and the LDPE in the 2-step extruded-$60(LDPE_{KB\ 16.7\ CNT\ 4.2})/40PBE$ blend (Figure V- 5 (a) and (b), while the 1-step extruded- $60(LDPE_{KB\ 16.7\ CNT\ 4.2})/40PBE$ blend the CNT nanoparticles were found to be in both LDPE and PBE phases (Figure V- 5 (c) and (d)). Thus, the extrusion in two steps seems to necessary to avoid the transfer of the conductive fillers to the PBE phase in order to preserve the elastic properties of the PBE and create more conductive networks between the charges.

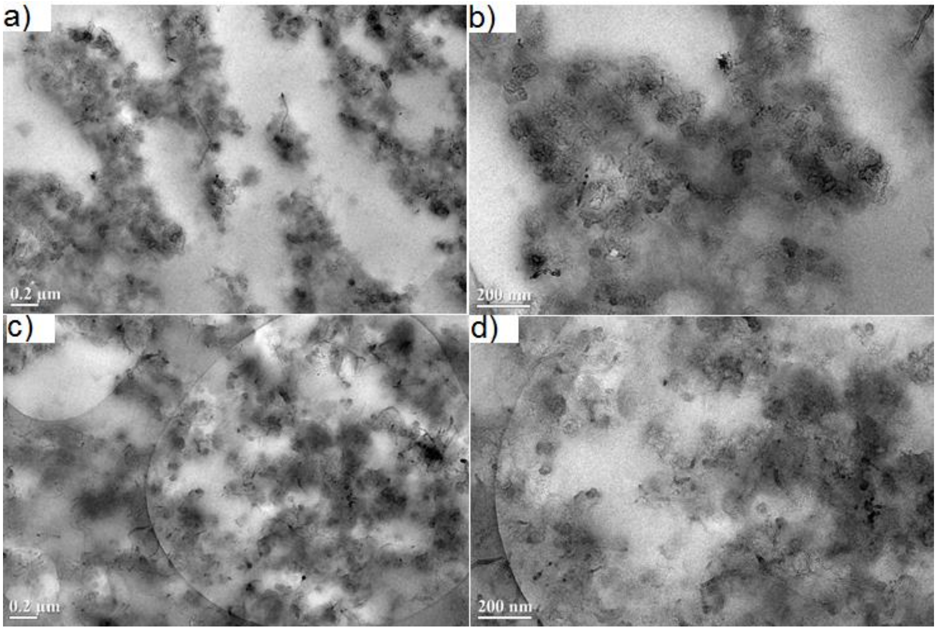

Figure V- 5 TEM images in the transverse direction of the 2-step ((a) and (b)) and 1-step ((c) and (d)) extruded $60(\mathrm{LDPE}_{\mathrm{KB\ 16.7\ CNT\ 4.2}})/40\mathrm{PBE}$ blend: location of the KB and CNT nanoparticles. LDPE is darker and the PBE is whiter. [206]

V.4 Morphology of CPCs/PBE blends

The co-continuity and nodular structures of CPC/PBE or virgin LDPE/PBE blends were also observed using SEM analysis. As formerly discussed, the morphology of the biphasic blends hardly defined their mechanical and electrical properties. (Figure V- 6). In the case of virgin polymer blends such as 60%LDPE/40%PBE and 40%LDPE/60%PBE, nodular structures were found. Indeed, depending on which polymer is predominant, nodules of PBE in LDPE or nodules of LDPE in PBE are observed [206]. Consequently, these blends cannot be utilized to manufacture flexible 3D-PPOT materials as both phases are not co-continuous. The selective location of fillers in the various CPC/PBE blends might allow to get the co-continuity of each phase.

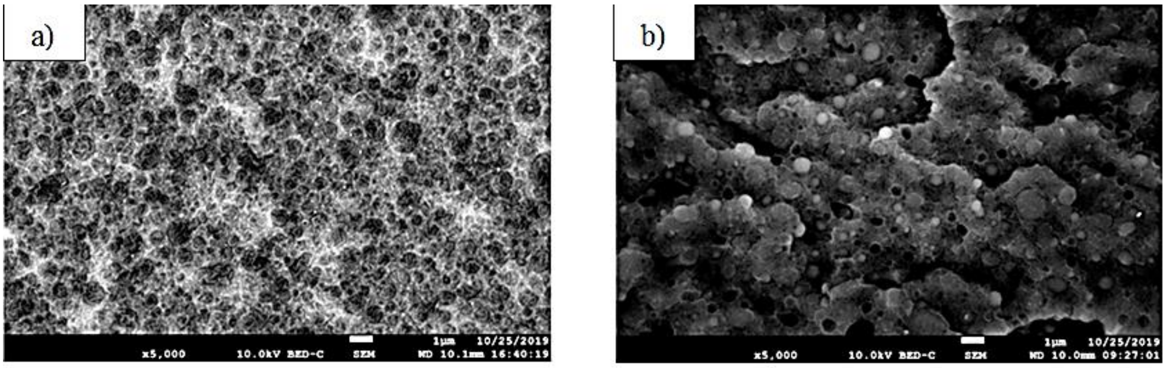

Figure V- 6 SEM images of the cross sections of 60%LDPE/40%PBE and 40%LDPE/60%PBE. LDPE is whiter and in the PBE is darker [206]

Moreover, it was noticed that by adding up to 10 wt% of KB in the CPCs, the morphology of the biphasic blends was not co-continuous. Indeed, in the $40(LDPE_{KB\,10})\ /60PBE$ blend displayed in Figure V- 7, nodules of LDPE-based CPCs in PBE are observed in the transverse direction (Figure V- 7 (a) and (b)), while a fibrillary structure with two distinct phases were detected in the longitudinal direction (Figure V- 7 (c) and (d)). The same morphology was achieved for the $40(LDPE_{KB\,5})/60PBE$ blend. [206]

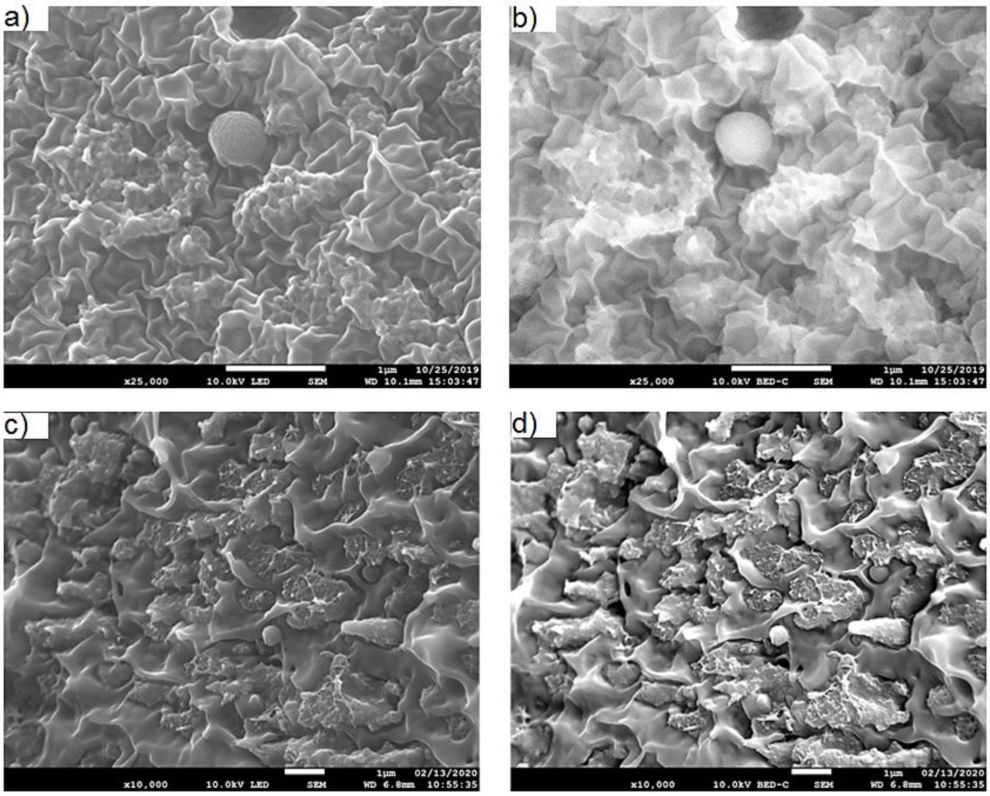

Figure V- 7 SEM images of the $\boldsymbol{40(LDPE_{KB\,10})/60PBE}$ blend in the transverse (a and b) and longitudinal directions (c and d). (a) and (c) are in normal LED mode and (b) and (d) in backscattered mode. LDPE is whiter and the PBE is darker. [206]

Nonetheless, the addition of both CNT and KB in LDPE prior to the blending process creates co-continuous phases of CPCs and PBE due to the selectively located charges as revealed in Figure V- 8. Indeed, as they are located at the interface, the CNTs and KBs might have modified the existing interfacial tension between the two polymeric phases [206]. In addition, the presence of KB in LDPE contributed in extending its phase to a co-continuous one. The findings were obtained for two conducting biphasic blends: $40(\mathrm{LDPE}_{\mathrm{KB}\ 10\ \mathrm{CNT}\ 5})/60\mathrm{PBE}$ and $60(\mathrm{LDPE}_{\mathrm{KB}\ 10})/40\mathrm{PBE}$. Similar results were found by A. Nuzzo *et al.* who demonstrated that co-continuous phases were observed in orgaoclay, sepiolite and carbon nanotubes-filled Polylactic acid (PLA)/Polyamide 11 (PA11) blends because of the preferential location of the fillers in the minor PA11 phase that was originally in a nodular morphology [209]. This finding was explained by the capacity of the nanoparticle networks to decrease the interfacial tension of the two phases and deform the shapes of the phases [209].

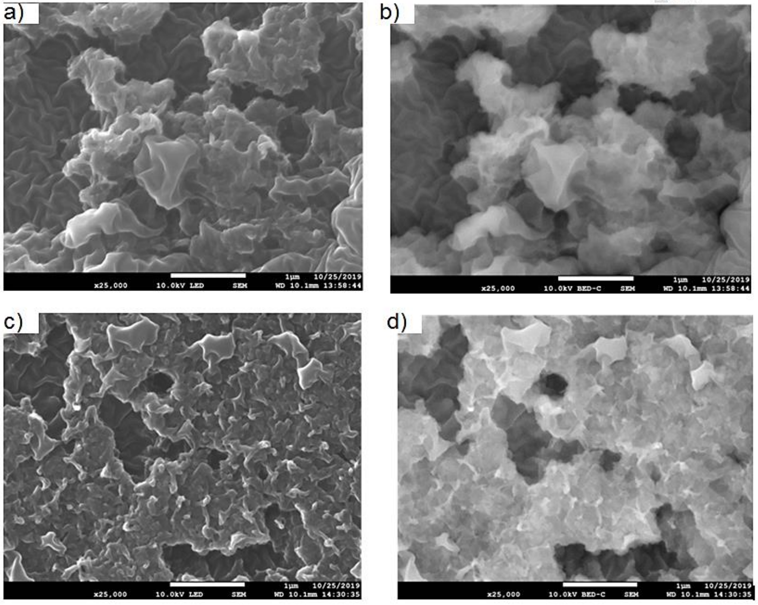

Figure V- 8 SEM images of the $\boldsymbol{40(LDPE_{KB\ 10\ CNT\ 5})/60PBE}$ (a and b) and $\boldsymbol{60(LDPE_{KB\ 10\ CNT\ 5})/40PBE}$ (c and d) in the transverse directions. (a) and (c) are in normal LED mode and (b) and (d) in backscattered mode. LDPE is whiter and the PBE is darker. [206]

In the second experiment, the morphology of the blends $60(LDPE_{KB\ 16.7\ CNT\ 4.2})/40PBE$ and $80(LDPE_{KB\ 12.5\ CNT\ 3.1})/20PBE$ was also visualized through SEM images (Figure V- 9-Figure V- 10) in order to confirm the morphology observed in the first experiment, and thus, understand the impact of the extrusion scenario on the morphology of the biphasic blends [206]. A co-continuity of the two phases is noticed in both blends. Nevertheless, the two phases cannot easily be distinguished because of an important quantity of fillers. Indeed, a merge of both phases is perceived, especially in the case of 1-step extrusion process, i.e. when the two polymers and the fillers are blended in one stage.

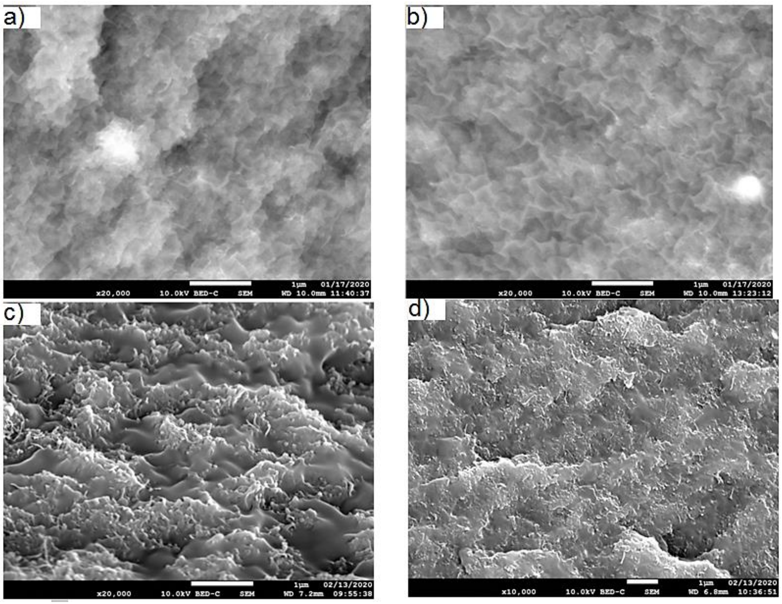

Figure V- 9 SEM images of the $60(LDPE_{KB\ 16.7\ CNT\ 4.2})/40PBE$ to obtain globally in the blend 10% KB and 2.5% CNT. ((a) -(b)) And ((c) -(d)) represent the cross section and longitudinal views respectively, of the blend using one step and two-steps extrusions. LDPE is whiter and the PBE is darker. [206]

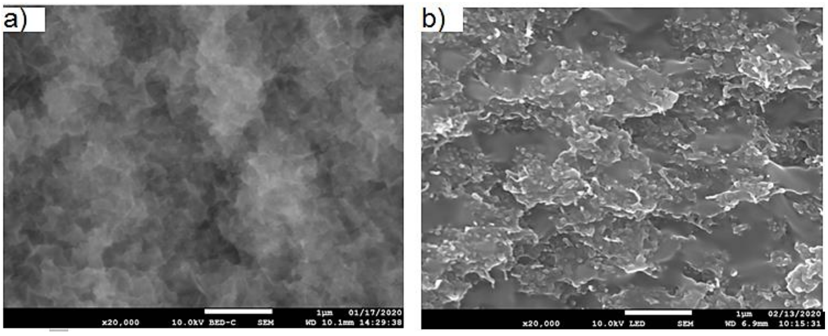

Figure V- 10 SEM images of the $80(LDPE_{KB\ 15.6\ CNT\ 3.9})/20PBE$ to obtain globally in the blend 10% KB and 2.5% CNT. The figures ((a) -(b)) represent the cross section and longitudinal views respectively, of the blend using two-steps extrusions. LDPE is whiter and the PBE is darker. [206]

V.5 Thermal and rheological properties of the CPCs/PBE blends

V.5.1 Thermal properties of CPCs/PBE blends

The crystallization and melting curves of the LDPE, PBE, 40wt%PBE/60wt% and 60wt%PBE/40wt%LDPE (Figure V- 11 (a) and (b)). First of all, one melting (T_m =115°C) and two crystallization (T_{c1} =110° and T_{c2} =65°) temperatures are detected for LDPE while two melting peaks and two crystallization peaks are recorded for PBE. The peaks framed in brown (T_m =65°C and T_c =100°) and green (T_m =40°C and T_c =70°) correspond to the ones of ethylene and propylene respectively, two components of the PBE. In the case of LDPE/PBE blends, the melting and the crystallization of LDPE and PBE were merged. Indeed, two crystallization peaks at about 105°C and 38°C and one melting peak at 110°C were visualized for both blends [206].

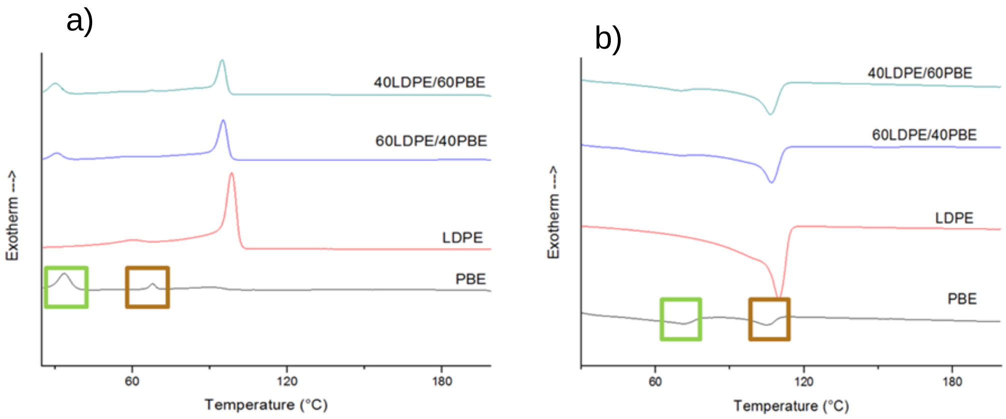

Figure V- 11 DSC curves of PBE, LDPE and PBE/LDPE blends. (a) represents the crystallization curves and (b) the melting curves. [206]

The influence of the fillers (CNT and KB nanoparticles) on the crystallinity behavior of the CPCs and CPC/PBE blends was also investigated. Both the melting and crystallization curves were displayed in Figure V- 12. It was revealed that the crystallization of LDPE –based CPCs was impacted by the KB and CNT fillers [206]. In the CPCs, a shift the crystallization temperatures to upper temperatures were observed while rising the percentage of CNT. This might be explained by the nucleation effect of the CNT nanoparticles placed at the interface [135,210,211,211,212]. The same trends of results are achieved for all the blends as shown Figure V- 12. Moreover, the addition of up to 5 wt. % of KB and CNT nanoparticles had a quadratic and no effect on crystallization temperature respectively. (Figure V- 13).

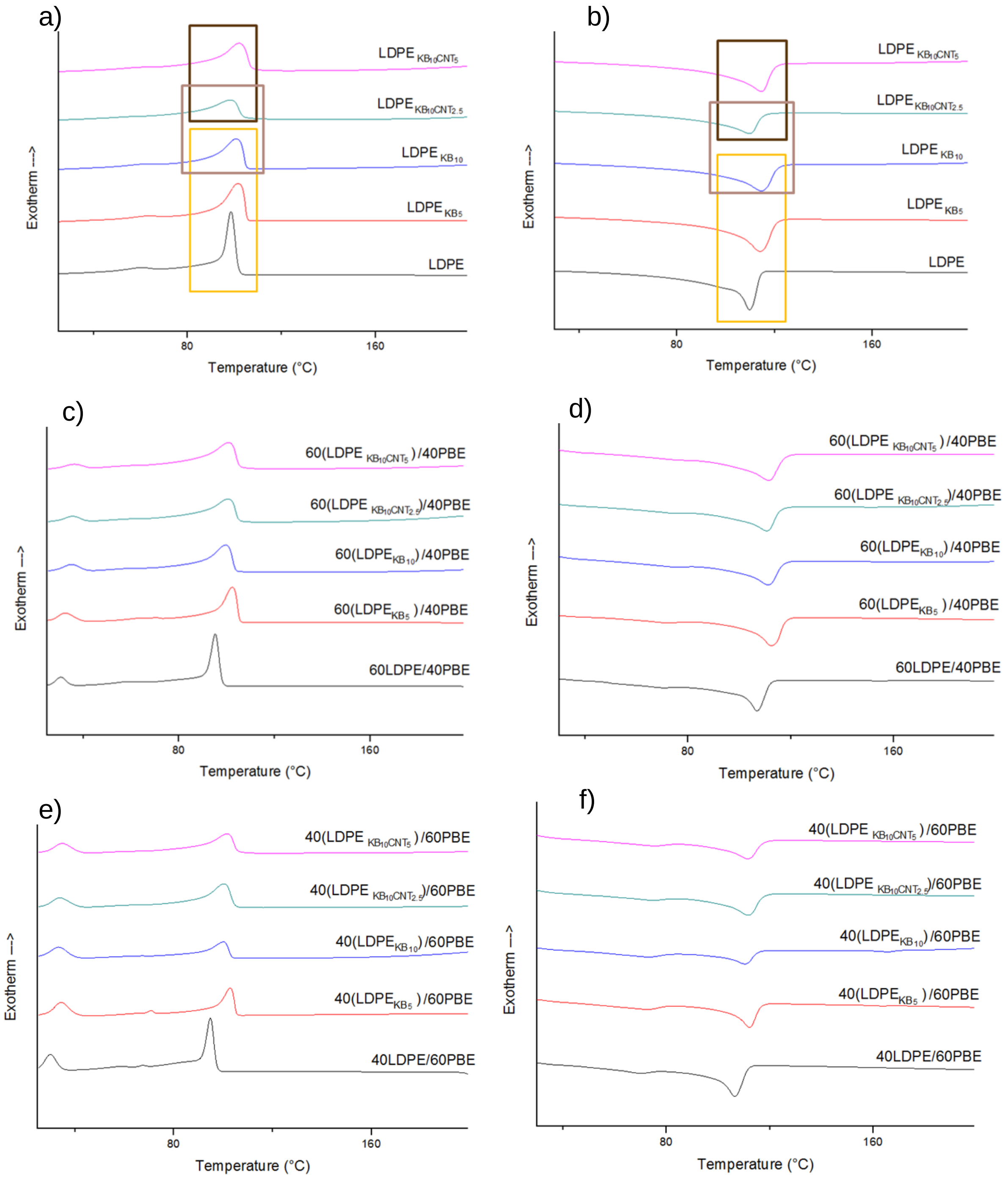

Figure V- 12 Crystallization (a-c-e) and melting (b-d-f) curves of the conducting biphasic polymers using different ratios of PBE, KB and CNT fillers [206]

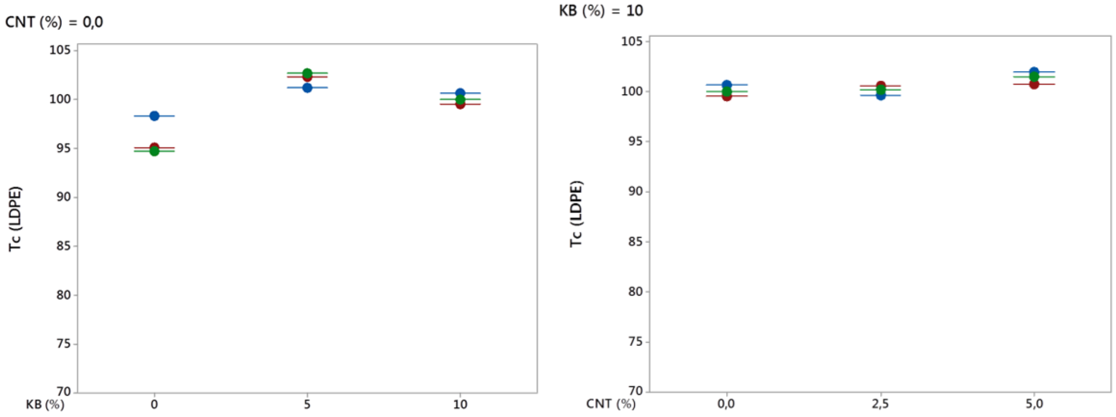

Figure V- 13 Effect of percentages of KB (on the right) and CNT (on the left) on the $\boldsymbol{T_c}$ (°C) of the conducting biphasic LDPE- based CPC/PBE blends. The blend 100%LDPE- based CPC/ 0%PBE, 60% LDPE- based CPC/ 40% PBE and 40% LDPE- based CPC/ 60%PBE are represented in blue, red and green respectively [206].

V.5.2 Rheological properties of CPCs/PBE blends

The rheology of the CPCs/PBE blends is an important property that supports our scientific knowledge in terms of processability of the blends using 3D printing process. Indeed, prior to process it through FDM process (or 3D printing), it is essential to define the melt flow index of the polymeric material. For this reason, the rheological properties of PBE, LDPE and LDPE/PBE blends of the first experiment were explored by measuring the melt flow index (MFI) value and presented in Figure V- 14. It was found that the MFI of PBE (11.7±0.1 g/10min) was more important than the one of LDPE (8.4±0.2 g/10min) [206]. The MFI values of the two blends LDPE40/PBE60 and LDPE60/PBE40 revealed that by rising the ratio of PBE the MFI increased [206]. In addition, it could be noticed that the MFI of the blends were bigger than the one of the PBE. These observations were similar than the phenomenon found by Ku and Lin [213]. It can be explained by a rise of the surface area of incompatible inter-phases of the polymeric blends [213]. In our study, biphasic polymer blends were used with an increase of the surface area between the phase of each polymer. This phenomenon might happen in some cases but remains rare.Based on the values of the MFI obtained for the different blends, the process-ability of the CPCs through 3D printing was significantly enhanced [206].

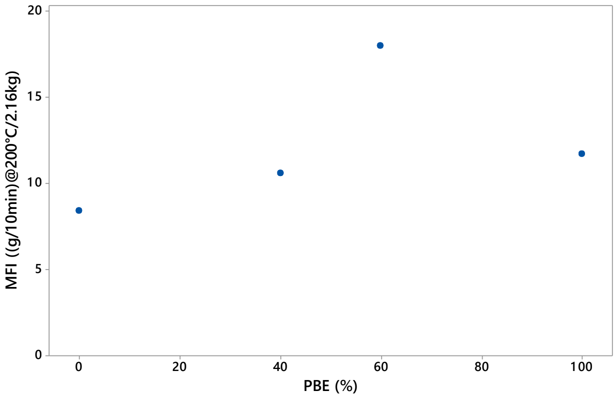

Figure V- 14 MFI (200°C/2.16kg) values: effect of PBE percentage in LDPE/PBE blends without fillers [206]

The influence of CNT and KB nanoparticles on the rheological properties was also approached and displayed in Figure V- 15. Higher MFI values of the CPCs and CPCs/PBE blends were observed with an increase of the KBs. This might be due to the creation of larger networks between the KB fillers selectively located in the biphasic blends that reduced the molecular chains of the LDPE.

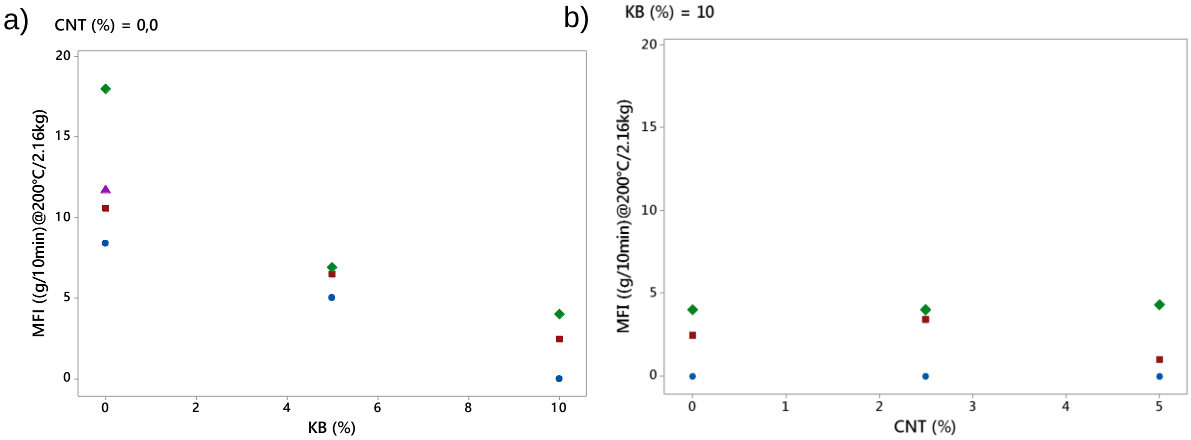

Figure V- 15 Effect of percentages of CNT (a) and KB (b) on the MFI (g/min @ 200 °C/2.16Kg) of the conducting biphasic blends depending on the percentage of PBE. The blends containing 0%, 40%, 60% and 100% of PBE are represented in blue, red, green and purple [206]

In addition, a higher ratio of CNT did not significantly impact the MFI of the CPC/PBE blends. This could be explained by the very high amount of KB nanoparticles compared to the ratios of CNT [206].

Furthermore, the melt flow index at 200°C/2.16kg and 245°C/10kg of the CPCs and CPC/PBE blends of the second design of experiment are described in Figure V - 16 and Figure V- 17. The MFI measurements were executed at two different temperatures (200 and 245°C) and with two weights (2.16 and 10kg) to compare the values of these blends with the ones of the first experiment (200°C/2.16kg) and because some of the blends were highly viscous and had to be processed with higher temperature and pressure defined by the weight.

The fixed temperature (245°C) for the MFI test was also used for the 3D printing process onto textiles [206]. At 200°C, it can be noticed that $60(\mathrm{LDPE}_{\mathrm{KB}\,16.7\,\mathrm{CNT}\,4.2})/40\mathrm{PBE}$ blends extruded in two steps showed higher MFI compared to the other blends (Figure V - 16). The observation could be due to the selective location of the fillers. Besides, the blends of the second experiment are more viscous that the one of the first experiments due to higher amount of charges dispersed in the LDPE and PBE matrices selectively located (Figure V- 15 and Figure V - 16) [206].

In addition, in the case of the use of 2-step extrusion process to manufacture the biphasic blends the fillers were selective located with no noticeable transfer to the PBE phase (Figure V- 17) leading to a rise of their MFI of about 20% compared to the 1-step extrusion. However, the MFI of the 1-step extruded $80(LDPE_{KB\ 12.5\ CNT\ 3.1})/20PBE$ blend revealed to be inferior to the one of $LDPE_{KB\ 10\ CNT\ 2.5}$ [206].

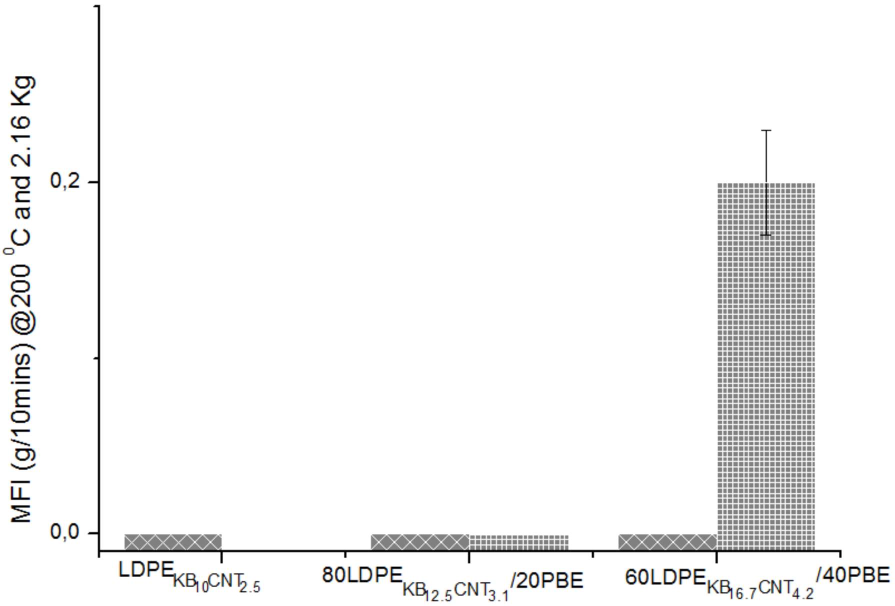

Figure V - 16 *MFI (g/min @ 200 °C/2.16Kg) of the conducting biphasic blends using 1-step (*▨*)or 2-step (*▦*) extrusion* [206]

This result might find an explanation in the dispersion and selective location of higher quantity of conductive charges that considerably blocked the mobility of molecular chains and thus, reduced its MFI. An increase of the ratio of PBE led to rise the MFI. The MFI value of the $60(LDPE_{KB\ 15.6\ CNT\ 3.9})/40PBE$ extruded through 2-step mode is also the highest (Figure V- 14) due to the higher volume of PBE in the blend and no migration of fillers to the PBE phase (Figure V- 9) [206].

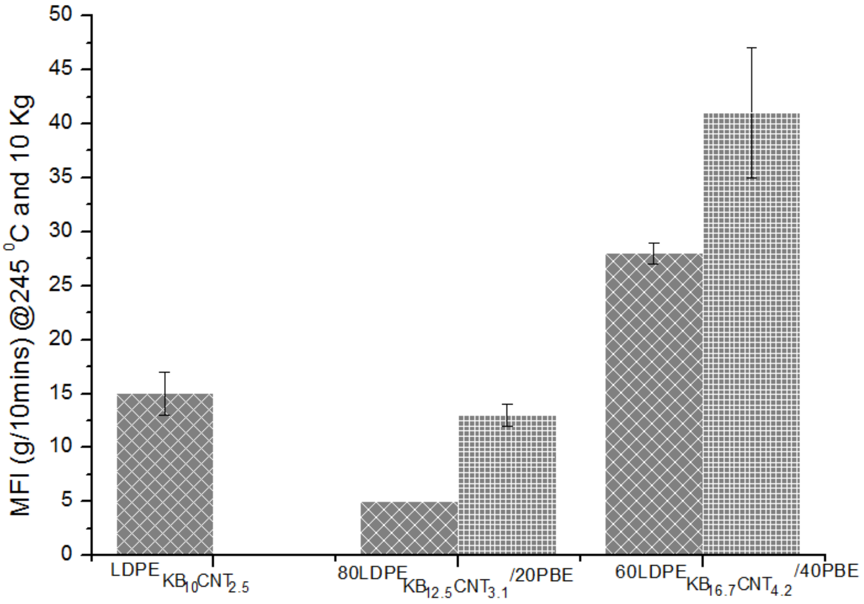

Figure V- 17 *MFI (g/min @ 245 °C/10Kg) of the conducting biphasic blends using 1-step (▨)or 2-step (▦) extrusion* [206]

V.6 Electrical conductivity of CPCs/PBE blends

V.6.1 General findings

The electrical resistance (or conductivity) is one of the fundamental properties of the CPCs and CPC/PBE blends that need to optimize in order for the blends to be used in functional textiles field. The main idea was to develop conducting biphasic blends which only contain co-continuous phases in order to reduce the percolation threshold and use lower quantity of conductive fillers [33,209]. First, the quantity and dispersion of both fillers greatly impacted the electrical conductivity. It was demonstrated that the rise of the KB and CNT percentages led to enhance the electrical conductivity as described in Figure V- 18 [206].

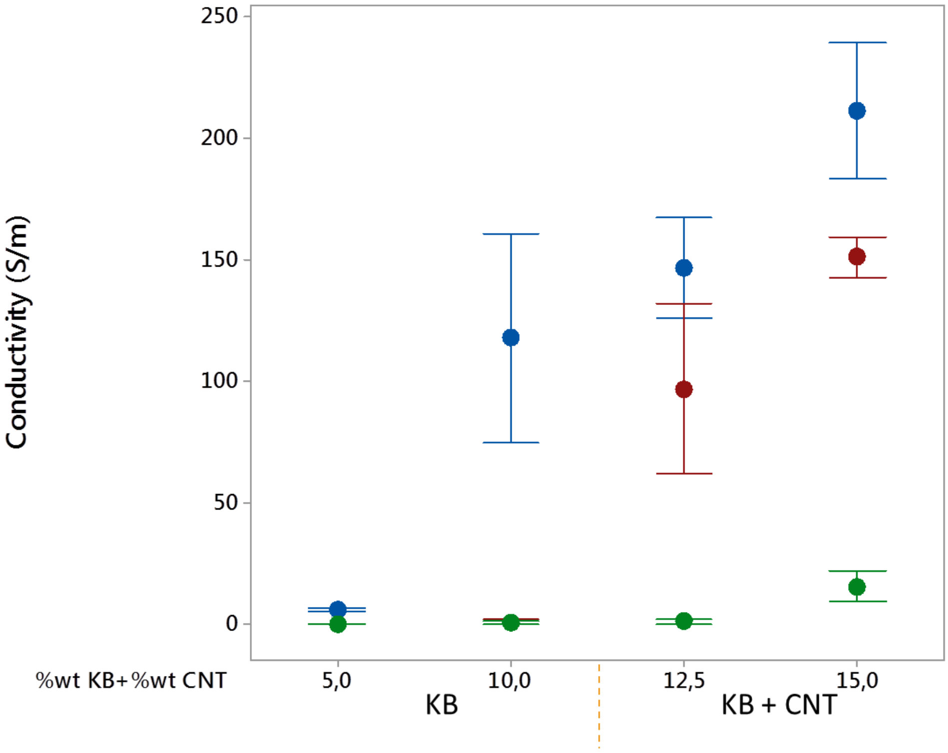

Figure V- 18 Electrical conductivity (S/m) as a function of KB and CNT ratios in conducting blends. The CPCs without PBE are presented in blue, the 60CPCs/40PBE blends in red and the 40CPCs/60PBE blends in green. [206]

This is mainly due to the synergistic effect explained by the formation of inter-networks between the conductive charges. At a certain KB and/or CNT filler contents, the percolation threshold might have been reached and the CPC/PBE blends started to be conductive. In addition, in the LDPE/PBE blends, a diminution of the electrical conductivity was observed with an increase of the PBE ratios. The lowest electrical conductivity was obtained in the blends which only contain KB fillers because of the nodular and fibrillary structures of the blends (Figure V- 7) [206]. A different dispersion and distribution of the fillers in a bigger volume of biphasic blends and different morphology of the blends could modify the percolation threshold. A double percolation happens : a percolation of fillers and the one of the CPC phases [206].

V.6.2 Fillers' dilution phenomenon in the immiscible polymer blends

With the CPC/PBE blends of the first experiment, the comparison between the CPC and CPC/PBE blends showed that with an increase of PBE ratio the percolation threshold changed because of the dilution of fillers in a bigger volume of the biphasic blends. Therefore, the global (i.e. real) percentage of KBs and CNTs in the blends determine the electrical conductivity value (Figure V- 19 and Figure V- 20) [206]. Indeed, a drastic decrease of the electrical conductivity was revealed in the blends in which there is a predominance of PBE compared to the KB and CNT- filled LDPE as defined in Figure V- 20. Therefore, it is important for the fillers to be at the interface instead of in one of the phase in order to avoid this dilution phenomeon.

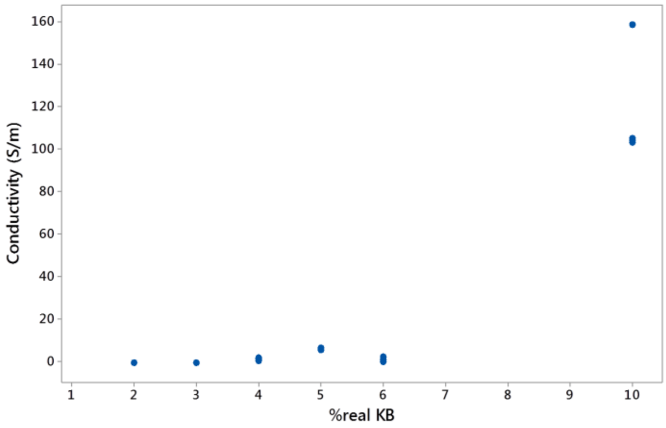

Figure V- 19 Electrical conductivity (S/m) as a function of the real KB percentage in the biphasic blends

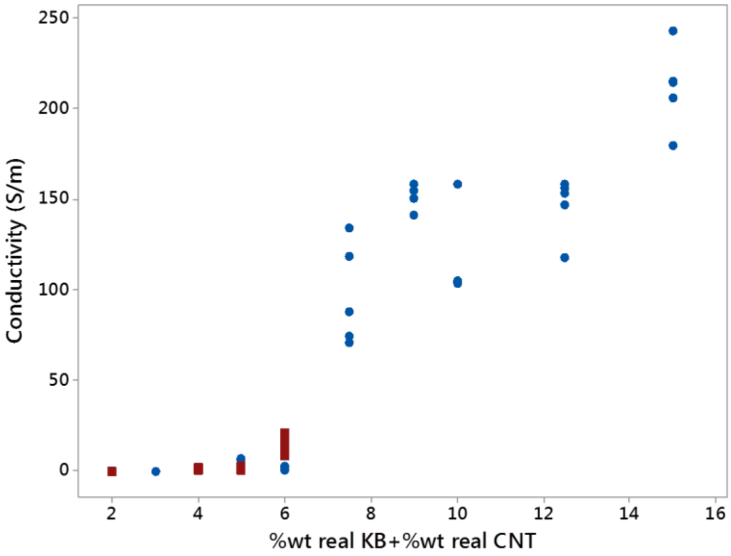

Figure V- 20 Electrical conductivity (S/m) as a function of the real KB and CNT percentages in the biphasic blends with a dominance of LDPE (in blue) and dominance of PBE (in red) [206]

In the second experiment, the global amount of KBs and CNTs in the CPC/PBE blends was 10 and 2.5 wt% respectively, to improve the electrical conductivity. Thus, prior to the extrusion process, a higher and precise amount of KBs and CNTs was incorporated mechanically mixed in LDPE (for the 1-step extrusion) and in LDPE and PBE (for the 2-step extrusion). In other words, the quantity of CNT and KB (in wt%) incorporated into the LDPE was calculated depending on the ratios of CNT and KB –filled LDPE and PBE added to the biphasic blends. The desired final weight percentages of CNT and KB were equal to 2.5wt% and 10wt% respectively. Therefore, the filler ratios in the blends were maintained constant in this experiment. It was found that the electrical conductivity of these blends (second design of experiment) was similar or higher to the 10wt%KB and 2.5%CNT- filled LDPE [206]. These findings are explained by the selective location of KBs and CNTs in the blends and sometimes migration of CNTs in some blends that could enhance the electrical conductivity. The impact of the extrusion scenarios on the electrical conductivity [206].

V.6.3 Influence of extrusion scenarios on the electrical conductivity

The influence of the extrusion scenario (1-step and 2 step extrusion) on the electrical properties of the CPC/PBE blends was investigated for the conducting biphasic blends and presented in Figure V- 21. Compared to the 2–step extrusion, the 1-step scenario led to a better electrical conductivity in the case of all the blends. It could be explained by the formation of additional networks between the CNT and KB nanoparticles [206]. The spreading and interconnections between the fillers, impact the electrical paths within the materials. Indeed, it might be explained by the location of the fillers in both phases in the case of the 1-step extrusion leading to change the morphology of the blends. However, the electrical conductivity of the conductive monofilament is not the only crucial property for the development of flexibility and highly conductive 3D-PPOT materials. The flexibility and the mechanical (stress and strain) and electrical properties of the 3D-PPOT remain important.

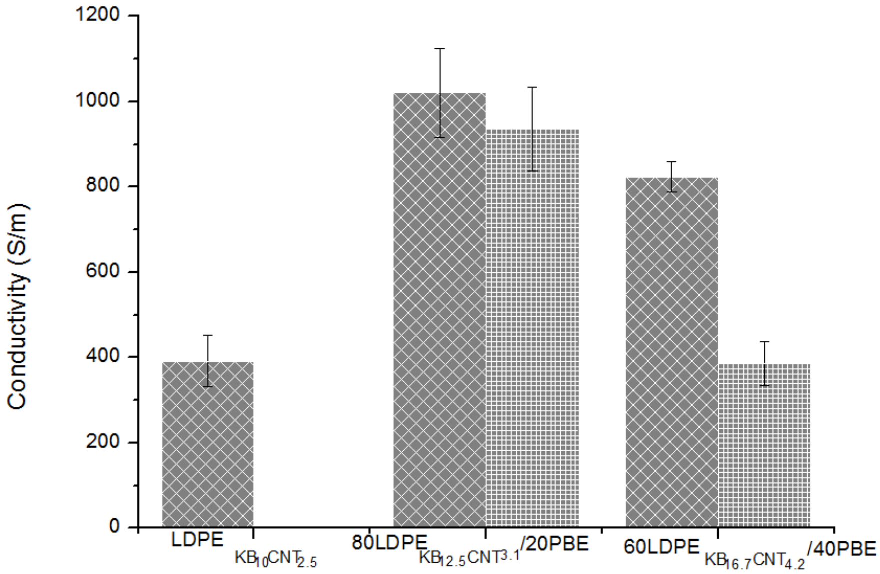

Figure V- 21 *Electrical conductivity (S/m) of the conducting biphasic blends produced by a 1-step (▨)or 2-step (▦) extrusion* [206]

Therefore, after presenting the properties of the CPCs and CPC/PBE blends, in the next sub-section the mechanical and electrical properties of the 3D-PPOT materials were discussed to evaluate the enhancement of their flexibility and tensile properties.

V.7 Improvement of the 3D-PPOT material deformation and tensile properties

V.7.1 Findings on deformation enhancement

The flexibility of the 3D-PPOT materials using the CPC/PBE blends of the second experiment was examined by measuring the permanent and elastic deformations and its improvement was accessed by comparing them to the values of the CPC without PBE. Previously, in Chapter IV, it was demonstrated that the permanent and elastic deformations of 3D-PPOT materials made of 2.5wt% CB – filled PLA were three times lower than the ones of the woven fabrics [121]. As a reminder, the deformability of the 3D-PPOT materials could be enhanced if the PLA is replaced by the LDPE which has a lower glass temperature. Nevertheless, similar to the PLA, the addition of the fillers in LDPE highly reduces the mobility of the molecular chains. For this reason, the development of LDPE- based/PBE blends, with co-continuous phases and global KB and CNT contents of 10 wt% and 2.5wt% respectively, was preferred. The findings revealed that the elastic and permanent deformations of CNT and KB –filled LDPE/PBE blends were more than ten times higher than the CNT and KB –filled LDPE and the elastic deformation of the blends was close to the ones of the original woven fabric (Figure V- 22 and Figure V- 23) [206]. Additionally, the permanent deformation of the blends was about twice inferior to the one of the woven fabric, which demonstrated that the blends had a higher dimensional stability than the fabric prior to FDM process. Similar trend of results between the 1-step and 2-step extrusions was obtained when printing either in the cross direction or the machine direction.

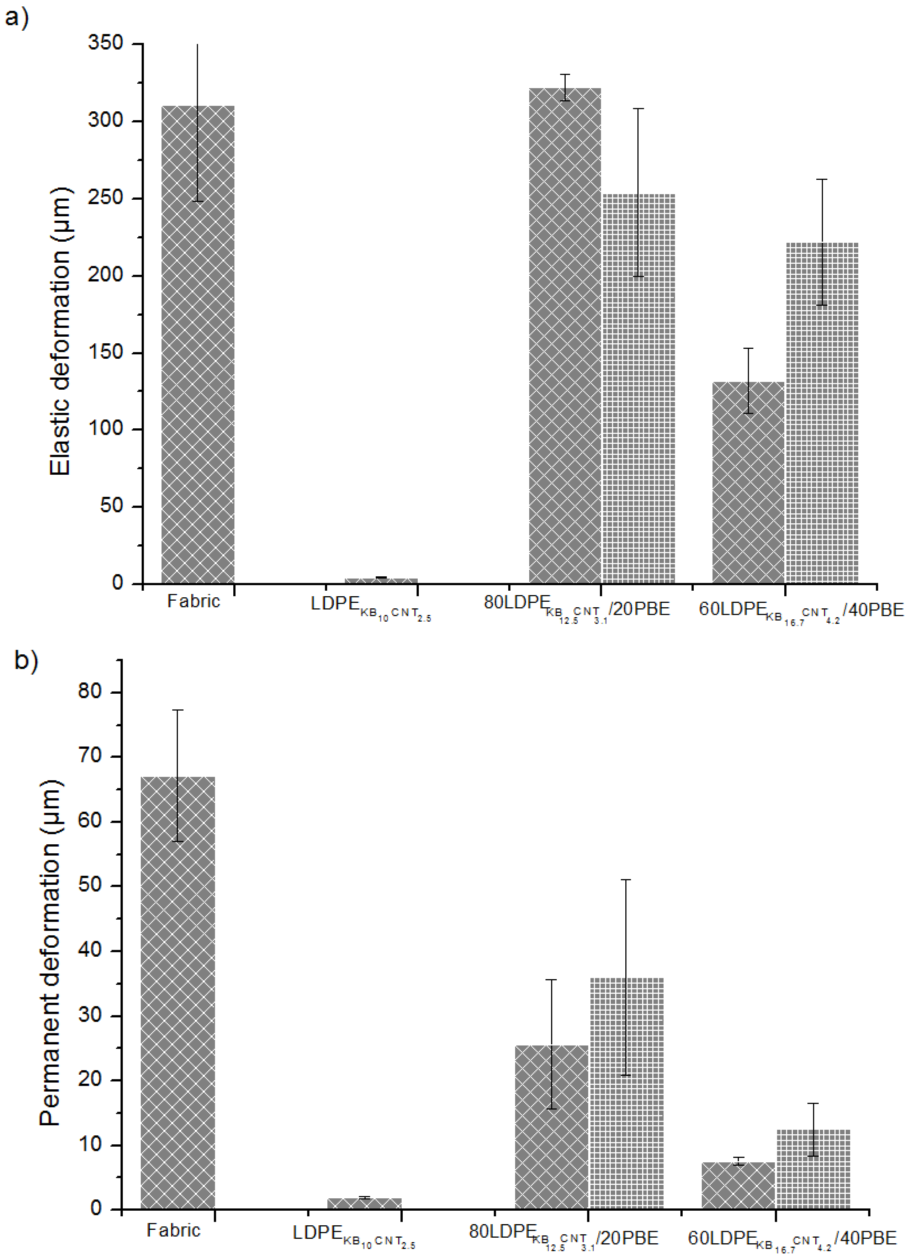

Figure V- 22 *Elastic (a)* [206] *and permanent (b) deformations (µm) of the 3D-PPOT materials made of conducting biphasic blends produced by a 1-step (▨)or 2-step (▦) extrusion printing on PET fabric in the cross direction*

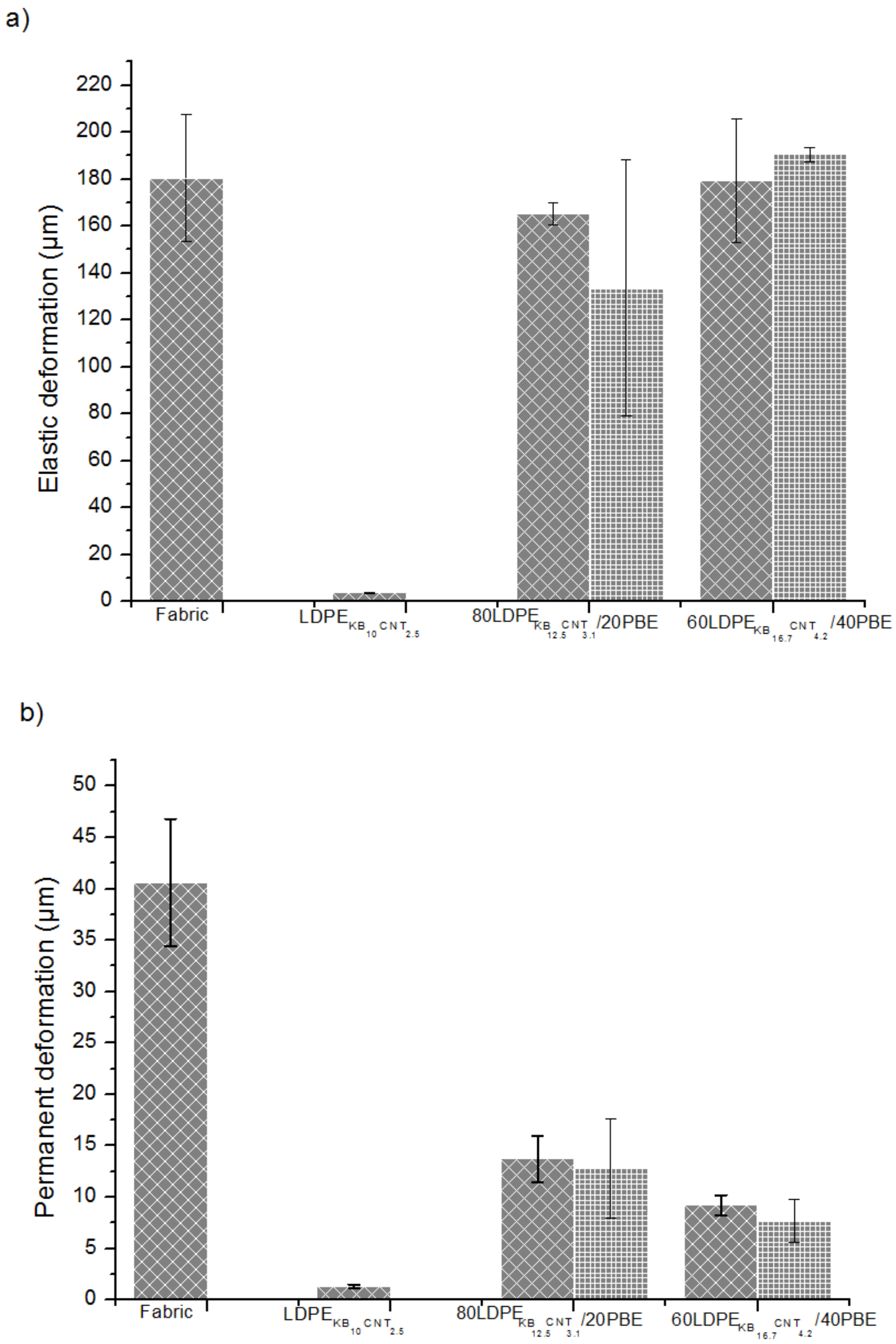

Figure V- 23 *Elastic (a) and permanent (b)* [206] *deformations (µm) of the 3D-PPOT materials made of conducting biphasic blends produced by a 1-step (▩)or 2-step (▦) extrusion printing on PET fabric in the machine direction*

A higher ratio of PBE led to increase the elastic deformation and decrease the permanent deformation of the 3D-PPOT materials using CNT and KB-filled LDPE/PBE blends. In general, the 2-step extrusion process conferred similar or better elastic and permanent deformations compared to the 1-step process.

V.7.2 Findings on the improvement of the tensile properties

The tensile properties of the 3D-PPOT materials made of the CPC and CPC/PBE blends of the second experiment, including the maximum stress and strain at rupture, were explored in the machine and cross directions. As a reminder, the printing directions (cross and machine) describe the orientation of the woven material during the FDM process. Also, the impact of the extrusion scenarios on the maximum stress and strain at rupture of the 3D-PPOT was studied [206].

On one hand, the findings are shown in Figure V- 24. In both directions, the stress of the 3D-PPOT materials made of the various blends revealed to be same or higher than the one of the CPC. In general, the stress was improved when applying a 2-step extrusion in comparison with a 1-step extrusion. Based on the results, the highest stress at rupture in the machine direction was obtained for the $60(LDPE_{KB\ 16.7\ CNT\ 4.2})/40PBE$ blend using the 2-step extrusion. This finding could be explained by its high MFI value (Figure V-17) leading to a better penetration throughout the textile structure and entanglement with the fibers located on the surface of the PET woven fabric. The fibers might have enhanced the stress at rupture of the material [206]. Indeed, the polymer chains might have been slithly degraded by the second extrusion process and the change in the location of the fillers reducing the macromolecular chains of the polymers and that led to a lower viscosity.

a) Cross direction

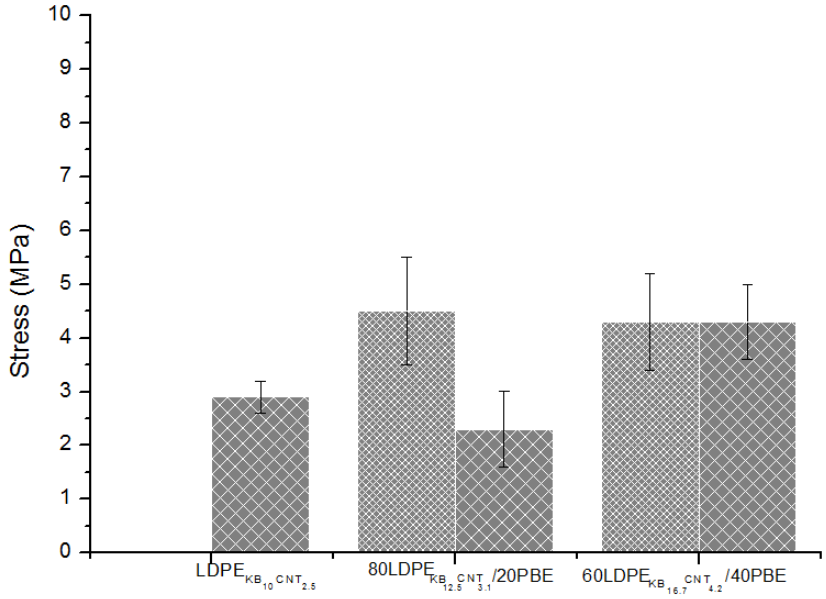

b) Machine direction

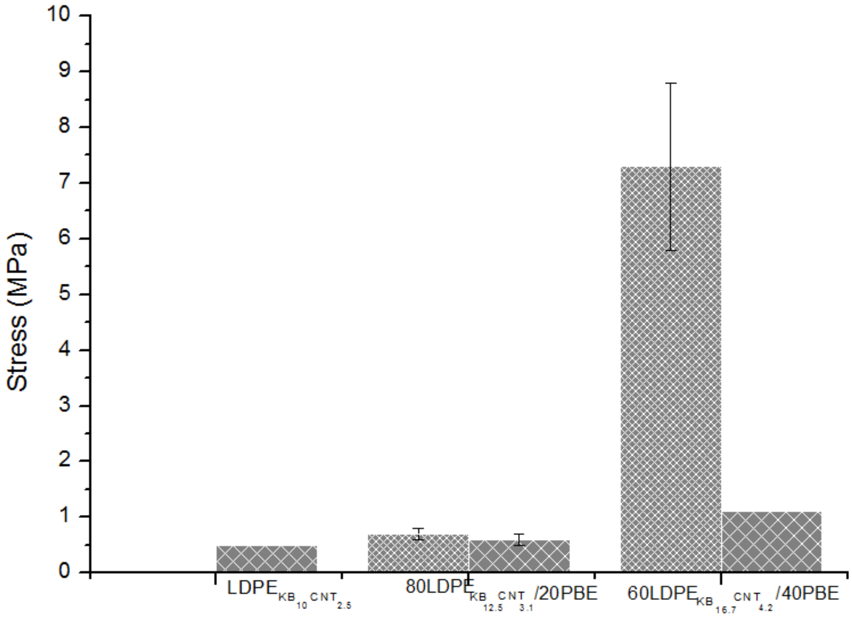

Figure V- 24 Stress (MPa) of the conducting biphasic blends produced by a 1-step (▨) or 2-step (▦) extrusion, 3D printed onto textile materials in the cross (a) and machine (b) directions of the fabric [206]

On the other hand, the maximum strain at rupture of the 3D-PPOT materials made of the various blends was better than the one of the original fabric (Figure V 25). The selective location of the fillers in the LDPE phase and at the interface (V.3) and not in the PBE allowed to keep the mechanical properties, for instance, its elasticity and flexibility conferred by its soft segments. In addition, the strain at rupture was found to be affected by the 1-step extrusion, i.e. the 3D-PPOT manufactured in 1-step extruded CPCs/PBE blends elongated less than the 2-step extruded CPCs/PBE blends. This result can be explained by the migration of the fillers to the elastomer's phase (V.3) [206].

a) Cross direction

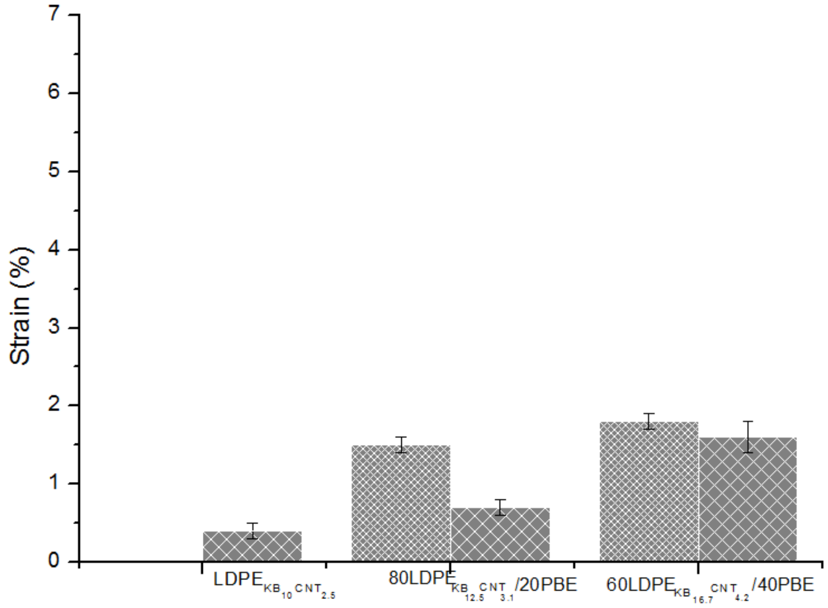

b) Machine direction

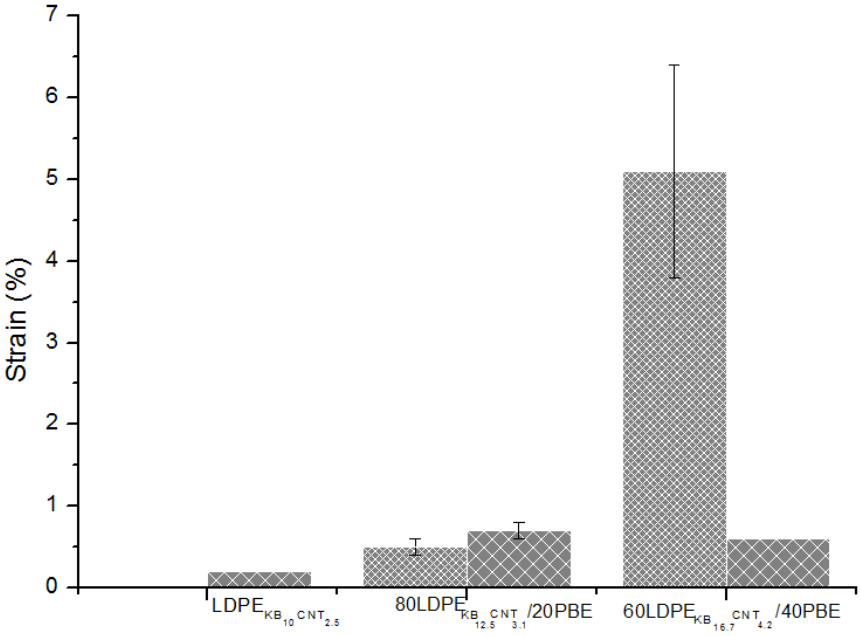

Figure V 25 *Strain (%) of the conducting biphasic blends produced by a 1-step (▨)or 2-step (▦) extrusion 3D printed onto textile materials in the cross (a) and machine (b) directions of the fabric* [206]

V.8 *Improvement of electrical properties of 3D-PPOT materials*

The electrical surface conductivity of the 3D-PPOT materials made of the CPC and CPC/PBE blends of the second experiment was determined and described in Figure V- 26. The same trends of findings were obtained in the case of monofilaments (V.6.1) and 3D-PPOT materials. Indeed, the surface electrical conductivity of $60(\mathrm{LDPE}_{\mathrm{KB}\ 16.7\ \mathrm{CNT}\ 4.2})/40\mathrm{PBE}$ and $80(\mathrm{LDPE}_{\mathrm{KB}\ 12.5\ \mathrm{CNT}\ 3.1})/20\mathrm{PBE}$ blends was higher than the one of $\mathrm{LDPE}_{\mathrm{KB}\ 10\ \mathrm{CNT}\ 2.5}$. Finally, the manufacturing of the blends through 1-step extrusion demonstrated an enhancement of the electrical conductivity in comparison with the 2-step extrusion process. This result can also be explained by the creation of more conducting networks due to the migration of the CNT fillers in the LDPE (V.5) [206]. The rheological findings formerly described in part V.5.2 showed that the MFI of the 1-step extrusion is lower than the one of the 2-step extrusion i.e. the blends produced using the 1-step method is more viscous. Therefore, during the deposition process of this monofilament might have led to obtain a thicker and more compact 3D printed structure; and thus, the electrical conductivity was better.

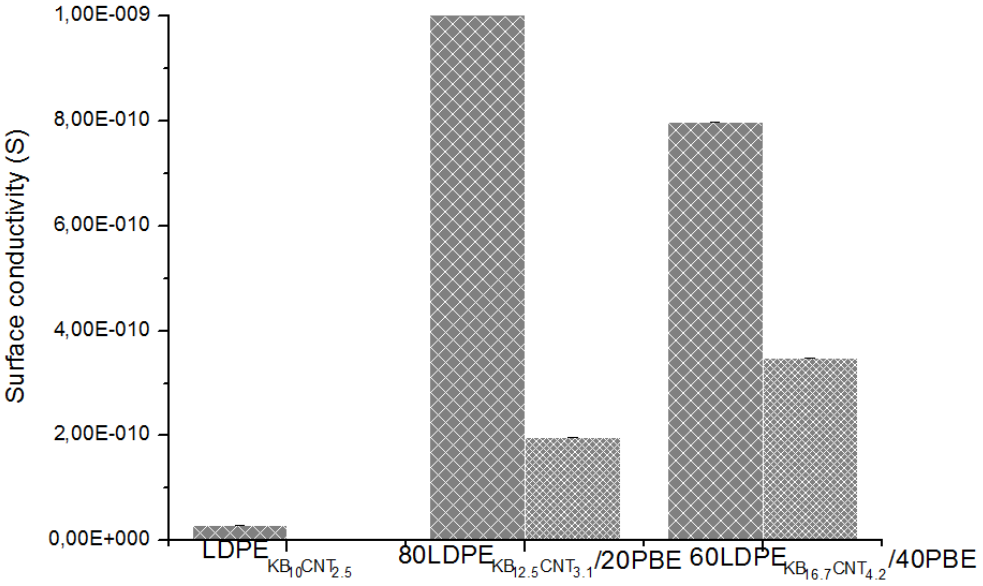

Figure V- 26 Surface conductivity (S) of the 3D-PPOT materials made of conducting biphasic blends produced by a 1-step and 2-step extrusions [206]

V.9 Conclusion

In this chapter, immiscible and biphasic CNT and KB - filled LDPE/PBE blends at different percentages were developed to enhance the flexibility, stress and strain at rupture and electrical conductivity of 3D-PPOT materials. These properties can be enhanced only if two conditions are respected: the co-continuity of both the thermoplastic (i.e. LDPE) and the elastomer (i.e. PBE) phases and the selective location of the conductive fillers in the thermoplastic phase (i.e. LDPE) or at the interface of the two immiscible polymers (i.e. LDPE and PBE). Indeed, these requirements are necessary to guarantee the creation of a highly structured network between the KB and CNT fillers while preserving the flexibility and elasticity of the PBE phase given by its soft segments.

CNT and KB filled – LDPE/PBE following two different extrusion scenarios, named the 1-step and 2-step, were manufactured. The 1-step extrusion consisted in mechanically dispersed the conductive fillers in both LDPE and PBE in one step while the two-step one described the dispersion and extrusion of conductive fillers in LDPE followed by blending and extrusion of the LDPE- based CPC with PBE.

First of all, the blends manufactured through 2-step melt processing, both the CNT and KB nanoparticles were found to be preferentially located at the LDPE/PBE interface and in the LDPE phase. This location was partially predicted through specific models and confirmed by SEM and TEM images. Consequently, the extensions of both the LDPE and PBE phases over a much larger composition range are noticed, allowing the co-continuity of the phases. Thus, with these blends, the viscosity and electrical conductivity monofilament form, the strain and stress, the deformation under compression and the electrical conductivity of the 3D-PPOT materials were significantly enhanced compared to the KB and CNT-filled LDPE CPCs.

Finally, this work demonstrated interesting potential in developing conductive biphasic blends that could be used in the domain of 3D printing of polymer onto textiles with greater mechanical and electrical properties than the ones already existing.

Conclusion and future work

As part of the European program named Sustainable Management and Design for Textiles (SMDTex), this thesis was the follow-up research work of the thesis Dr. Sanatgar untitled "FDM 3D printing of conductive polymer nanocomposites: A novel process for functional and smart textiles" and defended in 2019.

This thesis aims at developing functional textiles by applying a novel and reliable process named FDM (or 3D printing) process of polymers onto textile materials. As shown in the Chapter I, this technology limits the unnecessary use of water, chemicals, energy and minimizes the waste of raw materials (monofilament and granulates), allows free customization of patterns onto textiles and diminishes the textile supply chain. However, many challenges remain present in the development of functional textiles using this technique, for instance, their final mechanical properties that should be at least same or better than the ones the textile materials and the scalability and industrialization of the 3D printing process onto textiles at production level.

The entire research work presented in this thesis supports to give answers to the two research questions already raised in Chapter I:

3) What are the most impacting textiles' properties on the mechanical properties (adhesion, tensile, abrasion, wash ability, deformation)?
4) How can we enhance the adhesion and the flexibility of the 3D-PPOT materials while maintaining or increasing its electrical conductivity?

The first research question was answered in the Chapter III and IV. In these chapters, the properties of the PET woven fabrics considered were the weft density, the fabric direction, the pattern, the roughness, the porosity (i.e. the mean pore size), the thermal conductivity, and the elastic, permanent and total deformations characterized as defined in Chapter II.

On one hand, in chapter III, it was shown that the weft density, the pattern, the fabric direction, roughness coefficient, the mean pore size and thermal conductivity highly impacted the adhesion properties of the 3D printed polymers onto textiles. Indeed, greater adhesion was obtained with more porous, rough PET woven materials with low thermal conductivity. Statistical models between the adhesion and the textile properties (roughness, mean pore size and thermal conductivity) were successfully developed. This phenomenon was justified by the mechanical interlocking theory described in Chapter I. Besides, the adhesion strength of 3D-PPOT materials is influenced by the standardized washing process and the 3D-PPOT that had better adhesion properties before washing process resist better.

On the other hand, the tensile, abrasion and deformation properties of the 3D-PPOT materials were summarized in the Chapter IV. In general, the weft density and the fabric direction influenced the three properties. The tensile and deformation of the 3D-PPOT were found to be lower than the ones of the textile

materials while the abrasion strength is higher. The tensile properties including the stress and strain at rupture of 3D-PPOT materials were enhanced by printing in the cross direction on PET woven fabrics with low weft density. In addition, the stress at rupture is affected by the washing process. Additionally, the elastic, permanent and total deformations of 3D-PPOT materials are very low compared to the textile materials, i.e. the materials are stiffer and dimensionally stable. Statistical models between the stress at rupture of the 3D-PPOT materials and the elastic and permanent deformations were successfully developed showing a quadratic effect. In the case of abrasion resistance, the end point and the weight loss of the 3D-PPOT materials were influenced by the weft density, the printing direction and the weave pattern. Fused polymer deposited onto denser PET plain woven presented the best abrasion resistance of 3D-PPOT materials. The abrasion resistance significantly influenced the electrical properties of the 3D-PPOT.
It was demonstrated that higher adhesion resistance provoked higher tensile properties but lower abrasion resistance. For the platform temperature higher than the crystallization temperature, adhesion properties of 3D-PPOT materials are improved while the abrasion and tensile properties are affected.

The answers of the second question could be found in the Chapter III and V. First, several solutions were given in Chapter III to enhance the adhesion resistance of the 3D-PPOT materials. The atmospheric plasma treatment onto PET woven fabrics and the grafting of acrylic acid process applied onto PLA monofilament and PET woven materials prior to the application of PSA and PU film adhesives were the two processes suggested in this thesis. The improvement is noticed after using both methods, however, only the grafting method with adhesives demonstrated significant changes. The application of PU film adhesive onto acrylic acid grafted PET woven showed the best adhesion resistance. The use of PET non-woven materials demonstrated better adhesive than the PET woven fabrics before and after atmospheric plasma treatment due to higher porosity and roughness.
In Chapter V, the research work on the improvement of the flexibility and electrical properties of the 3D-PPOT materials was presented. Indeed, in previous studies presented in Chapter I and Chapters III and IV of this thesis, PLA – based monophasic CPCs were used. The final 3D-PPOT materials were brittle and not flexible at all. For these reasons, novel immiscible and biphasic CNT and KB - filled LDPE (thermoplastic) /PBE (elastomer) blends at different percentages were developed to improve the flexibility and electrical properties. In order to guarantee optimal properties while using low amount of fillers, the co-continuity of the phases and the selective location of the fillers are important. The extrusion process has to be executed in two steps, by first mixing the fillers to the LDPE and then blend the CPCs with the elastomer with a ratio of 60/40 to obtain the best deformability of the materials while demonstrating high electrical properties. For most of the blends developed the CNT and KB were found to be located at the interface and both at the interface and in the LDPE respectively. These results were in accordance with the ones obtained through theoretical models. The deformation, the tensile and electrical properties were significantly improved for the blends having both the co-continuous phases and selective located fillers.

The entire thesis work reveals a great potential in the development of non-conductive and conductive 3D-PPOT materials with greater deformation and tensile properties. Further research in the following areas has to be highlighted:

- Development of the functional materials (sensors, antennas, etc.) using the flexible biphasic blends which are the best mechanical and electrical properties
- Utilization of the 3D-Printing onto textiles for several applications in textile domain others than functional textiles.
- Modification of the 3D printer to be used in large scale
- Demonstration of the same properties of 3D-PPOT materials in large scale

Appendices

List of Tables

List of Figures

Appendix A: XPS analysis

The XPS results of the untreated and treated PET fabric and treated and untreated conductive and non-conductive PLA printed layer are presented in Table A- 4, **Table A- 6** and **Error! Reference source not found.**. Three peaks could be observed at the binding energies of 285.0, 286.7 and 289.1 eVin the C 1s core-level spectrum of untreated and treated PET (**Error! Reference source not found.**) , which correspond to the C-C/C-H, C-O and O-C=O functional groups, respectively. No significant increase in aliphatic carbon content (285.0 eV) was seen in our data. Thus, we could not demonstrate the presence of grafted acrylic acid on PET fabric. Additionally, there would be an expected increase in the intensity of the O-C=O peak relative to the C-O peak in response to grafting of acrylic acid, as there is no C-O environment in acrylic acid, but there is in PET. If we compare the treated and untreated samples, there is an increase in the O-C=O to C-O ratio but this difference is minor. Besides, the following decomposition of the O 1s peaks is detected and various peaks presented in **Table A- 6**can be observed: at 532.1 eV as O-Si, O=Cand 533.6 eV as O-CO oxygen. . The low intensity of the peak at 530.5 eV, combined with the slight sodium contamination of the samples suggests that it is probably due to deprotonated hydroxyl groups with a sodium counterion. Additionally, the amount of solution adhesive or the acrylic acid might have been introduced at a too low onto the textile fabrics and thus, the effect of the grafting of the acrylic acid could hardly be observed.

In the case of non-conductive and conductive PLA printed tracks, the evolution of the concentration of carbon and oxygen showed that the effect of the grafting process was removed after 3D printing (Table A- 4, Table A- 6 and **Error! Reference source not found.**). It might be due to the high temperature and shear force applied to the treated conductive and non-conductive PLA monofilaments when going through the extruder during the 3D printing that degrade the applied coating.

Table A- 4 Detailed atomic concentration (%) determined by XPS for treated and untreated PET fabric with and without adhesive, for treated and untreated non-conductive and conductive PLA and for Polyurethane (PU) film

	Concentration /at.%									
Sample	**Na 1s**	**Fe 2p**	**F 1s**	**O 1s**	**Cd 3d**	**N 1s**	**K 2s**	**Ca 2p**	**C 1s**	**Si 2p**
Untreated PET fabric	0.26 ± 0.12	-	-	25.35 ± 0.21	-	0.07 ± 0.12	-	0.03 ± 0.06	72.94 ± 0.29	1.36 ± 0.06
Treated PET	0.19 ± 0.13	-	-	24.89 ± 0.66	-	0.11 ± 0.13	-	-	73.86 ± 0.7	0.95 ± 0.05
Treated PET + Adhesive	0.21 ± 0.04	0.02 ± 0.04	0.45 ± 0.19	22.75 ± 0.06	0.02 ± 0.02	0.28 ± 0.13	-	0.04 ± 0.08	73.17 ± 0.26	3.05 ± 0.12
Untreatednon-conductive PLA	0.12 ± 0.11	-	-	32.71 ± 0.76	-	0.28 ± 0.19	0.17 ± 0.15	-	63.52 ± 0.71	3.19 ± 0.27
Untreated conductive PLA	0.03 ± 0.06	-	-	30.46 ± 0.36	-	0.53 ± 0.27	-	-	65.01 ± 0.43	3.97 ± 0.13
Treated non-conductive PLA	-	-	-	32.93 ± 1.95	-	0.44 ± 0.16	-	-	63.55 ± 1.53	3.08 ± 0.36
Treated conductive PLA	-	-	-	32.43 ± 2.12	-	0.28 ± 0.07	-	-	64.2 ± 2.18	3.08 ± 0.13
PU	0.23 ± 0.12	-	-	20.18 ± 0.79	-	0.32 ± 0.1	-	-	78.55 ± 1.16	0.71 ± 0.35

Table A- 5 Detailed carbon 1s component, binding energy FWHM and atomic concentration for treated and untreated PET fabric with and without adhesive, for treated and untreated non-conductive and conductive PLA and for Polyurethane (PU) film

	Carbon 1s			
Sample	**Component**	**Binding energy /eV**	**FWHM /eV**	**Concentration /at. %**
Untreated PET fabric	C-C	285 ± 0	1.11 ± 0.01	47.32 ± 0.28
	C-O	286.7 ± 0	1.11 ± 0.01	13.79 ± 0.1
	O-C=O	289.1 ± 0	0.83 ± 0.02	8.95 ± 0.35
	π*←π	291.4 ± 0.2	3.55 ± 0.9	2.86 ± 0.67
Treated PET	C-C	285 ± 0	1.08 ± 0.02	47.35 ± 0.85
	C-O	286.7 ± 0	1.08 ± 0.02	14.12 ± 0.19
	O-C=O	289.1 ± 0	0.82 ± 0.03	9.64 ± 0.14
	π*←π	291.5 ± 0.1	2.85 ± 0.14	2.75 ± 0.22
Treated PET + Adhesive	C-C	285 ± 0	1.15 ± 0.01	54.68 ± 0.34
	C-O	286.8 ± 0	1.15 ± 0.01	10.37 ± 0.05
	O-C=O	289.2 ± 0	0.83 ± 0.01	6.79 ± 0.1
	π*←π	291.9 ± 0.1	2.32 ± 0.32	1.33 ± 0.23
Untreatednon-conductive PLA	Unknown	284.3 ± 0	1.2 ± 0.05	23.77 ± 1.65
	C-C	285 ± 0	1.2 ± 0.05	13.23 ± 0.35
	OC-C-O	286.9 ± 0	1.12 ± 0.01	13.25 ± 0.35
	O-C=O	289 ± 0	1.08 ± 0.04	13.27 ± 0.35
Untreated conductive PLA	Unknown	284.3 ± 0	1.1 ± 0.02	29.81 ± 0.79
	C-C	285 ± 0	1.1 ± 0.02	11.72 ± 0.13
	OC-C-O	286.9 ± 0	1.14 ± 0.03	11.73 ± 0.12
	O-C=O	288.9 ± 0	1.07 ± 0.02	11.75 ± 0.12
Treated non-conductive PLA	Unknown	284.4 ± 0	1.24 ± 0.06	22.32 ± 4.22
	C-C	285 ± 0	1.24 ± 0.06	13.73 ± 0.9
	OC-C-O	286.9 ± 0	1.13 ± 0.01	13.75 ± 0.9
	O-C=O	289 ± 0	1.08 ± 0.03	13.77 ± 0.9
Treated conductive PLA	Unknown	284.4 ± 0.1	1.2 ± 0.1	24.07 ± 4.94
	C-C	285 ± 0	1.2 ± 0.1	13.36 ± 0.93
	OC-C-O	286.9 ± 0.1	1.08 ± 0.02	13.38 ± 0.93
	O-C=O	289 ± 0.1	1.05 ± 0.01	13.4 ± 0.93
PU film	C-C	285 ± 0	0.92 ± 0.03	39.15 ± 0.9
	C-N	285.8 ± 0	1.24 ± 0.07	1.35 ± 0.44
	C-O	286.3 ± 0	0.92 ± 0.03	36.7 ± 1.42
	N-C=O	288.9 ± 0.1	1.24 ± 0.07	1.35 ± 0.44

Table A- 6 Detailed oxygen 1s component, binding energy FWHM and atomic concentration for treated and untreated PET fabric with and without adhesive, for treated and untreated non-conductive and conductive PLA and for Polyurethane (PU) film

	Oxygen 1s			
Sample	**Component**	**Binding energy /eV**	**FWHM /eV**	**Concentration /at. %**
Untreated PET fabric	Unknown	530.5 ± 0.1	1.24 ± 0.01	0.33 ± 0.02
	O-Si, O=C	532.1 ± 0	1.24 ± 0.01	14.4 ± 0.22
	O-CO	533.6 ± 0	1.24 ± 0.01	10.2 ± 0.14
	π*←π 1	535.9 ± 0.3	0.57 ± 0.18	0.1 ± 0.04
	π*←π 2	538.8 ± 0	2.02 ± 0.07	0.32 ± 0.03
Treated PET	Unknown	530.4 ± 0.1	1.23 ± 0	0.13 ± 0.11
	O-Si, O=C	532.1 ± 0	1.23 ± 0	13.6 ± 0.33
	O-CO	533.6 ± 0	1.23 ± 0	10.55 ± 0.34
	π*←π 1	535.9 ± 0.1	0.89 ± 0.24	0.19 ± 0.04
	π*←π 2	538.8 ± 0.2	2 ± 0.73	0.42 ± 0.08
Treated PET + Adhesive	Unknown	-	-	-
	O-Si, O=C	532.2 ± 0	1.27 ± 0.01	14.24 ± 0.1
	O-CO	533.8 ± 0	1.27 ± 0.01	8.44 ± 0.02
	π*←π 1	-	-	-
	π*←π 2	538.7 ± 0.2	1 ± 0	0.08 ± 0.04
Untreatednon-conductive PLA	Unknown	530.3 ± 0.2	1.38 ± 0.01	0.67 ± 0.33
	O-Si, O=C	532 ± 0	1.38 ± 0.01	18.71 ± 0.65
	O-CO	533.5 ± 0	1.38 ± 0.01	13.33 ± 0.42
Untreated conductive PLA	Unknown	530.3 ± 0.2	1.36 ± 0.01	0.47 ± 0.06
	O-Si, O=C	531.9 ± 0	1.36 ± 0.01	18.56 ± 0.28
	O-CO	533.5 ± 0	1.36 ± 0.01	11.43 ± 0.44
Treated non-conductive PLA	Unknown	530.3 ± 0.1	1.38 ± 0.02	0.29 ± 0.15
	O-Si, O=C	532 ± 0	1.38 ± 0.02	18.77 ± 0.72
	O-CO	533.6 ± 0	1.38 ± 0.02	13.87 ± 1.37
Treated conductive PLA	Unknown	530.5 ± 0.1	1.36 ± 0.01	0.6 ± 0.29
	O-Si, O=C	532 ± 0.1	1.36 ± 0.01	18.67 ± 1.25
	O-CO	533.6 ± 0.1	1.36 ± 0.01	13.17 ± 1.16
PU film	O=C-N	531 ± 0.1	1.09 ± 0.05	0.49 ± 0.11
	O-C	532.5 ± 0	1.09 ± 0.05	19.7 ± 0.7

Appendix B : Abrasion findings of 3D-PPOT samples

Table B-1. Mean weight loss (%) after different rubbing cycles : 1000, 2000, 5000, 10,000, 15,000 and 20,000. A, B, C and D are the pattern, the weft density, the fabric orientation and the printing bed temperature, respectively. [167]

A	B	C	D	Mean Weight Loss (%) after Different Rubbing Cycles					
				1000	2000	5000	10,000	15,000	20,000
−1	1	1	−1	0.31	0.31	0.55	1.05	1.33	1.76
1	0	−1	1	0.56	0.87	1.41	2.91	4.04	4.98
1	1	1	−1	0.28	0.28	1.02	1.98	4.01	4.74
−1	1	−1	−1	0.31	0.31	0.55	1.05	1.33	1.76
−1	0	−1	−1	0.58	0.69	1.65	2.86	4.31	5.28
1	0	−1	−1	0.56	0.87	1.41	2.91	4.04	4.98
1	−1	1	−1	0.56	1.61	1.75	2.39	3.87	4.65
−1	1	1	1	0.31	0.31	0.55	1.05	1.33	1.76
1	−1	−1	−1	0.56	1.61	1.75	2.39	3.87	4.65
−1	−1	1	−1	0.24	0.24	1.03	2.13	2.98	3.71
−1	−1	−1	−1	0.24	0.24	1.03	2.13	2.98	3.71
1	0	1	−1	0.56	0.87	1.41	2.91	4.04	4.98
1	−1	1	1	0.56	1.61	1.75	2.39	3.87	4.65
−1	0	1	1	0.58	0.69	1.65	2.86	4.31	5.28
1	1	−1	−1	0.28	0.28	1.02	1.98	4.01	4.74
1	1	1	1	0.28	0.28	1.02	1.98	4.01	4.74
−1	−1	1	1	0.24	0.24	1.03	2.13	2.98	3.71
−1	−1	−1	1	0.24	0.24	1.03	2.13	2.98	3.71
−1	0	−1	1	0.58	0.69	1.65	2.86	4.31	5.28
−1	1	−1	1	0.31	0.31	0.55	1.05	1.33	1.76
1	1	−1	1	0.28	0.28	1.02	1.98	4.01	4.74
1	−1	−1	1	0.56	1.61	1.75	2.39	3.87	4.65
−1	0	1	−1	0.58	0.69	1.65	2.86	4.31	5.28
1	0	1	1	0.56	0.87	1.41	2.91	4.04	4.98

Table B-2 . Mean weight loss (%) after different cycles : 1000, 2000, 5000, 10,000, 15,000 and 20,000 and maximum number of cycles (end point). A, B, C and D are the pattern, the weft density, the fabric orientation and the printing bed temperature, respectively. [167]

A	B	C	D	Mean Weight loss (%) after Different Cycles			Mean end Point (cycles)
				5000	20,000	30,000	–
−1	1	1	−1	0.00	0.00	0.00	50,000
1	0	−1	1	0.22	3.33	4.31	30,000
1	1	1	−1	0.44	0.44	0.59	50,000
−1	1	−1	−1	0.00	0.00	0.00	50,000
−1	0	−1	−1	0.16	0.22	0.23	50,000
1	0	−1	−1	0.00	0.93	2.25	30,000
1	−1	1	−1	0.44	0.27	1.09	50,000
−1	1	1	1	0.02	0.42	0.49	50,000
1	−1	−1	−1	0.00	1.18	2.13	30,000
−1	−1	1	−1	0.04	0.63	0.91	50,000
−1	−1	−1	−1	0.00	0.00	0.00	50,000
1	0	1	−1	0.21	0.28	0.31	50,000
1	−1	1	1	0.00	1.96	1.96	30,000
−1	0	1	1	0.23	1.39	2.11	30,000
1	1	−1	−1	0.00	0.23	0.36	40,000
1	1	1	1	0.00	0.99	1.01	50,000
−1	−1	1	1	0.07	2.44	2.97	30,000
−1	−1	−1	1	0.06	0.37	1.67	40,000
−1	0	−1	1	0.03	0.03	0.03	50,000
−1	1	−1	1	0.00	0.34	0.47	50,000
1	1	−1	1	0.24	0.70	0.98	30,000
1	−1	−1	1	0.00	1.00	2.01	30,000
−1	0	1	−1	0.02	0.12	0.62	30,000
1	0	1	1	0.00	0.96	1.39	30,000

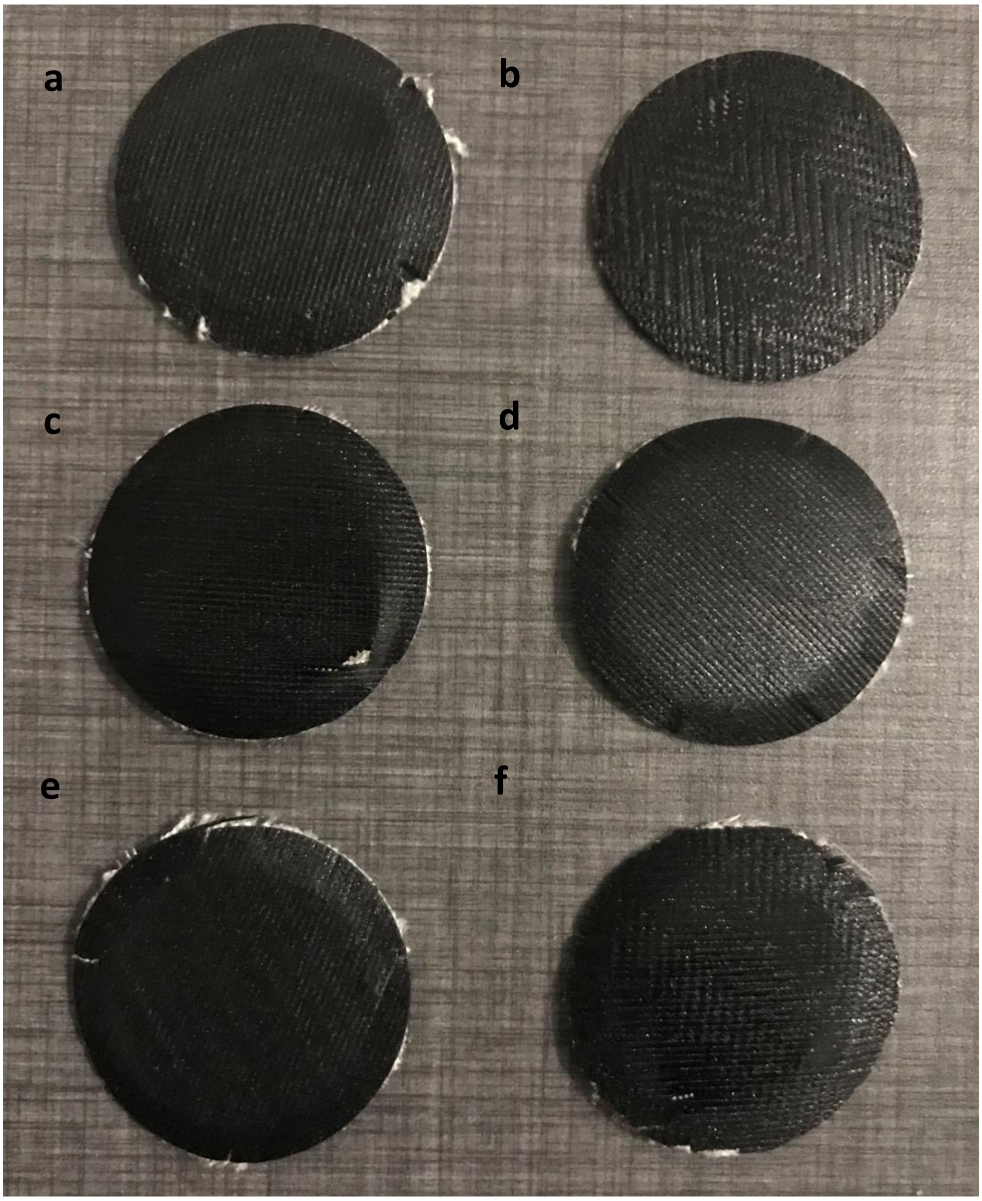

Figure B-1. 3D-PPOT samples after abrasion experiment using (**a,c,e**) 14, 18 and 22 picks/inch plain fabrics, respectively, and (**b,d,f**) 14, 18 and 22 picks/inch twill fabrics, respectively. [167]

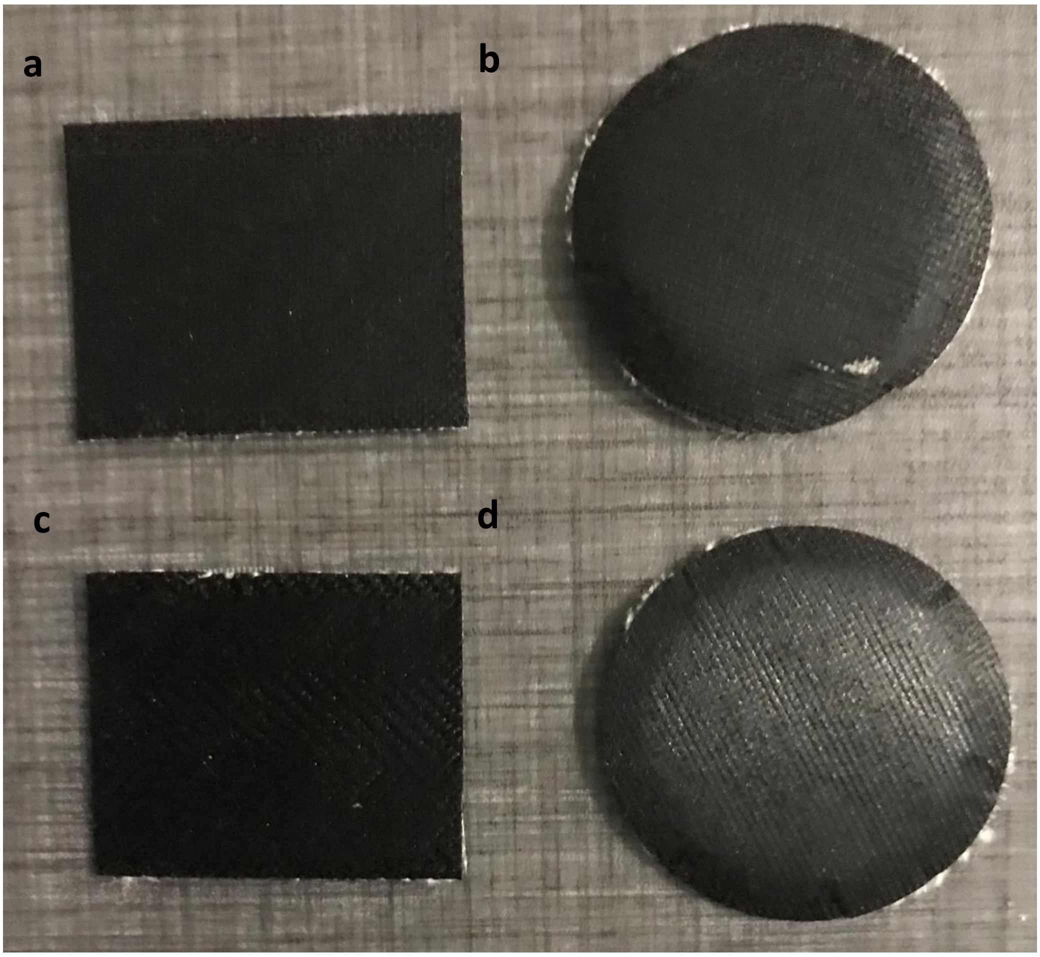

Figure B-2. D-PPOT samples (**a**,**c**) before and (**b**,**d**) after abrasion experiment. (**a**,**b**) represent 3D-PPOT made of 18 picks/inch plain fabrics; (**c**,**d**) ones made from 18 picks/inch twill fabrics. [167]

Appendix C : Detailed design of experiments – Chapter V

Table C-1. Sample descriptions of the first design of experiment [206]

Sample reference	Composition of (KB and CNT)- filled LDPE [1]			Composition of KB and CNT- filled LDPE/PBE blends			
	wt% KB *	wt% CNT	wt% LDPE	wt% (KB and CNT)- filled LDPE			wt% PBE
				wt% KB	wt% CNT	wt% LDPE	
A1	0	0	100	0	0	60	40
A2	5	0	95	5	0	95	0
A3	10	0	90	10	0	90	0
A4	10	2.5	87.5	10	2.5	87.5	0
A5	10	5	85	10	5	85	0
A6	5	0	95	3	0	57	40
A7	10	0	90	6	0	54	40
A8	10	2.5	87.5	6	1.5	52.5	40
A9	10	5	85	6	3	51	40
A10	5	0	95	2	0	38	60
A11	10	0	90	4	0	36	60
A12	10	2.5	87.5	4	1	35	60
A13	10	5	85	4	2	34	60
A14	0	0	100	0	0	40	60

[1] (KB and CNT)- filled LDPE means LDPE filled with KB and CNT nanoparticles

Table C-2. Sample descriptions of the second design of experiments [206]

Sample reference	**Composition of KB and CNT-filled LDPE formulations**			**Composition of KB and CNT- filled LDPE/PBE blend formulations**				**Extrusion scenario**
				wt% (KB and CNT)- filled LDPE				
	wt % KB	wt% CNT	wt% LDPE	wt% KB	wt% CNT	wt% LDPE	wt % PBE	
B1	10	2.5	87.5	10	2.5	87.5	0	1-step[1]
B2	12.5	3.1	84.4	10	2.5	67.5	20	1-step
B3	16.7	4.2	79.1	10	2.5	47.5	40	1-step
B4	12.5	3.1	84.4	10	2.5	67.5	20	2-step[2]
B5	16.7	4.2	79.1	10	2.5	47.5	40	2-step

[1] dispersion of the KB and CNT in LDPE and PBE in one step

[2] dispersion of the KB and CNT in LDPE and then blend with PBE

Appendix D: Extrusion scenarios

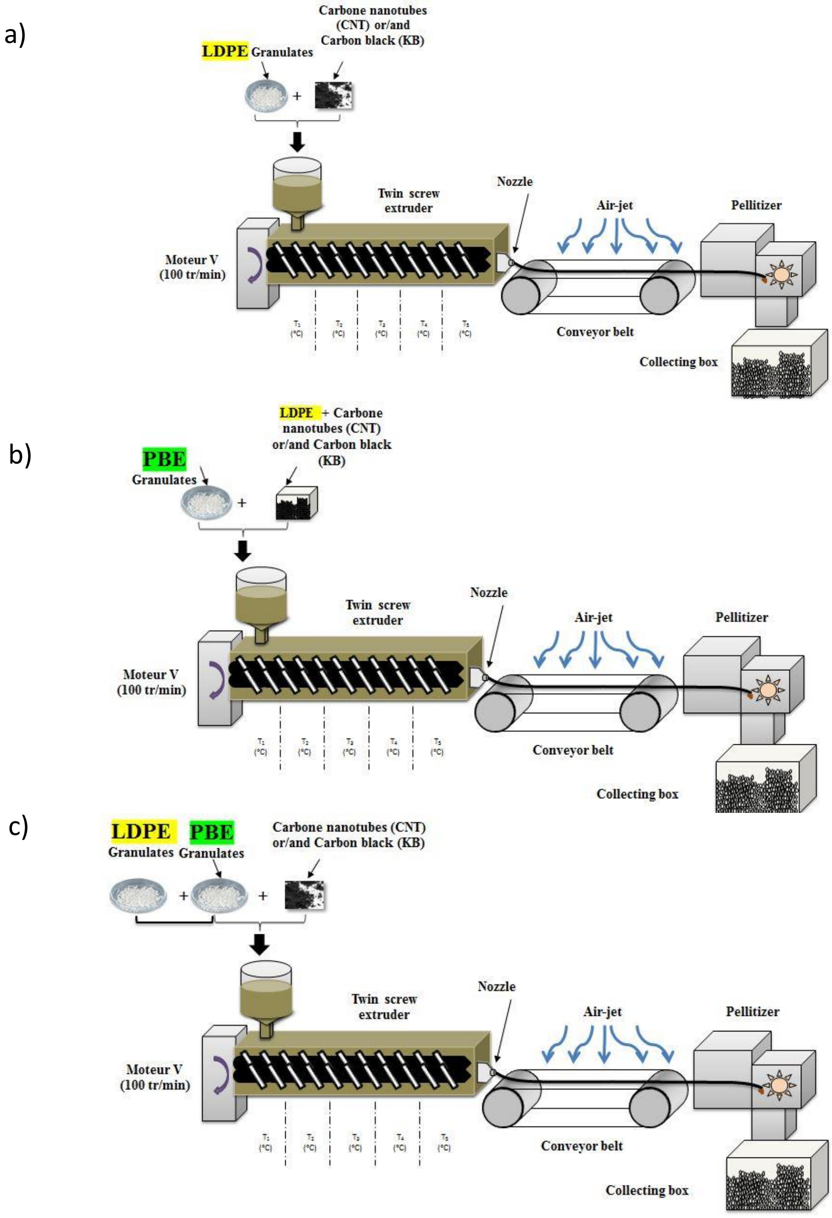

Figure D-1. Scheme of the 2-step extrusion (a and b) and 1-step extrusion (c). The first step of the two-step extrusion is presented in (a) and the second step in (b). [206]

References

[1] A.R. Torrado Perez, D.A. Roberson, R.B. Wicker, Fracture surface analysis of 3D-printed tensile specimens of novel ABS-based materials, J. Fail. Anal. Prev. 14 (2014) 343–353. https://doi.org/10.1007/s11668-014-9803-9.

[2] R. Hashemi Sanatgar, C. Campagne, V. Nierstrasz, Investigation of the adhesion properties of direct 3D printing of polymers and nanocomposites on textiles: Effect of FDM printing process parameters, Appl. Surf. Sci. 403 (2017) 551–563. https://doi.org/10.1016/J.APSUSC.2017.01.112.

[3] T. Spahiu, M. Al-Arabiyat, Y. Martens, A. Ehrmann, E. Piperi, E. Shehi, Adhesion of 3D printing polymers on textile fabrics for garment production, IOP Conf. Ser. Mater. Sci. Eng. 459 (2018). https://doi.org/10.1088/1757-899X/459/1/012065.

[4] E.P. T. Spahiu, N. Grimmelsmann, A. Ehrmann, E. Shehi, Effect of 3D printing on textile fabric, in: Eng. Entrep., 2017.

[5] A.E. Christopher Dopke, Nils Grimmelsmann, 3D printing on knitted fabrics, Int. Melliand. (2017) 97–98.

[6] E. Pei, J. Shen, J. Watling, Direct 3D printing of polymers onto textiles: Experimental studies and applications, Rapid Prototyp. J. 21 (2015) 556–571. https://doi.org/10.1108/RPJ-09-2014-0126.

[7] G.W. Ma, L. Wang, Y. Ju, State-of-the-art of 3D printing technology of cementitious material—An emerging technique for construction, Sci. China Technol. Sci. (2017) 1–21. https://doi.org/10.1007/s11431-016-9077-7.

[8] T.D. Ngo, A. Kashani, G. Imbalzano, K.T.Q. Nguyen, D. Hui, Additive manufacturing (3D printing): A review of materials, methods, applications and challenges, Compos. Part B Eng. 143 (2018) 172–196. https://doi.org/10.1016/j.compositesb.2018.02.012.

[9] V. Koncar, Smart textiles for monitoring and measurement applications, 2019. https://doi.org/10.1016/b978-0-08-102308-2.00001-2.

[10] About Additive Manufacturing, (n.d.). https://www.lboro.ac.uk/research/amrg/about/the7categoriesofadditivemanufacturing/materialextrusion/ (accessed October 18, 2020).

[11] J. Korpela, A. Kokkari, H. Korhonen, M. Malin, T. Narhi, J. Seppalea, Biodegradable and bioactive porous scaffold structures prepared using fused deposition modeling, J. Biomed. Mater. Res. - Part B Appl. Biomater. 101 (2013) 610–619. https://doi.org/10.1002/jbm.b.32863.

[12] T.C. Okwuosa, D. Stefaniak, B. Arafat, A. Isreb, K.W. Wan, M.A. Alhnan, A Lower Temperature FDM 3D Printing for the Manufacture of Patient-Specific Immediate Release Tablets, Pharm. Res. 33 (2016) 2704–2712. https://doi.org/10.1007/s11095-016-1995-0.

[13] M.S. Bayar, Z. Aziz, Rapid Prototyping and Its Role in Supporting Architectural Design Process, J. Archit. Eng. 24 (2018). https://doi.org/10.1061/(ASCE)AE.1943-5568.0000307.

[14] I. Celik, Modeling and Production of Solid Model of South Panel , Tuncbilek Open Pit by 3D Printer, (2018).

[15] S. Vyavahare, S. Teraiya, D. Panghal, S. Kumar, Fused deposition modelling: a review, Rapid Prototyp. J. 26 (2020) 176–201. https://doi.org/10.1108/RPJ-04-2019-0106.

[16] C.B. Williams, R. Ilardo, Design and manufacture of a Formula SAE intake system using fused deposition modeling and fiber-reinforced composite materials, Rapid Prototyp. J. 16 (2010) 174–179. https://doi.org/10.1108/13552541011034834.

[17] M.D. Monzon, N. Diaz, A.N. Benitez, M.D. Marrero, P.M. Hernandez, Advantages of Fused Deposition Modeling for making electrically conductive plastic patterns, Proc. - 2010 Int. Conf. Manuf. Autom. ICMA 2010. (2010) 37–43. https://doi.org/10.1109/ICMA.2010.18.

[18] D. Espalin, K. Arcaute, D. Rodriguez, F. Medina, M. Posner, R. Wicker, Fused deposition modeling of patient-specific polymethylmethacrylate implants, Rapid Prototyp. J. 16 (2010) 164–173. https://doi.org/10.1108/13552541011034825.

[19] O. Diegel, S. Singamneni, B. Huang, I. Gibson, Getting rid of the wires: Curved layer fused deposition modeling in conductive polymer additive manufacturing, Key Eng. Mater. 467–469 (2011) 662–667. https://doi.org/10.4028/www.scientific.net/KEM.467-469.662.

[20] R. Van Noort, The future of dental devices is digital, Dent. Mater. 28 (2012) 3–12. https://doi.org/10.1016/j.dental.2011.10.014.

[21] N. Xu, X. Ye, D. Wei, J. Zhong, Y. Chen, G. Xu, D. He, 3D artificial bones for bone repair prepared by computed tomography-guided fused deposition modeling for bone repair, ACS Appl. Mater. Interfaces. 6 (2014) 14952–14963. https://doi.org/10.1021/am502716t.

[22] S. Shaffer, K. Yang, J. Vargas, M.A. Di Prima, W. Voit, On reducing anisotropy in 3D printed polymers via ionizing radiation, Polym. (United Kingdom). 55 (2014) 5969–5979. https://doi.org/10.1016/j.polymer.2014.07.054.

[23] R.M. JONES, Mechanics of Composites Materials.pdf, (1998) 554.

[24] A.B. Strong, Fundamentals of composites manufacturing: materials, methods and applications, 2008. https://doi.org/10.1016/0956-7143(91)90159-e.

[25] J.S. Bergstrom, Mechanics of solid polymers: theory and computational modeling., 2015.

[26] H. Gao, P.T. Minh, H. Wang, S. Minko, J. Locklin, T. Nguyen, S. Sharma, High-performance flexible yarn for wearable piezoelectric nanogenerators, SMART Mater. Struct. 27 (2018). https://doi.org/10.1088/1361-665X/aad718.

[27] S. Farah, D.G. Anderson, R. Langer, Physical and mechanical properties of PLA, and their functions in widespread applications — A comprehensive review, Adv. Drug Deliv. Rev. 107 (2016) 367–392. https://doi.org/10.1016/j.addr.2016.06.012.

[28] A.J.R. Lasprilla, G.A.R. Martinez, B.H. Lunelli, A.L. Jardini, R.M. Filho, Poly-lactic acid synthesis for application in biomedical devices - A review, Biotechnol. Adv. 30 (2012) 321–328. https://doi.org/10.1016/j.biotechadv.2011.06.019.

[29] C.G. Schirmeister, T. Hees, E.H. Licht, R. Mülhaupt, 3D printing of high density polyethylene by fused filament fabrication, Addit. Manuf. 28 (2019) 152–159. https://doi.org/10.1016/j.addma.2019.05.003.

[30] S.E.M. Selke, Packaging: Polymers in Flexible Packaging, Ref. Modul. Mater. Sci. Mater. Eng. (2019) 1–5. https://doi.org/10.1016/b978-0-12-803581-8.02168-8.

[31] R.H. Sanatgar, A. Cayla, C. Campagne, V. Nierstrasz, Morphological and electrical characterization of conductive polylactic acid based nanocomposite before and after FDM 3D printing, J. Appl. Polym. Sci. (2018) 47040. https://doi.org/10.1002/app.47040.

[32] L. Marischal, A. Cayla, G. Lemort, C. Campagne, D. Éric, Selection of immiscible polymer blends filled with carbon nanotubes for heating applications, Polymers (Basel). 11 (2019) 1–16. https://doi.org/10.3390/polym11111827.

[33] A. Cayla, C. Campagne, M. Rochery, E. Devaux, Electrical, rheological properties and morphologies of biphasic blends filled with carbon nanotubes in one of the two phases, Synth. Met. 161 (2011) 1034–1042. https://doi.org/10.1016/j.synthmet.2011.03.012.

[34] J.F. Feller, I. Linossier, G. Levesque, Conductive Polymer Composites (CPCs): Comparison of electrical properties of poly(ethylene-co-ethyl acrylate)-carbon black with poly(butylene terephthalate)/poly(ethylene-co-ethyl acrylate)-carbon black, Polym. Adv. Technol. 13 (2002) 714–724. https://doi.org/10.1002/pat.254.

[35] T. Villmow, S. Pegel, A. John, R. Rentenberger, P. Pötschke, Liquid sensing: Smart polymer/CNT composites, Mater. Today. 14 (2011) 340–345. https://doi.org/10.1016/S1369-7021(11)70164-X.

[36] H. Deng, R. Du, L. Duan, Q. Fu, Strain sensing conductive polymer composites: Sensitivity and stability, AIP Conf. Proc. 1713 (2016). https://doi.org/10.1063/1.4942297.

[37] L. Paredes-Madrid, A. Matute, J.O. Bareño, C.A.P. Vargas, E.I.G. Velásquez, Underlying physics of conductive polymer composites and Force Sensing Resistors (FSRs). A study on creep response and dynamic loading, Materials (Basel). 10 (2017). https://doi.org/10.3390/ma10111334.

[38] A. Dorigato, V. Moretti, S. Dul, S.H. Unterberger, A. Pegoretti, Electrically conductive nanocomposites for fused deposition modelling, Synth. Met. 226 (2017) 7–14. https://doi.org/10.1016/j.synthmet.2017.01.009.

[39] S.M. Lebedev, O.S. Gefle, E.T. Amitov, D.Y. Berchuk, D. V. Zhuravlev, Poly(lactic acid)-based polymer composites with high electric and thermal conductivity and their characterization, Polym. Test. 58 (2017) 241–248. https://doi.org/10.1016/j.polymertesting.2016.12.033.

[40] K. Gnanasekaran, T. Heijmans, S. van Bennekom, H. Woldhuis, S. Wijnia, G. de With, H. Friedrich, 3D printing of CNT- and graphene-based conductive polymer nanocomposites by fused deposition modeling, Appl. Mater. Today. 9 (2017) 21–28. https://doi.org/10.1016/j.apmt.2017.04.003.

[41] V. Koncar, Smart textiles for In Situ Monitoring of Composites, Elsevier, 2018. https://www.elsevier.com/books/smart-textiles-for-in-situ-monitoring-of-composites/koncar/978-0-08-102308-2.

[42] N. Chantarapanich, P. Puttawibul, K. Sitthiseripratip, S. Sucharitpwatskul, S. Chantaweroad, Study of the mechanical properties of photo-cured epoxy resin fabricated by stereolithography process, Songklanakarin J. Sci. Technol. 35 (2013) 91–98.

[43] J.R.C. Dizon, A.H. Espera, Q. Chen, R.C. Advincula, Mechanical characterization of 3D-printed polymers, Addit. Manuf. 20 (2018) 44–67. https://doi.org/10.1016/j.addma.2017.12.002.

[44] O.S. Es-Said, J. Foyos, R. Noorani, M. Mendelson, R. Marloth, B.A. Pregger, Effect of layer orientation on mechanical properties of rapid prototyped samples, Mater. Manuf. Process. 15 (2000) 107–122. https://doi.org/10.1080/10426910008912976.

[45] S.H. Ahn, M. Montero, D. Odell, S. Roundy, P.K. Wright, Anisotropic material properties of fused deposition modeling ABS, 2002. https://doi.org/10.1108/13552540210441166.

[46] A.R. Torrado, C.M. Shemelya, J.D. English, Y. Lin, R.B. Wicker, D.A. Roberson, Characterizing

the effect of additives to ABS on the mechanical property anisotropy of specimens fabricated by material extrusion 3D printing, Addit. Manuf. 6 (2015) 16–29. https://doi.org/10.1016/j.addma.2015.02.001.

[47] M. Somireddy, A. Czekanski, Mechanical Characterization of Additively Manufactured Parts by FE Modeling of Mesostructure, J. Manuf. Mater. Process. 1 (2017) 18. https://doi.org/10.3390/jmmp1020018.

[48] J.F. Rodríguez, J.P. Thomas, J.E. Renaud, Design of Fused-Deposition ABS Components for Stiffness and Strength, J. Mech. Des. 125 (2003) 545. https://doi.org/10.1115/1.1582499.

[49] T. Letcher, M. Waytashek, Material Property Testing of 3D-Printed Specimen in PLA on an Entry-Level 3D Printer, Vol. 2A Adv. Manuf. (2014) V02AT02A014. https://doi.org/10.1115/IMECE2014-39379.

[50] B. Rankouhi, S. Javadpour, F. Delfanian, T. Letcher, Failure Analysis and Mechanical Characterization of 3D Printed ABS With Respect to Layer Thickness and Orientation, J. Fail. Anal. Prev. 16 (2016) 467–481. https://doi.org/10.1007/s11668-016-0113-2.

[51] S. Guessasma, S. Belhabib, H. Nouri, O. Ben Hassana, Anisotropic damage inferred to 3D printed polymers using fused deposition modelling and subject to severe compression, Eur. Polym. J. 85 (2016) 324–340. https://doi.org/10.1016/j.eurpolymj.2016.10.030.

[52] C. Wendt, M. Batista, E. Moreno, A.P. Valerga, S.R. Fernández-Vidal, O. Droste, M. Marcos, Preliminary Design and Analysis of Tensile Test Samples Developed by Additive Manufacturing, Procedia Eng. 132 (2015) 132–139. https://doi.org/10.1016/j.proeng.2015.12.489.

[53] C. Ziemian, M. Sharma, S. Ziemi, Anisotropic Mechanical Properties of ABS Parts Fabricated by Fused Deposition Modelling, Mech. Eng. (2012). https://doi.org/10.5772/34233.

[54] I. Durgun, R. Ertan, Experimental investigation of FDM process for improvement of mechanical properties and production cost, Rapid Prototyp. J. 20 (2014) 228–235. https://doi.org/10.1108/RPJ-10-2012-0091.

[55] B.H. Lee, J. Abdullah, Z.A. Khan, Optimization of rapid prototyping parameters for production of flexible ABS object, J. Mater. Process. Technol. 169 (2005) 54–61. https://doi.org/10.1016/j.jmatprotec.2005.02.259.

[56] A.K. Sood, R.K. Ohdar, S.S. Mahapatra, Experimental investigation and empirical modelling of FDM process for compressive strength improvement, J. Adv. Res. 3 (2012) 81–90.

https://doi.org/10.1016/j.jare.2011.05.001.

[57] J. Cantrell, S. Rohde, D. Damiani, R. Gurnani, L. DiSandro, J. Anton, A. Young, A. Jerez, D. Steinbach, C. Kroese, P. Ifju, Experimental Characterization of the Mechanical Properties of 3D Printed ABS and Polycarbonate Parts, (2017) 89–105. https://doi.org/10.1007/978-3-319-41600-7_11.

[58] P. Henrique, C. Camargo, K.G. Satyanarayana, F. Wypych, Nanocomposites : Synthesis , Structure , Properties and New Application Opportunities, Mater. Res. 12 (2009) 1–39. https://doi.org/10.1590/S1516-14392009000100002.

[59] J.Z. Manapat, Q. Chen, P. Ye, R.C. Advincula, 3D Printing of Polymer Nanocomposites via Stereolithography, Macromol. Mater. Eng. 302 (2017) 1–13. https://doi.org/10.1002/mame.201600553.

[60] J.Z. Manapat, J.D. Mangadlao, B.D.B. Tiu, G.C. Tritchler, R.C. Advincula, High-Strength Stereolithographic 3D Printed Nanocomposites: Graphene Oxide Metastability, ACS Appl. Mater. Interfaces. 9 (2017) 10085–10093. https://doi.org/10.1021/acsami.6b16174.

[61] J.H. Koo, R. Ortiz, B. Ong, H. Wu, Polymer nanocomposites for laser additive manufacturing, Laser Addit. Manuf. Mater. Des. Technol. Appl. (2016) 205–235. https://doi.org/10.1016/B978-0-08-100433-3.00008-7.

[62] D. Lin, S. Jin, F. Zhang, C. Wang, Y. Wang, C. Zhou, G.J. Cheng, 3D stereolithography printing of graphene oxide reinforced complex architectures, Nanotechnology. 26 (2015). https://doi.org/10.1088/0957-4484/26/43/434003.

[63] Xingyu Li (North Carolina State University), Key Material Factors of Digital Printing on Textiles. Case : Pigment on Woven Polyester, 2017.

[64] S.H. Masood, W.Q. Song, Development of new metal/polymer materials for rapid tooling using Fused deposition modelling, Mater. Des. 25 (2004) 587–594. https://doi.org/10.1016/j.matdes.2004.02.009.

[65] Q. Sun, G.M. Rizvi, C.T. Bellehumeur, P. Gu, Effect of processing conditions on the bonding quality of FDM polymer filaments, Rapid Prototyp. J. 14 (2008) 72–80. https://doi.org/10.1108/13552540810862028.

[66] P.K. Gurrala, S.P. Regalla, Part strength evolution with bonding between filaments in fused deposition modelling: This paper studies how coalescence of filaments contributes to the strength

of final FDM part, Virtual Phys. Prototyp. 9 (2014) 141–149. https://doi.org/10.1080/17452759.2014.913400.

[67] K.S. Boparai, R. Singh, H. Singh, Wear behavior of FDM parts fabricated by composite material feed stock filament, Rapid Prototyp. J. 22 (2016) 350–357. https://doi.org/10.1108/RPJ-06-2014-0076.

[68] H. Prajapati, D. Ravoori, R.L. Woods, A. Jain, Measurement of anisotropic thermal conductivity and inter-layer thermal contact resistance in polymer fused deposition modeling (FDM), Addit. Manuf. 21 (2018) 84–90. https://doi.org/10.1016/j.addma.2018.02.019.

[69] D. Popescu, A. Zapciu, C. Amza, F. Baciu, R. Marinescu, FDM process parameters influence over the mechanical properties of polymer specimens: A review, Polym. Test. 69 (2018) 157–166. https://doi.org/10.1016/j.polymertesting.2018.05.020.

[70] A. Equbal, A.K. Sood, V. Toppo, R.K. Ohdar, S.S. Mahapatra, Prediction and analysis of sliding wear performance of fused deposition modelling-processed ABS plastic parts, Proc. Inst. Mech. Eng. Part J J. Eng. Tribol. 224 (2010) 1261–1271. https://doi.org/10.1243/13506501JET835.

[71] Mukesh K. Agarwala, Vikram R. Jamalabad, Noshir A. Langrana, Ahmad Safari, Philip J. Whalen and, Stephen C. Danforth, Structural quality of parts processed by fused deposition, Rapid Prototyp. J. (1996).

[72] M.E. Haque, D. Banerjee, S.B. Mishra, B.K. Nanda, A numerical approach to measure the surface roughness of FDM build part, Mater. Today Proc. 18 (2019) 5523–5529. https://doi.org/10.1016/j.matpr.2019.07.659.

[73] R. Anitha, S. Arunachalam, P. Radhakrishnan, Critical parameters influencing the quality of prototypes in fused deposition modelling, J. Mater. Process. Technol. 118 (2001) 385–388. https://doi.org/10.1016/S0924-0136(01)00980-3.

[74] J.F. Rodríguez, J.P. Thomas, J.E. Renaud, Design of fused-deposition ABS components for stiffness and strength, J. Mech. Des. Trans. ASME. 125 (2003) 545–551. https://doi.org/10.1115/1.1582499.

[75] W. Jo, O.C. Kwon, M.W. Moon, Investigation of influence of heat treatment on mechanical strength of FDM printed 3D objects, Rapid Prototyp. J. 24 (2018) 637–644. https://doi.org/10.1108/RPJ-06-2017-0131.

[76] M. Korger, Michael; Bergschneider, J; Lutz, B; Finsterbusch, K; Rabe, Possible Applications of 3D Printing Technology on Textile Substrates Possible Applications of 3D Printing Technology on

Textile Substrates, in: IOP Conf. Ser. Mater. Sci. Eng., 2016. https://doi.org/10.1088/1757-899X/141/1/012011.

[77] M. Spoerk, J. Gonzalez-Gutierrez, J. Sapkota, S. Schuschnigg, C. Holzer, Effect of the printing bed temperature on the adhesion of parts produced by fused filament fabrication, Plast. Rubber Compos. (2017) 1–8. https://doi.org/10.1080/14658011.2017.1399531.

[78] N. Grimmelsmann, M. Kreuziger, M. Korger, H. Meissner, A. Ehrmann, Adhesion of 3D printed material on textile substrates, Rapid Prototyp. J. 24 (2018) 166–170. https://doi.org/10.1108/RPJ-05-2016-0086.

[79] S.K. Leist, D. Gao, R. Chiou, J. Zhou, Investigating the shape memory properties of 4D printed polylactic acid (PLA) and the concept of 4D printing onto nylon fabrics for the creation of smart textiles, Virtual Phys. Prototyp. 12 (2017) 290–300. https://doi.org/10.1080/17452759.2017.1341815.

[80] M.G. Tadesse, D. Dumitrescu, C. Loghin, Y. Chen, L. Wang, V. Nierstrasz, 3D Printing of NinjaFlex Filament onto PEDOT:PSS-Coated Textile Fabrics for Electroluminescence Applications, J. Electron. Mater. (2017). https://doi.org/10.1007/s11664-017-6015-6.

[81] J.A. von Fraunhofer, Adhesion and Cohesion, Int. J. Dent. 2012 (2012) 951324. https://doi.org/10.1155/2012/951324.

[82] A. Al-kawaz, Theories of adhesion, (n.d.). https://doi.org/10.1002/0470014229.ch18.

[83] N. Graupner, H. Fischer, G. Ziegmann, J. Müssig, Improvement and analysis of fibre/matrix adhesion of regenerated cellulose fibre reinforced PP-, MAPP- and PLA-composites by the use of Eucalyptus globulus lignin, Compos. Part B Eng. 66 (2014) 117–125. https://doi.org/10.1016/J.COMPOSITESB.2014.05.002.

[84] B.R. Anvar, A. Akbarzadeh, Roll bonding of AA5052 and polypropylene sheets : Bonding mechanisms , microstructure and mechanical properties, J. Adhes. 93 (2017) 550–574. https://doi.org/10.1080/00218464.2015.1116067.

[85] J. Dy, P. Mun, Z. Chen, Understanding the bonding mechanisms of directly sputtered copper thin film on an alumina substrate, Thin Solid Films. 634 (2017) 6–14. https://doi.org/10.1016/j.tsf.2017.05.005.

[86] B. Bonpain, M. Stommel, Influence of surface roughness on the shear strength of direct injection molded plastic-aluminum hybrid-parts, Int. J. Adhes. Adhes. 82 (2018) 290–298.

https://doi.org/10.1016/j.ijadhadh.2018.02.003.

[87] W. Jiao, Y. Cai, W. Liu, F. Yang, L. Jiang, W. Jiao, R. Wang, Preparation of carbon fiber unsaturated sizing agent for enhancing interfacial strength of carbon fiber/vinyl ester resin composite, Appl. Surf. Sci. 439 (2018) 88–95. https://doi.org/10.1016/j.apsusc.2017.12.226.

[88] S. Periyasamy, G. Krishna Prasad, A.S.M. Raja, P.G. Patil, Submicron surface roughening of aliphatic polyamide 6,6 fabric through low temperature plasma and its effect on interfacial bonding in rubber composite, J. Ind. Text. 47 (2018) 2029–2049. https://doi.org/10.1177/1528083717720202.

[89] A.A. El-Saftawy, M.S. Ragheb, S.G. Zakhary, Electron beam irradiation impact on surface structure and wettability of ethylene-vinyl alcohol copolymer, Radiat. Phys. Chem. 147 (2018) 106–113. https://doi.org/10.1016/j.radphyschem.2018.02.001.

[90] A. Rodriguez-Contreras, D. Guadarrama Bello, A. Nanci, Surface nanoporosity has a greater influence on osteogenic and bacterial cell adhesion than crystallinity and wettability, Appl. Surf. Sci. 445 (2018) 255–261. https://doi.org/10.1016/j.apsusc.2018.03.150.

[91] H. Jing, E. Sahle-Demessie, G.A. Sorial, Inhibition of biofilm growth on polymer-MWCNTs composites and metal surfaces, Sci. Total Environ. 633 (2018) 167–178. https://doi.org/10.1016/j.scitotenv.2018.03.065.

[92] I.. Bozaci, E.; Sever, K.; Sarikanat, M.; Seki, Y.; Demir, A.; Ozdogan, E.; Tavman, Effect of the atmospheric plasma treatments on surface and mechanical properties of flax fiber and adhesion between fiber-matrix for composite materials.PDF, Compos. Part B Eng. 45 (2013) 565–572.

[93] I.A. Porras, A.; Maranon, A.; Ashcroft, Characterization of a novel natural cellulose fabric from Manicaria saccifera palm as possible reinforcement of composite materials.PDF, Compos. Part B Eng. 74 (2015) 66–73.

[94] E. Sassoni, S. Andreotti, A. Bellini, B. Mazzanti, M.C. Bignozzi, C. Mazzotti, E. Franzoni, Influence of mechanical properties, anisotropy, surface roughness and porosity of brick on FRP debonding force, Compos. Part B Eng. 108 (2017) 257–269. https://doi.org/10.1016/j.compositesb.2016.10.020.

[95] M.P. Ho, H. Wang, J.H. Lee, C.K. Ho, K.T. Lau, J. Leng, D. Hui, Critical factors on manufacturing processes of natural fibre composites, Compos. Part B Eng. 43 (2012) 3549–3562. https://doi.org/10.1016/j.compositesb.2011.10.001.

[96] L. Yan, N. Chouw, K. Jayaraman, Flax fibre and its composites - A review, Compos. Part B Eng. 56 (2014) 296–317. https://doi.org/10.1016/j.compositesb.2013.08.014.

[97] H. Krump, I. Hudec, M. Jaššo, E. Dayss, A.S. Luyt, Physical-morphological and chemical changes leading to an increase in adhesion between plasma treated polyester fibres and a rubber matrix, Appl. Surf. Sci. 252 (2006) 4264–4278. https://doi.org/10.1016/j.apsusc.2005.07.003.

[98] C. Staszel, A.L. Yarin, Polymer adhesion in heat-treated nonwovens, J. Appl. Polym. Sci. 46165 (2017) 1–12. https://doi.org/10.1002/app.46165.

[99] H.M. Ayu, S. Izman, R. Daud, G. Krishnamurithy, A. Shah, S.H. Tomadi, Surface Modification on CoCrMo Alloy to Improve the Adhesion Strength of Hydroxyapatite Coating, Procedia Eng. 184 (2017) 399–408. https://doi.org/10.1016/j.proeng.2017.04.110.

[100] M. Björkman, Improved Adhesion of Polyolefin Laminates to Textiles Using New Plasma Technology, Master Sci. Thesis, Chalmers Univ. Thecnology, Sweden. (2012) 53.

[101] P.A. Eutionnat-Diffo, Y. Chen, J. Guan, C. Aurelie, C. Christine, Z. Xianyi, N. Vincent, Optimization of adhesion of poly lactic acid 3D printed onto polyethylene terephthalate woven fabrics through modelling using textile properties, Rapid Prototyp. J. (2020). https://doi.org/10.1108/RPJ-05-2019-0138.

[102] M. Areir, Y. Xu, R. Zhang, D. Harrison, J. Fyson, E. Pei, A study of 3D printed active carbon electrode for the manufacture of electric double-layer capacitors, J. Manuf. Process. 25 (2017) 351–356. https://doi.org/10.1016/j.jmapro.2016.12.020.

[103] L. Sabantina, F. Kinzel, A. Ehrmann, K. Finsterbusch, Combining 3D printed forms with textile structures - Mechanical and geometrical properties of multi-material systems, IOP Conf. Ser. Mater. Sci. Eng. 87 (2015). https://doi.org/10.1088/1757-899X/87/1/012005.

[104] N. Grimmelsmann, H. Meissner, A. Ehrmann, 3D printed auxetic forms on knitted fabrics for adjustable permeability and mechanical properties, IOP Conf. Ser. Mater. Sci. Eng. 137 (2016). https://doi.org/10.1088/1757-899X/137/1/012011.

[105] P. Meyer, C. Döpke, A. Ehrmann, Improving adhesion of three-dimensional printed objects on textile fabrics by polymer coating, J. Eng. Fiber. Fabr. 14 (2019). https://doi.org/10.1177/1558925019895257.

[106] N.S. Mpofu, J.I. Mwasiagi, L.C. Nkiwane, D. Njuguna, Use of regression to study the effect of fabric parameters on the adhesion of 3D printed PLA polymer onto woven fabrics, Fash. Text. 6

(2019). https://doi.org/10.1186/s40691-019-0180-6.

[107] T. Kozior, C. Döpke, N. Grimmelsmann, I. Juhász Junger, A. Ehrmann, Influence of fabric pretreatment on adhesion of three-dimensional printed material on textile substrates, Adv. Mech. Eng. 10 (2018). https://doi.org/10.1177/1687814018792316.

[108] A. Baldan, Adhesion phenomena in bonded joints, Int. J. Adhes. Adhes. 38 (2012) 95–116. https://doi.org/10.1016/J.IJADHADH.2012.04.007.

[109] B.R. Anvar, A. Akbarzadeh, Roll bonding of AA5052 and polypropylene sheets : Bonding mechanisms , microstructure and mechanical properties, J. Adhes. 93 (2017) 550–574. https://doi.org/10.1080/00218464.2015.1116067.

[110] M. Adamiak, Abrasion Resistance of Materials, in: Anal. Abrasion Charact. Text., IntechOpen, 2012. https://doi.org/10.5772/29784.

[111] P. Bhimaraj, D.L. Burris, J. Action, W.G. Sawyer, C.G. Toney, R.W. Siegel, L.S. Schadler, Effect of matrix morphology on the wear and friction behavior of alumina nanoparticle / poly (ethylene) terephthalate composites, 258 (2005) 1437–1443. https://doi.org/10.1016/j.wear.2004.09.077.

[112] P. Bhimaraj, D. Burris, W.G. Sawyer, C.G. Toney, R.W. Siegel, L.S. Schadler, Tribological investigation of the effects of particle size , loading and crystallinity on poly (ethylene) terephthalate nanocomposites, 264 (2008) 632–637. https://doi.org/10.1016/j.wear.2007.05.009.

[113] N. Özdil, G.Ö. Kayseri, G.S. Mengüç, Analysis of Abrasion Characteristics in Textiles, Abrasion Resist. Mater. (2012) 119–146. https://doi.org/10.5772/711.

[114] H.K. Kaynak, M. Topalbekiroğlu, Influence of fabric pattern on the abrasion resistance property of woven fabrics, Fibres Text. East. Eur. 16 (2008) 54–56.

[115] M. Akgun, B. Becerir, H.R. Alpay, Investigation of the relation between surface roughness and friction properties of polyester fabrics after abrasion, J. Text. Inst. 5000 (2018) 0. https://doi.org/10.1080/00405000.2017.1344117.

[116] G. Pamuk, F. Çeken, Comparative study of the abrasion resistance of automobile seat covers, Fibres Text. East. Eur. 16 (2008) 57–61.

[117] M. Åkerfeldt, M. Strååt, P. Walkenström, Influence of coating parameters on textile and electrical properties of a poly(3,4-ethylene dioxythiophene): Poly(styrene sulfonate)/polyurethane-coated textile, Text. Res. J. 83 (2013) 2164–2176. https://doi.org/10.1177/0040517513487786.

[118] ASTM D4966-12(2016), Standard Test Method for Abrasion Resistance of Textile Fabrics (Martindale Abrasion Tester Method), ASTM International, West Conshohocken, PA, 2016, n.d.

[119] ASTM D4060-14, Standard Test Method for Abrasion Resistance of Organic Coatings by the Taber Abraser, ASTM International, West Conshohocken, PA, 2014, www.astm.org, n.d.

[120] F. Kalaoğlu, E. Önder, B. Özipek, Influence of Varying Structural Parameters on Abrasion Characteristics of 50/50 Wool/Polyester Blended Fabrics, Text. Res. J. 73 (2003) 980–984. https://doi.org/10.1177/004051750307301108.

[121] P.A. Eutionnat-Diffo, Y. Chen, J. Guan, A. Cayla, C. Campagne, X. Zeng, V. Nierstrasz, Stress, strain and deformation of poly-lactic acid filament deposited onto polyethylene terephthalate woven fabric through 3D printing process, Sci. Rep. 9 (2019). https://doi.org/10.1038/s41598-019-50832-7.

[122] R. Winters, A. Winters, R.G. Amedee, Statistics: A Brief Overview, Ochsner J. 10 (2010) 213–216. http://www.ochsnerjournal.org/content/10/3/213.

[123] L. Linsell, P. Hardy, Statistics in medical research, Introd. to Res. Methodol. Spec. Trainees. (2017) 110–118. https://doi.org/10.1017/9781107585775.016.

[124] J. Gould, Variables in Research Designs, Concise Handb. Exp. Methods Behav. Biol. Sci. 3 (2001) 75–110. https://doi.org/10.1201/9781420040869.ch4.

[125] Z. Ali, S.B. Bhaskar, Basic statistical tools in research and data analysis, Indian J. Anaesth. 60 (2016) 662–669. https://doi.org/10.4103/0019-5049.190623.

[126] A. Yosipof, K. Shimanovich, H. Senderowitz, Materials Informatics: Statistical Modeling in Material Science, Mol. Inform. 35 (2016) 568–579. https://doi.org/10.1002/minf.201600047.

[127] G. Piir, I. Kahn, A.T. García-Sosa, S. Sild, P. Ahte, U. Maran, Best practices for QSAR model reporting: Physical and chemical properties, ecotoxicity, environmental fate, human health, and toxicokinetics endpoints, Environ. Health Perspect. 126 (2018) 1–20. https://doi.org/10.1289/EHP3264.

[128] V. Venkatraman, P.O. Åstrand, B.K. Alsberg, Quantitative structure-property relationship modeling of Grätzel solar cell dyes, J. Comput. Chem. 35 (2014) 214–226. https://doi.org/10.1002/jcc.23485.

[129] A. Sosnowska, M. Barycki, A. Gajewicz, M. Bobrowski, S. Freza, P. Skurski, S. Uhl, E. Laux, T. Journot, L. Jeandupeux, H. Keppner, T. Puzyn, Towards the Application of Structure–Property Relationship Modeling in Materials Science: Predicting the Seebeck Coefficient for Ionic

Liquid/Redox Couple Systems, ChemPhysChem. (2016) 1591–1600. https://doi.org/10.1002/cphc.201600080.

[130] D. Xue, P. V. Balachandran, J. Hogden, J. Theiler, D. Xue, T. Lookman, Accelerated search for materials with targeted properties by adaptive design, Nat. Commun. 7 (2016) 1–9. https://doi.org/10.1038/ncomms11241.

[131] J.N. Grima, D. Attard, R. Gaff, R.N. Cassar, A novel process for the manufacture of auxetic foams and for their re-conversion to conventional form, Adv. Eng. Mater. 11 (2009) 533–535. https://doi.org/10.1002/adem.200800388.

[132] J. Neuß, M. Kreuziger, N. Grimmelsmann, M. Korger, A. Ehrmann, Interaction between 3D deformation of textile fabrics and imprinted lamellae, (2016).

[133] and A.E. E. Kreikebaum, M. Kreuziger, M. Doerfel, K. Finsterbusch, 3D printing of Braille on textiles, Tech. Text. Int. 59 (2016) 187–188.

[134] L. Bouapao, H. Tsuji, K. Tashiro, J. Zhang, M. Hanesaka, Crystallization, spherulite growth, and structure of blends of crystalline and amorphous poly(lactide)s, Polymer (Guildf). 50 (2009) 4007–4017. https://doi.org/10.1016/j.polymer.2009.06.040.

[135] D. Battegazzore, S. Bocchini, A. Frache, Crystallization kinetics of poly(lactic acid)-talc composites, Express Polym. Lett. 5 (2011) 849–858. https://doi.org/10.3144/expresspolymlett.2011.84.

[136] Natalia Herrera Vegas, Processing and Properties of Nanocomposites Based on Polylactic Acid, Chitin and Cellulose, 2017.

[137] M. Studebaker, Compounding with Carbon Black, in: Reinf. Elastomers, Interscience Publishers, 1965.

[138] J.B. Donnet, E. Custodero, Reinforcement of Elastomers by Particulate Fillers, Sci. Technol. Rubber. (2005) 367–400. https://doi.org/10.1016/B978-012464786-2/50011-0.

[139] Extrusion of polymers, (n.d.). http://www.substech.com/dokuwiki/doku.php?id=extrusion_of_polymers (accessed May 14, 2020).

[140] K.J.H. George, N. Andrew, Development of a Co-Rotating , Fully Intermeshing Twin-Screw Extruder Model for the Extrusion of Natural Fibre Suspensions Keywords, 2019.

[141] Single and twin screw extruders, (n.d.). http://ptfe-machinery.com/polymer-screw-extrusion/

(accessed May 14, 2020).

[142] D.B. Malpass, Introduction to Industrial Polyethylene: Properties, Catalysts, Processes, (2010).

[143] Polyethylene (PE): LDPE, LLDPE and HDPE Properties Comparison, (n.d.). https://omnexus.specialchem.com/selection-guide/polyethylene-plastic/hdpe-ldpe-lldpe-comparison (accessed May 12, 2020).

[144] T. Graunke, K. Schmitt, J. Wöllenstein, Organic Membranes for Selectivity Enhancement of Metal Oxide Gas Sensors, J. Sensors. 2016 (2016). https://doi.org/10.1155/2016/2435945.

[145] Polyolefin-Based Thermoplastic Elastomers, in: Handb. Thermoplast. Elastomers, n.d.

[146] X. Wang, S. Hu, Y. Guo, G. Li, R. Xu, Toughened high-flow polypropylene with polyolefin-based elastomers, Polymers (Basel). 11 (2019) 1–16. https://doi.org/10.3390/polym11121976.

[147] S. Iijima, Helical microtubules of graphitic carbon, Nature. 354 (1991) 56–58.

[148] M. Monthioux, Carbon Meta-Nanotubes: Synthesis, Properties and Applications, Carbon Meta-Nanotubes Synth. Prop. Appl. (2011) 1–426. https://doi.org/10.1002/9781119954743.

[149] KETJENBLACK Highly Electro-Conductive Carbon Black, (n.d.). https://www.lion-specialty-chem.co.jp/en/product/carbon/carbon01.htm (accessed May 12, 2020).

[150] Y. Song, H. Do, H. Joo, D. Lim, H. Kim, Y. Song, H. Do, H. Joo, Effect of grafting of acrylic acid onto PET film surfaces by UV irradiation on the adhesion of PSAs Effect of grafting of acrylic acid onto PET film surfaces by UV irradiation on the adhesion of PSAs, 4243 (2012). https://doi.org/10.1163/156856106778456564.

[151] POLLEN PAM (PELLET ADDITIVE MANUFACTURING), (n.d.). https://erpro-group.com/en/pollen-pam (accessed June 19, 2020).

[152] M. Sotton, G.U.Y. Nemoz, New surface treatments and new fibers: the challenge to satisfy new requirements for technical textiles, 24 (1994) 138–151.

[153] F. Leroux, C. Campagne, A. Perwuelz, L. Gengembre, Atmospheric air plasma treatment of polyester textile materials. Textile structure influence on surface oxidation and silicon resin adhesion, Surf. Coatings Technol. 203 (2009) 3178–3183. https://doi.org/https://doi.org/10.1016/j.surfcoat.2009.03.045.

[154] B. Ghimire, D.P. Subedi, R. Khanal, Improvement of wettability and absorbancy of textile using atmospheric pressure dielectric barrier discharge, AIP Adv. 7 (2017).

https://doi.org/10.1063/1.4993084.

[155] C.W. Kan, W.S. Man, Surface characterisation of atmospheric pressure plasma treated cotton fabric-Effect of operation parameters, Polymers (Basel). 10 (2018). https://doi.org/10.3390/polym10030250.

[156] F. Leroux, A. Perwuelz, C. Campagne, N. Behary, Atmospheric air-plasma treatments of polyester textile structures, J. Adhes. Sci. Technol. 20 (2006) 939–957. https://doi.org/10.1163/156856106777657788.

[157] Q. Wei, Y. Liu, D. Hou, F. Huang, Dynamic wetting behavior of plasma treated PET fibers, J. Mater. Process. Technol. 194 (2007) 89–92. https://doi.org/https://doi.org/10.1016/j.jmatprotec.2007.04.001.

[158] F. et al. Leroux, Etude des traitements par plasma à pression atmosphérique - Applications à l’industrie textile, ENSAIT, 2006.

[159] Textile chemistry, (n.d.). http://drmsparmar.blogspot.com/2014/10/desizing-using-low-temperature-plasma.html (accessed May 15, 2020).

[160] CHROMOJET, (n.d.). https://www.zimmer-kufstein.com/en/content/chromojettabletop-printer (accessed May 15, 2020).

[161] M. Chabal, What does ‘digital transformation’ really mean?, Mark. Week. (2016) 1–12. http://goo.gl/ZugH9L.

[162] Y. Xiao, J. Che, A. Bergeret, C. Mao, J. Shen, Hydrodegradation of starch incorporated polylactic acid with acrylic acid as interfacial linker, E-Polymers. (2010). https://doi.org/10.1515/epoly.2010.10.1.57.

[163] B. Liu, H. Wang, Q.H. Qin, Modelling and characterization of effective thermal conductivity of single hollow glass microsphere and its powder, Materials (Basel). 11 (2018). https://doi.org/10.3390/ma11010133.

[164] B.E.W. Fischer, H.J. Sterzel, G. Wegner, Investigation of the structure of solution grown crystals of lactide copolymers by means of chemical reactions, 990 (1973) 980–990.

[165] A. Dittler, G. Kasper, A Critical Analysis of Capillary Flow Porometry with Regard to its Application to Non-Woven Fibrous Filter Media, (2018).

[166] D.H. Lee, N.G. Cho, Assessment of surface profile data acquired by a stylus profilometer, Meas.

Sci. Technol. 23 (2012). https://doi.org/10.1088/0957-0233/23/10/105601.

[167] P.A. Eutionnat-diffo, Y. Chen, J. Guan, A. Cayla, C. Campagne, V. Nierstrasz, Study of the Wear Resistance of Conductive Poly Lactic Acid Monofilament 3D Printed onto Polyethylene Terephthalate Woven Materials, Materials (Basel). 13 (2020) 2334. https://doi.org/10.3390/ma13102334.

[168] I. Erukhimovich, M.O. de la Cruz, Phase equilibria and charge fractionation in polydisperse polyelectrolyte solutions, (2004) 1808–1820. https://doi.org/10.1002/polb.

[169] D. Wu, Q. Lv, S. Feng, J. Chen, Y. Chen, Y. Qiu, X. Yao, Polylactide composite foams containing carbon nanotubes and carbon black: Synergistic effect of filler on electrical conductivity, Carbon N. Y. 95 (2015) 380–387. https://doi.org/10.1016/j.carbon.2015.08.062.

[170] O. Falode, E. Manuel, Wettability Effects on Capillary Pressure, Relative Permeability, and Irredcucible Saturation Using Porous Plate, J. Pet. Eng. 2014 (2014) 1–12. https://doi.org/10.1155/2014/465418.

[171] F.M. Fowkes, ATTRACTIVE FORCES AT INTERFACES, Ind. Eng. Chem. 56 (1964) 40–52. https://doi.org/10.1021/ie50660a008.

[172] R. Cardinaud, T. McNally, Localization of MWCNTs in PET/LDPE blends, Eur. Polym. J. 49 (2013) 1287–1297. https://doi.org/https://doi.org/10.1016/j.eurpolymj.2013.01.007.

[173] E. Karaca, N. Kahraman, S. Omeroglu, B. Becerir, Effects of fiber cross sectional shape and weave pattern on thermal comfort properties of polyester woven fabrics, Fibres Text. East. Eur. 92 (2012) 67–72.

[174] S.A. Mooneghi, S. Saharkhiz, S.M.H. Varkiani, Surface Roughness Evaluation of Textile Fabrics : A Literature Review, 9 (2014).

[175] N. Ezazshahabi, M. Latifi, K. Madanipour, Modelling of surface roughness based on geometrical parameters of woven fabrics Modelling of surface roughness based on geometrical parameters of woven fabrics, (2017).

[176] N. Song, X. Xin, H. Liu, B. Xu, B. Li, Y. Li, S. Hou, Y. Yu, Effects of different macrodiols as soft segments on properties of waterborne polyurethane, J. Polym. Res. 26 (2019). https://doi.org/10.1007/s10965-019-1793-6.

[177] P.A. Eutionnat-diffo, Y. Chen, J. Guan, A. Cayla, C. Campagne, V. Nierstrasz, Enhancement of adhesion properties of polylactic acid monofilament 3D printed onto polyethylene terephthalate

fabrics through surface functionalization and use of adhesives, Submitt. Rapid Prototyp. J. (2020).

[178] Z.M. Mahdieh, S. Shekarriz, F.A. Taromi, M. Montazer, Obtention of 74:26 polyester/cellulose fabric blend with super-hydrophobic and super-hydrophilic properties by air corona discharge treatment and their characterization, Carbohydr. Polym. 198 (2018) 17–25. https://doi.org/10.1016/j.carbpol.2018.06.007.

[179] T.-T.-N. Nguyen, Y.-H. Chen, M.-Y. Chen, K.-B. Cheng, J.-L. He, Multifunctional Ti-O coatings on polyethylene terephthalate fabric produced by using roll-to-roll high power impulse magnetron sputtering system, Surf. Coat. Technol. 324 (2017) 249–256. https://doi.org/10.1016/j.surfcoat.2017.05.082.

[180] Y. Wang, W. Yu, Surface Characterization of Low Temperature Plasma-Induced Cashmere Fibre by Air Gas, FIBRES Text. East. Eur. 25 (2017) 37–41. https://doi.org/10.5604/01.3001.0010.4625.

[181] I.B. Khalifa, N. Ladhari, B. Nemeshwaree, C. Campagne, Crosslinking of Sericin on air atmospheric plasma treated polyester fabric, J. Text. Inst. 108 (2017) 840–845. https://doi.org/10.1080/00405000.2016.1193983.

[182] P. Mendhe, G. Arolkar, S. Shukla, R. Deshmukh, Low-temperature plasma processing for the enhancement of surface properties and dyeability of wool fabric, J. Appl. Polym. Sci. 133 (2016). https://doi.org/10.1002/APP.43097.

[183] N.A. Ibrahim, M.M. Hashem, M.A. Eid, R. Refai, M. El-Hossamy, B.M. Eid, Eco-friendly plasma treatment of linen-containing fabrics, J. Text. Inst. 101 (2010) 1035–1049. https://doi.org/10.1080/00405000903205467.

[184] K.N. Pandiyaraj, V. Selvarajan, Non-thermal plasma treatment for hydrophilicity improvement of grey cotton fabrics, J. Mater. Process. Technol. 199 (2008) 130–139. https://doi.org/10.1016/j.jmatprotec.2007.07.046.

[185] G. Rosace, R. Canton, Influence of low-temperature plasma conditions on wicking properties of PA/PU knitted fabric, J. Appl. Polym. Sci. 107 (2008) 3702–3706. https://doi.org/10.1002/app.27547.

[186] C. Riccardi, R. Barni, E. Selli, G. Mazzone, M.R. Massafra, B. Marcandalli, G. Poletti, Surface modification of poly(ethylene terephthalate) fibers induced by radio frequency air plasma treatment, Appl. Surf. Sci. 211 (2003) 386–397. https://doi.org/https://doi.org/10.1016/S0169-4332(03)00265-4.

[187] A.M. WROBEL, M. KRYSZEWSKI, W. RAKOWSKI, M. OKONIEWSKI, Z. KUBACKI, EFFECT OF PLASMA TREATMENT ON SURFACE-STRUCTURE AND PROPERTIES OF POLYESTER FABRIC, Polymer (Guildf). 19 (1978) 908–912. https://doi.org/10.1016/0032-3861(78)90197-0.

[188] T. Vatu\vna, P. Špatenka, J. Píchal, J. Koller, L. Aubrecht, J. Wiener, PES fabric plasma modification, Czechoslov. J. Phys. 54 (2004) C475. https://doi.org/10.1007/BF03166441.

[189] T. Sebastian, T. Lusiola, F. Clemens, Ferroelectric hybrid fibers to develop flexible sensors for shape sensing of smart textiles and soft condensed matter bodies, SMART Mater. Struct. 26 (2017). https://doi.org/10.1088/1361-665X/aa5bd2.

[190] C.X. Wang, Y. Ren, Y.P. Qiu, Penetration depth of atmospheric pressure plasma surface modification into multiple layers of polyester fabrics, Surf. Coatings Technol. 202 (2007) 77–83. https://doi.org/https://doi.org/10.1016/j.surfcoat.2007.04.077.

[191] C.X. Wang, M. Du, Y.P. Qiu, Influence of pore size on penetration of surface modification into woven fabric treated with atmospheric pressure plasma jet, Surf. Coatings Technol. 205 (2010) 909–914. https://doi.org/https://doi.org/10.1016/j.surfcoat.2010.08.056.

[192] N. Vrinceanu, M.I. Guignard, C. Campagne, S. Giraud, R.I. Prepelita, D. Coman, V.D. Petrescu, D.D. Dumitrascu, N. Ouerfelli, M.P. Suchea, Correlation between surface engineering and deformation response of some natural polymer fibrous systems, J. Eng. Fiber. Fabr. 13 (2018).

[193] A. Kausar, Contemporary applications of carbon black-filled polymer composites: An overview of essential aspects, 2017. https://doi.org/10.1177/8756087917725773.

[194] M. Narkis, Electrical Behavior and Structure of Polypropylene / Ultrahigh Molecular Weight Polyethylene / Carbon Black Immiscible Blends, (2001) 104–115.

[195] C. Zhang, C.-A. Ma, P. Wang, M. Sumita, Temperature dependence of electrical resistivity for carbon black filled ultra-high molecular weight polyethylene composites prepared by hot compaction, Carbon N. Y. 43 (2005) 2544–2553. https://doi.org/10.1016/j.carbon.2005.05.006.

[196] J.J. Kolstad, Crystallization kinetics of poly(L-lactide-co-meso-lactide), J. Appl. Polym. Sci. 62 (1996) 1079–1091. https://doi.org/10.1002/(SICI)1097-4628(19961114)62:7<1079::AID-APP14>3.0.CO;2-1.

[197] W. Zhai, Y. Ko, W. Zhu, A. Wong, C.B. Park, A study of the crystallization, melting, and foaming behaviors of polylactic acid in compressed CO2, Int. J. Mol. Sci. 10 (2009) 5381–5397.

https://doi.org/10.3390/ijms10125381.

[198] M.C. (National R.C. of I. for C. and P.P. Righetti, Crystallization of Polymers Investigated by Temperature-Modulated DSC, (2017). https://doi.org/10.3390/ma10040442.

[199] V. Taubner, R. Shishoo, Influence of processing parameters on the degradation of poly(L-lactide) during extrusion, J. Appl. Polym. Sci. 79 (2001) 2128–2135. https://doi.org/10.1002/1097-4628(20010321)79:12<2128::AID-APP1020>3.0.CO;2-#.

[200] H. Ma, Y. Li, Y. Luo, The Effect of Fiber Yarns Structure on the Mechanical Properties of Natural Fiber Reinforced Composites, in: 18TH Int. Conf. Compos. Mater., 2011.

[201] M.P. Saiman, M.S. Wahab, M.U. Wahit, The Effect of Fabric Weave on Tensile Strength of Woven Kenaf Reinforced Unsaturated Polyester Composite, Int. Colloqium Text. Eng. Fash. Appar. Des. 2014. (2014) 52–56. https://doi.org/10.4028/www.scientific.net/AMM.564.422.

[202] N. GAA, Effect of weave structure and weft density on the physical and mechanical properties of micro polyester woven fabrics, Life Cycle J. 9 (2012) 1326–1331.

[203] Z.A. Malik, A. Tanwari, H. Sheikh, Influence of Plain and Twill (3/1) Weave Designs on the Tensile Strength of PC Blended Fabrics, Mehran Univerisity Res. J. Eng. Technol. 30 (2011) 23–28.

[204] P.S. Chum, K.W. Swogger, Olefin polymer technologies-History and recent progress at The Dow Chemical Company, Prog. Polym. Sci. 33 (2008) 797–819. https://doi.org/10.1016/j.progpolymsci.2008.05.003.

[205] G. Wu, B. Li, J. Jiang, Carbon black self-networking induced co-continuity of immiscible polymer blends, Polymer (Guildf). 51 (2010) 2077–2083. https://doi.org/10.1016/j.polymer.2010.03.007.

[206] P.A. Eutionnat-Diffo, Y. Chen, J. Guan, A. Cayla, X. Zeng, V. Nierstrasz, C. Campagne, Development of Flexible and Conductive Immiscible Thermoplastic/Elastomer Monofilament for Smart Textiles Applications using 3D Printing, 12(10), 23 (2020). https://doi.org/https://doi.org/10.3390/polym12102300.

[207] D.K. Owens, R.C. Wendt, Estimation of the surface free energy of polymers, J. Appl. Polym. Sci. 13 (1969) 1741–1747. https://doi.org/10.1002/app.1969.070130815.

[208] S.J. Park, J.S. Kim, Surface energy characterization of modified carbon blacks and its relationship to composites tearing properties, J. Adhes. Sci. Technol. 15 (2001) 1443–1452. https://doi.org/10.1163/156856101753213295.

[209] A. Nuzzo, E. Bilotti, T. Peijs, D. Acierno, G. Filippone, Nanoparticle-induced co-continuity in immiscible polymer blends - A comparative study on bio-based PLA-PA11 blends filled with organoclay, sepiolite, and carbon nanotubes, Polymer (Guildf). 55 (2014) 4908–4919. https://doi.org/10.1016/j.polymer.2014.07.036.

[210] Z. Refaa, M. Boutaous, S. Xin, D.A. Siginer, Thermophysical analysis and modeling of the crystallization and melting behavior of PLA with talc: Kinetics and crystalline structures, J. Therm. Anal. Calorim. 128 (2017) 687–698. https://doi.org/10.1007/s10973-016-5961-1.

[211] Z. Yang, H. Peng, W. Wang, T. Liu, Crystallization behavior of poly(ε-caprolactone)/layered double hydroxide nanocomposites, J. Appl. Polym. Sci. 116 (2010) 2658–2667. https://doi.org/10.1002/app.

[212] X. Shi, Z. Jing, G. Zhang, Influence of PLA stereocomplex crystals and thermal treatment temperature on the rheology and crystallization behavior of asymmetric poly(L-Lactide)/poly(D-lactide) blends, J. Polym. Res. 25 (2018). https://doi.org/10.1007/s10965-018-1467-9.

[213] T.H. Ku, C.A. Lin, Rheological properties of thermoplastic polyvinyl alcohol and polypropylene blend melts in capillary extrusions, J. Polym. Res. 12 (2005) 23–29. https://doi.org/10.1007/s10965-004-0985-9.